

**Structure analysis of Phospholipase C -  
A virulence factor from *Pseudomonas aeruginosa***

Inaugural-Dissertation

zur Erlangung des Doktorgrades  
der Mathematisch-Naturwissenschaftlichen Fakultät  
der Heinrich-Heine-Universität Düsseldorf

vorgelegt von

**Nishika Sabharwal**

aus Sunam, Punjab, India

**Hamburg, July 2023**

aus dem Institut für  
der **Heinrich-Heine-Universität Düsseldorf**

Gedruckt mit der Genehmigung der  
Mathematisch-Naturwissenschaftlichen Fakultät der  
Heinrich-Heine-Universität Düsseldorf

Berichterstatter:

1. Prof. Dr. Jörg Labahn
2. Prof. Dr. Henrike Heise

Tag der mündlichen Prüfung:  
02 Oktober, 2024

*Dedicated to my Parents....*

## Contents

Abbreviations .....	i
List of Tables.....	iv
List of Figures .....	vi
1 Introduction .....	1
1.1 <i>Pseudomonas aeruginosa</i> - Gram-negative bacteria .....	1
1.2 Virulence factors of <i>P. aeruginosa</i> .....	3
1.3 Secretion systems in <i>P.aeruginosa</i> .....	5
1.4 The Phospholipases .....	9
1.5 The Phospholipase C of <i>Pseudomonas aeruginosa</i> .....	16
1.6 Aim of this study .....	21
2 Materials and methods .....	23
2.1 Instruments and Materials .....	23
2.1.1 Biological Materials.....	24
2.1.2 Kits and Buffers .....	25
2.2 Cloning .....	27
2.2.1 Site-directed mutagenesis .....	30
2.3 <i>In vivo</i> Expression .....	31
2.4 Protein Purification.....	31
2.4.1 Affinity Chromatography.....	32
2.4.2 Size Exclusion Chromatography.....	32
2.5 Protein Identification .....	34
2.5.1 SDS-PAGE and Western blot .....	34
2.5.2 Mass spectrometry and LC/mass-mass .....	35
2.6 Biophysical Characterization.....	37
2.6.1 Mass Photometry .....	37
2.6.2 Dynamic Light Scattering .....	37
2.6.3 Circular Dichroism.....	38
2.6.4 Fluorescence Spectroscopy .....	40
2.6.5 SEC-SAXS.....	41
2.6.6 Atomic Force Microscopy .....	44
2.7 Biochemical Characterization.....	45

2.7.1 In vivo (MTT assay) .....	45
2.7.2 In vitro.....	48
2.7.3 Hemolytic assay .....	48
2.8 Structure solution.....	49
2.8.1 X-ray Crystallography .....	49
2.8.2 Electron Microscopy .....	54
3 Results .....	58
3.1 Cloning of PLCH, PLCN, and PLCHR2.....	58
3.2 Expression of PLCHR2 complex and, PLCN .....	59
3.3 PLCN and PLCHR complex was purified in high quality and quantity. ....	62
3.3.1 PLCN purification.....	62
3.3.2 PLCHR2 complex purification .....	63
Identity and integrity of PLCN and PLCHR complex .....	65
3.4 Biophysical Characterization.....	70
3.4.1 Mass Photometry .....	70
3.4.2 Dynamic Light Scattering .....	71
3.4.3 Circular Dichroism of PLCN and PLCHR Complex.....	73
3.4.4 Fluorescence Spectroscopy .....	75
3.4.5 SEC-SAXS.....	79
3.5 Biochemical Characterization.....	87
3.5.1 In vitro activity assay .....	87
3.5.2 In vivo cellular assay.....	91
3.5.3 Qualitative Hemolytic Assay for PLCN and PLCHR Complex .....	93
3.5.4 Atomic Force Microscopy .....	93
3.6 X-ray crystallography for PLCN .....	104
3.6.1 Crystallization of PLCN .....	104
3.6.2 Crystallization of PLCN with trypsin .....	108
3.6.3 Data Processing and model building.....	110
3.7 Electron Microscopy for PLCHR .....	117
3.7.1 Mono-dispersed particles in Negative staining.....	117
3.7.2 Cryo-EM data processing at 0°, 30°, 45° .....	117
4 Discussion .....	127
4.1 Overexpression and Functionality of PLCs of <i>P. aeruginosa</i> PA14.....	127
4.2 PLCs in Microbial Infections .....	133
4.3 Structures of the Gram-negative PLCs (Novel class of PLCs) .....	137

4.4 Insights into the proposed branched mechanism of <i>Pseudomonas</i> PLCs .....	152
4.5 Outlook .....	158
Summary .....	159
Zusammenfassung .....	161
Bibliography .....	163
Appendices .....	177
Appendix I: DNA and protein sequences .....	177
Appendix II: Primers .....	180
Appendix III Vectors .....	181
Appendix IV Space group and diffraction image .....	182
Appendix V Activity standards and sequence alignment .....	184
Acknowledgments .....	187
Erklärung .....	188

## Abbreviations

$\beta$ -mercaptoethanol (BME)  
Acid phosphatase A (AcpA)  
Agarose Gel Electrophoresis (AGE)  
Atomic Force Microscopy (AFM)  
ATP-binding cassette (ABC) transporter  
Beta Structure Selection (BeStSel)  
Bioliver (BL)  
Cardiolipin Synthetase (CLS)  
Ceramide (CM)  
Chronic Obstructive Pulmonary Disease (COPD)  
Circular Dichroism (CD)  
Complex Formation Significance Score (CSS)  
Deutsches Elektronen-Synchrotron (DESY)  
Dihydroxy Acetophenone (DHAP)  
Dimyristoyl-sn-Glycero-3-Phosphocholine (DMPC)  
Domain of Unknown Function (DUF)  
Dynamic Light Scattering (DLS)  
Electrospray Ionization (ESI)  
Electron Microscopy (EM)  
Ethylenediaminetetraacetic Acid (EDTA)  
False Discovery Rate (FDR)  
Fluorescence Spectrometry (FL)  
Gram- Negative Bacteria (GNB)  
Hemolytic Phospholipase C (PLCH)  
Higher-Order Structure (HOS)  
Horseradish Peroxidase (HRP)  
Hydrolase (PLC)  
Immobilized Metal Affinity Chromatography (IMAC)

Isopropyl  $\beta$ -D-1-thiogalactopyranoside (IPTG)

Lethal Dose (LD)

Lipopolysaccharides (LPS)

Liquid chromatography Mass/Mass Spectrometry (LC-MS/MS)

Lysogeny Broth (LB)

Mass Photometry (MP)

Mass Spectrometry (MS)

Mass-to-Charge Ratios (m/z)

Matrix-Assisted Laser Desorption/Ionization (MALDI)

Melting Temperature (TM)

Molecular Weight (MW)

Mono-Tezolium (MTT)

Multi-Angle Laser Light Scattering (MALLS)

Multi Drug Resistant (MDR)

Non-Hemolytic Phospholipase C (PLCN)

Nonspecific Phospholipase C (NPC)

Outer Membrane (OM)

P-nitrophenylphosphorylcholine (p-NPPC)

Pathogenicity Island (PAI)

Peptide Mass Fingerprint (PMF)

Phosphate (Pi)

Phosphatidic acid (PA)

Phosphatidylcholine (PC)

Phosphatidylinositol (PI)

Phospholipase (PLCH)

Phospholipase A (PLA)

Phospholipase B (PLB)

Phospholipase C (PLC)

Phospholipase C Specific of Phosphatidyl-ethanolamine (PLCB)

Phospholipase D (PLD)

Phospholipids (PLs)

Phosphatidylserine (PS)  
Polyethylene Glycol (PEG)  
Polymerase Chain Reaction (PCR)  
Polyvinylidene Difluoride (PVDF)  
Phospholipase R - Chaperon of PLCH (PLCR2)  
Quasi Elastic Light Scattering (QELS)  
Red Blood Cells (RBCs)  
Refractive Index (RI)  
Scanning Probe Microscopy (SPM)  
Site-Directed Mutagenesis (SDM)  
Size Exclusion Chromatography (SEC)  
Small - Angle X-ray Scattering (SAXS)  
Sodium Dodecyl Sulphate Polyacrylamide Gel Electrophoresis (SDS-PAGE)  
Sphingomyelinase (SMase)  
Super Optimal Broth (SOB)  
Supported lipid Bilayers (SLBs)  
Transmission Electron Microscope (TEM)  
Trichloroethanol (TCE)  
Twin Arginine Translocase (TAT)  
Twin-Arginine Translocation (TAT)  
Type I-VI Secretion System (T1-6SS)  
Ventilator-Associated Pneumonia (VAP)

## List of Tables

Table 1.1 Bacterial Plcs That Contribute To Virulence (Table Adapted From Flores-Díaz Et.Al.) <sup>32</sup> .....	12
Table 2.1 Instruments.....	23
Table 2.2 Materials.....	23
Table 2.3 Biological Strains.....	24
Table 2.4 Expression Vectors.....	25
Table 2.5 Medium For Bacterial And Mammalian Culture.....	25
Table 2.6 Buffers For Gel Electrophoresis.....	25
Table 2.7 Sodium Dodecyl Sulphate–Polyacrylamide Gel Electrophoresis (Sds-Page) .....	26
Table 2.8 Buffers For Purification .....	27
Table 2.9 Pcr Reaction Components .....	28
Table 2.10 Pcr Program.....	28
Table 2.11 Restriction Enzyme Digestion Reaction .....	29
Table 2.12 Dpn1 Digestion Reaction .....	30
Table 2.13 Phosphorylation Reaction .....	31
Table 2.14 Parameters For Cryo-Em Data Collection .....	57
Table 3.1 Molecular Description Of Plch, Plcr2 And Plcn.....	58
Table 3.2 N Terminal To C Terminal Sequence Coverage From Lc-Mass/Mass.....	66

Table 3.3 Physical Characterization Of Plcn Using Dls .....	72
Table 3.4 Physical Characterization Of Plchr2 Using Dls .....	72
Table 3.5 Deconvolutions Of Cd Signal Of Plchr2 Complex And Plcn .....	75
Table 3.6 Sec-Saxs, Malls And Parameter Summary For Plchr2 .....	82
Table 3.7 Crystallization Hits For Initial Crystallization Screen And Optimization Steps. ..	107
Table 3.8 Data Collection And Refinement Statistics For A Plcn Crystal .....	112
Table 3.9 Cryo-Em Structure Refinement Statistics For Plch Monomer.....	122
Table 4.1 Comparison Of Secondary Structures Of Plcn Measured From X-Ray Crystallography And Cd Spectrometry (190-250nm).....	145
Table 4.2 Comparison Of Secondary Structures Of Plchr2 Measured From X-Ray Crystallography And Cd Spectrometry (190-250nm).....	146

## List of Figures

Figure 1.1 A High Resolution Image Of <i>Pseudomonas Aeruginosa</i> (Figure Adapted From Tsang Et Al. <sup>5</sup> ).....	1
Figure 1.2 Comparison Of Pao1 And Pa14 Strains Of <i>Pseudomonas Aeruginosa</i> (Figure Adapted From Grace Et.Al. <sup>6</sup> ).....	2
Figure 1.3 Schematic Presentation Of The Main Virulence Factors Used By <i>P. Aeruginosa</i> During Respiratory Infections ( <i>Figure Adapted From Pollack Et.Al.<sup>12</sup></i> ).....	4
Figure 1.4 Secretion Systems In <i>P. Aeruginosa</i> (Figure Adapted From Filloux Et.Al. <sup>15</sup> ).....	6
Figure 1.5 Schematic Diagram Of Type Two Secretion System (T2ss) (Figure Adapted From Sauvage Et.Al. <sup>28</sup> ).....	8
Figure 1.6 Different Classes Of Plc Based On Their Mode Of Action (Figure Adapted From Vasil Et.Al. <sup>31</sup> ).....	10
Figure 1.7 Domain Structures Of Mammalian Plc Isozymes (Figure Adapted From Singh Et.Al. <sup>47</sup> ).....	14
Figure 1.8 Structure Of Plc-B2 (Pdb 2zkm) With Domains (Figure Adapted From Singh Et.Al. <sup>47</sup> ).....	15
Figure 1.9 Potential Products Generated By Plcs Of <i>Pseudomonas Aeruginosa</i> (Figure Adapted From Vasil Et.Al. <sup>31</sup> ).....	18
Figure 1.10 Genetic Makeup Of Plc Genes (Figure Adapted From Stonehouse Et.Al. <sup>53</sup> ).....	20
Figure 1.11 Mode Of Action Of Plch And Plcn Of <i>Pseudomonas Aeruginosa</i> .....	21
Figure 1.12 Correlation Of Virulence Phenotypes And Gene Expression Data Of 414 Clinical Isolates ( <i>Figure Adapted From Kordes Et.Al.<sup>76</sup></i> ).....	22
Figure 2.1 This Image Illustrates The Process Of Size Exclusion Chromatography (Sec) ( <i>Figure Adapted From Barth Et.Al.<sup>96</sup></i> ).....	33
Figure 2.2 Maldi-Tof Workflow (Figure Adapted From Hou Et.Al. <sup>106</sup> ).....	36

Figure 2.3: Cd Spectra Displaying Types Of Secondary Structures : A-Helix, A B-Sheet, And A Random Coil ( <i>Figure Adapted From Rogers Et.Al.<sup>114</sup></i> ) .....	39
Figure 2.4: Jablonski's Diagram Illustrating Transitions Associated With Fluorescence And Phosphorescence ( <i>Figure Adapted From Lakowicz Et.Al.<sup>117</sup></i> ) .....	40
Figure 2.5 Sec-Saxs/Tda Set-Up At The Embl-P12 Beamline ( <i>Figure Adapted From Blanchet Et.Al.<sup>119</sup></i> ) .....	43
Figure 2.6 Schematic Diagram Of Atomic Force Microscopy ( <i>Figure Adapted From Khurshudov Et.Al.<sup>128</sup></i> ) .....	44
Figure 2.7 Schematic Diagram Of Mtt Assay ( <i>Figure Adapted From Losada-Garcia Et.Al.<sup>131</sup></i> ) .....	47
Figure 2.8 Chemical Reaction Showing The Cleavage Of The Nppc (P - Nitrophenylphosphorylcholine) By Plc .....	48
Figure 2.9 Different Types Of Hemolysis ( <i>Figure Adapted From Savardi Et.Al.<sup>136</sup></i> ).....	49
Figure 2.10 The Phase Diagram For The Crystallization Of Macromolecules ( <i>Figure Adapted From Mcpherson Et.Al.<sup>138</sup></i> ) .....	51
Figure 3.1 Schematic Diagram For Gene Constructs Of Plch, Plcr2 And Plcn .....	58
Figure 3.2 Agarose Gel Showing Colony Pcr (Cpcr).....	59
Figure 3.3 Sds Page Showing Expression And Solubility Test Of Plcn .....	60
Figure 3.4 Sds Page Showing Expression And Solubility Test Of Plch And Plcr2.....	61
Figure 3.5 Purification Profile Of Plcn .....	63
Figure 3.6 Purification Profile Of Plchr2 .....	64
Figure 3.7 Plchr2 Complex Polished With Sec .....	65
Figure 3.8 Anti His Western Blot A. Plch And Plcr2, B. Plcn .....	66

Figure 3.9 Maldi/Tof M/Z Spectrum A: Plchr2 And B: Plcn .....	67
Figure 3.10 Peptides Identification By Lc-Ms/Ms Analysis .....	69
Figure 3.11 Mass Distribution Histogram Of A: Plcn B: Plchr2 .....	71
Figure 3.12 Autocorrelation Function And Distribution Of Particle Sizes Using Dls Of Plcn	71
Figure 3.13 Autocorrelation Function And Distribution Of Particle Sizes Using Dls Of Plchr2 .....	72
Figure 3.14 Cd Spectroscopy Of Plcn .....	74
Figure 3.15 Cd Spectroscopy Of Plchr2 Complex .....	75
Figure 3.16 Fluorescence Spectrometry Of Plcn .....	76
Figure 3.17 Fluorescence Spectrometry Of Plchr2 Complex .....	78
Figure 3.18 A. Malls, $\text{Cm}^{-1}$ (Blue) And Dri, $\text{Ml.G}^{-1}$ (Red) Data Obtained For The Sec Of Plchr2. ....	80
Figure 3.19 Final Merged Saxs Profile Of The Plchr2 Complex, And Corresponding Linear Guinier Plot (Inset).....	80
Figure 3.20 A. A Kratky Plot Representation Of The Saxs Data. B. The Calculated $P(R)$ Vs Profile Of The Compact Plchr2 Complex. ....	81
Figure 3.21 The Most Likely Predicted Shape Topology Of Plchr2.....	84
Figure 3.22 Alphafold Predicted Models Of Plch And Plcr2 (Yielding Relatively High Confidence). ....	85
Figure 3.23 Coral-Refined Rigid Body Models Of Plcr2 Bound To The N-Terminal Domain Of Plch.....	87
Figure 3.24 <i>In Vitro</i> Enzyme Activity Using Nppc Assay.....	88
Figure 3.25 <i>In Vitro</i> Activity Using Nppc Assay For Point Mutants Of The Active Site .....	89

Figure 3.26 Comparison Of Wild Type <i>In Vitro</i> Enzymatic Activity Using Nppc Assay Mutants.....	90
Figure 3.27 Effect Cations Ca <sup>2+</sup> , Mg <sup>2+</sup> , Zn <sup>2+</sup> And Edta On Enzymatic Activity .....	90
Figure 3.28 <i>In Vivo</i> Enzyme Activity Using Mtt Assay .....	92
Figure 3.29 Qualitative Hemolytic Assay .....	93
Figure 3.30 Afm Image Of Mica Freshly Cleaved Mica .....	94
Figure 3.31 Afm Image Of Pbs Buffer On Mica.....	95
Figure 3.32 Afm Image Of Phospholipase C (Plchr2) In Pbs Buffer On Mica .....	95
Figure 3.33 Afm Image Of Lipid Membrane In Pbs Buffer On Mica .....	96
Figure 3.34 Afm Image Of Lipid Membrane In Pbs Buffer On Mica .....	97
Figure 3.35 Afm Image With Plchr2 With Lipid Bilayer In Buffer On Mica Scanned For 7 To 21 Minutes.....	98
Figure 3.36 The Average Volume Of The Digested Membrane Incubated With Plchr2 From 475 S To 1287 S.....	99
Figure 3.37 Analysis Of Afm Image With Plchr2 With Lipid Bilayer In Buffer On Mica After 20 Minutes.....	100
Figure 3.38 Afm Image With Plchr2 With Lipid Bilayer In Buffer On Mica Scanned For 24 To 30 Minutes .....	100
Figure 3.39 Analysis Of Afm Image With Plchr2 With Lipid Bilayer In Buffer On Mica After 30 Minutes.....	101
Figure 3.40 The Average Volume Of The Ring-Like Structures At The Top Of The Hole Rims From 1444 S To 1788 S After The Enzyme Incubation. ....	102
Figure 3.41. Afm Image With Plchr2 With Lipid Bilayer In Buffer On Mica Scanned For 48 To 68 Minutes .....	103

Figure 3.42 Analysis Of Afm Image With Plchr2 With Lipid Bilayer In Buffer On Mica After 1 Hour.....	103
Figure 3.43 Thin Needle Crystals Of Plcn Under Visible (A-F) Light And Uv (G,H).....	105
Figure 3.44 Needle Crystals Of Plcn Obtained After 10-14 Weeks Using Fine Screen Under Visible (A-F) Light And Uv (G,H) .....	106
Figure 3.45 Sds Page Of Plcn In Solution And Plcn As A Crystal.....	108
Figure 3.46 Plcn Crystals Obtained After 15 Days Of Incubation Under Visible (A, B) And Uv Light (C, D) .....	109
Figure 3.47 Data Processing Of Plcn Crystal.....	109
Figure 3.48 Topology And Secondary Structure Content Of Plcn.....	111
Figure 3.49 Coordination Of Calcium Ion Present In The Active Site Of Plcn.....	112
Figure 3.50 Ramachandran Plot Obtained After Phenix Refine With Calcium And B-Mercaptoethanol.....	113
Figure 3.51 Dimeric Structure Of Plcn, The Arrow Denotes The Non-Crystallographic Molecular 2-Fold Symmetry Axis.....	114
Figure 3.52 Active Site Of Plcn .....	115
Figure 3.53 Stereographic Drawing Of The Plcn Active Center .....	116
Figure 3.54 Micrographs Negatively Stained With 1% Uranyl Acetate Showing Monodispersed Particles (A) Using Buffer (B) As A Control .....	117
Figure 3.55 Cryo-Em Processing Of Monomeric Plch A. Workflow Of Single-Particle Cryo-Em Analysis .....	119
Figure 3.56 Cryoem Data Processing Of Monomeric Plch.....	120
Figure 3.57 Plch Alpha Fold Model Fitted Into The Map Constructure By Cryoem .....	121

Figure 3.58 Active Center Of Plch.....	121
Figure 3.59 Topology And Secondary Structure Content Of Plch Monomer.....	124
Figure 3.60 Two Classes Of Plch Trimer Obtained From Cryoem Data Processing,.....	125
Figure 3.61 Two Classes Of Trimer Obtained After Data Processing.....	126
Figure 4.1 Visualization Of Tm At The Inflection Point And The Change In The Slope ( $T_{onset}$ ) .....	130
Figure 4.2 Far Uv Cd Spectrum Of Native Sample Sand Denatured Samples. ....	131
Figure 4.3 Graph Between Fl Signals At Excitation Temperature Vs Wavelength (295nm)	132
Figure 4.4 Two Possible Asymmetric Units In Crystal Structure Of Plcn .....	140
Figure 4.5 X-Ray Crystallography Structure Of Plcn (Brown) Superposed On Alphafold Model Of Plcn (Blue).....	142
Figure 4.6 X-Ray Crystallography Structure Of Plcn (Brown) Aligned With The Acpa Acid Phosphatase Of <i>Francisella Tularensis</i> (Yellow) .....	143
Figure 4.7 Micrograph Obtained From Cryoem Showing Different Oligomers 1. Monomer, 2, Dimer 3. Trimer.....	144
Figure 4.8 Alpha Fold Model Of Plch Used To Fit The Maps Obtained From Cryoem Data Processing.....	146
Figure 4.9 X-Ray Crystallography Structure Of Plcn (Brown) Aligned With Cryo Em Structure Of Plch (Magenta) .....	149
Figure 4.10 Cryo Em Structure Of Plch (Magenta) Superposed On Alphafold Model Of Plch (Blue).....	149
Figure 4.11 Cryoem Structure Of Plch (Magenta) Aligned With The Acpa Acid Phosphatase From <i>Francisella Tularensis</i> (Yellow) .....	150
Figure 4.12 The Proposed Mechanisms Of Action Of Phospholipase C (Plcs).....	152

Figure 4.13 Proposed Branched Pathway For Plcs Of *Pseudomonas Aeruginosa*. ..... 157

## 1 Introduction

### 1.1 *Pseudomonas aeruginosa* - Gram-negative bacteria

Hans Christian Gram invented Gram staining in 1884<sup>1</sup>. The Gram-staining procedure distinguishes two types of bacteria: gram-positive and -negative bacteria. Because Gram-positive bacteria lack an outer membrane, they are more sensitive to antibiotics. Antibiotics are less effective against Gram-negative bacteria (GNB) because they have an outer membrane and are more pathogenic than Gram-positive bacteria<sup>2</sup>. Because of their high antibiotic resistance, Gram-negative bacteria are considered the world's most serious public health issue<sup>3</sup>. These bacteria are clinically significant as they cause severe morbidity and mortality<sup>2</sup>. *Pseudomonas aeruginosa*, *Acinetobacter baumannii*, *Burkholderia cepacia*, *Burkholderia pseudomallei*, *Stenotrophomonas*, *Alcaligenes*, and *Moraxella* are the most common Non fermenter Gram-Negative bacteria that cause human diseases<sup>2</sup>.

*P. aeruginosa* is a prevalent bacterium in soil and water, as well as on animals and plants. This Gram-negative bacillus is aerobic, saccharolytic, and does not generate spores<sup>4</sup>. It measures 0.5 to 0.8  $\mu\text{m}$  by 1.5 to 3.0  $\mu\text{m}$ <sup>4</sup> (Figure 1.1). *P. aeruginosa* is a non-fermenting bacterium that is an obligate aerobe, yet it may grow anaerobically by using nitrate and arginine as final electron acceptors when  $\text{O}_2$  is unavailable<sup>4</sup>.



**Figure 1.1** A high resolution image of *Pseudomonas aeruginosa* (Figure adapted from Tsang et al. <sup>5</sup>)

A high-power scanning electron micrograph of *Pseudomonas aeruginosa* with polar pili adherent to the collagen surface. Scale bar=1  $\mu\text{m}$

## 1. Introduction

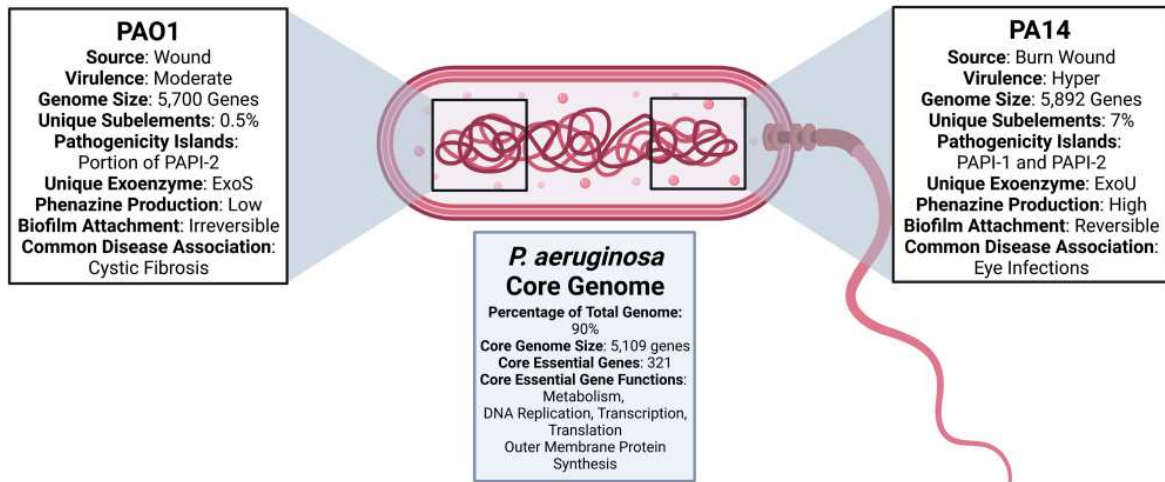


**Figure 1.2 Comparison of PAO1 and PA14 strains of *Pseudomonas aeruginosa*** (Figure adapted from Grace et.al.<sup>6</sup>)

*Pseudomonas aeruginosa* is a deadly and rising public health hazard worldwide, particularly in underdeveloped countries<sup>7</sup>. It remains a leading cause of illness and death in humans. It is the fourth most common nosocomial pathogen and can be challenging to eliminate due to its resistance to many antibiotics<sup>7</sup>. *Pseudomonas aeruginosa* is the most common cause of infections such as urinary tract infections, pneumonia, and bacteremia. It has also been detected in individuals with burns, surgical wounds, pus, and accidental lesions. When a patient's immune system is compromised, complications like chronic obstructive pulmonary disease (COPD), cystic fibrosis, cancer, traumas, burns, sepsis, and ventilator-associated pneumonia (VAP) including those caused by COVID-19 become worse<sup>8,9,10</sup>. *P. aeruginosa* being a Multi Drug Resistant (MDR) bacteria is intrinsically resistance to several antimicrobial agents and has gained resistance to the final stage antibiotics, such as carbapenems; beta-lactams (e.g., imipenem and meropenem)<sup>10</sup>. *P. aeruginosa* has been classified by WHO as a "critical" pathogen in desperate need of novel antibiotics<sup>10</sup>. PAO1 and PA14 have proven crucial in developing novel drug targets, testing novel therapies, and providing critical genetic knowledge on this pathogenic bacteria<sup>6</sup> (Figure 1.2). In this study, recombinant proteins from PA14 strain are used.

## 1.2 Virulence factors of *P. aeruginosa*

A microorganism's virulence is determined by its capacity to attach to a potential host, enter that host, reproduce there, and eventually the sickness will overwhelm the host and potentially kill it, whether it is local or systemic<sup>11</sup>. The genetic makeup of *P. aeruginosa* is the most extensively studied of all *Pseudomonas* species. All three common mechanisms of gene recombination—conjugation, transduction, and transformation are present in *P. aeruginosa*, unlike other *Pseudomonas* species making it important for studying antibiotic resistance<sup>9</sup>. In order to study the virulence factors of *Pseudomonas aeruginosa*, many genetic approaches have been applied such as transposon mutagenesis and molecular cloning along with classical techniques like chemical mutagenesis, conjugation, and transduction. These have helped significantly in isolating and characterizing virulence factors like toxins, hemolysins, lipases, proteases, however it is difficult to be precise. Thereby, recombinant DNA technology combined with the above approaches have been found to be the best for characterization of virulence factors. *P. aeruginosa* exhibits a wide variety of factors that contribute to virulence, including cell-associated and extracellular, that are involved in pathogenesis and are regulated by extremely intricate, linked regulatory circuits and signaling systems, giving it tremendous adaptability<sup>12</sup>.

As shown in Figure 1.3, there are several virulence factors that aid in a successful infection. Lipopolysaccharides (LPS) function as a poison to host cells and facilitates attachment, recognition by host receptors and tissue damage<sup>10</sup>. These have also been suggested to be involved in biofilm formation and drug resistance. Outer membrane proteins assist in causing antibiotic resistance by nutrient exchange, and adhesion<sup>10</sup>. Other factors that contribute to biofilm formation and ultimately to drug resistance are flagellum, pili, and other adhesins. Additionally, the six major secretion systems play a major role in the virulence of *P. aeruginosa*. Lastly, exopolysaccharides like alginate, inhibits bacterial clearance by helping in biofilms formation<sup>10</sup>. *Pseudomonas aeruginosa* can also manipulate the host immune response by secreting molecules that interfere with cytokine signaling and neutrophil function, aiding in immune evasion<sup>13</sup>

## 1. Introduction

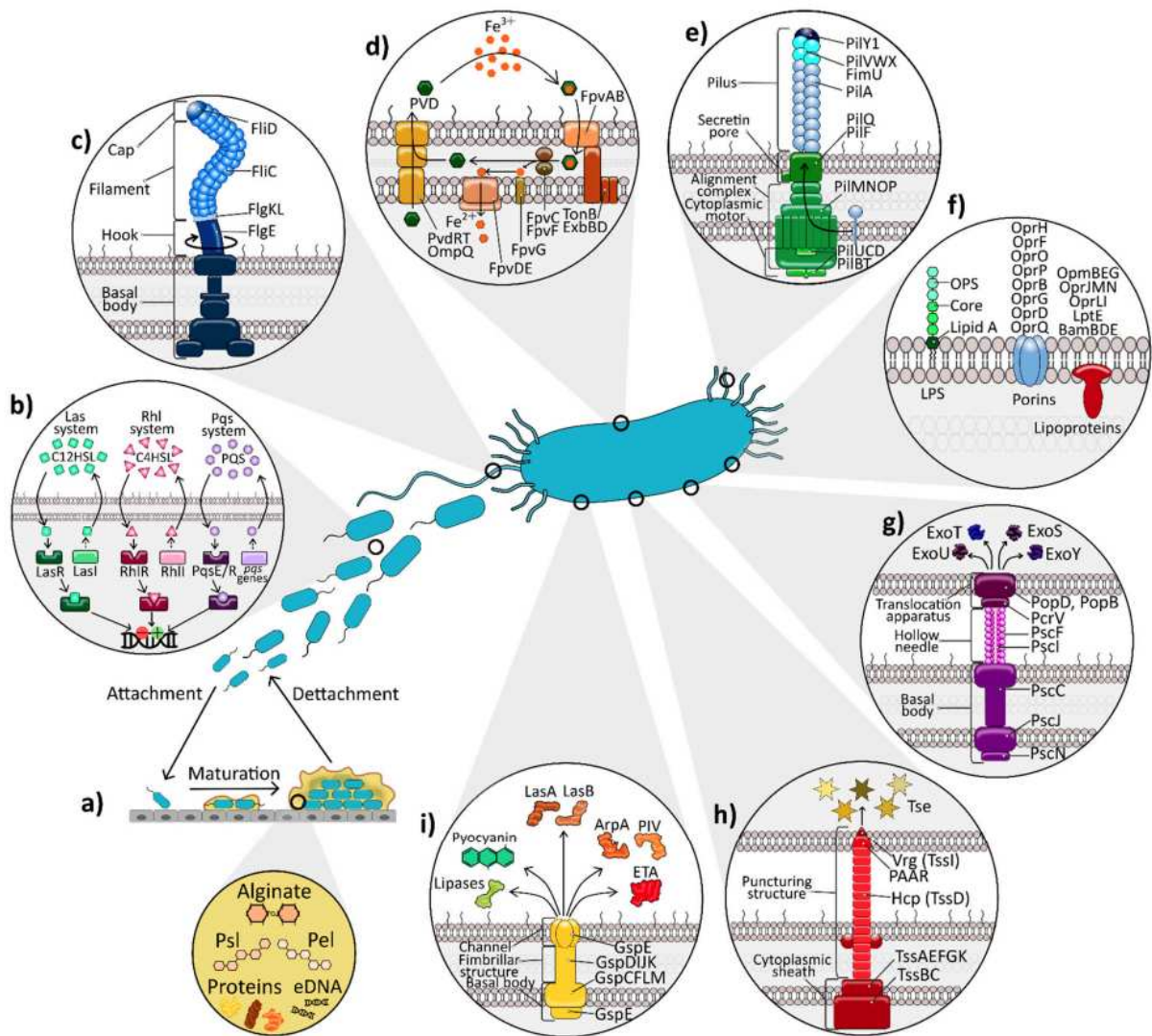


**Figure 1.3 Schematic presentation of the main virulence factors used by *P. aeruginosa* during respiratory infections (Figure adapted from Pollack et.al.<sup>12</sup>)**

(a) biofilm formation ability and composition of the extracellular matrix of biofilms (exopolysaccharides, proteins and extracellular DNA); (b) the three main quorum sensing (QS) systems (Las, Rhl and Pqs); (c) flagellins FliC and FliD incorporated within the flagellar structure; (d) pyoverdine (PVD) siderophore as an iron uptake system; (e) type 4 pili (T4P); (f) lipopolysaccharide (LPS) and outer membrane proteins (OMPs); (g) the type III secretion system (T3SS) and its four main effectors; (h) the type VI secretion system (T6SS); (i) the type II secretion system (T2SS) and the compounds it releases to the extracellular milieu: lytic enzymes (lipases, proteases (AprA ad PIV) and elastases (LasA and LasB)), exotoxin A (ETA), and pyocyanin

### 1.3 Secretion systems in *P.aeruginosa*

Gram-negative bacteria's double membrane envelopes offer two barriers for the movement of materials into and out of these microorganisms<sup>14</sup>. These two barriers are the hydrophobic membranes namely, outer cell membrane and inner cell membrane. They have a hydrophilic space between them known as the periplasm. The secretory proteins and toxins have to be transferred out of the cell through the hydrophilic channels stretching between the two membranes. These channels are constructed using the sophisticated macromolecular complexes known as secretion machinery<sup>15</sup>. These complexes vary in both composition and nature; however remain conserved throughout Gram-negative bacteria. Currently, six different types of secretion systems have been discovered, all distinguished by the properties of the proteins/components that comprise the secretion machine<sup>15</sup> (Figure 1.4). These are known as type I through type VI secretion systems (T1SS-T6SS). These secretion systems can also be divided into two other categories. First is, One-step secretion mechanisms that carry proteins through the bacterial cell membrane at once, hence directly from the cytoplasm to the cell surface. Second, the two-step secretion system where the proteins are released could pass via the periplasm before reaching the outer membrane<sup>15,16</sup>.

*Pseudomonas aeruginosa's* **Type I Secretion System (T1SS)** is a distinct secretion system that is involved in the release of numerous proteins, including virulence factors such as exotoxin A and proteases<sup>17</sup>. The T1SS is composed of up of an outer membrane protein, an ATP-binding cassette (ABC) transporter in the inner membrane, and a periplasmic membrane fusion protein. This is a single step transfer. In *P. aeruginosa*, there are two types of Type I secretion systems. First, the Apr system that is involved in the secretion of the alkaline protease AprA, a virulence factor in the host cells<sup>18</sup>. The second type of T1SS involves iron consumption and needs has genes. HasAp, a secreted protein, is a haemophore that binds haem from haemoglobin. HasAp is thought to be essential for *P. aeruginosa* survival in the early stages of infection<sup>18</sup>. The T1SS is responsible for bacterium pathogenicity by transporting enzymes and other toxic proteins directly to host cells, where they can disrupt cellular processes and cause tissue damage.

## 1. Introduction

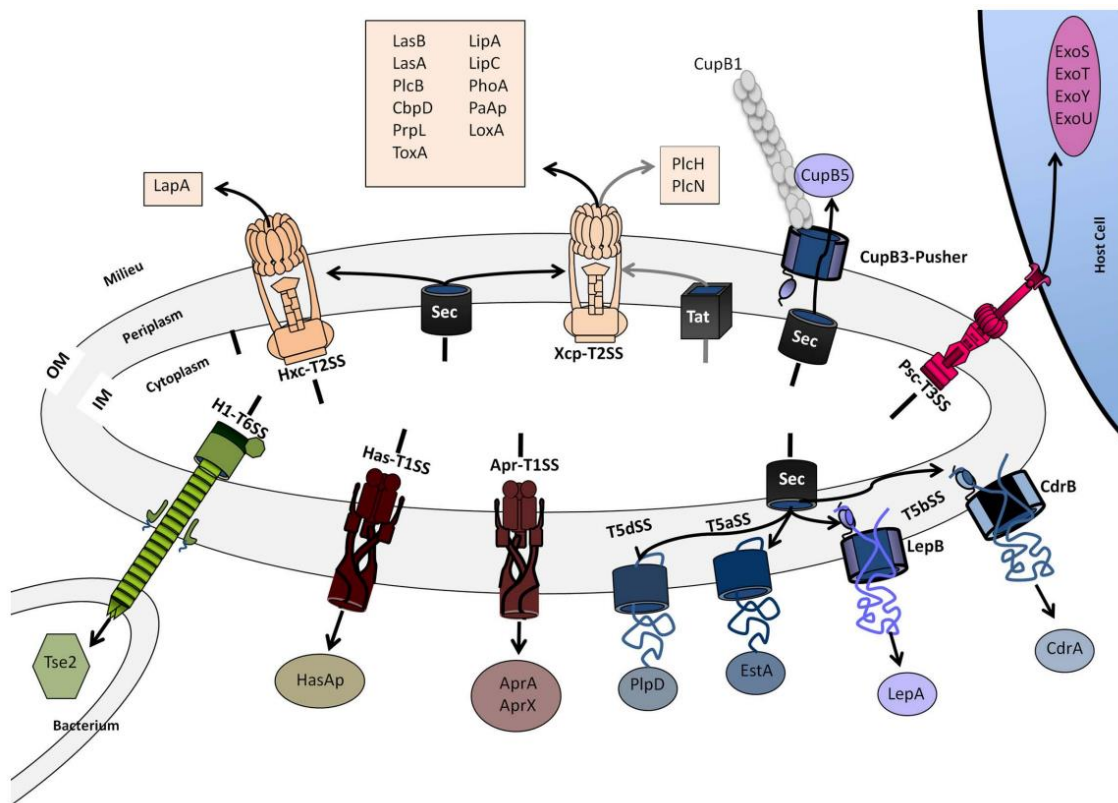


**Figure 1.4 Secretion systems in *P. aeruginosa*** (Figure adapted from Filloux et.al. <sup>15</sup>)

Image showing the secretion systems of *P. aeruginosa* Type I through Type VI secretion systems (T1SS-T6SS) secreting or injection different virulence factors for instance, PLCH, EXOU, LepA, HasAp etc.

*Pseudomonas aeruginosa*'s **Type III Secretion System (T3SS)** is an essential virulence factor. Using T3SS bacterium delivers its effector proteins into host cells, permitting it to manipulate host cell signaling pathways and interfere with immune responses<sup>17</sup>. T3SS is a transmembrane complex consisting of a cytoplasmic part, the basal body, and an extracellular part, also known as injectisome that permits the bacterium to introduce its effector proteins (called toxins) into the cytoplasm of the host cell<sup>19</sup>. The T3SS is activated upon interaction with host cells, subsequently the needle complex expands, enabling the effector proteins to be delivered directly into the cytosol of eukaryotic cell. The effector proteins like ExoS, ExoT, ExoU, and ExoY, perform a distinct function to increase bacterial survival and infection<sup>20,21</sup>.

*Pseudomonas aeruginosa*'s **Type IV Secretion System (T4SS)** is also known as a type IV pilus system. These structures are formed as multi subunit complexes, consists of an ATPase and bacterial conjugation that transport proteins and nucleoprotein complexes across membranes<sup>22</sup>. Type IV pili (T4P) perform a variety of roles such as deoxyribonucleic acid absorption, surface

## 1. Introduction

attachment, formation of biofilms and twitching motility<sup>23</sup>. T4P is essential for adhesion to host epithelial cells. T4P is required for most types of attachment of *P. aeruginosa* to host cells<sup>18</sup>. T4P deficiency in *P. aeruginosa* causes a decrease of adhesion to eukaryotic cells<sup>18</sup>. T4P is divided into two subfamilies: IVa pili (T4aP) and IVb pili (T4bP). T4bP have a subtype known as tight adherence pili (Tad). Each of the three T4P classes has its own assembly system<sup>18</sup>. Furthermore, the T4SS is involved in the translocation of protein effectors, such as ExoT and ExoY, into host cells, where they modulate cellular processes and promote bacterial survival.

*P. aeruginosa*'s **Type V Secretion System (T5SS)** consists of five subtypes (Va to Ve). They export proteins across the inner membrane via the Sec pathway<sup>10</sup>. T5SS is found in many Gram-negative bacteria and is the simplest secretion system. It allows proteins linked with microbial adherence and pathogenicity to be secreted through the bacterial membrane. T5SS, like T2SS, operates in a two-step process. Via the Sec export machinery, proteins first cross the inner membrane to reach the periplasm and then cross an outer membrane (OM) channel formed by a Beta barrel protein<sup>17</sup>. Finally, exoproteins may remain attached to the OM's outer face or discharged by T5SS into the extracellular media upon proteolytic cleavage. Gram-negative bacteria have two forms of T5SS: autotransporters (AT or T5aSS and T5cSS) and 2-partner secretion (TPS or T5bSS)<sup>15,17,24</sup>. Autotransporter proteins secreted by the T5SS in *Pseudomonas aeruginosa* include proteases, adhesins, and toxins. These secreted proteins contribute to various aspects of bacterial pathogenesis, including host colonization, immune evasion, and tissue damage. For example, the LasA protease and alkaline protease degrade host immune factors, while adhesins promote bacterial attachment to host tissues and surfaces. Autotransporter toxins, such as the hemolytic phospholipase C, can cause cytotoxicity and tissue damage<sup>24</sup>.

*Pseudomonas aeruginosa*'s **Type VI secretion system (T6SS)** is a route of administration for toxic effector proteins. *P. aeruginosa* encodes three T6SSs: H1-, H2-, and H3-T6SS. Each T6SS has its own effectors, whose roles are not entirely understood<sup>25</sup>. T6SS is a complex secretion system involved in interbacterial competition, biofilm formation, and pathogenicity. Structurally, T6SS follows a one-step transport mechanism and is composed of a phage-like tail along with several sub-complexes that secret toxins into host cells<sup>25</sup>. The conserved genes in T6SS are named from TssA to TssM, among those TssJ, TssL, and TssM contributes in the formation of membrane core complex that aids in baseplate assembly and a T6SS docking station<sup>25,15,17</sup>.

## 1. Introduction

*Pseudomonas aeruginosa*'s **Type II Secretion System (T2SS)** is a two-step secretion system. The excretory proteins first cross the inner membrane through general secretory (Sec) or twin-arginine translocation (TAT) pathway and are released into the periplasm<sup>10</sup>. Thereafter a brief instant the T2SS secretes the effectors into the extracellular medium. The Sec pathway is made up of a protein targeting part, a motor protein, and a membrane-integrated conducting channel known as SecYEG translocase, through which proteins are released with a SecB-specific signal sequence that can be directed to the periplasm<sup>10,16,26</sup>. In Gram-negative bacteria, twin-arginine translocation (TAT) pathway consists of TatA and TatB, which determine whether released protein is maintained in the periplasm or translocated to the extracellular space via a twin-arginine motif<sup>10,16,26</sup>. T2SS is not well characterized and is assumed that it transfers only properly folded proteins. The type II secretion pathway is expressed by a minimum of 12 genes and particularly facilitates the transport of a set of seemingly distinct proteins over the outer membrane<sup>27</sup>.

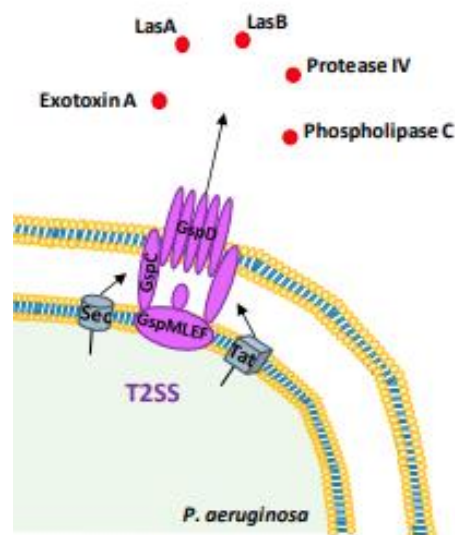


**Figure 1.5 Schematic diagram of Type two Secretion System (T2SS)** (Figure adapted from Sauvage et.al.<sup>28</sup>)

Type 2 Secretion system excretes the proteins (virulent factors like PLCN, PLCH, LasA, LasB) into the extracellular medium with the help of TAT (twin-arginine translocation) or SEC (general secretory) pathway.

T2SS of *P. aeruginosa* is composed of 12 Xcp proteins<sup>15,29</sup>. XcpA participates in the synthesis of the XcpT-X pseudopilins<sup>17,29</sup>. The aggregation of these pseudopilins leads to the formation of a pilus-like structure known as a pseudopilus<sup>29</sup>. XcpR is a cytosolic membrane-linked protein

## 1. Introduction

that falls under the 'traffic ATPases' family of proteins that contribute to the transport processes such as DNA uptake, and type II and IV secretory pathways<sup>29</sup>. Another notable feature of the secretin is the presence of a homomultimeric complex in the membrane's outer layer generated by the secretin family member XcpQ<sup>17</sup>. Secretins play vital roles in type II secretion<sup>29</sup>. Exoproteins such as LapA-Alkaline phosphatase, LasB Metalloproteinase (Elastase), Las A Staphylolytic and elastolytic, PLCH Hemolytic phospholipase, PLCN Non hemolytic phospholipase C, PLCB Phospholipase C specific of phosphatidyl-ethanolamine, ToxA AB Toxin ADP-ribosyl transferase, PmpA, Putative metalloprotease, PrpL Lysine specific endopeptidase (Protease IV), LipA Triacyl glycerol acyl hydrolase, LipC Lipase, PhoA Alkaline phosphatase, PaAP Aminopeptidase that are released by this secretion system are majorly linked to the infections caused in the patients with some underlying lung disease like, bronchiectasis, Cystic Fibrosis, diffuse panbronchiolitis or also burn patients<sup>17</sup>.

This study is based on one of the category of exoproteins of T2SS i.e. Phospholipase C of *Pseudomonas aeruginosa* PA14.

### 1.4 The Phospholipases

Phospholipases are a heterogeneous groups of enzymes, which can hydrolyze one or more ester bond in glycerophospholipids. They belong to the class of lipolytic enzymes, i.e. acyl hydrolyses and phosphodiesterases<sup>30</sup>. Phospholipases play an extraordinary range of roles in both medicine and biology. Phospholipases have been demonstrated to be far more complicated than anticipated, and their impact on a variety of basic physiological processes in eukaryotes, including tumor development and inflammation, has become widely recognized. Similarly, phospholipases have numerous activities in bacterial biology, including significant contributions to microbial pathogenicity<sup>31</sup>.

While every phospholipase has phospholipids as its primary substrate, however, they differ in the place where they cleave on the lipid molecule, their function, how they work, and how they are regulated. Phospholipases are categorized according to the region of cleavage, and are classified into four classes, namely, A, B, C, and D in order to distinguish between them and designate the particular bond in the phospholipids molecule that is being attacked<sup>30,31,32</sup>.

**Phospholipase A (PLA)** belongs to a class of phospholipases that constitute the most diverse group of phospholipid-modifying enzymes and accordingly, display a remarkable range of biological functions. This class is subdivided into two classes: phospholipase A1 and phospholipase A2. The acyl chain in different phospholipids can be removed and replaced by

## 1. Introduction

the enzyme subgroups through hydrolysis, esterification, and trans-esterification<sup>30</sup>. Along with the free fatty acids, the PLA1 and PLA2 enzymes produce either 2-acyl lysophospholipids or 1-acyl lysophospholipids, respectively<sup>30,31,32</sup>.

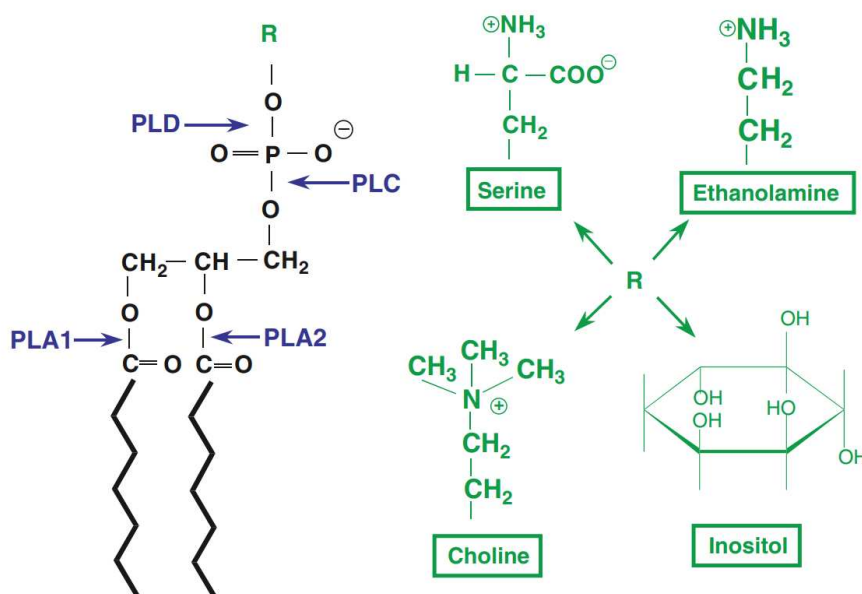


**Figure 1.6 Different classes of PLC based on their mode of action** (Figure adapted from Vasil et.al.<sup>31</sup>)

PLCs are categorized based on cleavage sites into four types: PLA, PLB, PLC, and PLD. PLA forms 2-acyl or 1-acyl lysophospholipids and free fatty acids. PLB acts as a hydrolase and transacylase, cleaving fatty acid esters. PLC cleaves phosphodiester bonds, forming phosphorylated head groups (choline, serine, etc.) and DAG. PLD hydrolyses glycerophospholipid bonds, resulting in phosphatidic acid and the free head group.

PLA1 is essential for phospholipidosis and pathogenesis, with industrial applications in emulsifiers. Lysophospholipids are versatile in food, cosmetics, and pharmaceuticals. PLA1 is used to prepare specific phospholipids. PLA2 is well known for participating in physiological and pathophysiological processes. Various types of PLA2 enzymes have been identified. PLA2 has roles in venom toxicity, bacterial infections, and industrial uses. In *P.aeruginosa*, the PLA2 known as ExoU is released into the host cell by T3SS<sup>33</sup>. ExoU is found only in 30% of the clinical isolates but is extremely cytotoxic and is present in 90% of the serious cases<sup>34</sup>.

**Phospholipase B (PLB)** exhibits three different activities i.e. sn-1 and sn-2 fatty acid ester hydrolase, lysophospholipase, and transacylase activity<sup>30</sup>. PLBs have been found in a variety

## 1. Introduction

of organisms, including bacteria, fungus, guinea pigs, rats, and human epidermis. PLBs could be used in processes in industry requiring phospholipid hydrolysis, such as the degumming of vegetable oils and the creation of beneficial phospholipid compounds for the food and pharmaceutical industries because they have broad substrate specificities<sup>35</sup>.

**Phospholipase C (PLC)** was the first enzyme found to be involved in the mode of action of a bacterial toxin and was shown by Macfarlane and Knight in 1941 by demonstrating the PLC activity of the extremely cytotoxic  $\alpha$  toxin of *C. perfringens*<sup>31,36</sup>. PLCs hydrolyze the phosphodiester bond present between the phosphate and the head group (at the sn-3 position) of the phospholipids. The susceptibility of a glycerophospholipid substrate to the enzymatic activity of a C-type phospholipases is determined by the phospho head groups or the acyl chains. PLCs are characterized as phosphatidylinositol (PI) specific, phosphatidylcholine (PC) favoring, or nonspecific PLCs with or without sphingomyelinase (SMase) activity based on their preferred substrate. In pathogenic bacteria, four structurally distinct forms of PLCs have been identified as having a role in virulence<sup>32</sup>. Other pathogenic bacteria that have shown PLC activity include *Staphylococcus aureus*, *Legionella pneumophila*, *Helicobacter pylori*, *Mycoplasma species*, *L. monocytogenes*, *Mycobacterium tuberculosis*, *Francisella tularensis*, *Burkholderia pseudomallei* and *Pseudomonas aeruginosa*<sup>31</sup>. Many reports have been published regarding the Zn<sup>2+</sup> metallophospholipase PLCs, produced by Gram positive PLCs such as, Bacillus, Listeria, and Clostridium.

They are composed of one or two domains, have three conserved Zn(II) ions in the substrate binding pocket, and although their substrate selectivity varies, their catalytic activity is easily reduced by D609, a competitive inhibitor<sup>32</sup>. Metal independent or Gram negative PLCs, also known as phospholipase Cs from the acid phosphatase superfamily have not been well characterized both structurally and mechanistically<sup>31,32</sup>. *Pseudomonas aeruginosa* secretes four phospholipase C i.e. PLCH (hemolytic), PLCN (Non-hemolytic), PLCB and PLCA<sup>31</sup> (see section 1.5).

## 1. Introduction

**Table 1.1 Bacterial PLCs that contribute to virulence** (Table adapted from Flores-díaz *et.al.*)<sup>32</sup>)

Enzyme type	Example	Mass (kDa)	Structural features	Substrate(s)	Secretion type
PI-specific PLCs	<i>Listeria monocytogenes</i> PlcA	~34	Modified 8-stranded $\alpha/\beta$ barrel similar to triose phosphate isomerase; active site: H32 general base, H82 general acid, R69 phosphate-activating residue	PIP <sub>3</sub>	Secreted, SP <sup>a</sup>
Zn <sup>2+</sup> -metalloPLCs	<i>Bacillus cereus</i> PLC	~29	Single-domain PLC; all $\alpha$ -helix protein, requires Zn <sup>2+</sup> for catalysis	PC (mainly), PE, PS	Secreted, Sec dependent
	<i>Clostridium perfringens</i> alpha-toxin	~43	Two-domain PLC: N terminal all $\alpha$ -helical, C terminal all $\beta$ -structure; requires Zn <sup>2+</sup> for catalysis	PC, SM, PE, PI, PG	Secreted, SP
PLCs from the acid phosphatase superfamily	<i>Pseudomonas aeruginosa</i> PlcH/PlcS	~78	No requirement for metal ions; Thr178 is likely the nucleophile (data derived from the <i>F. tularensis</i> homologue AcpA)	PC, lyso-PC, SM	Secreted by the Tat- and type II Xcp-dependent systems
Other PLCs	<i>Legionella pneumophila</i> PlcA, PlcB, PlcC/CegC1	~47	Require Zn <sup>2+</sup> for activity	PlcA/PlcB: PG; PlcC/CegC1: PC, PG, PE PI, PS, SM	SP in PlcA and PlcB, PlcA and likely PlcB are secreted by the type II Lsp SS; PlcA is secreted by Tat in some strains; PlcC/CegC1 injected into host cell by the Dot/Icm type IVB SS

**Phospholipase D (PLD)** has been known for more than several decades, although its exact function is not yet understood. PLD enzymes catalyze the hydrolysis of glycerophospholipid phosphodiester bonds, resulting in phosphatidic acid and the free headgroup<sup>37,38</sup>. They hydrolyze PC to generate choline and phosphatidic acid (PA). Members of the PLD family are found in organisms ranging from viruses and bacteria to plants and mammals, and they have a variety of substrate specificities, are modulated by a variety of molecules, and have been linked to a variety of cellular processes such as receptor signaling, cytoskeletal regulation, and membrane trafficking<sup>37</sup>. While the roles of PLDs in eukaryotic cells are well-studied, their functions in prokaryotes remain largely unknown due to their rarity in bacteria. However, some prokaryotes possess members of the PLD Superfamily, such as cardiolipin synthetase (CLS), involved in phospholipid synthesis<sup>31</sup>. Among bacterial PLDs, *Pseudomonas aeruginosa's* PldA is periplasmic and interacts with phospholipids, playing a potential role in signaling events. PldA's presence is associated with a pathogenicity island (PAI) containing vgr genes, which may contribute to *P. aeruginosa's* evolution through recombination and horizontal gene transfer<sup>31</sup>. Eukaryotic PLDs have diverse functions in cell biology, including meiosis,

## 1. Introduction

phagocytosis, and signal transduction. In *Arabidopsis*, PLDs are upregulated in response to *Pseudomonas syringae*, causing a hypersensitive response.

Bacterial phospholipases are tightly controlled to regulate cellular processes, with regulation occurring at the transcriptional and post-translational levels<sup>39,40</sup>. Bacteria can respond to environmental signals through regulation, such as the quorum sensing system in *Pseudomonas aeruginosa*, which coordinates gene expression based on cell population density<sup>41</sup>. Factors like temperature, pH, and nutrient availability also influence phospholipase activity<sup>42</sup>. Other proteins or small molecules can modulate phospholipase activity or substrate interactions.

Beyond lipid metabolism and membrane, remodeling, bacterial phospholipases have diverse functions. They contribute to bacterial virulence by aiding in tissue invasion, immune evasion, and dissemination<sup>43</sup>. Phospholipases can disrupt host cell membranes, leading to tissue damage and cytolysis. They also play a role in biofilm formation, which promotes bacterial persistence and antibiotic resistance<sup>44,45</sup>. Additionally, phospholipases generate lipid mediators that act as signaling molecules, influencing host immune responses and inflammation.

Understanding the structure, function, and regulation of bacterial phospholipases is crucial for comprehending their importance in bacterial biology and pathogenesis. Such knowledge can aid in developing strategies to control bacterial infections, including targeting phospholipase activity or regulation for therapeutic purposes. Specific inhibitors against bacterial phospholipases could serve as novel antimicrobial agents. Further research is needed to fully uncover the complex roles of bacterial phospholipases and their potential as therapeutic targets in combating bacterial infections.

Apart from the bacterial PLCs several studies have been done on the mammalian PLCs. The mechanism and structures are better characterized for mammalian PLC. In animals, endogenous phospholipase C (PLC) specifically triggers the breakdown of the less common phospholipid phosphatidylinositol 4,5-bisphosphate (PIP<sub>2</sub>) at the glycerol side of the phosphodiester bond. This enzymatic process plays a crucial role in controlling numerous cellular functions and has a far-reaching impact on hundreds of other processes indirectly<sup>46</sup>. When Ca<sup>2+</sup> is present, phospholipase C (PLC) is recruited to the cell's plasma membrane, where it interacts with the hydrophilic part of phosphatidylinositol 4,5-bisphosphate (PIP<sub>2</sub>). More specifically, PLC binds to the inositol ring of PIP<sub>2</sub>, located towards the cytosol<sup>47</sup>. The active site of PLC contains positively charged amino acid residues that play a crucial role in the interaction with positions four and five of the inositol ring in PIP<sub>2</sub>. This interaction triggers the activation of the 2-hydroxy

## 1. Introduction

group of the inositol ring, leading to an attack on 1-phosphate. As a result, 1, 2-cyclic phosphate and DAG (diacylglycerol) intermediates are formed<sup>47,225</sup>. These cyclic intermediates eventually convert into an acyclic inositol derivative known as IP<sub>3</sub>. While DAG remains within the plasma membrane due to its hydrophobic nature, IP<sub>3</sub> and DAG both serve as secondary messengers, participating in downstream signaling processes<sup>47</sup>. These secondary messengers play significant roles in various cellular responses and signaling pathways<sup>47</sup>. In mammals, there are 13 different isozymes of phospholipase C (PLC) that have been identified and grouped into six distinct subfamilies, labeled as  $\beta$ ,  $\gamma$ ,  $\delta$ ,  $\epsilon$ ,  $\zeta$ , and  $\eta$ <sup>46,47</sup>. The structural makeup of these PLC isozymes is characterized by various domains and motifs<sup>47</sup>. Notably, the pleckstrin homology (PH) domain, EF-hand motifs, X and Y domains, and C2 domains exhibit significant similarity, with more than 40% to 50% shared sequence<sup>48</sup>. All the PLC isozymes share core domains, common to all members. However, PLC- $\zeta$  stands as the sole exception, as it lacks the pleckstrin homology (PH) domain (Figure 1.7)<sup>49</sup>. Figure 1.8 shows all the domains of PLCs with the structure of PLC- $\beta$ 2 (PDB 2ZKM)

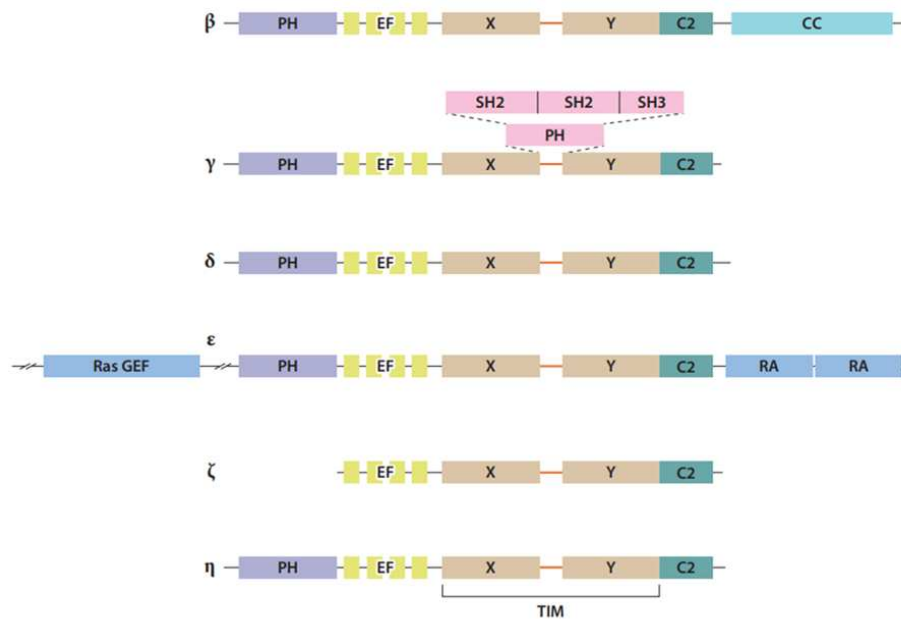


**Figure 1.7 Domain structures of mammalian PLC isozymes** (Figure adapted from Singh *et.al.*<sup>47</sup>)

Different domains are abbreviated as follows: PH, pleckstrin homology; EF, EF hands; CC, coiled coil; SH2/SH3, Src homology 2/3; RA, Ras association; Ras GEF, Ras GDP/GTP exchange factor; X and Y, N- and C-terminal portions of the TIM barrel.

## 1. Introduction

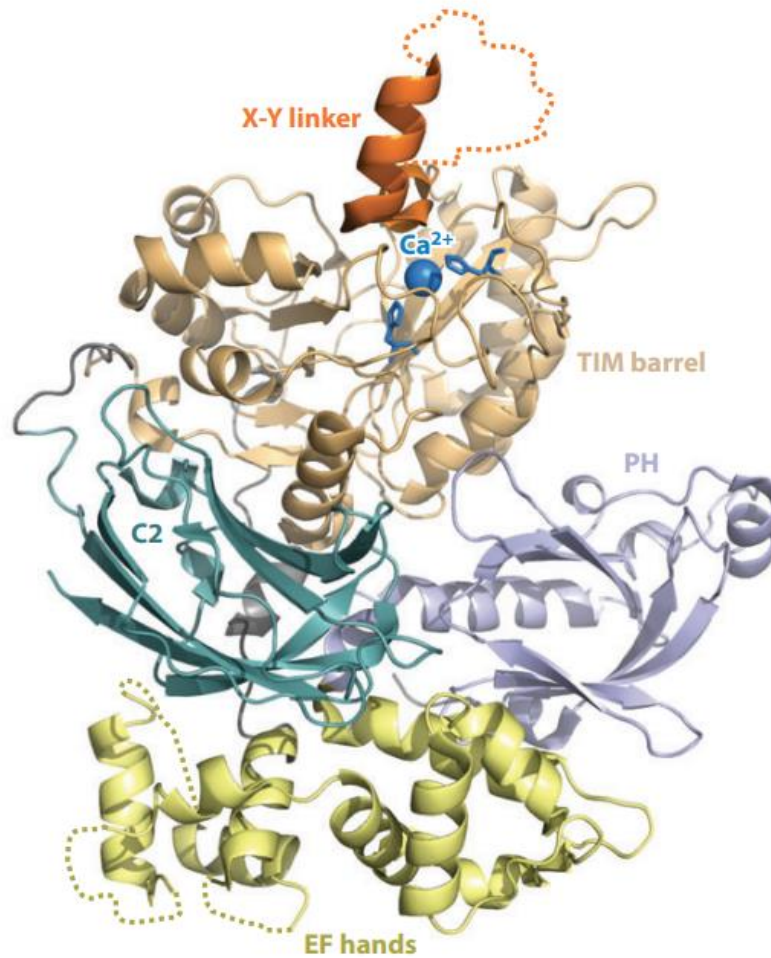


**Figure 1.8 Structure of PLC-β2 (PDB 2ZKM) with domains** (*Figure adapted from Singh et.al.<sup>47</sup>*)

Perspective is looking down at the active site from the plane of the bilayer, at a slight angle. Bound Ca<sup>2+</sup> near the catalytic site is shown as a blue ball, and the two catalytic histidines are blue. The X-Y linker region is orange. The disordered parts of the X-Y linker and the EF hands are depicted as dotted lines. The construct used to obtain this structure lacked the coiled-coil domain and most of the linker following the C2 domain.

### 1.5 The Phospholipase C of *Pseudomonas aeruginosa*.

This study is focusing on the PLCs of *Pseudomonas aeruginosa*. Different strains of *Pseudomonas* secrete different types of phospholipases C. *P.aeruginosa* till date is known to secrete four different PLCs, namely, PLCH, PLCN, PLCB and PLCA<sup>31,50,51,52</sup>. The hemolytic PC-PLC in *P. aeruginosa* was the initial member of a subsequently expanded group of enzymes possessing PC-PLC, SMase, and phosphatase capabilities, which have been detected in several microbial pathogens such as *Mycobacterium tuberculosis*, *Bordetella pertussis*, *Francisella tularensis*, *Burkholderia pseudomallei*, and *Xanthomonas campestris*<sup>53</sup>. There were just two identified phospholipases for a long time, PLCH and PLCN. They both belong to a phosphatase superfamily (growing family of homologous proteins) and have remarkably comparable sequences. PLCH and PLCN have a high degree of homology, with more than 40% identity and 60% similarity<sup>53</sup>. PLC activity is most commonly seen in prokaryotes with high G+C content (e.g., *Pseudomonas spp.*, *Mycobacterium spp.*, *Streptomyces spp.*, *Burkholderia spp.*, *Bordetella spp.*, *Xanthomonas spp.*, *Caulobacter spp.*)<sup>31</sup> and some of them are recognized as virulence factors. Proteins from this unique class of PLCs have been found in fungi (e.g., *Aspergillus*) and plants (e.g., *Arabidopsis*). As previously noted, these PLCs are an entirely different class of PLCs<sup>31</sup>. They are not related to the GP-PLCs discussed above in terms of sequence or biochemistry. However, recently the analysis of the TAT ( $\Delta$ TAT), PLCH( $\Delta$ PLCH) and PLCN ( $\Delta$ PLCN) mutants resulted in the discovery of a third PLC of *P. aeruginosa* i.e. PLCB that corresponds to the GP-PLC class of PLCs<sup>54</sup>. Recently a newly PLC i.e. PLCA in *P. aeruginosa* was discovered. According to preliminary results, its expression was not promoted by Pi-limiting conditions but appears to be affected by choline. Compared to the choline-induced production of PLCH, the presence of choline in the media inhibits the expression of PLCA. An even more coordinated effort will be required to elicit additional information about PLCA's functionality in *P. aeruginosa*<sup>55,31</sup>. However, PLCA is not found in the strain PA14 of *P. aeruginosa*. Table 1.2 below shows a list of PLCs of *P. aeruginosa* PA14.

## 1. Introduction

**Table 1.2: PLCs of *P. aeruginosa* PA14**

PLC	Gene organisation	Chaperone	Other genes in operon	Secretory pathway	Substrates
PLCH (hemolytic)	3 Gene operon	PLCR	Glycosyl-transferase	TAT, Xcp	PC, SM, CL, PE, PG <sup>56</sup>
PLCN (non-hemolytic)	Single gene	-	-	TAT, Xcp	PS, PC
PLCB	3 gene operon	peptidyl-prolyl-isomerase	1 Hypothetical Protein	Sec, Xcp	PE, PC, PS, SM

**PC: phosphatidylcholine, SM: sphingomyelin, PS: phosphatidylserine, PE: phosphatidylethanolamine**

*P. aeruginosa*'s hemolytic phospholipase C, PLCH (82.6kDa), is a pioneering member of a developing family of PLCs. In 1966, Liu discovered that the hemolytic phospholipase (PLCH) is more commonly produced under phosphate (Pi)-limiting scenarios and is heat labile<sup>57,58,59,60</sup>. In the 1980s, PLCH was also discovered to have phospholipase activity<sup>53</sup>. This prompted many authors to believe that the primary function of PLCH, along with phosphatases, is to absorb Pi by metabolizing the phospholipids. While this may be beneficial to *P. aeruginosa* in a Pi-limiting environment, it offers a very limited view of the true potential of this virulence determinant<sup>31</sup>. However, subsequently it was shown by Shortridge et.al. that the operon carrying three genes PLCH, PLCR and another unknown gene (now known as a Glycosyl-transferase) was expressed also under Pi sufficient conditions due to the control by a different promoter<sup>61</sup>. This led to the belief that it can also now produce other products using phospholipids as shown in Figure 1.9. The formation of components like glycine betaine from the cleavage products of phospholipids adds to the virulence exhibited by PLCs<sup>62</sup>. After the expression of PLCH, it is secreted into the periplasm using the twin arginine translocase (TAT) system into the periplasm. From the periplasm, it is secreted into the extracellular medium through T2SS (as explained in section 1.3). PLCH can be secreted alone into the periplasm or with its chaperon PLCR<sup>63</sup>. PLCR gene is present at the 3' end of the operon and encodes two overlapping genes PLCR1 and PLCR2<sup>64,65</sup>. The signal sequence is not the only thing that sets PLCR1 (Sec signal sequence) and PLCR2 apart; the mature forms of PLCR1 include an extra 36 amino acids, 10 of which

## 1. Introduction

are proline residues and 15 are other hydrophobic residues. While the PLCR1-specific domain may serve as a membrane anchor, these proteins are likely soluble hydrophilic periplasmic and cytoplasmic proteins<sup>65</sup>. PLCR1 is thought to be essential for secretion across the outer membrane, while PLCR2 may be involved in transporting PLCH across the inner membrane. This difference may be due to the function of chaperonins as well as a different secretion machinery in each membrane<sup>65</sup>. Figure 1.10 shows the genetic makeup of of PLCH gene and its chaperon, PLCR (PLCR1 and PLCR2).

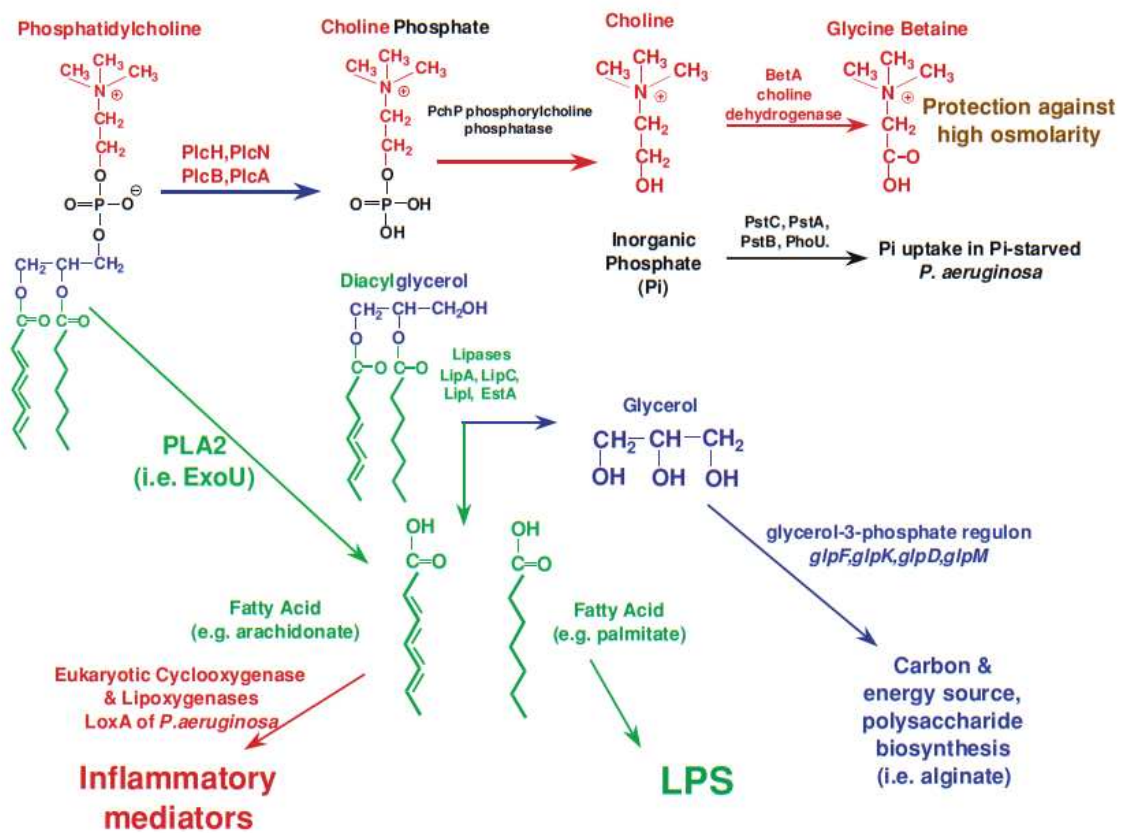


**Figure 1.9 Potential products generated by PLCs of *Pseudomonas aeruginosa*** (Figure adapted from Vasil et.al.<sup>31</sup>)

PLCs cleave phospholipids into phosphocholine and DAG. Bacteria use these byproducts for survival. Phosphate provides nutrition, while choline is converted into glycine betaine to withstand high osmolarity in the host's lung. DAG is cleaved into glycerol which is used as a carbon source and free fatty acids, which can lead to inflammation.

## 1. Introduction

In addition, Luberto et al. confirmed that PLCH possesses PLC and SMase, but that its SM synthase activity is conditional on the presence or absence of ceramide (CM)<sup>66</sup>. It synthesizes SM and DAG by transferring the choline phosphate head group from PC to CM. This function requires phospholipid-derived choline phosphate, demonstrating its specificity. PLCH will not process choline phosphate from nonlipid substrates such as nitrophenyl-phosphorylcholine. Without CM, PLCH removes the phosphocholine from SM to generate CM. No SM-to-DAG phosphorylcholine head group transfer occurs. Thus, PC, SM, and CM concentrations dictate whether PLCH has SMase, PLC (hydrolase), or SM synthase activity. Given its three enzymatic activities, what are PLCH's physiologically relevant substrates and products? *P. aeruginosa*'s environment is expected to determine the answer. Lung surfactant contains PC, SM, and minimal CM. Thus, PLCH may behave as a PLC or SMase. However, because PLCH promotes death in endothelial cells rather than proliferation, its cytotoxicity is likely due to its SMase activity rather than its PLC activity. CM triggers apoptosis in eukaryotic cells while DAG causes cell growth and transformation<sup>31</sup>. *P. aeruginosa* PLCH hydrolyzes lung surfactants, which disperses microorganisms and disrupts alveoli. Catabolism of PLCH-released phosphorylcholine provides nutrition, triggers biofilm formation, and promotes bacterial survival in the lungs. SM breakdown by PLCH and CM buildup in epithelial cells may contribute to *P. aeruginosa* lung infections by preventing the activity of the cystic fibrosis transmembrane Cl channel, causing the production of thick mucus that clogs airways and promotes bacterial growth. PLCH lyse human erythrocytes and preferentially cytotoxic to endothelium cells<sup>67</sup>. PLCH is able to hydrolyse all kinds of phospholipids except for phosphatidylserine (PS)<sup>56</sup>. In mice and humans granulocytes, it reduces the neutrophil respiratory burst and generates a significant chemokine response<sup>68</sup>. PLCH recruits and activates platelets at the endothelium in vivo, causing thrombotic lesions comparable to *P. aeruginosa* sepsis. PLCH-deficient *P. aeruginosa* mutants are less virulent and cause less mortality<sup>69,70</sup>. *P. aeruginosa*'s genome contains a neutral ceramidase that improves PLCH/PLCS' hemolytic activity<sup>32</sup>. Remarkably, PLCH/PLCS is also needed for *P. aeruginosa* to cause disease in *Arabidopsis thaliana* as well as *G. melonella* and to kill *Candida albicans* filaments suggesting that the antagonism with this fungus may have contributed to its evolution and maintenance<sup>32</sup>.

## 1. Introduction

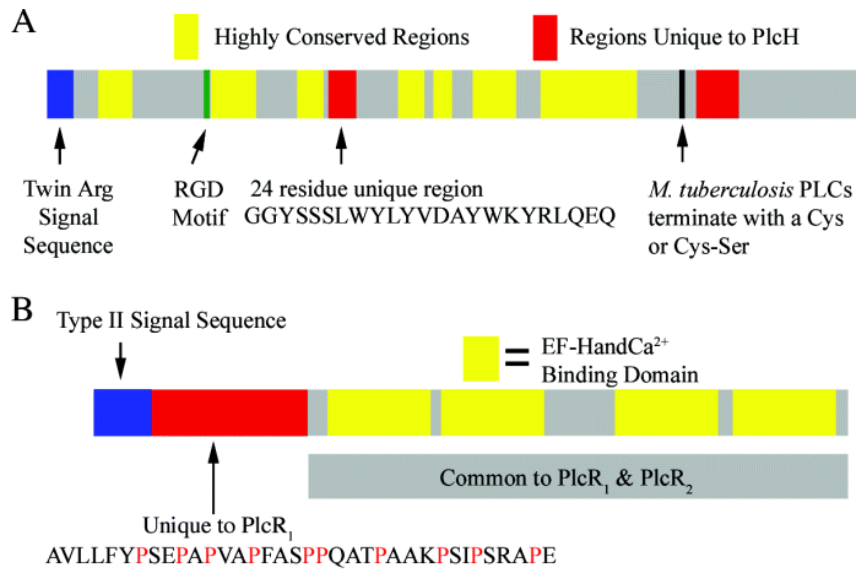


**Figure 1.10 Genetic makeup of PLC genes** (Figure adapted from Stonehouse et.al.<sup>53</sup>)

PLCH has a TAT signal sequence, RGD motif and 24 unique amino acids. PLCR (PLCR1 and PLCR2) is PLCH's chaperon having EF Hand, which is a Ca<sup>2+</sup> binding domain.

PLCN is exported from *P. aeruginosa* through the twin-arginine translocation (TAT) pathway, migrates from the inner cell membrane to the periplasm, and through the outer membrane using the xcp secretion pathway<sup>71</sup>. PLCN has a substrate selectivity for phosphatidylserine (PS) and phosphatidylcholine (PC), however its affinity for PS is higher than for PC<sup>31</sup>. Studies on the virulence of PLCN are sparse, compared to PLCH for which vast studies that have been conducted and analyzed. It has been demonstrated, however, that the secreted PLCN is involved in the production of biofilms, and due to its strong PS-affinity, PLCN may raise apoptosis rates within eukaryotic cells of infected tissue<sup>72, 31</sup>. PLCN is not able to break down SM and is just 30 – 50% as efficient as PLCH in cleaving PC and has been hypothesized that the lack of hemolytic activity of PLCN may be due to its substrate specificity in relation to the composition of the erythrocyte membrane<sup>73</sup>. Several groups have assessed the enzymatic activity of PLCH and PLCN both in vivo and in vitro, but they isolated them from *P. aeruginosa*<sup>67,74</sup>. In this study, I am characterizing the PLCs of *Pseudomonas* expressed in *E.coli*.

Understanding the structural composition, function, and ultimately the crystal structure of the protein could provide insight into PLC's pathogenicity. Despite the fact that certain medication options are available for individuals with *P. aeruginosa* infections, antibiotic resistance remains

## 1. Introduction

a major problem<sup>75</sup>. The identification of virulence factors may thus aid in the understanding of the system and, ultimately, the development of viable treatments for *P. aeruginosa* infections.

### 1.6 Aim of this study

Ramsay et al. provided evidence for the genomic versatility of *P. aeruginosa* by demonstrating that, whereas environmental isolates are often responsive to antimicrobials, their nosocomial counterparts are rather resistant to antibiotics. Although *P. aeruginosa* strains that are naturally resistant to antimicrobials in the environment can cause infections in humans, it is expected that these strains will develop resistance throughout the course of an illness, perhaps under the impact of antimicrobial therapy. It is becoming increasingly common to find observations in the literature that isolates of multi-drug resistant *P. aeruginosa* are more virulent than those of more sensitive strains<sup>50</sup>.

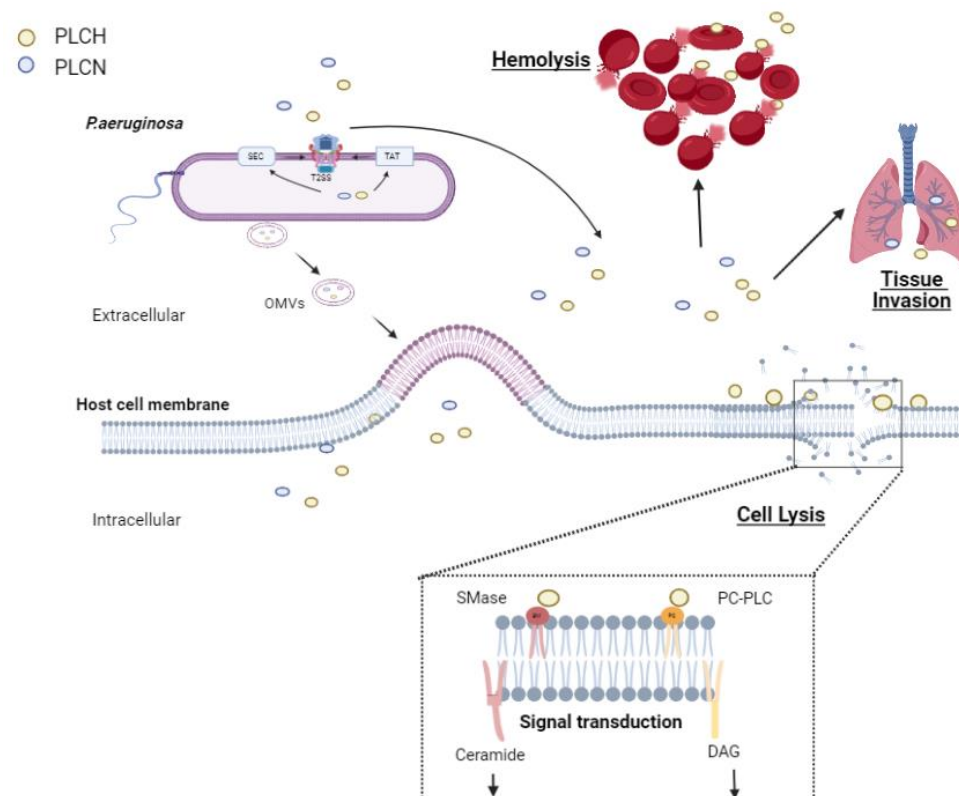


**Figure 1.11 Mode of Action of PLCH and PLCN of *Pseudomonas aeruginosa***

PLCH and PLCN can both lyse cells by digesting phospholipids in the cell membrane, leading to tissue invasion and cell death. PLCH exhibits an additional hemolytic property, allowing it to also lyse red blood cells.

## 1. Introduction

As discussed above, the PLCs of *P.aeruginosa* has various roles in virulence such as it cleaves the phospholipids and causes cell lysis. It can utilize phospholipids as a sole source of carbon, nitrogen, and phosphate. Secondary messengers released as the products can start a signal cascade, leading to cancer or apoptosis.

The research conducted below is a subset of a wider study focusing on *Pseudomonas*. Professor Häußler (HZI/Twincore) from Hannover, conducted a screening of 414 clinical isolates and confirmed the differential expression of hundreds of genes during acute pathogenicity<sup>76</sup>. Figure 1.11 shows the correlation between the virulence traits of 414 clinical isolates and the gene expression data of those isolates. Here, the X-axis shows the  $-\log$  of FDR (false discovery rate) and Y-axis shows the fold change in the virulence<sup>76</sup>. The positive Y-axis value represents the upregulated genes and vice versa. In this investigation, the FDR value for PLCH, PLCR and PLCN was given to be 0.0072, 0.00044 and 0.879 respectively<sup>76</sup>. The FDR value for PLCs shows the importance and contribution in the acute virulence exhibited by *P.aeruginosa*.

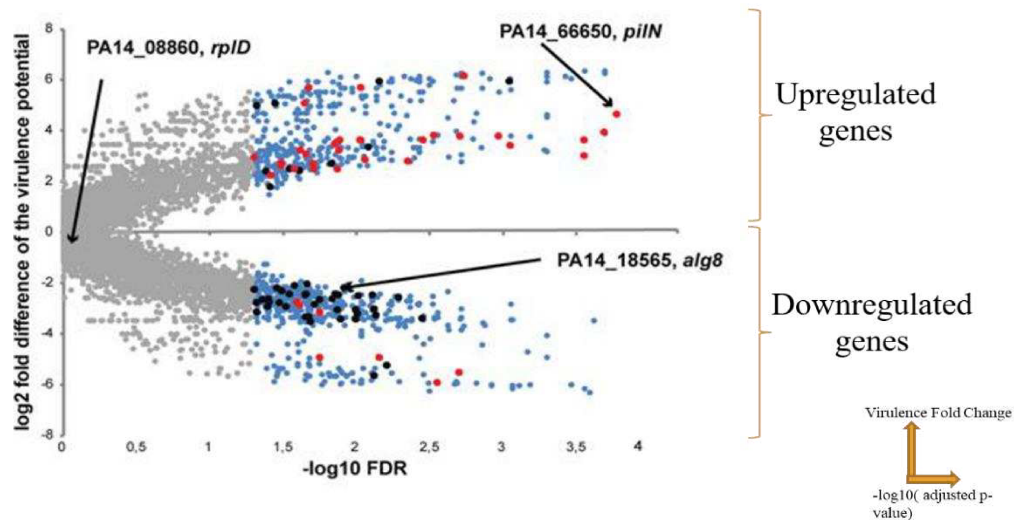


**Figure 1.12 Correlation of virulence phenotypes and gene expression data of 414 clinical isolates** (Figure adapted from Kordes et.al.<sup>76</sup>)

The purpose of this research is to investigate the biophysical and biochemical characteristics of the virulent PLCs produced by *P. aeruginosa*. In addition to performing characterization, the goal of this research is to determine the 3D structure using X-ray crystallography or Cryo-EM. This will make it possible for subsequent research to identify PLC inhibitors.

**2 Materials and methods****2.1 Instruments and Materials****Table 2.1 Instruments**

<b>Instruments</b>	<b>Company</b>
Benchtop centrifuge 5417R	Eppendorf
Benchtop centrifuge Sigma 1-14K	Sigma
Superspeed Centrifuge Sorvall LYNX 6000	Thermo Scientific
NanoDrop™ 2000 Spectrophotometer	Thermo Scientific
Ultracentrifugation OPTIMA XPN 90	Beckman Coulter
Cell disrupter EmulsiFlex-C3	Avestin, Inc.
Akta Explorer	GE Healthcare Life Science
T100 Thermal cycler	Bio-Rad
Bio-rad mini sub-cell GT	Bio-Rad
Bio-rad mini protein tetra cell	Bio-Rad
Trans-Blot Turbo Transfer System	Bio-Rad
ChemiDoc MP Imaging System	Bio-Rad
AVIV Model CD 425	AVIV
UNITRON plus Incubator Shaker	INFORS AG
Tecan plate reader Spark 20M	Tecan
T80 UV-VIS Spectrophotometer	PG Instruments Limited

**Table 2.2 Materials**

<b>Materials</b>	<b>Company</b>
BenchMark Protein Ladder	Thermo Scientific
FastDigest restriction enzyme	Thermo Scientific
T4 DNA ligase	Thermo Scientific
GeneRuler DNA ladder	Thermo Scientific
GeneJET Plasmid Miniprep Kit	Thermo Scientific
GeneJET Gel Extraction Kit	Thermo Scientific
Zeba Spin Desalting Columns	Thermo Scientific
Phusion Hot Start II DNA Polymerase	Thermo Scientific
Detergents (Fos-14, DDM)	Cube Biotech

## 2. Materials and Methods

Polymers (SMA, DIBMA)	Cube Biotech
Affinity resin (Ni-NTA resin, Rho1D4 Agarose)	Cube Biotech
Rho1D4 peptide	Cube Biotech
Lipids	Anatrace
PD-10 desalting column	GE Healthcare Life Science
PVDF membrane	GE Healthcare Life Science
Size-exclusion chromatography columns	GE Healthcare Life Science
Nanosep MF and NAB Centrifugal Devices	Pall Laboratory
Pre-stained Protein Marker	Jena Bioscience
Protein Labeling Kit RED-NHS 2nd Generation	NanoTemper
Monolith NT.115 Premium Capillaries	NanoTemper
MTT solution	0.5mg/ml of MTT powder in media without serum

All chemicals are purchased from Carl Roth and AppliChem.

### 2.1.1 Biological Materials

**Table 2.3 Biological strains**

Strains	Genotype
Top10	F- mcrA $\Delta$ (mrr-hsdRMS-mcrBC) $\phi$ 80lacZ $\Delta$ M15 $\Delta$ lacX74 nupG recA1 araD139 $\Delta$ (ara-leu)7697 galE15 galK16 rpsL(StrR) endA1 $\lambda$ -
BL21 (DE3)	F- ompT gal dcm lon hsdSB(rB-mB-) $\lambda$ (DE3 [lacI lacUV5-T7p07 ind1 sam7 nin5]) [malB+]K-12( $\lambda$ S)
HeLa cells	Originated from Homo sapiens, epithelial cell

The genotypes of the strains are obtained from [https://openwetware.org/wiki/E.\\_coli\\_genotypes](https://openwetware.org/wiki/E._coli_genotypes).

## 2. Materials and Methods

**Table 2.4 Expression vectors**

Vectors	Inducer	Resistance	DNA inserted
pET-28a	IPTG	Kanamycin	(i) PLCN (ii) PLCR2
pACYC_DUET1	IPTG	Chloramphenicol	PLCH

**Table 2.5 Medium for bacterial and mammalian culture**

Media	Compositions
Lysogeny broth (LB)	Yeast extract (5 g/l) Tryptone (10 g/l) Sodium chloride (10 g/l)
Super Optimal Broth (SOB)	2% w/v tryptone 0.5% w/v Yeast extract 10mM NaCl 2.5mM KCl add 10mM MgCl <sub>2</sub> and 10mM MgSO <sub>4</sub> before use
Advanced RPMI media	DMEM 5% FBS 1% penicillin and streptomycin 2% L-glutamine

### 2.1.2 Kits and Buffers

**Table 2.6 Buffers for gel electrophoresis**

Buffers	Compositions
Agarose gel running buffer (50X TAE)	2M Tris-base 1 M acetic acid 50 mM EDTA pH:8.0
SDS-Sample buffer (5X)	62 mM Tris, 2 % (w/v) SDS 5 % (v/v) β-Mercaptoethanol 20%(w/v) Glycerol 0.2 % (w/v) Bromophenol blue

## 2. Materials and Methods

SDS-PAGE running buffer	25 mM Tris 192 mM Glycine 0.1 % (w/v) SDS%
Blue silver staining solution	10% Phosphoric acid 10% Ammonium sulfate 1.2g/L Coomassie G-250 20% (v/v) Methanol
Transfer Buffer for Western blot	39 mM Glycine 48 mM Tris base 20% (v/v) Methanol
TBS buffer	20 mM Tris base pH 7.6 137 mM NaCl
TBS-T buffer	TBS buffer with 0.1% (w/v) Tween 20
Blocking buffer	TBS-T buffer with 5% (w/v) non-fat milk

**Table 2.7 Sodium dodecyl Sulphate–polyacrylamide gel electrophoresis (SDS-PAGE)**

	<b>10% resolving gel (20ml)</b>	<b>12% resolving gel (20ml)</b>	<b>15% resolving gel (20ml)</b>	<b>5% stacking gel (5ml)</b>
H <sub>2</sub> O	7.9 ml	6.6 ml	4.6 ml	3.4 ml
30% Acrylamide	6.7 ml	8.0 ml	10.0 ml	0.83 ml
1.5 M Tris, pH8.8	5.0 ml	5.0 ml	5.0 ml	-
1 M Tris, pH 6.8	-	-	-	0.63 ml
10 % SDS	0.2 ml	0.2 ml	0.2 ml	0.05 ml
10 % Ammonium Persulfate	0.2 ml	0.2 ml	0.2 ml	0.05 ml
TEMED	8 µl	8 µl	8 µl	5 µl
0.5% Trichloroethanol (TCE) (optional)	0.1 ml	0.1 ml	0.1 ml	-

**Table 2.8 Buffers for purification**

Buffers	Compositions
Lysis Buffer	50 mM Tris, pH 7.5, 500mM NaCl, 3mM $\beta$ ME, 0.5mg/ml Lysozyme, 10ug/ml DNase I, 1uM E64, 1uM Pepstatin A, 1uM Leupeptin, 1mM AEBSF, 1mM PMSF, 1mM Benzamindine
Ni-NTA washing buffer	50 mM Tris, pH 7.5, 1MmM NaCl, 3mM $\beta$ ME 15mM Imidazole
Ni-NTA elution buffer	50 mM Tris, pH 7.5, 1MmM NaCl, 3mM $\beta$ ME 350mM Imidazole
SEC buffer	25 mM Tris, pH 7.5, 100MmM NaCl, 3mM $\beta$ ME

## 2.2 Cloning

Cloning is a technique used to create multiple identical copies of a DNA molecule of interest by isolating and propagating it in a host cell. This allows for the study of the genes and protein products contained within it, and the universal nature of DNA enables accurate copying and use across organisms<sup>77</sup>. Polymerase Chain Reaction (PCR), a method that selectively amplifies DNA/RNA segments up to 2kb by enzymatic primer extension in repeated cycles using Taq polymerase is used to exponentially increase the target sequences and high sensitivity with even a single cell's DNA/RNA content<sup>78,79</sup>. In classical cloning, the PCR-amplified genes and desirable cloning vectors/plasmids are specifically digested with the important tools of molecular biology called Restriction enzymes<sup>80</sup>. The digested vector and target gene are then ligated using the DNA Ligase enzyme followed by the transformation in the *E.coli*. cloning strains.<sup>81</sup>.

In this project, the desired genes were taken from the genomic DNA of strain PA14 of *Pseudomonas aeruginosa*. The primers corresponding to the full-length target genes i.e. Hemolytic Phospholipase C (PLCH), the PLCH chaperon (PLCR2), and the Non- hemolytic Phospholipase C (PLCN) were designed with the help of online software provided by Thermo Fischer. (See Appendix I for primers, DNA, and protein sequences). At the N-terminal, a six Histidine (His) tag was added in all the designed primers were synthesized from BioTeZ Berlin-Buch GmbH, Germany, and diluted with ddH<sub>2</sub>O to a final concentration of 50  $\mu$ M. The PCR reaction mixture was set up as shown in Table 2.9.

## 2. Materials and Methods

**Table 2.9 PCR reaction components**

Components	100 $\mu$ L reaction	Final concentration
5X Phusion GC Buffer	20 $\mu$ L	1X
10 mM dNTPs	2 $\mu$ l	200 $\mu$ M
Forward primer	2.5 $\mu$ l	0.5 $\mu$ M
Reverse primer	2.5 $\mu$ l	0.5 $\mu$ M
Template DNA	1 $\mu$ l	5 ng
DMSO	1.5 $\mu$ l	3%
Phusion Hot Start II DNA Polymerase	1 $\mu$ l	0.02 U/ $\mu$ L
H2O	Up to 100 $\mu$ l	

Gradient PCR experiment was set up at different annealing temperatures with preliminary reactions of lesser volume (10 $\mu$ l). At the optimal annealing temperature, the reaction volume was scaled up to 50 $\mu$ l. The PCR program is shown in Table 2.10. The PCR products and GeneRuler 1 kb DNA Ladder Thermo Scientific™ were analyzed using Agarose Gel Electrophoresis(AGE)<sup>82</sup>.

**Table 2.10 PCR program**

Steps	Temperature	Duration	Number of cycles
Initial denaturation	98 °C	30s	1
Denaturation	98 °C	10s	
Annealing	55-72°C	30s	25-30
Extension	72°C	40s per kb	
Final extension	72°C	5 mins	1
Hold	4°C	$\infty$	

The bands from the agarose gel at the corresponding gene size were cut and extracted using GeneJET Gel Extraction Kit from Thermo Fisher. The concentration of extracted DNA was measured using NanoDrop™ 2000 Thermo Scientific by measuring absorbance at 260nm. The amplified genes and preferred plasmid/vectors were digested using relative restriction enzymes at 37°C for 1 hour. The digested products were then analyzed on agarose gel, purified by Gel

## 2. Materials and Methods

Extraction kit, and the respective concentrations were measured by NanoDrop. 3:1 molar ratio of the purified digested gene and vector were then ligated with the aid of T4 DNA polymerase at 16°C, overnight. The reaction mixture for the above reactions are shown below in the tables.

**Table 2.11 Restriction enzyme digestion reaction**

Components	50 µL reaction
10X FastDigest Green Buffer	5 µl
DNA	1 µg
FastDigest enzyme I	1 µl
FastDigest enzyme II	1 µl
Nuclease-free water	Up to 50 µl

**Table 2.14 Ligation Reaction**

Components	20 µL reaction
10X Ligase Reaction Buffer	2 µl
Vector DNA (For LIC)	70 µg
Insert DNA (For LIC)	3 times molar ratio to vector DNA
Linear (For self-ligation)	70 ng
T4 DNA Ligase	0.2 µl
Nuclease-free water	Up to 20 µl

The ligation mixture was transformed into *E.coli*: Top10 cloning strain. The reaction mixture was incubated with competent Top10 *E.coli*. cells on ice for 30 mins followed by 90 secs of heat shock at 42°C and then again on ice for 5 mins. Thereafter, the cells were incubated with 800ul of LB broth at 37°C, shaking, for three generations and plated onto LB agar plates with the desired antibiotic for selection. The next day, colonies were picked and incubated in LB broth media at 37°C, shaking at 180rpm, overnight. From the overnight culture, plasmids with desired genes were isolated using GeneJET Plasmid Miniprep Kit. Positive clones were conformed by restriction digestion and colony PCR. Further, for confirmation, the plasmids were sent for sequencing to Microsynth Company, Germany.

### 2.2.1 Site-directed mutagenesis

Site-directed Mutagenesis (SDM) is a crucial technique for investigating the relationship between the structure and function of a gene. By using a basic PCR process that involves complementary oligonucleotide pairs that overlap, it is possible to introduce almost any desired mutation (substitutions, deletions, and insertions) to a gene carried on a plasmid<sup>83,84,85</sup>.

In this study, to understand the relevance of residues at the active site, Threonine residue at the active site was point mutated to Alanine in both constructs of Phospholipases C i.e. PLCH and PLCN. The primers for these mutations were generated with the aid of the software NEBase changer from New England Biolabs. (See Appendix 1 for primers, DNA, and protein sequences). Here also the synthesized primers were diluted to a final concentration of 50  $\mu$ M in ddH<sub>2</sub>O. The wild type/original construct was used here as a template for PCR amplification and the PCR reaction was set similarly to the above-mentioned classical cloning. The obtained PCR product was then incubated with DpnI enzyme at 37°C for, 1hour to digest the remaining parental DNA in the reaction mixture to avoid contamination. Thereafter, the purified mutated linear PCR product was subjected to 5'-end phosphorylation by T4 polynucleotide kinase from Thermo Fisher to add gamma phosphate from ATP to the 5'-end of DNA or RNA<sup>86</sup>. Ligation was done at 16°C, overnight with the help of a DNA ligase enzyme. The ligation mixture was transformed into *E.coli*. Top 10 competent cells as explained above. Colonies were picked up the next day for incubation at 37°C, overnight at 180 rpm. From the overnight culture, the plasmid was isolated using GeneJET Plasmid Miniprep Kit and further sent for sequencing at Microsynth Company, Germany.

The Tables 2.12 & 2.13 below show the components for the above-mentioned reactions.

**Table 2.12 Dpn1 digestion reaction**

Components	40 $\mu$ L reaction
10X Reaction Buffer	4 $\mu$ l
DNA	30 $\mu$ l
DpnI	1 $\mu$ l
Nuclease-free water	Up to 40 $\mu$ l

**Table 2.13 Phosphorylation Reaction**

Components	50 $\mu$ L reaction
10x reaction buffer A for T4 Polynucleotide Kinase	5 $\mu$ l
DNA (from DpnI digestion)	39 $\mu$ l
10mM ATP	4 $\mu$ l
T4 Polynucleotide Kinase	2 $\mu$ l

### 2.3 *In vivo* Expression

After confirming clones by DNA sequencing, the constructs of PLCH, PLCR2, and PLCN were used for the recombinant protein expression. The vectors employed here belong to the pET systems, which represent the most potent method to date for cloning and expressing recombinant proteins within *E.coli*.<sup>87</sup> These plasmids were transformed (as described above) into *E.coli* expression strains<sup>88</sup>. The clones were selected and grown in 50ml LB broth containing appropriate antibiotics at 37°C and 180 rpm overnight. This primary culture was then utilized to seed the secondary culture at a ratio of 1:100, indicating that 10ml of the primary culture was added to 1L of LB media supplemented with corresponding antibiotics and incubated at 37°C and 180 rpm. When the OD600 of the culture reached between 0.4-0.6, 0.5mM Isopropyl  $\beta$ -D-1-thiogalactopyranoside (IPTG) was introduced, followed by further incubation at 20°C and 180 rpm for 18 hours. The next day, culture was pelleted down at 6000xg for 20mins. The pellet was washed with 1X PBS and again centrifuged at 6000xg for 20mins. The harvested pellets were weighed and flash-frozen in liquid nitrogen to be preserved at -80°C for later usage.

### 2.4 Protein Purification

To isolate overexpressed proteins, the frozen pellets were unfrozen on ice and re-suspended in respective lysis buffer (Table 2.8) in a ratio of 1g cell pellet with 30 ml of lysis buffer. Afterward, it was incubated with protease inhibitors cocktail, 0.5mg/ml lysozyme, and 10ug/ml DNase 1 while stirring for 1 hour in the cold room. All the steps were performed on ice and maintained the cell lysate temperature at 4°C. The cell lysis was performed using an EmulsiFlex C3 cell disruptor. The first step was to clean the system using ethanol, water, and the lysis buffer. Then, the cell lysate was passed through the system while gradually increasing the pressure to reach 15,000 PSI. The lysate was passed through the high-pressure cell disruptor 3-

## 2. Materials and Methods

4 times. The system was washed with buffer, water and left in 70% ethanol. The lysed cells were centrifuged at 900 x g for 10 minutes at 4°C to remove unopened cells and the supernatant was then again centrifuged at 10,000 x g for 50 minutes at 4°C to remove inclusion bodies. After centrifugation, the supernatant was collected. The fusion proteins with 6 X His tag were purified using Ni-NTA- Immobilized Metal Affinity Chromatography (IMAC)<sup>89</sup>.

### 2.4.1 Affinity Chromatography

There are traditional ways of purifying a recombinant protein based on its properties, but they can be time-consuming. Simpler and faster methods have been developed using a tag attached to the protein. Examples include GST, protein A, epitope-tagging, and histidine-tagging techniques<sup>89</sup>. In this project, Ni-NTA and Co-NTA- Immobilized Metal Affinity Chromatography (IMAC) has been used to purify the His-tagged recombinant proteins<sup>89</sup>. The N-terminal 6X His tagged proteins were purified in a bind-wash and elute procedure<sup>90,91</sup>. The indigo Ni-NTA resin and cobalt resin for the PLCHR complex and PLCN respectively were put in sufficient quantities in gravity columns and it was equilibrated with the equilibration buffer (Table 2.8). The soluble proteins obtained in the supernatant were passed through the equilibrated resins 2 -3 times. Thereafter, the resin was washed with a 5-column volume of wash buffer and eluted using the elution buffer (Table 2.8). All the fractions namely, flow-through, wash fractions, and eluted proteins were collected for further analysis.

### 2.4.2 Size Exclusion Chromatography

Size exclusion chromatography (SEC), which is also called gel filtration chromatography, is a method that can be employed for protein separation and purification based on their size. This technique includes using a stationary phase composed of porous beads with pores of known sizes, which allows proteins of different sizes to diffuse through them. Larger proteins cannot penetrate the pores and are eluted first, whereas smaller proteins can and are eluted later. This process is commonly used in protein purification to isolate the target protein from other substances, such as impurities, aggregates, and small molecules<sup>92</sup>. The elution volume of a globular protein is directly proportional to the logarithm of its molecular weight<sup>93</sup>. To establish a calibration curve for a particular column, one should apply and elute at least five suitable standard proteins in the correct fractionation range, determine the elution volume for each protein standard, and plot the logarithm of molecular weight against  $V_e/V_0$ . Once a protein with an unknown molecular weight is run through the same column under the same conditions, its molecular weight can be determined by using the elution volume of the protein and the calibration curve<sup>94,95</sup>. The calibration of the SEC columns was conducted using the Gel

## 2. Materials and Methods

Filtration Markers Kit from SIGMA, which uses protein molecular weights ranging from 29,000 to 700,000 Da as standards. In this study, different SEC columns with different molecular weight fractionation ranges, including Superdex 200 Increase 10/300 GL, and HiLoad 16/600 Superdex 200 pg were used. The eluted proteins from affinity chromatography were subjected to another step of size exclusion/ gel filtration chromatography. The eluted proteins were concentrated using Amicon® Ultra-15 50,000 MWCO from Merk. Before loading the proteins onto the column, it was washed with 1 CV of filtered and degassed ddH<sub>2</sub>O and then equilibrated with 1 CV of SEC buffer (Table 2.8) followed by a protein sample which was filtered using a 0.22 µm filter. The concentration of protein in the elution fractions obtained from SEC was calculated by measuring their absorption at 280 nm using a Nanodrop.

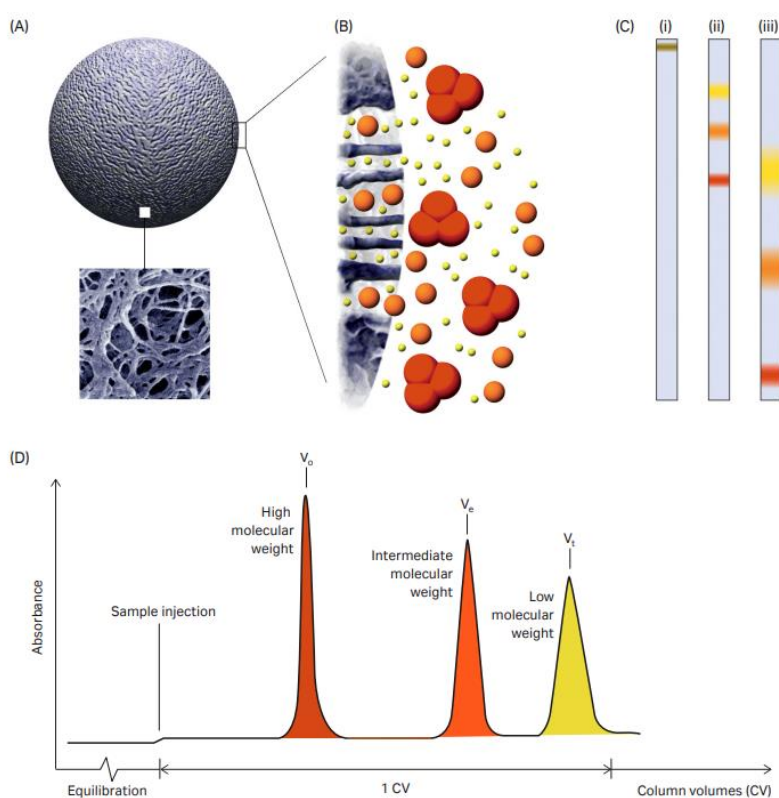


**Figure 2.1** This image illustrates the process of Size Exclusion Chromatography (SEC)

*(Figure adapted from Barth et.al.<sup>96</sup>)*

(A) shows a schematic of a particle with an enlarged electron microscopic image. (B) shows the diffusion of sample molecules into the pores of the particle. The separation process is graphically represented in panel (C), which shows that the smallest molecule (yellow) is more delayed than the largest molecule (dark orange), resulting in the largest molecule being eluted first from the column. Band broadening during chromatography leads to significant dilution of protein zones. Finally, panel (D) provides a schematic chromatogram.

## 2.5 Protein Identification

The elution fractions from IMAC and proteins eluted from the final step of purification i.e. Size exclusion chromatography were then further studied for their identity and integrity using different methods like SDS-PAGE, Western Blot, Mass spectrometry, and LC/Mass Mass, as explained below.

### 2.5.1 SDS-PAGE and Western blot

Sodium Dodecyl Sulfate (SDS) Polyacrylamide gel electrophoresis (PAGE) is used to separate proteins according to their molecular sizes and charges. It was first developed by Ulrich K. Laemmli in 1970<sup>97,98</sup>. The characteristics of the gel, including its elasticity, density, and pore size, are dictated by the concentrations of acrylamide and crosslinking agent employed. Gels with larger pore sizes are capable of quickly separating larger proteins, while gels with higher density are more effective at separating smaller molecules<sup>99</sup>. Protein samples were prepared by mixing them with 5X SDS loading dye and incubating them for 3 minutes at 95°C to achieve complete binding of the dye and denaturation of the proteins. Proteins are denatured with the detergent sodium dodecyl sulfate (SDS), and an electric current is used to pass and hence separate the negatively charged proteins based on size from cathode to anode<sup>100,99</sup>. Proteins on PAGE can be detected by staining with Coomassie Brilliant Blue or silver stain. When proteins containing tryptophans are mixed with certain compounds like 2,2,2-Trichloroethanol (TCE), they emit visible light under UV light, which can also be used to detect them on SDS-PAGE gels<sup>8</sup>. Coomassie Brilliant Blue binds non-specifically allowing proteins to appear as blue bands in the gel. However, Silver staining is more sensitive than Coomassie Brilliant Blue. In this study, the Blue silver stain has been used for more sensitivity.

Western blotting is a widely used technique in protein analysis that involves separating proteins using gel electrophoresis, transferring them to a membrane, and selectively detecting a target antigen using antibodies. This method relies on the specificity of antibody-antigen interactions and is valuable for identifying specific proteins and their molecular weights in complex mixtures in a qualitative or semi-quantitative manner<sup>101</sup>. The proteins that were separated using SDS-PAGE were transferred to a polyvinylidene difluoride (PVDF) membrane via electrophoresis, using the standard program on the Trans-Blot Turbo Transfer System from Bio-Rad. To prevent non-specific binding, the membrane was placed in 5% non-fat dry milk that was dissolved in TBS-T buffer for an hour at room temperature. The primary antibody, which was diluted in TBS-T buffer, was then added and incubated with the membrane either for an hour at room temperature, or overnight at 4°C. Subsequently, the membrane was washed

## 2. Materials and Methods

with TBS-T buffer and TBS buffer, and His-tag detection was performed without secondary antibodies. The primary antibody for His-tag was conjugated with horseradish peroxidase (HRP) enzyme, which oxidized luminol in the presence of H<sub>2</sub>O<sub>2</sub> to produce a signal<sup>102,103</sup>. The signal was detected using Chemiluminescent detection on ChemiDoc MP Imaging System.

### 2.5.2 Mass spectrometry and LC/mass-mass

Mass spectrometry (MS) is a technique that identifies and measures molecules by analyzing the mass-to-charge ratios ( $m/z$ ) of molecular ions. The resulting mass spectrum helps determine the identity of different molecules in a sample, and this method can analyze any ionized susceptible biological molecule. MS owes its success to several important discoveries, including electrospray ionization (ESI) and matrix-assisted laser desorption/ionization (MALDI) techniques discovered by John Fenn and Koichi Tanaka, respectively<sup>104,105</sup>. MALDI TOF MS is a powerful combination of the MALDI source and TOF mass that is a fast, high-throughput, low-cost, and efficient system that requires less pre-analysis workup<sup>106</sup>. To prepare a sample for analysis using MALDI MS, it is mixed or coated with a matrix solution that contains an energy-absorbent organic compound. As the matrix crystallizes on drying, the sample is also entrapped and co-crystallizes. The sample is then ionized using a laser beam, generating singly protonated ions from the analytes. These ions are then accelerated at a fixed potential, allowing them to separate based on their mass-to-charge ratio ( $m/z$ ). Different types of mass analyzers, such as quadrupole and ion trap analyzers, are used to detect and measure charged analytes. The mass-to-charge ratio ( $m/z$ ) of an ion is determined in MALDI-TOF analysis by measuring the time it takes for the ion to travel the length of the flight tube. The ions are then reflected back through the flight tube to a detector using an ion mirror, which corrects small differences in energy among ions. The resulting peptide mass fingerprint (PMF) spectrum provides information about the analytes in the sample<sup>107</sup>.

## 2. Materials and Methods

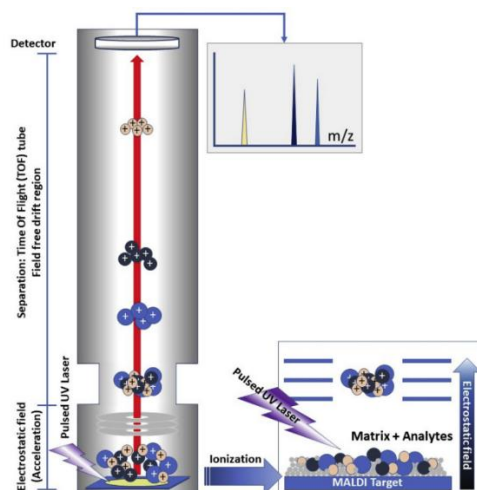


**Figure 2.2 MALDI-TOF workflow** (Figure adapted from Hou et.al.<sup>106</sup>)

MALDI-TOF works by ionizing biomolecules in a crystalline matrix using a laser. The ions are then accelerated through an electric field and their time-of-flight to a detector is measured. This allows for precise determination of the molecules' mass-to-charge ratios, enabling their identification and analysis.

In this study, a purified protein sample was analyzed at EMBL Hamburg's Protein characterization facility using a Bruker Autoflex™ Speed MALDI/TOF System. The sample was filtered and diluted with SEC buffer to a final concentration of 40uM. A mixture of 1ul protein sample, 1ul of 0.1% trifluoroacetic acid, and 1ul of supersaturated dihydroxy acetophenone (DHAP) matrix was spotted in duplicates onto a MALDI target plate. The system was calibrated with a Bruker protein standard II(20 – 66 kDa).

Liquid chromatography separates molecules based on their solubility or interaction with a mobile and stationary phase. Analytes first interact with functionalized particles (stationary phase) and are then eluted when their interaction with the solvent (mobile phase) is stronger<sup>108</sup>. The choice of solvent and stationary phase depends on the analysis being performed. Liquid chromatography coupled with tandem mass spectrometry (LC-MS/MS) separates analytes from matrix components, improving sensitivity, specificity, and precision.<sup>108</sup> LC-MS/MS is highly selective and useful for quantitative analysis. To perform quantitative analysis, the specimen is pretreated, diluted, or purified to remediate matrix complexities, and then injected into the liquid chromatography system. The liquid chromatography eluent carries the analyte into the source of the mass spectrometer where gas phase ions are produced. The first mass analyzer filters incoming ions and allows only precursor ions to move forward toward the collision cell. In the collision cell, precursor ions are fragmented into product ions, which are analyzed in the

last stage of the tandem mass spectrometer. The resulting mass spectrum shows only the product ions. To perform quantitative analyses, selected reaction monitoring is used by focusing on particular precursor/product ion pairs<sup>108</sup>. The stained protein bands were cut and sent to EMBL-Heidelberg Proteomics Core Facility. The protein identification was performed with in-gel in-gel trypsin digestion and in gel acid hydrolysis followed by LC-MS/MS on a Dionex Ultimate 3000 HPLC coupled to an Orbitrap Fusion Lumos System.

### 2.6 Biophysical Characterization

#### 2.6.1 Mass Photometry

The technique known as Mass Photometry (MP) utilizes light scattering to detect unlabeled molecules in diluted solutions. This method has the capability to precisely measure molecular masses ranging from 40 kDa to 5 MDa, and it can also determine the relative abundance of various molecular species through molecular counting<sup>109</sup>. The outcome of the MP measurement is a molecular mass distribution that represents the molecular makeup of the sample<sup>109</sup>.

The Mass Photometry protocol used, is from Wu and Piszczek 2021. The measurements were performed using a Re-Feyn One MP mass photometer, with a maximum error mass of 2.5%. Initially, 18  $\mu$ L of buffer were applied to the lens grid and measured, after which 2  $\mu$ L of 80 nM protein sample were added to achieve a working concentration of 8 nM, and the sample was measured. The Re-Feyn software was utilized to extract data on particles by converting the acquired video data into individual landing events. The software plotted signal counts against the molecular weight, with mass calibration derived from previously measured protein standards. The distribution peaks were then fitted to a Gaussian distribution function as described by Wu and Piszczek in 2021.

#### 2.6.2 Dynamic Light Scattering

When a beam of monochromatic light interacts with a solution containing macromolecules, the light scatters in all directions depending on the size and shape of the macromolecules. Static light scattering analyzes the time-averaged intensity of scattered light, providing valuable information on the molecular weight and radius of gyration of the macromolecules. On the other hand, dynamic light scattering measures the Brownian motion of the macromolecules in solution by analyzing the intensity fluctuations of the scattered light. This technique relates the motion to the size or diffusion coefficient of the particles. The temperature accuracy is crucial for dynamic light scattering measurements since the viscosity of the solvent depends on the temperature. By monitoring the movement of particles over time, information on the size of the

## 2. Materials and Methods

macromolecules can be obtained, as larger particles diffuse more slowly than smaller particles, resulting in similar positions at different time points<sup>110</sup>.

Dynamic light scattering (DLS) is a technique used for determining the hydrodynamic radius ( $R_h$ ) or Stokes radius ( $R_s$ ) of molecules in solution<sup>111</sup>. The  $R_s$  represents the radius of a theoretical sphere that would undergo diffusion at an equal rate to that of the molecule under analysis. DLS measures the intensity of light scattered by molecules in the sample over time, from which the translational diffusion coefficient ( $D$ ) can be obtained using an auto-correlation function. The RS can then be derived from the Stokes-Einstein equation, which takes into account the diffusion coefficient, temperature, viscosity, and radius of the molecule<sup>111</sup>.

$$D\tau = \frac{kBT}{6\pi\eta R_h}$$

Where  $k_B$  is Boltzmann coefficient ( $1.380 \times 10^{-23} \text{kg.m}^2.\text{s}^{-2}.\text{K}^{-1}$ ),  $T$  is an absolute temperature, and  $\eta$  is the viscosity of medium. DLS measurements were carried out at 20°C on DynaPro® NanoStar® and the measurements were processed using the Wyatt DYNAMICS analysis software, which was utilized to generate graphs and determine radii and poly dispersity.

### 2.6.3 Circular Dichroism

Circular Dichroism (CD) is based on the distinction in the absorption of left and right circularly polarized radiation by chromophores that can be inherently chiral or can be positioned in chiral environments<sup>112</sup>. The use of Circular Dichroism (CD) spectroscopy is crucial in the field of structural biology. It has various applications, such as identifying the protein's secondary structure content, detecting protein folding and unfolding, determining protein stability, assessing the formation of macromolecular complexes, and characterizing interactions between proteins and ligands<sup>113</sup>. The Far-UV CD refers to the region in the spectrum ranging from 160 to 240 nm. This specific range is of significant interest because the protein's backbone peptide bond singlet electronic transitions occur at 190 and 220 nm (also known as the amide chromophore N-C=O). The 220 nm transition is due to the lone pair on oxygen to  $\pi^*$  antibonding orbital ( $n\pi^*$  transition), and the 190 nm transition is from a non-bonding  $\pi$  orbital to the  $\pi^*$  orbital ( $\pi_{nb}\pi^*$  transition)<sup>114</sup>. These two transitions interact in the protein's chiral environment, leading to unique spectra for each secondary structural component present in the protein. For an  $\alpha$ -helix, the exciton splitting of the  $\pi_{nb}\pi^*$  transition produces a positive peak at 190 nm and a negative peak at 208 nm besides a negative peak at 220 nm due to the  $n\pi^*$  transition<sup>115</sup>. In  $\alpha$ -helical structures, the electronic transitions at 190 nm and 208 nm are

## 2. Materials and Methods

polarized parallel and perpendicular to the helix axis, respectively. Additional secondary structural motifs, such as  $\beta$ -sheet and random coil, have their characteristic CD spectra.

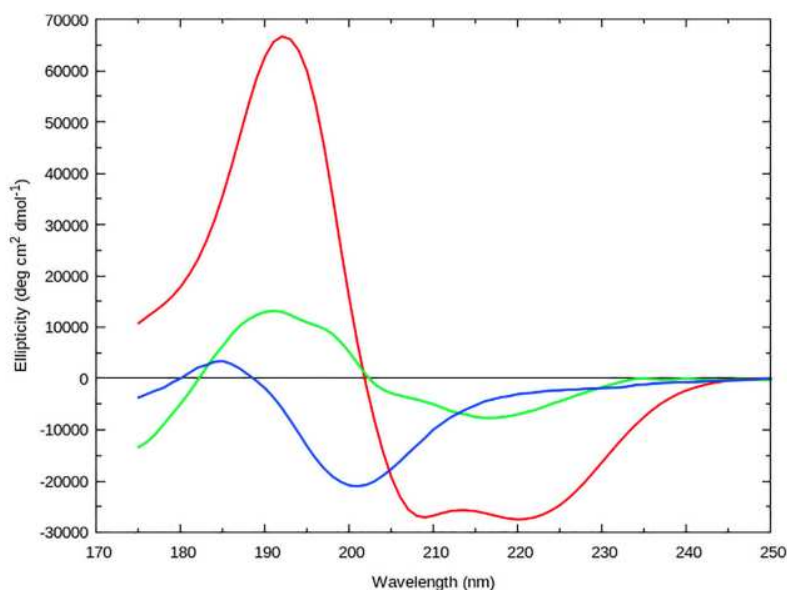


**Figure 2.3: CD spectra displaying types of secondary structures :  $\alpha$ -helix, a  $\beta$ -sheet, and a random coil (Figure adapted from Rogers *et.al.*<sup>114</sup>)**

$\alpha$ -helical proteins display negative peaks at 222 nm and 208 nm and positive peaks at 193 nm. In contrast, proteins with distinct anti-parallel  $\beta$ -pleated sheets exhibit negative peaks at 218 nm and positive peaks at 195 nm. On the other hand, disordered proteins demonstrate low ellipticity beyond 210 nm and negative peaks around 195 nm.

To exchange the sample buffer from SEC buffer to CD buffer, 0.5 mL Zeba™ spin desalting columns were used. The spin column was equilibrated three times with 300  $\mu$ L CD buffer and the buffer was discarded. Subsequently, 150  $\mu$ L of protein sample was passed through the column by centrifugation and collected in a separate reaction tube. This process was repeated once, resulting in 300  $\mu$ L of the sample being exchanged into CD buffer. The sample was stored on ice. Circular dichroism (CD) measurements were performed on an Aviv CD425 spectrometer and the spectra were collected from wavelength 260 nm to 190 nm in 1 nm increments and 9 s averaging time at 4°C. Temperature scans were conducted at a heating rate of 2 °C per cycle, with an average time of 9 seconds, spanning from 4 °C to 98 °C. The resulting

## 2. Materials and Methods

CD spectra are typically normalized to the mean residue ellipticity for comparison, which is calculated using the following equation:

$$[\theta]_{\text{mrw},\lambda} = \text{MRW} * \theta\pi / (10d * c).$$

Here,  $[\theta]_{\text{mrw},\lambda}$  represents the mean residue ellipticity in  $\text{deg}\times\text{cm}^2\times\text{dmol}^{-1}$ , MRW is the mean residue weight calculated using the molecular weight and number of residues (see equation below),  $\theta$  is the observed ellipticity (in degrees),  $d$  is the path length (in cm), and  $c$  is the protein concentration (in mg/mL).

$$\text{MRW} = \text{molecular weight} / \text{number of residues} - 1$$

The buffer baselines were subtracted from the sample spectra. The online server DichroWeb (<http://dichroweb.cryst.bbk.ac.uk/html/home.shtml>) and the BESTSEL program were utilized to perform deconvolutions of CD data and evaluate the secondary structure<sup>116</sup>.

### 2.6.4 Fluorescence Spectroscopy

Fluorescence is a type of luminescence that arises from electronically excited singlet states of a chromophore, constituting one of two such phenomena. When photons of a certain energy are absorbed by a fluorophore, singlet electronic high-energy states such as S1, S2, etc. are populated. Within these states, there exists a range of sub-vibrational energy levels, designated 0, 1, 2, and so forth. From the higher vibrational states, a rapid relaxation process called internal conversion takes place, leading to the lowest vibrational level of S1. Electrons then return from singlet excited states to the ground state in a spin-allowed process that involves the emission of photons, known as fluorescence. Due to partial energy dissipation during internal conversions, fluorescence occurs at lower energies or longer wavelengths (known as the Stokes' shift)<sup>117</sup>.

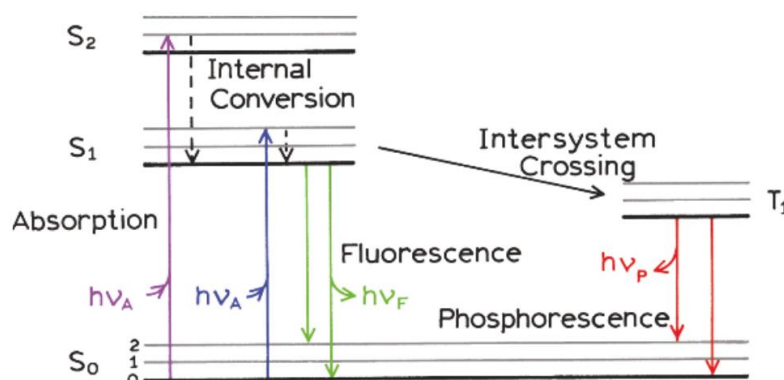


**Figure 2.4: Jablonski's diagram illustrating transitions associated with fluorescence and phosphorescence** (Figure adapted from Lakowicz *et.al.*<sup>117</sup>)

## 2. Materials and Methods

Fluorescence spectroscopy is a non-destructive analytical technique used to study the properties and behavior of fluorescent molecules. It involves the excitation of molecules to higher energy states by absorption of light, followed by the emission of light at longer wavelengths upon relaxation back to lower energy states. This emitted light can be detected and used to gather information about the structure, dynamics, and environment of the fluorescent molecules<sup>117</sup>. The inherent fluorescence exhibited by aromatic amino acids within proteins has served as a method to observe the unfolding and refolding transitions that are prompted by chemical denaturants, changes in temperature, pH levels, and pressure. Trp is the most prevalent of the three fluorescent amino acid components in proteins, with concentrations of approximately 1 mol % in soluble, cytoplasmic proteins and up to 3 mol % in membrane proteins<sup>118</sup>. The indole group present in tryptophan makes it the most dominant fluorophore. One notable characteristic of the emission spectra is that they are generally independent of the excitation wavelength, a feature that has been utilized to eliminate interference from weak fluorophores. By examining the position of fluorescence maxima, researchers can infer the location of the corresponding fluorophore within the protein, since this is highly sensitive to the fluorophore's environment. Fluorescence spectroscopy experiments were conducted using the AVIV Model 425 spectrometer, with an excitation wavelength of 295 nm and emission spectra collected in the range of 450 nm to 260 nm. Thermal denaturation experiments were carried out over a temperature range of 4 °C to 98 °C at a heating rate of 2 °C per minute, with an average time of 1 second.

### 2.6.5 SEC-SAXS

Small - angle X-ray scattering (SAXS) is a technique for obtaining global structural features and shape information at resolutions ranging from nanometres to micrometres<sup>119</sup>. Phospholipase C and the chaperon PLCR was investigated for structural characteristics with Small angle X-ray scattering (SAXS) using the EMBL-P12 bioSAXS beam line<sup>119</sup>. To acquire solution-based structural data and molecular weight (MW) estimates, the complex was subjected to size-exclusion chromatography (SEC)-SAXS studies in conjunction with parallel multi-angle laser light scattering (MALLS), dynamic light scattering (DLS), and refractive index (RI) measurements<sup>120</sup>.

SAXS data collection,  $I(s)$  vs  $s$ , where  $s = 4\pi\sin\theta/\lambda$ ;  $2\theta$  is the scattering angle and  $\lambda$  the X-ray wavelength (0.124 nm; 10 keV) was performed at 20C using a GE-Healthcare S200 Increase 10/300 analytical SEC column equilibrated in 25 mM Tris pH 7.5, 100 mM NaCl, 3 mM  $\beta$ -mercaptoethanol, at a flow rate of 0.7 ml.min<sup>-1</sup>. Automated sample injection and data collection

## 2. Materials and Methods

were controlled using the BECQUEREL beam line control software<sup>121</sup>. Three sequential sample injections were performed: 50 $\mu$ l at 3.5 mgml<sup>-1</sup>; 50 $\mu$ l at 7 mgml<sup>-1</sup> and 70 $\mu$ l at 14 mgml<sup>-1</sup>. The SAXS intensities were measured for each run as 2100 x 1 s individual X-ray exposures, from the continuously flowing column eluent, using a Pilatus 6M 2D-area detector at a sample to detector distance of 3 m. The 2D-to-1D data reduction, i.e., radial averaging of the data to produce 1D I(s) vs s profiles, were performed using the SASFLOW pipeline incorporating RADAVER from the ATSAS 2.8 suite of software tools<sup>122,123</sup>. The 2100 individual frames obtained for each SEC-SAXS run were processed using CHROMIXS<sup>124</sup>. Briefly, individual SAXS data frames were selected across the respective sample SEC-elution peaks and an appropriate region of the elution profile corresponding to SAXS data measured from the solute-free buffer, were identified, averaged and then subtracted to generate individual background-subtracted sample data frames. These data frames underwent further processing, specifically data merging due to the noted effects of X-ray induced radiation damage in the high concentration samples. Briefly, data merging between the high- and low-concentration samples was performed to obtain quality high-angle scattering data from the 14 and 7 mgml<sup>-1</sup> datasets that were then combined with the (scaled) low-angle scattering data from the 3.5 mgml<sup>-1</sup> that qualitatively appeared much-less effected by radiation damage to generate a final merged SAXS profile with contributions from all three SEC-SAXS runs.

The MALLS and DLS data were measured using a Wyatt Technologies Mini-Dawn TREOS with inbuilt quasi elastic light scattering (QELS) module coupled to a OptiLab T-Rex refractometer and Agilent 1260 UV spectrophotometer for protein concentration determination. The MALLS system was calibrated relative to the scattering from toluene and, in combination with concentration estimates obtained from refractive index (RI), was used to evaluate the MW distribution of species eluting from the SEC column (the dn/dc of the complex was taken as 0.185 mlg<sup>-1</sup>). The molecular weight estimates from MALLS/RI and the hydrodynamic radius, RH, derived from QELS were determined using Wyatt ASTRA7 software. The light scattering and RI measurements were performed at 25°C.

All SAXS data-data comparisons and data-model fits were assessed using the reduced  $\chi^2$  test and the Correlation Map, or CORMAP, p-value<sup>125</sup>. Fits within the  $\chi^2$  range of 0.9–1.1 or having a CORMAP p-values higher than the significance threshold cutoff of  $\alpha=0.01$  are considered excellent, i.e., no systematic differences are present between the data-data or data-model fits at the significance threshold.

## 2. Materials and Methods

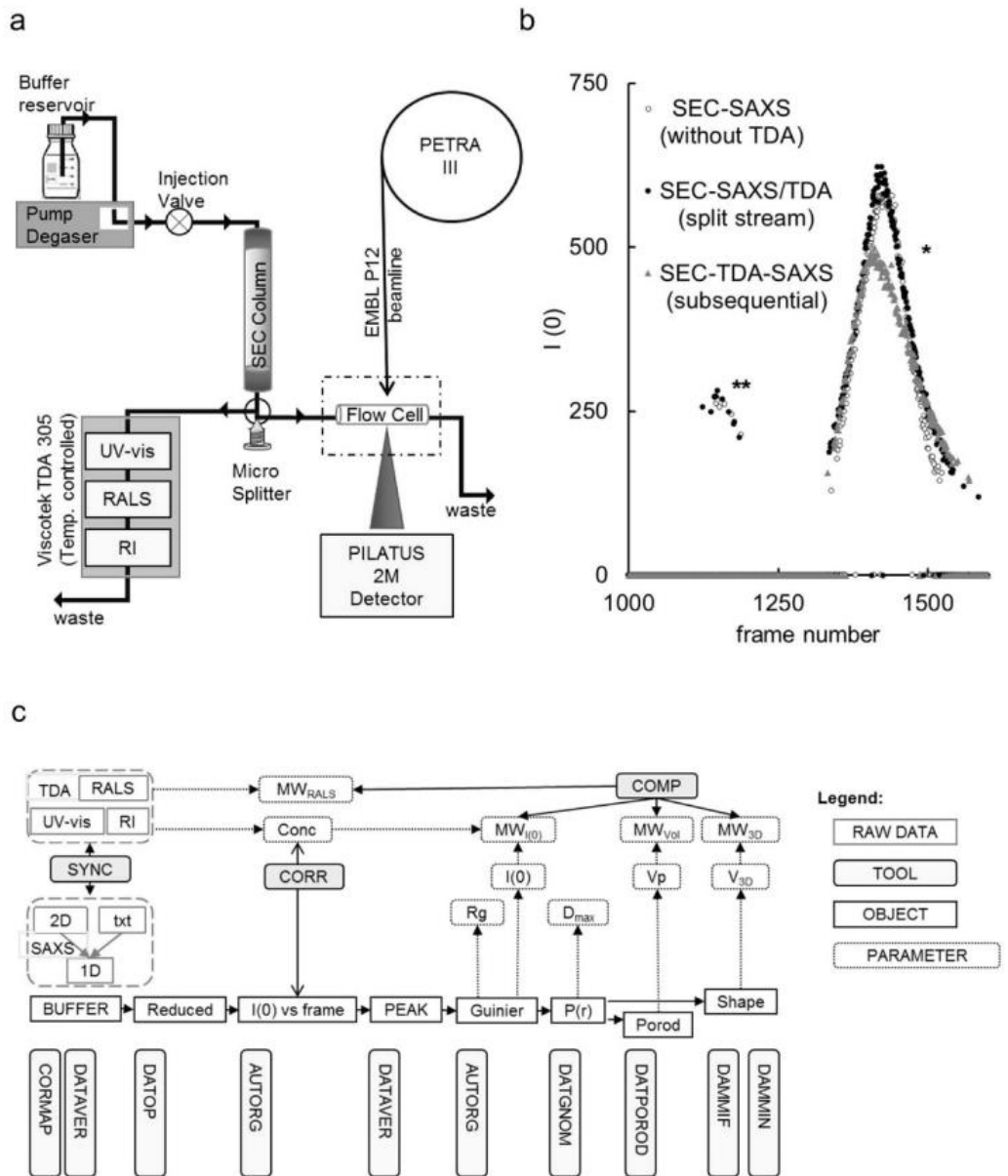


**Figure 2.5** SEC-SAXS/TDA set-up at the EMBL-P12 beamline (Figure adapted from Blanchet et al.<sup>119</sup>)

The SEC-SAXS workflow for analyzing biological samples involves several steps. First, the sample is purified and prepared for analysis. Then, it undergoes size-exclusion chromatography (SEC) to separate it based on size while eluting in a continuous flow. While eluting, the sample passes through an X-ray beam, recording a scattering pattern that captures structural information. The collected data is processed to obtain intensity and angle information, enabling the characterization of the sample's molecular structure. Lastly, data analysis interprets the processed information, providing insights into the sample's conformation and behavior.

### 2.6.6 Atomic Force Microscopy

Atomic Force Microscopy (AFM) is a high-resolution version of Scanning Probe Microscopy (SPM) that measures in nanometers<sup>126</sup>. The probe in AFM is a stylus (V - shaped cantilever) that engages with the sample's surface directly, determining the repulsive and attractive forces that exist between the probe and the surface in order to acquire a high-resolution 3D topographical image of the surface<sup>127</sup>.

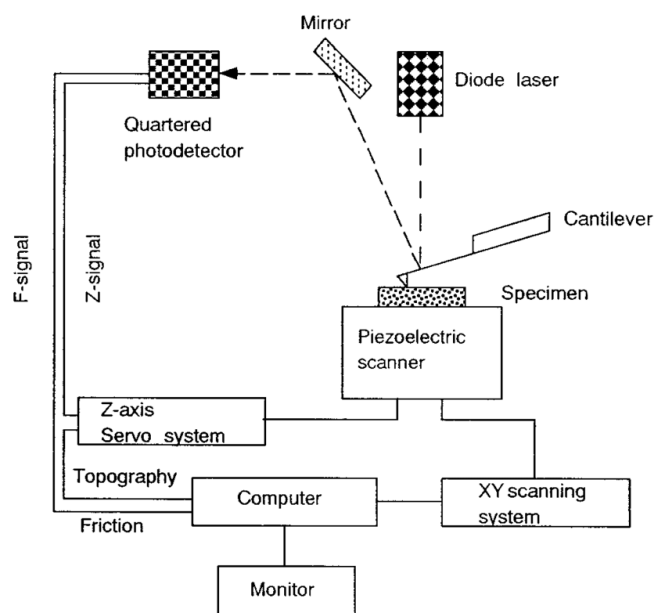


**Figure 2.6 Schematic diagram of Atomic Force Microscopy** (Figure adapted from *Khurshudov et.al.*<sup>128</sup>)

Atomic Force Microscopy (AFM) uses a sharp tip on a flexible cantilever to scan surfaces, measuring attractive and repulsive forces between the tip and atoms on the sample. It creates high-resolution topographical images, enabling nanoscale characterization and manipulation of materials.

In this experiment, 1, 2-Dimyristoyl-sn-Glycero-3-Phosphocholine (DMPC) was used in order to investigate the interaction of PLCHR2 with the membrane.

1,2-Dimyristoyl-sn-Glycero-3-Phosphocholine (DMPC) (Anatrace, USA) was dissolved in chloroform to 10 mg/ml stock concentration. The DMPC solution at the stock concentration was diluted with chloroform to a 1 mg/ml working concentration. The solution was dried by air blow and heated at 60 °C for 1 minute. A lipid membrane buffer containing 10 mM HEPES (pH 7.4), 150 mM NaCl, and 20 mM MgCl<sub>2</sub> was added to the dried lipid membrane powder to

## 2. Materials and Methods

restore the 1 mg/ml concentration. The solution was sonicated at 35% power for 2 minutes. The solution remained at 4 °C for 30 minutes and 60 °C for 30 minutes. The solution was set on this hot-cold cycle for 3 rounds. The solution was finally stored at 4°C overnight before use. The DMPC liposome solution was diluted with the lipid membrane buffer to 0.5 mg/ml concentration. The diluted solution was incubated on freshly cleaved mica (V1 grade, Ted Pella, USA) for 20 minutes. The liposome spread on the mica and formed supported lipid bilayers (SLBs). The SLBs were then rinsed with the PBS solution. The subsequent experiments were performed in the PBS solution. After the SLB formation was ensured, 5 µL of the phospholipase enzyme solution at 2 mg/ml concentration was added to the lipid membrane. AFM-based imaging in a liquid milieu was performed in the PeakForce tapping mode (NanoWizard ULTRA Speed 2, Bruker, USA) at room temperature. The scanned areas were 1-10 µm x 1-10 µm with a resolution of 256-512 x 256-512. The scanning speed was 2-4 Hz. A soft BioLever (BL-AC40TS-C2, Olympus, Japan) with a nominal spring constant of 0.09 N/m was calibrated with a contact-free thermal tune. The volume of the digested membrane was averaged from 11 holes after incubating with the enzyme (475 to 1287 s). The volume of the ring-like structures was averaged from 10 rings after incubating with the enzyme (1444 to 1788 s). The image processing and analysis were performed with the JPKSPM Data Processing software.

### 2.7 Biochemical Characterization

#### 2.7.1 In vivo (MTT assay)

The MTT reagent (3-(4,5-dimethylthiazol-2-yl)-2,5-diphenyl-2H-tetrazolium bromide), a mono-tetrazolium salt is composed of a positively charged quaternary tetrazole ring core having four nitrogen atoms surrounded by three aromatic rings with two phenyl moieties and one thiazolyl ring<sup>129,130</sup>. Because of its positive charge and lipophilic nature, the MTT reagent can pass through the cell membrane as well as the mitochondrial inner membrane of living cells and is converted to formazan by metabolically active cells<sup>129,130</sup>. Inside the cells the MTT is reduced, the core tetrazole ring is disrupted, resulting in the creation of formazan, a violet-blue water-insoluble molecule. Mosmann et al. created the MTT test in 1983 because the chromogenic nature of this redox chemical reaction allows a colorimetric-based assessment of intracellular formazan synthesis<sup>129</sup>. Nowadays, it is extensively used to represent cell toxicity, cell viability, and metabolic activity.

For this project, the MTT assay was used to determine the toxicity of the purified phospholipases C – PLCHR complex and PLCN on HeLa cells (The cell line was created from cervical cancer cells collected from Henrietta Lacks, who died of cancer in 1951). The HeLa

## 2. Materials and Methods

cells aliquot was obtained from Kolbe lab. In order to perform the MTT assay, HeLa cells were grown in suitable media using the following protocol.

An aliquot of HeLa adherent cells were taken from -196°C and was unfrozen in a water-bath at 37°C until it's all in liquid form. Then the content of the vial was transferred in 10 ml of pre-warmed (37°C) complete cell culture media i.e. RPMI media (see table 2.5). The cells were then centrifuged at 200 X g for 4 minutes at room temperature. The supernatant was discarded and the cells were re-suspended in 5 ml of pre-warmed complete media and then transferred in T25 cell culture flask. The cells were then incubated at 37°C, 5% CO<sub>2</sub> overnight. The next day, the cells were transferred to T75 cell culture flask and grown until they reach 90% confluency. All steps were performed in a sterile environment – the work was always conducted within a biosafety cabinet. First, the cell culture to be passaged was placed under the sterile hood. Then, using a 10 mL serological pipette, the old cell culture media was removed and discarded into a waste bottle. Subsequently, the cells were washed with 3-4 mL of PBS, gently adding it to the side of the flask. After removing the PBS and discarding it, 1.5 mL of Trypsin/EDTA was added to the cells, which were then incubated at 37°C for approximately 5 minutes until detachment occurred. To stop the enzymatic reaction, 3 mL of complete media was added. Next, the cell suspension was transferred into a fresh 15 mL Falcon tube. The cells were then spun down at 200 x g for 4 minutes at room temperature, and the supernatant was discarded. The cell pellet was gently resuspended in 1 mL of growth medium by pipetting up and down. A new 100 mm cell culture dish was prepared by adding 10 mL of growth medium. Approximately 100 µL of the cell suspension was added to the new T75 culture flask. Finally, the cells were incubated at 37°C with 5% CO<sub>2</sub> in a humidified atmosphere. MTT assay was performed once cells viability reached 90%.

Under sterile conditions, a 100-200 µL portion of the cell suspension was removed. An equal volume of Trypan Blue (with a dilution factor of 2) was added, and the mixture was gently pipetted to ensure thorough mixing. 5-10 µL of the cell suspension was added onto a clean hemacytometer, covered with a coverslip and viewed under a microscope for cell counting.. The number of viable cells (bright cells) and non-viable cells (stained blue) were counted. The number of viable cells were calculated using the following equation.

$$\text{Total } \frac{\text{cells}}{\text{ml}} = \frac{\text{Total cells counted} \times \text{Dilution factor} \times 10,000 \text{ cells/ml}}{\text{Number of squares counted}}$$

## 2. Materials and Methods

After a few passages, the cells were seeded into 96 well plate. Each well contained  $2 \times 10^4$  cells. 100ul of the cells were incubated with 100ul of the protein of different dilutions from 350 ng/ $\mu$ l to 0.0009 ng/ $\mu$ l for 12 hours at 37°C with 5% CO<sub>2</sub> in a humidified atmosphere. After 12 hrs of incubation, the solution was decanted and now the cells were incubated with 100  $\mu$ l MTT solution for 4 hours. Thereafter, the MTT solution was decanted again and 100  $\mu$ l of 0.04M of HCl (diluted in Isopropanol) was added and incubated at for 15 mins at room temperature in dark and continuous shaking. Then the absorbance at 570nm was measured using a Tecan Spark plate reader.

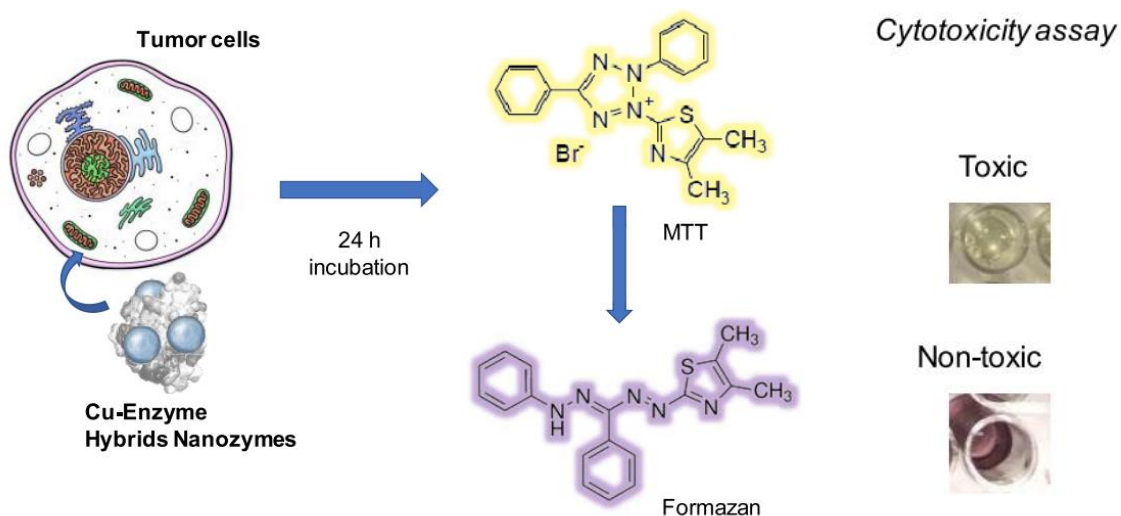


**Figure 2.7 Schematic diagram of MTT assay** (Figure adapted from Losada-Garcia et al.

131)

The MTT (3-(4,5-dimethylthiazol-2-yl)-2,5-diphenyltetrazolium bromide) assay assess cell viability and proliferation through the enzymatic reduction of MTT dye by living cells. Upon treatment with MTT, viable cells convert the yellow MTT dye into insoluble purple formazan crystals localized in their mitochondria. Subsequently, the formazan crystals can be dissolved, and their absorbance is measured using a spectrophotometer. The intensity of the purple coloration is directly proportional to the number of viable cells present, allowing quantitative determination of cell viability, proliferation, and cytotoxicity.

### 2.7.2 In vitro

P-nitrophenylphosphorylcholine (p-NPPC), a substrate analog, is often used to identify phospholipase C (PLC) activity in vitro. A yellow color compound namely, p-nitrophenol (p-NP) is produced as a cleavage product by PLC and can be measured at 405nm<sup>132</sup>. In this project, the NPPC assay was performed using the Phospholipase C (PLC) Activity Assay Kit from Sigma Aldrich. The enzymatic activity was measured for both the PLCHR complex and PLCN. Along with the wild-type enzymatic activity, the enzymatic activity for the mutants T178A and T176A respectively, was also measured. Several Gram-positive PLCs need a cation for their activity. In order to understand the metal dependency for the PLCs of *Pseudomonas aeruginosa*<sup>133,134,74</sup>. Enzymatic activity with cations like Mg<sup>2+</sup>, Ca<sup>2+</sup>, Zn<sup>2+</sup>, and EDTA was also measured.

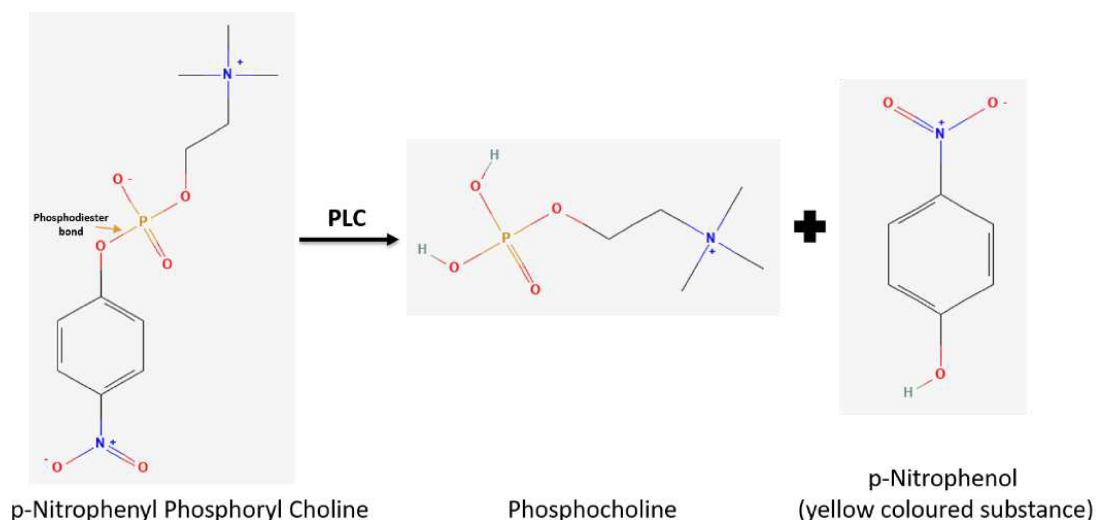


**Figure 2.8 Chemical reaction showing the cleavage of the NPPC (p - nitrophenylphosphorylcholine) by PLC**

This assay is based on the hydrolysis of NPPC by PLC, resulting in the release of p-nitrophenol, a yellow-colored compound. The rate of p-nitrophenol release is directly proportional to the PLC activity present in the sample. The yellow color compound can be measured at 405nm.

### 2.7.3 Hemolytic assay

Blood Agar is an enriched medium that is frequently used to grow fastidious organisms and discriminate against microorganisms depending on their hemolytic characteristics<sup>135</sup>. The blood agar plates can be used to determine the hemolytic property bacteria or proteins qualitatively.

## 2. Materials and Methods

There are major three types of hemolysis namely; Beta hemolysis ( $\beta$ ), Alpha hemolysis ( $\alpha$ ) and Gamma hemolysis ( $\gamma$ ). Figure 2.9 shows the difference between these three types of hemolysis. Here, the PLCHR complex and PLCN were both incubated on Columbia agar with 7% sheep blood plates from Thermo Fisher Scientific. 100 $\mu$ l of 70ug/ml of protein was added onto the plates and incubated at 37°C for 16 hours.

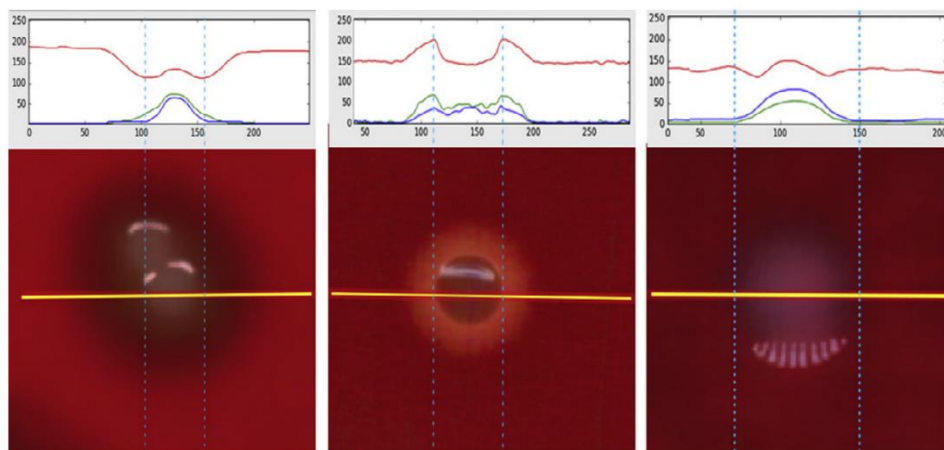


**Figure 2.9 Different types of hemolysis** (Figure adapted from Savardi et.al.<sup>136</sup>)

Color distribution (RGB channels) along the colony axis (yellow line) in the cases of Alpha (Left), Beta (Middle) and Gamma (Right) hemolysis

## 2.8 Structure solution

### 2.8.1 X-ray Crystallography

X-ray crystallography is the most used technique for the structure determination of biological macromolecules such as proteins, and nucleic acids. X-ray crystallography aims to extract a crystal's three-dimensional molecular structure<sup>137</sup>. A high quantity of purified material is crystallized and is then subjected to an X-ray beam<sup>137</sup>. The generated diffraction spot pattern can then be used to first comprehend the symmetry of the crystal packing and the dimensions of the unit cell of the crystal<sup>137</sup>. An electron density map can then be created by calculating the "structure factors" from the spot intensities<sup>137</sup>. This density map can be improved through a variety of techniques to allow the construction of a model. The generated model is then improved to more accurately fit the map and adopt a thermodynamically preferred conformation<sup>137</sup>.

### **2.8.1.1 Crystallization of PLCN and PLCHR2 complex**

Protein crystals of hemoglobin from worms and fishes were accidentally found 150 years ago and developed in the final years of the 19th century as a potent purification technique and chemical purity demonstration<sup>138</sup>. X-ray crystallography of biological macromolecules in the 1930s gave protein crystals a new and vital role. Bernal, Fankuchen, Crowfoot, and Perutz's early work rendered protein crystals essential because of their potential three-dimensional structural information. Protein crystallography matured in the years between the 1960s and 1970s, boosting demand for protein crystals<sup>139</sup>. There are two different yet interdependent phases involved in the formation of crystals of any molecule or collection of chemical species, including proteins i.e. nucleation and growth. Nucleation, a first-order phase change that orders molecules from a disordered state, is the most demanding theoretical and experimental challenge<sup>138</sup>. Critical nuclei are tiny, totally ordered assemblies that develop from partly ordered or paracrystalline intermediates, such as protein aggregates with short-range order. Critical nuclei have to consider molecule size, supersaturation, and molecular addition surface free energy<sup>138</sup>. For a few systems, the essential nuclear size has only been defined in terms of two-dimensional nuclei growing on the surfaces of existing crystals. In concentrated protein solutions, a "liquid protein phase" emerges, which leads to critical nuclei in complete order<sup>138</sup>.

Unlike nucleation, macromolecular crystal growth is widely known. Protein crystals form mostly through dislocation growth, two-dimensional nucleation, normal growth, and 3D nucleation. Nucleation and growth depend on the supersaturation of the mother liquor forming the crystals. Supersaturation controls both processes, their incidence, extent, and kinetics<sup>138</sup>. By employing automated robotic systems, the precise and efficient regulation of protein crystallization conditions is achieved, leading to accelerated protein structure discovery and facilitating advancements in drug development. The implementation of robotic automation simplifies the laborious protein crystallization process, enabling extensive experimentation and enhancing the probability of obtaining superior-quality crystals for X-ray crystallography investigation<sup>140,141</sup>.

## 2. Materials and Methods

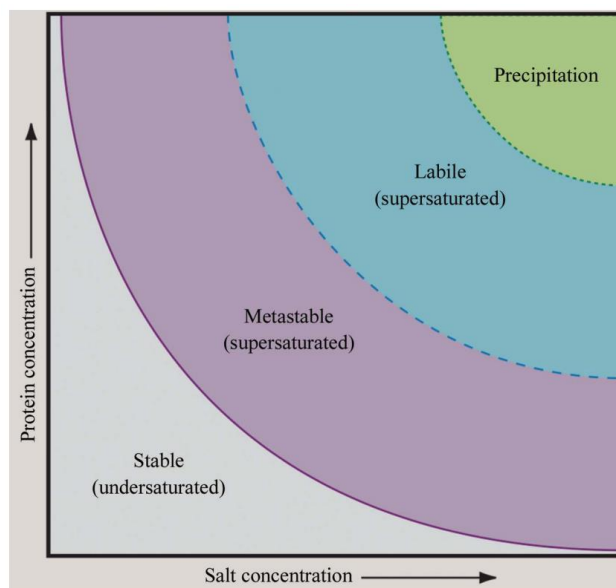


**Figure 2.10** The phase diagram for the crystallization of macromolecules (*Figure adapted from McPherson et.al.<sup>138</sup>*)

An Amicon® Ultra-15 30.000 MWCO centrifugal concentrator was used to concentrate the protein sample in SEC buffer (4.000 x g, 10-minute intervals, 4°C). The protein solution was concentrated to a concentration of 12 mg/mL, transferred to an Eppendorf tube, centrifuged to remove precipitation (15.000 x g, 20 min, 4°C). PLCHR complex and PLCN were subjected to crystallization. Purified protein sample was used to set up initial crystallization screens, comprising 480 conditions. Crystallization screens were prepared using a Mosquito LCP robot after the sample was delivered on ice to the EMBL protein characterization facility, Hamburg.

Several screens were chosen for this initial crystallization experiments: I and II of the JCSG Core, Morpheus™ HT-96 and Morpheus™ II from Molecular Dimensions, screens from Qiagen, such as PEGs II suite, pH clear II, NeXtal PEG, NeXtal AmSO4 suite. In order to prepare the sitting drop vapor diffusion experiment on 3-well UVP crystallization plates, drops of 300 nl were utilized in ratios of 2:1, 1:1, and 1:2 (protein: precipitant). The plates were placed in a crystallization chamber and incubated at 19°C.

Based on the results of the first round of crystallization, a fine screen was made. The Morpheus™ II screen settings that led to needle crystals was composed of: 10% (v/v) Polyethylene glycol (PEG) 8000, 20% (v/v) 1,5-Pentanediol, 0.1 M MOPSO/BisTris, pH 6.5, and the only difference was the chemicals (1 mM Alkali Mix 1 and 20 mM Monosaccharide Mix 2)<sup>142</sup>. A fine screen with a composition of 4-13% Polyethylene glycol (PEG) 8000, 11-

## 2. Materials and Methods

26% 1,5-Pentanediol, 0.1 M MOPSO/BisTris 6-7 pH, and with and without 1 mM Alkali Mix 1 and 20 mM Monosaccharide Mix 2. 384 fine screen conditions were made using Scorpion Screen Builder from art Robbins instruments at EMBL. Crystallization plates were prepared by setting up this fine screen with sitting drops of 150 nl (1:1 ratio) for each condition containing 10mg/ml of pure PLCN.

In-situ proteolysis is the proactive addition of minute quantities of non-specific proteases to assist in the crystallization of proteins and protein macromolecular complexes. It is the technique of choice for difficult targets due to its ease of execution and high rate of recovery. Herein, in this study also, PLCN protein was also subjected to trypsin proteolysis. For the stock solution, 20ug of Pierce™ Trypsin Protease, MS Grade was mixed in 20ul of 50 mM acetic acid (conc. 1 mg/ml). PLCN with a concentration of 9mg/ml (540µg) was mixed with trypsin in 1:1200 (0.083%) i.e. 0.4482 µg. Immediately after mixing, the crystallization plates were set up using the fine screen mentioned above.

### 2.8.1.2 Data Collection and data processing

In a microscope, when a specimen is illuminated by a light beam, the scattered light is focused into an image using a lens. X-ray diffraction, in principle, operates similarly, but it lacks an X-ray lens to focus the scattered X-rays from the crystal's electrons. As a result, direct interpretation through obtaining an image is not possible. Instead, crystallographers rely on measuring the intensities of the scattered X rays from the crystal and using this data, along with additional information explained below, to generate an image.

The reason to use a crystal is that detecting the signal from a single molecule would be too faint. The crystal behaves like a three-dimensional diffraction grating, scattering the incident X-ray beam only in specific directions. Since all the molecules in the crystal scatter collectively in these directions and there are a vast number of molecules (typically over  $10^{15}$  in most crystals), the scattered signal can be recorded before the specimen is damaged by radiation. It can be shown that the diffraction phenomenon is a result of combining the diffraction patterns produced by each atom in the unit cell. The amplitude of this diffraction for each atom is determined by factors such as the number of electrons and the size of the atom<sup>143</sup>. Additionally, the phase of the diffraction is influenced by the atom's position within the unit cell. When summing up these individual contributions, we obtain a vector with an amplitude denoted as  $|F(h)|$  and a phase represented by  $\alpha(h)$ , where 'h' corresponds to (hkl), and h, k, and l are the Miller indices defining the diffraction maxima. The amplitude  $|F(h)|$  and phase  $\alpha(h)$  of the vector can be expressed by a structure factor termed  $F(h)$ . This factor is solely dependent on the

## 2. Materials and Methods

scatterer's structure and can be mathematically expressed in terms of the  $f_j$ , which are individual scattering factors for each atom 'j' present in the unit cell, along with the atomic coordinates  $x_j$ <sup>143</sup>.

$$F(\underline{h}) = \sum_j f_j \exp 2\pi i(\underline{h} \cdot \underline{x}_j) = |F(\underline{h})| \exp i\alpha(\underline{h})$$

By rotating the crystal concerning the X-ray beam, it becomes feasible to record and determine the complete diffraction pattern of the crystal<sup>143</sup>. The crystallographer can measure  $|F(\underline{h})|$ , which directly correlates with the intensities of the diffraction maxima. However, the experimental measurement of the phase angle,  $\alpha(\underline{h})$ , is not possible. The missing phases must be retrieved using an alternative method<sup>143</sup>.

When both the amplitudes and phases of the scattered X-rays are known, they can be combined to generate an electron-density map of the contents of the crystal's unit cell, which is the repeating unit of the crystal. The electron density ( $\rho$ ) at any given position xyz in the unit cell is represented by the following equation (where 'i' equals the square root of -1)<sup>143</sup>.

$$\rho(x, y, z) = \sum_{hkl} |F(h, k, l)| \exp i\alpha(hkl) \exp -2\pi i(hx + ky + lz)$$

The data for PLCN was collected at the P11 beamline of the Deutsches Elektronen-Synchrotron (DESY), Hamburg, Germany<sup>144,145</sup>. The parameters for data collection can be found in Table 3.8. All of the measurements were carried out in a cryogenic stream of nitrogen at a temperature of 100 kelvin. Once crystals of a protein diffract X-rays to a reasonable resolution, the next crucial step is to obtain an interpretable electron-density map, which requires accurate phase angles ( $\alpha(hkl)$ ). Protein crystallographers typically employ three methods to obtain phase information:

**Multiple isomorphous replacement (MIR)** and anomalous scattering involve incorporating heavy atoms into the protein crystal. This can be achieved by either soaking the crystals in a solution containing the heavy atom or co-crystallizing the protein with a heavy-atom compound<sup>143,146,147</sup>. The heavy atom contributes to X-ray scattering, leading to measurable intensity differences in the diffraction pattern<sup>143,146,147</sup>. By preparing several crystals with different heavy atoms binding to distinct sites on the protein, the phase angles of the protein structure factors can be computed<sup>143,146,147</sup>. Using this information, an electron-density map is generated. Despite inherent challenges related to accurately measuring small intensity

## 2. Materials and Methods

differences and the lack of isomorphism between native and heavy-atom crystals, it is typically possible to identify regions matching the known sequence and construct a model consistent with the protein's polypeptide backbone and side chains<sup>143,146,147</sup>.

### **Anomalous-scattering methods**

Another approach for determining phase information involves using heavy atoms, exploiting the fact that atoms near their absorption edges exhibit anomalous scattering, leading to changes in amplitude and phase of scattered X-rays<sup>143,148</sup>. This method can be applied using a single heavy-atom derivative<sup>149</sup>. First, it helps identify the binding sites for the heavy atom, and then it computes the phases for the entire crystal. The effects are more significant when X-rays are measured near or at the absorption edge of the anomalous scatterer<sup>143</sup>. Using tunable X-ray sources from synchrotron radiation, the multiwavelength anomalous dispersion (MAD) procedure was developed, effectively solving the structure by Wayne Hendrickson and colleagues<sup>143</sup>. This method takes advantage of selenomethionine as an anomalous scatterer replacement for methionine<sup>148</sup>. An advantage of this approach is that it allows structure determination from a single crystal containing a suitable heavy atom<sup>143,148</sup>.

### **Molecular replacement**

In cases where the structure of a protein is expected to be closely related to another known protein structure, such as a mutant protein crystallized in a different form or a protein with high sequence homology to a known structure, the molecular-replacement method is utilized<sup>143,150</sup>. This method involves two stages: first, determining the rotation function to position the known molecule in the unit cell with the same orientation as the unknown molecule; then, using the translation function to find the position of the correctly oriented search molecule in the cell<sup>143</sup>. Molecular replacement is particularly powerful when the two molecules are not significantly dissimilar<sup>150</sup>. Several software packages, such as AMORE, MERLOT, and CCP-4, support the molecular-replacement method<sup>143,151</sup>.

After that, the data were indexed, integrated, and scaled using XDS<sup>152,153</sup>. Molecular replacement using an alpha-fold model was performed using MOLREP in ccp4 suit<sup>154</sup>. Phenix and coot were utilized in order to carry out rebuilding and model refining<sup>155,156,157,158</sup>.

### **2.8.2 Electron Microscopy**

Biological molecules like proteins and macromolecular complexes can be studied in detail by employing a technique called single particle electron microscopy (EM). Using a transmission electron microscope, researchers can take pictures of single particles that have been vitrified in

## 2. *Materials and Methods*

ice<sup>159</sup>. Preparing the sample for single particle EM involves spreading a thin layer of the particle solution across a grid. A small coating of sample is left on the grid after excess solution is blotted off. The sample is quickly frozen to a temperature that mimics its natural habitat, therefore preserving its structure. The term "vitrification" describes this procedure<sup>160</sup>. The electron microscope receives the grid with the frozen sample and passes a beam of high-energy electrons through it. After hitting the sample, the electrons scatter, projecting a picture onto a detector. The sample is filmed from many projection angles<sup>161</sup>. A three-dimensional model of the particle is reconstructed from these projection images. Aligning and merging the photos to create a high-resolution model requires the use of complex computing procedures, such as the standard "single-particle reconstruction" method. To do this, we must first determine the particle orientations in each image and then combine the results to produce a 3D model<sup>162</sup>. Single particle EM has been a huge help in determining the structures of many biological molecules and complexes, particularly those that are difficult to crystallize. Proteins, viruses, molecular machines, and other biological assemblies have benefited from this research<sup>163</sup>. Advances in electron microscope technology and computational tools have allowed scientists to explore smaller particles and get higher-resolution structures in recent years<sup>164</sup>.

In conclusion, single particle electron microscopy is an effective tool for investigating the molecular basis of biological processes<sup>159</sup>. It entails taking pictures of frozen particles and then utilizing computer analysis of numerous projection images to recreate their 3D structure<sup>162</sup>. This method has been essential in advancing our knowledge of structural biology and the complex machinery of living organisms<sup>163</sup>.

### **2.8.2.1 Negative Staining of PLCHR2 complex**

Glow discharge was performed for two minutes at the highest setting using the plasma cleaner PDC-002-CE (Harrick Plasma) on carbon-coated copper grids CF400-CU from Electron Microscopy Sciences. After that, the freshly glow-discarded grids were placed on top of a 5-10µl protein droplet or the buffer that was on Parafilm® (Amcor plc.), and the entire thing was allowed to incubate at room temperature for 1 minute. After incubation, the grids were soaked in water three times, excess liquid was blotted off using a filter paper. Following that, the samples were stained with a 1% uranyl acetate solution (Merck) for thirty seconds, and the excess liquid was once more removed with dry filter paper. Before continuing to work with the grids, at least ten minutes were spent allowing them to air dry with the sample side facing upwards. Five grids were prepared, four of which contained differing protein concentrations while the fifth included buffer as a control. Grids were either seen immediately or kept in a

grid holder at RT. The samples were observed using a transmission electron microscope (TEM) with a Ceta CMOS camera, model number Talos<sup>TM</sup> L120C (Thermo Fischer Scientific Inc.) at Cryo-EM facility at CSSB, Hamburg.

### 2.8.2.2 Single-particle Cryo-electron microscopy of PLCHR2 complex

For many years, X-ray crystallography was the go-to method for determining the structure of macromolecules at a high resolution. However, more recently, other methods have proven to be more effective<sup>165</sup>. Although it had significantly lower resolutions than crystallography, single-particle Cryo-EM was typically employed to provide insights into the shape of massive protein complexes that were resistant to crystallization. However, this technique is now being used for other purposes. Scientists are now able to employ Cryo-EM to solve near-atomic-resolution macromolecular structures. Despite the fact that the overall technique has not changed much over the years, relatively recent technological advancements in sample preparation, computation, and notably instrumentation have made it possible for this to happen<sup>165,166</sup>.

#### 2.8.2.2.1 Sample preparation and data collection

3.5 microliters of purified protein at 0.1 mg/ml after SEC was applied to a freshly glow-discharged holey carbon 2/1 200 mesh copper grid (Quantifoil). The grid was blotted for 4 s at 0 force before being plunge-vitrified in liquid propane ethane mixture using Mark IV Vitrobot (Thermo Fisher Scientific). The blotting chamber was maintained at 4°C and 100% humidity during grid freezing. Grids were screened using Artica for particle distribution and ice thickness. Selected grids were then used for data collection. Movies were collected using Titan Krios (voltage 300keV, spherical aberration 2.7 mm, amplitude contrast 0.1) (Thermo Fisher Scientific) equipped with a K3 camera and BioQuantum energy filter (Gatan). Data acquisition parameters are listed in Table 2.14.

Most of the particles appear to form a horseshoe-shaped trimer, clustered in the center of the holes. The trimer have a strong preferred orientation showing the horseshoe top or bottom views. Therefore, we collected data either with untilted or tilted specimen stage. Automated data acquisitions were set using EPU (0, and 30 degree of stage tilt) or serial EM (45 degree of stage tilt). Several data sets were collected as mentioned below:

- 7833 micrographs untilted: Quantifoil R x/y grid, GloQube parameters, Vitrobot parameters. Each micrographs includes 40 frames with equal exposure for a total dose of 45 e/Å<sup>2</sup>. The nominal defocus interval was set from -2.25 to -0.75 μm

## 2. Materials and Methods

- 6948 micrographs with stage tilted 30°: Quantifoil R x/y grid, GloQube parameters, Vitrobot parameters. Each micrographs includes 40 frames with equal exposure, total dose 45 e/Å<sup>2</sup>, defocus -2.25 to -0.75 μm
- 1785 micrographs with stage tilted 45°: Quantifoil R x/y grid, GloQube parameters, Vitrobot parameters. Each micrographs includes 40 frames with equal exposure, total dose 45 e/Å<sup>2</sup>, defocus -2.25 to -0.75 μm
- 1922 micrographs with stage tilted 45°: Quantifoil R x/y grid, GloQube parameters, Vitrobot parameters. Each micrographs includes 34 frames with equal exposure, total dose 45 e/Å<sup>2</sup>, defocus range -2.25 to -0.75 μm The pixel size for the micrographs in all the data sets is 0.85 Å/pixel.

**Table 2.14 Parameters for Cryo-EM data collection**

<b>Dataset</b>	<b>0 degree tilt</b>	<b>30 degree tilt</b>	<b>45 degree tilt</b>
Microscope	Titan krios G3i	Titan krios G3i	Titan krios G3i
Voltage (keV)	300	300	300
Detector	K3	K3	K3
Magnification	105,000	105,000	105,000
Pixel size(Å)	0.85	0.85	0.85
Spot size	5	5	5
Probe	npEFTEM	npEFTEM	npEFTEM
C2 Aperture (μM)	70	70	70
Slit width (ev)	20	20	20
Dose rate (e <sup>-</sup> /px/s)	15.421	15.376	13.65
Total dose (e <sup>-</sup> /Å <sup>2</sup> )	45.33	45.19	47.38
Number of frames	40	40	43
Defocus range (μm)	-0.7 to -2.25	-0.7 to -2.25	-0.7 to -2.25
Mode	Super resolution with binning of 2	Super resolution with binning of 2	Super resolution with binning of 2
Stage tilt degree (°)	0	30	45
Software	EPU	EPU	SerialEM
Number of movies	7832	6948	3718

### 3 Results

#### 3.1 Cloning of PLCH, PLCN, and PLCR2

Three different constructs were made pET28a\_PLCN, pET28a\_PLCR2 and pACYC\_DUET1\_PLCH. The gene-specific stop codon is incorporated into the reverse primer, which makes it possible to make use of only the N-terminal His tag while avoiding the use of its counterpart at the C-terminal position. The schematic diagram of gene constructions is shown here in Figure 3.1.

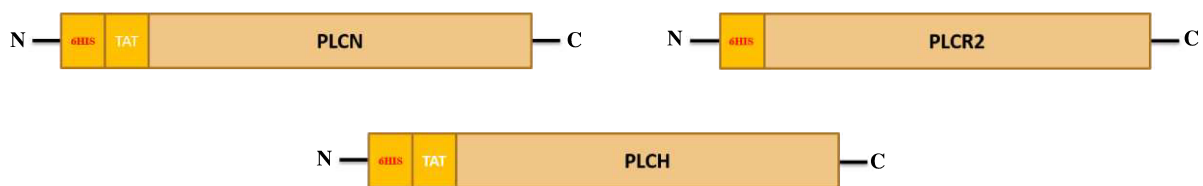


**Figure 3.1 Schematic diagram for gene constructs of plch, plcr2 and plcn**

PLCN, PLCH and PLCH constructs were made by amplifying the respective genes from the genomic DNA of *Pseudomonas aeruginosa*. All the constructs had 6X His tag at the N-terminal end. PLCN: 2079bps, PLCH: 2193bps, PLCR: 456 bps

**Table 3.1 Molecular description of PLCH, PLCR2 and PLCN**

Gene	Base pair	Amino acids	Vector	Tag
PLCH	2193	730 (82.6 kDa)	pACYCDUET-1	N terminal His tag +TAT signal sequence
PLCR2	456	151 (17.1 kDa)	pET28a+	N terminal His tag
PLCN	2079	692 (79.4 kDa)	pET28a+	N terminal His tag +TAT signal sequence

Random colonies were picked and were validated by colony PCR and sent for sanger sequencing. Microsynth's Sanger sequencing with T7 forward and T7 reverse primers was used

### 3. Results

to verify the nucleotide sequence (for further information, see the appendix I). The description of the genes can be found in the Table 3.1.

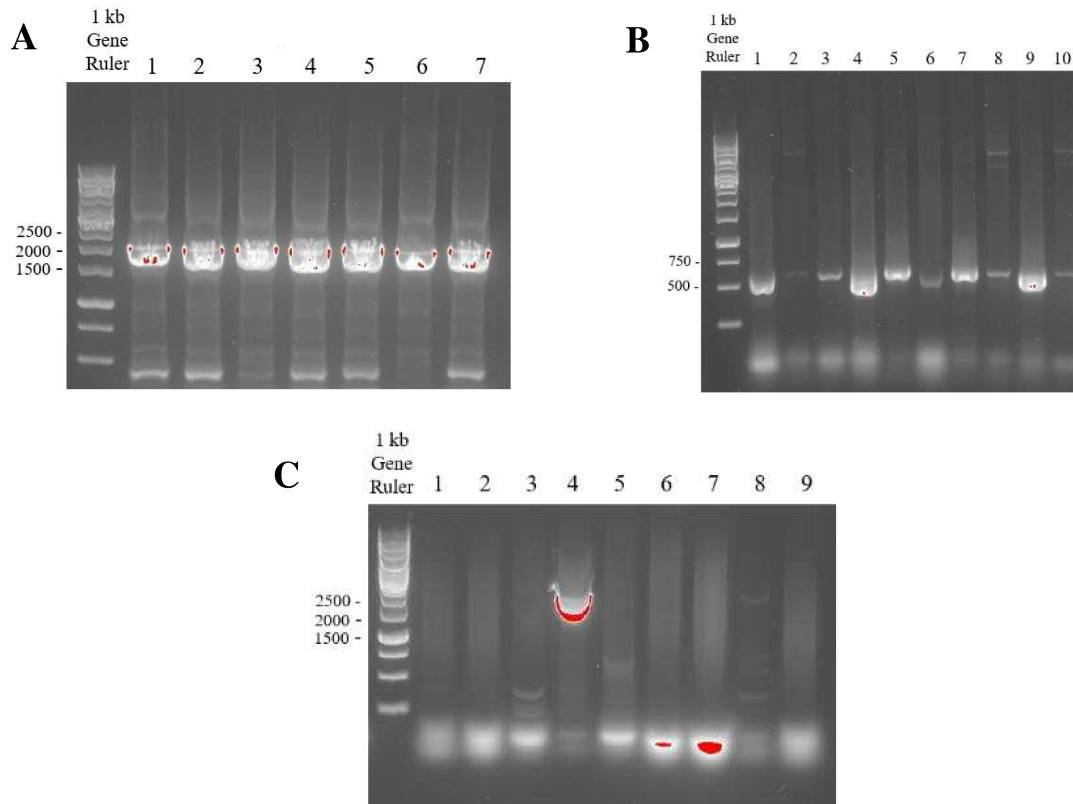


**Figure 3.2 Agarose gel showing colony PCR (cPCR)**

Colony PCR showed all positive clones for PLCH, and PLCH2 and one positive clone for PLCN. Lanes 1-9 are the number of colonies tested for cPCR. PLCN: 2079bps, PLCH: 2193bps, PLCH2: 456 bps A. PLCH, B. PLCH2 and C. PLCN

All genes were effectively cloned in their respective vectors, which were then utilized to overexpress the proteins in *E.coli* expression strains.

### 3.2 Expression of PLCHR2 complex and, PLCN

The genes that were successfully cloned were subsequently transformed into *E.coli* strains that could express them. In order to evaluate the amounts of protein expression and solubility, a variety of strains of bacteria were utilized such as *E.coli* C43, *E.coli* shuffle, and *E.coli* DE3 star. All of the aforementioned strains exhibited expression of the genes PLCH, PLCH2, and PLCN. Following the induction process, which was carried out between 0.4 and 0.6 OD600

### 3. Results

using a final concentration of 1 mM IPTG, the bacterial culture was incubated at 37°C with 180 rpm for a period of 4 hours. It was found that PLCH and PLCN were overexpressed in *E.coli* shuffle and *E.coli* DE3 star, and there was no expression in *E.coli* C43, although PLCR2 was expressed in all three strains. The overexpressed proteins were not toxic to the *E.coli* cells (Figure 3.4).

The solubility of all three proteins was determined by lysing only a small amount (10 milliliter) of the cell culture grown at 37°C. The cells were lysed on ice with a sonicator set to 65% amplitude for 30 seconds on and 1 minute off for 10 cycles. After that, the lysed cells were centrifuged at a speed of 10000 x g for a period of 30 minutes so that the inclusion bodies could be separated. Following, the cell pellet and the cell supernatant were separated and analyzed using SDS-PAGE. It was found that PLCH and PLCN were present as inclusion bodies in *E.coli* DE3 and *E.coli* shuffle strains. PLCR2, on the other hand, was soluble in each of the strains.

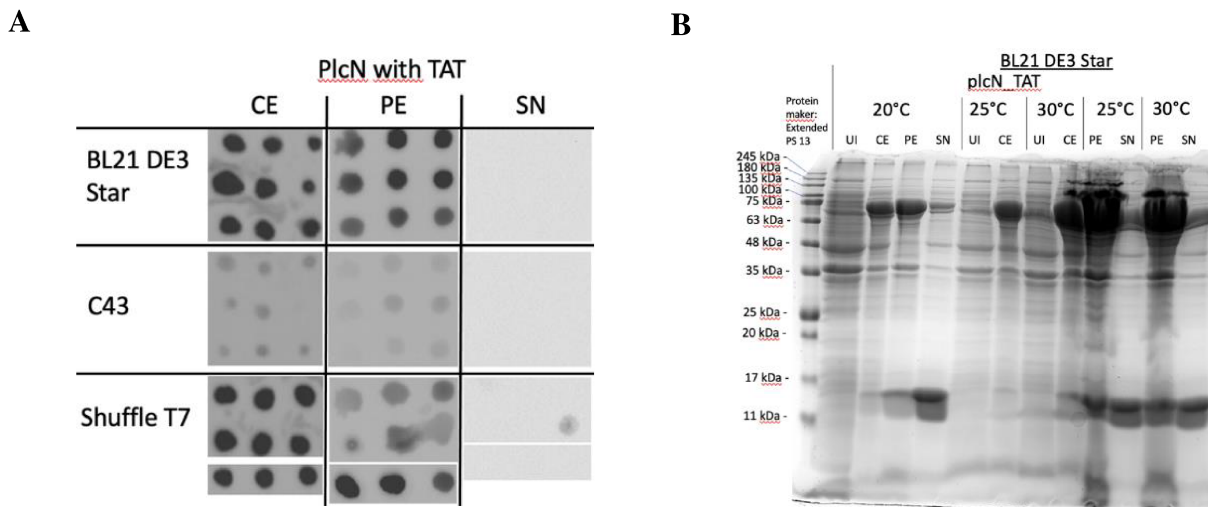


**Figure 3.3 SDS PAGE showing expression and solubility test of PLCN**

**A.** PLCN expressed in DE3 star and shuffle T7 and not soluble at 37°C, **B.** PLCN soluble at 20°C

### 3. Results

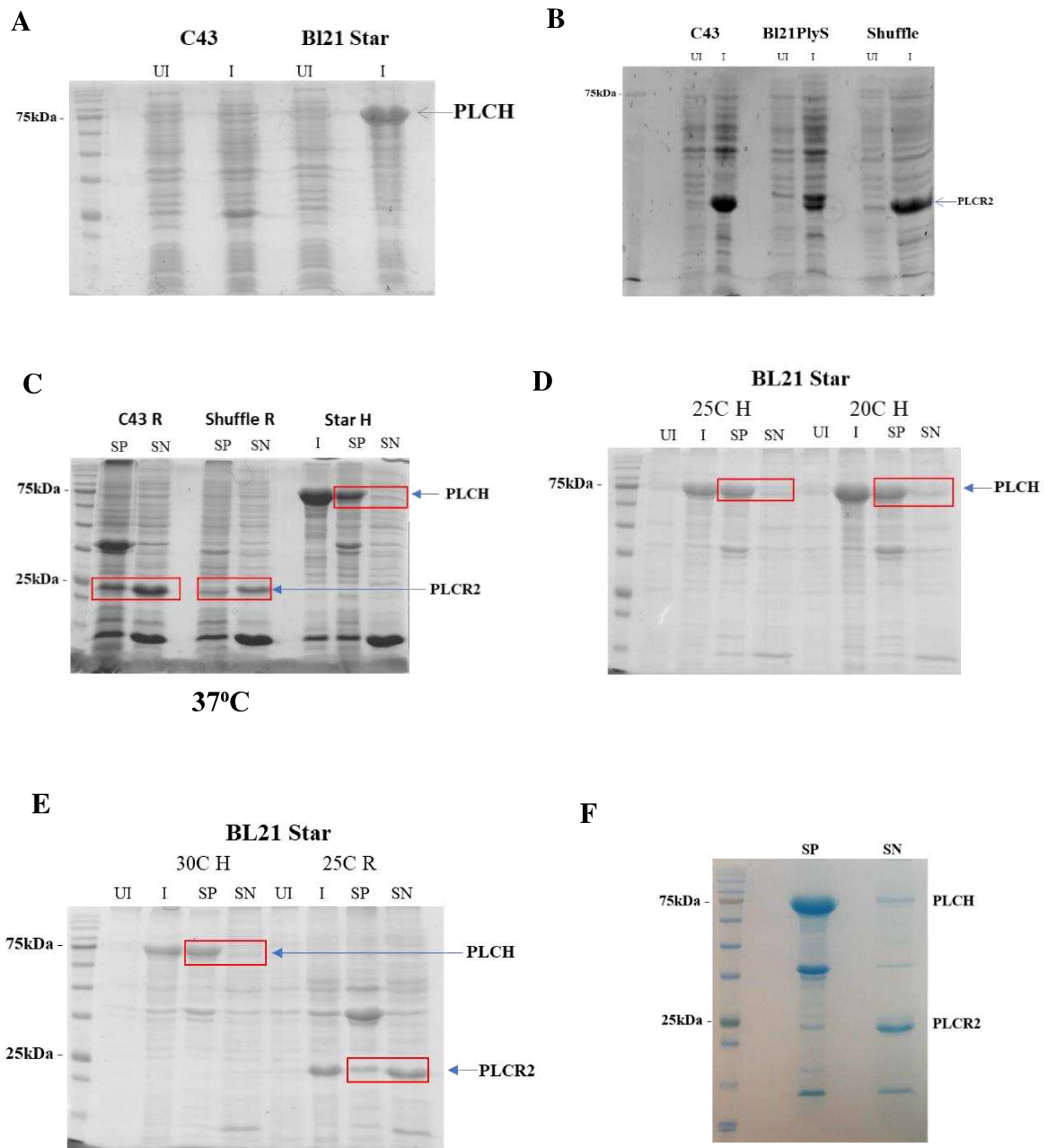


**Figure 3.4 SDS PAGE showing expression and solubility test of PLCH and PLCR2**

A. PLCH only expressed in BL21 star, B. PLCR2 expressed in all strains (C43, DE3 star, shuffle), C, D, E PLCR2 is soluble in all strains at all temperature i.e. 20°C, 30°C, 37°C; PLCH not soluble in any strain or at any temperature, F. PLCHR2 was expressed as a complex and soluble at 20°C.

### 3. Results

The cells were induced at different low temperatures i.e. 20°C, 25°C, and 30°C, in order to achieve increased solubility. In a procedure similar to the one described previously, the cells were lysed and examined for their solubility. After further investigation, it was found that the PLCN was soluble at each of the three temperatures and both the strains that were tested (Figure 3.3). PLCH, on the other hand, remained insoluble even at all of these lower temperatures.

It has been demonstrated in the literature that PLCH is not soluble when produced by itself in *E.coli*; hence, in order to obtain soluble PLCH, it was co-transformed with its chaperon PLCHR2 in *E.coli* DE3 start cells. Then the proteins were expressed at 20°C overnight at 180 rpm. The PLCHR2 complex was shown to be overexpressed and soluble (Figure 3.4)

In conclusion, in accordance with the findings presented above, the PLCN and PLCHR2 complex was overexpressed in *E.coli* DE3 cells by inducing the expression using a final concentration of 0.5 mM of IPTG and incubating at 20°C, 180 rpm overnight. Several liters of cultures were grown, and the cell pellets were harvested by centrifuging at 5000 x g for 15 mins and stored at -80 degrees Celsius for future use.

### **3.3 PLCN and PLCHR complex was purified in high quality and quantity.**

#### **3.3.1 PLCN purification**

Following the lysis of the cells, the supernatant that was collected was put to use in the subsequent purification of the PLCHR complex and the PLCN. The purification was accomplished with the use of metal affinity chromatography (IMAC), namely indigo Ni<sup>2+</sup>-NTA and cobalt-based TALON affinity chromatography. In order to obtain a highly purified protein, the next step in the purification process was size exclusion chromatography (SEC). SDS-PAGE was used to evaluate the proteins quality and the apparent molecular weight that were obtained from the chromatography elution fractions.

Figure 3.5 A. shows the SDS PAGE of PLCN purification profile obtained from Co<sup>2+</sup>- IMAC, and Figure 3.5 B shows the SEC chromatograph with a single sharp peak. The calculated mass of the PLCN protein construct is approximately 79.3kDa, which agrees with the experimentally determined molecular weight of PLCN, as it runs with a molecular weight between from 75 to 100 kDa. The SEC chromatograph (Figure 3.5C) also shows a single peak indicating high purity and a apparent molecular weight of 76 kDa as it elutes at a volume of 82.61ml from a Superdex-200 (16/600).

### 3. Results

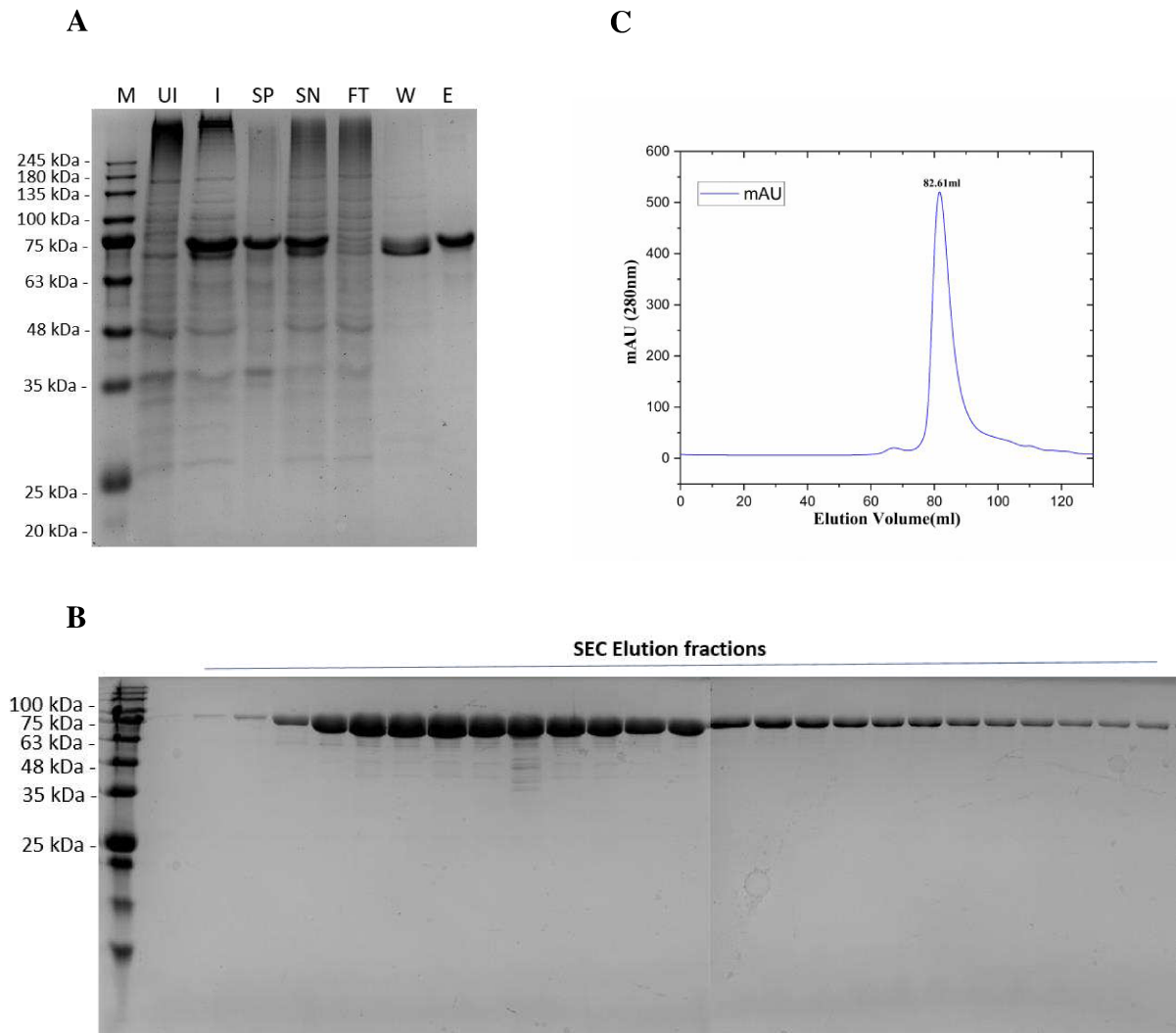


**Figure 3.5 Purification profile of PLCN**

**A.** SDS PAGE of Ni-NTA purification, **B** SDS PAGE of Size Exclusion chromatography, **C.** Gel filtration chromatogram. M: Marker, UI: Uninduced, I: Induced, SP: Sonicated pellet, SN: Sonicated supernatant, FT: Flow-through, W: Wash, E: Elution

Therefore, a highly pure PLCN protein in large amounts was produced with a yield of 20mg/ml 3.5g of cell pellet obtained from 1L of culture. The purified protein was used to conduct further biophysical and biochemical studies.

#### 3.3.2 PLCHR2 complex purification

As mentioned above, PLCH alone was not soluble and hence was expressed as a complex with its chaperon PLCR2. PLCHR2 complex was purified from the supernatant via affinity

### 3. Results

chromatography using Indigo Ni<sup>2+</sup> NTA column and was followed by another step of purification i.e. size exclusion chromatography using Superdex- 200 (16/600) and Superdex-200 (10/300) columns. The PLCH and PLCR2 proteins of the complex showed the expected molecular weight in both SEC and SDS-PAGE, which is 84.3 kDa for the PLCH protein and 19.3 kDa for the PLCR2 protein (Figure 3.6 A&B) Since it is known that the theoretical molecular weight of proteins does not always correspond well in SDS PAGE, it was presumed that the purified bands represent the proteins of interest. In addition, the SEC profile also indicated that the PLCHR2 complex has an apparent molecular weight of 106 kDa as elution volume of 15.31ml in analytical Superdex- 200 (10/300) column (Figure 3.7).

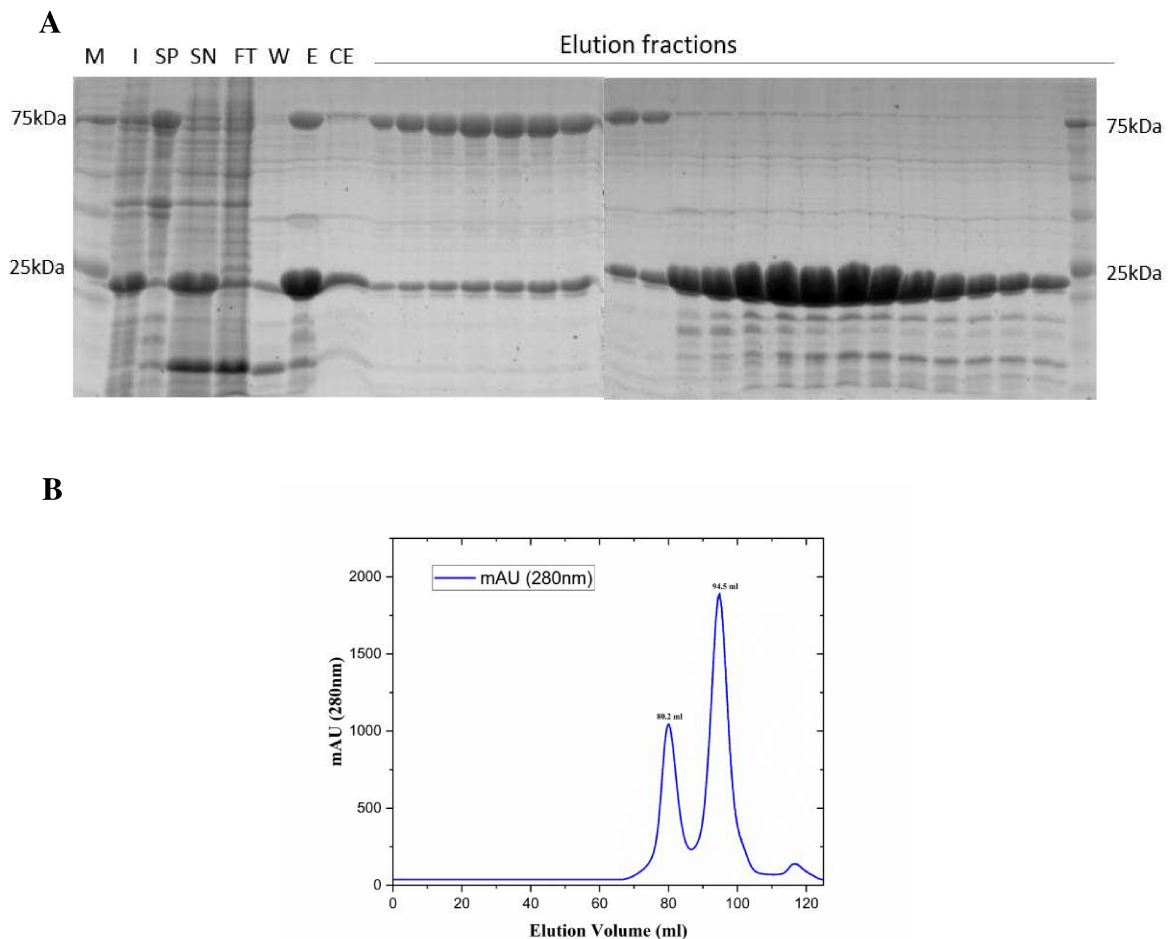


**Figure 3.6 Purification profile of PLCHR2**

**A.** Ni-NTA and SEC purification profile of PLCHR2, M: Marker, UI: Uninduced, I: Induced, SP: Sonicated pellet, SN: Sonicated supernatant, FT: Flow-through, W: Wash, E: Elution, CE: Concentrated elution **B.** Gel filtration chromatogram of PLCHR2 and PLCR2.

### 3. Results

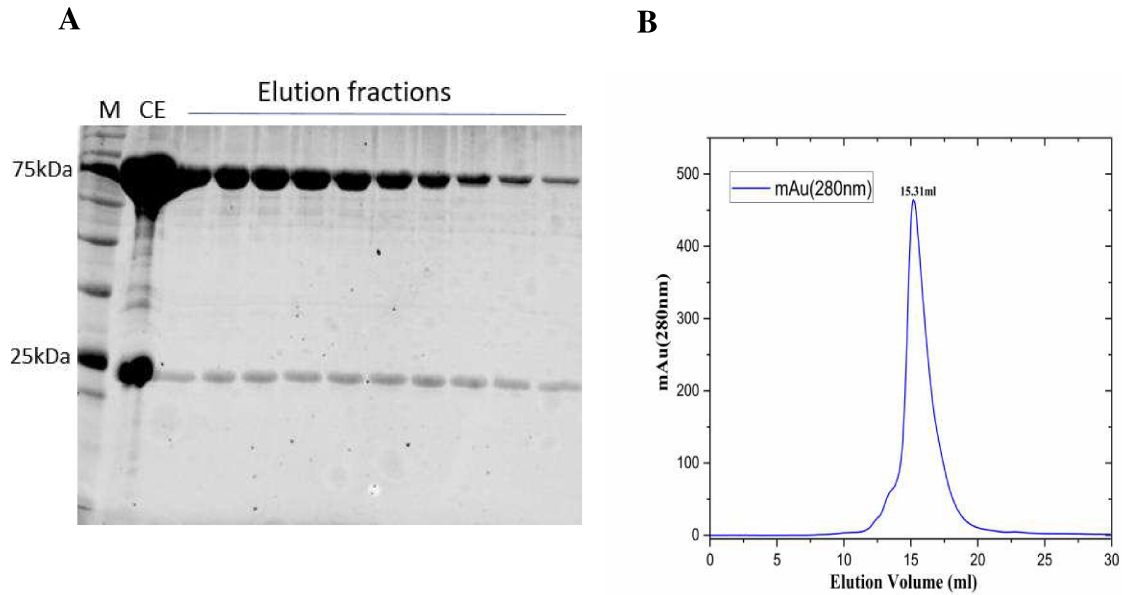


**Figure 3.7 PLCHR2 complex polished with SEC**

A. SEC profile of PLCHR2, M: Marker, CE: Concentrated elution B. Gel filtration chromatogram of PLCHR2.

However, in order to establish the identity and integrity of the targeted proteins, several more studies, such as LC mass/mass and western blotting, were carried out. Additionally, SEC-SAXS was carried out in order to gain an understanding of the stoichiometry of PLCH and PLCHR2 in the complex (for more information, please see section 3.5.5)

#### **Identity and integrity of PLCN and PLCHR complex**

The next step was to use western blotting, Mass spectrometry and LC/mass mass to verify identity and integrity the PLCN and PLCHR complex. Anti-His antibodies were used for detection since PLCN, PLCH, and PLCHR2 all have a 6X His tag at their N termini. The western blot signal for the three purified proteins is shown in the Figure 3.8 below at their respective molecular weight. However, in the PLCHR2 complex, the PLCH signal is considerably stronger than the PLCHR2 signal. This may be because proteins of different sizes migrate to the membrane at different rates, suggesting that PLCHR2 travels outside the membrane for a strong PLCH signal. Since all three bands were detected from the western signal, it is confirmed that the N-terminal end is intact in the protein post purification.

### 3. Results

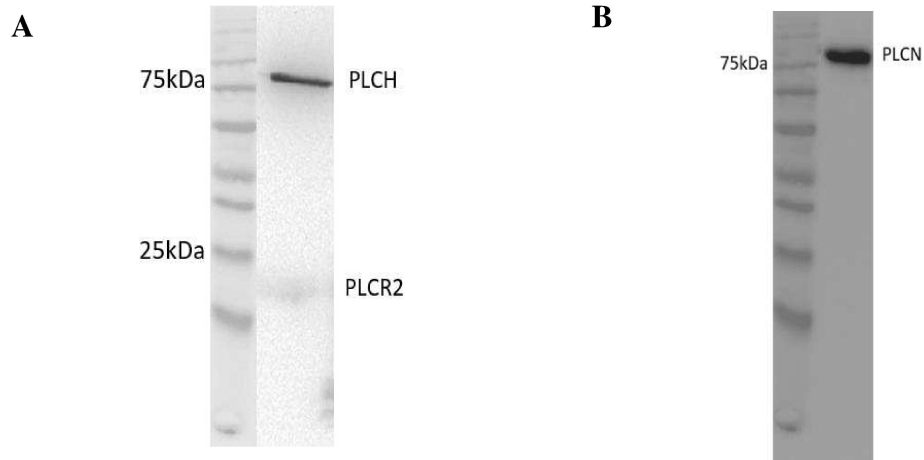
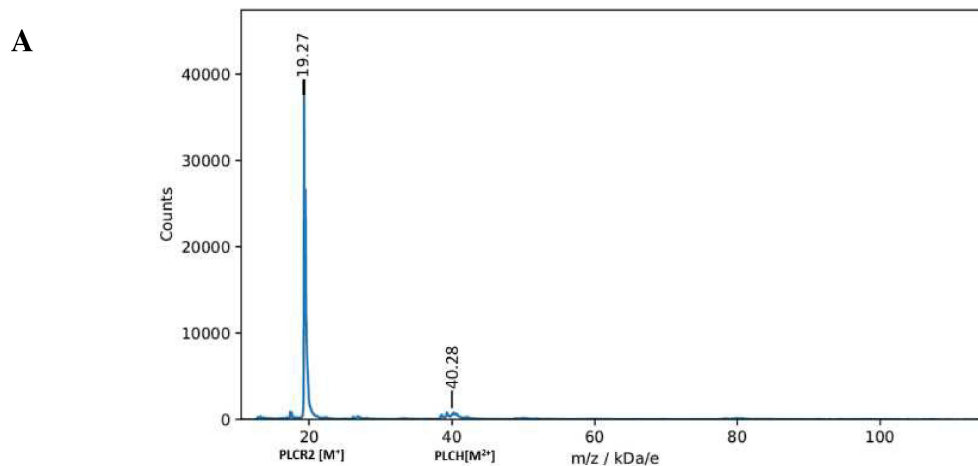


**Figure 3.8 Anti His Western blot A. PLCH and PLCR2, B. PLCN**

The expression of PLCH, PLCR2 and PLCN in *E.coli* cells were analyzed with His-tag western blot. PLCH showed a molecular weight of ~ 84kDa , PLCR2 ~ 19kDa and PLCN ~79kDa

**Table 3.2 N terminal to C terminal sequence coverage from LC-mass/mass**

Proteins	Sequence Coverage
PLCH (84.3kDa)	96.5 %
PLCR2 (19.3kDa)	87.2 %
PLCN (79.3kDa)	74.3%



### 3. Results

**B**

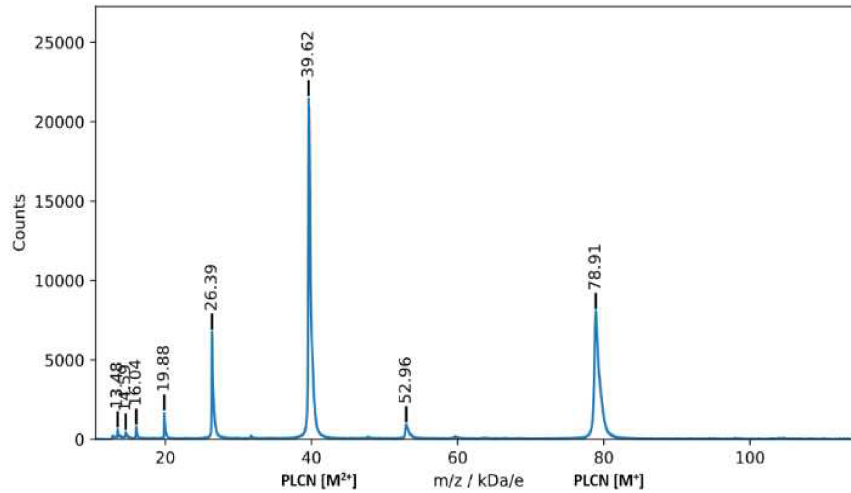


**Figure 3.9 MALDI/TOF m/z spectrum A: PLCHR2 and B: PLCN**

Results from MALDI-TOF show a homogenous sample of PLCN, and PLCHR2. For PLCN peak at 78.91 kDa/e corresponds to  $M^{1+}$ , 39.62 kDa/e to  $M^{2+}$  and 26.39 kDa/e to  $M^{3+}$ . For PLCH only  $M^{2+}$  species at 40.28 kDa/e and PLCHR2, peak at 19.27 kDa/e corresponds to  $M^{1+}$  species was observed.

The next step was to confirm the mass more accurately using mass spectrometry. Protein standards with masses ranging from 10 to 66 kDa were used to calibrate the mass spectrometer. The MALDI-TOF can therefore only perform a reliable analysis of masses that fall within that spectrum. It could be anticipated that the double-charged ion will have a stronger peak than the intensity peak for proteins with a molecular weight greater than 50 kDa. This is because double-charged ions have a higher charge density<sup>224</sup>.

Figure 3.9B shows that the  $M^{2+}$  species of PLCN matches well to the strongest peak, which comes in at 39.62 kDa/e. The peak for the  $M^{1+}$  species comes in at 78.91 kDa/e, while the peak for the  $M^{3+}$  species comes in at 26.39 kDa/e. As seen in Figure 3.9A ionization leads to the dissociation of the PLCHR2 complex. With a mass of 19.27kDa/e for  $M^{1+}$  species, the R2 was observed to great precision.  $M^{1+}$  species of PLCH were not found at all; however,  $M^{2+}$  species were observed, albeit with a very weak peak at 40.28kDa/e.

Integrity of all the proteins were monitored by LC-Mass/mass. The in-gel tryptic digest workflow was used for PLCHR2 complex. For PLCN the in-gel acid hydrolysis workflow was used. This workflow was used in order to determine the boundaries of the protein. Hydrochloric acid cleaves proteins arbitrarily, whereas trypsin cleaves at specific peptide bonds on the C-

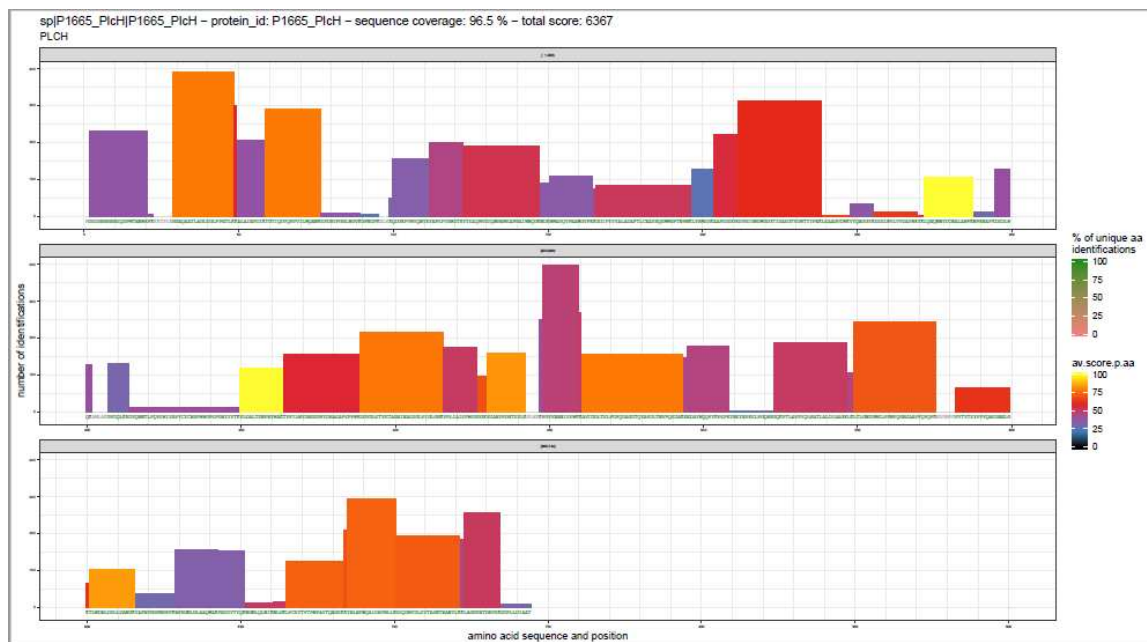
### 3. Results

terminal side of lysine and arginine residues. Peptides were analyzed on the Lumos system. In order to account for impurities that come from the expression host, the protein sequence was added to the database of *E.coli* expression host before the analysis was carried out.

The detection of multiple peptides with identical N- or C-termini is an indication for the N- or C-terminus of a protein. The amino acid sequence of PLCN, PLCH and PLCR2 was sequenced to a coverage of 74.3%, 96.5 % and 87.2 % respectively (See supplementary). The protein's C-terminus is shielded from degradation, but the N-terminus is not. This may be because the His6-tag is poorly ionized and therefore infrequently detected. The molecular weight was determined to be 79338.2 Da for PLCN, 84281.89 Da for PLCH and 19352.41 Da for PLCR2. This information indicates that the purified protein is of full length, uncut during the purification process. When analyzed for any posttranslational modifications, it was found the PLCH was very likely to be phosphorylated at T176. Since in gel acid hydrolysis was done for PLCN, the presence of a phosphate was not confirmed.

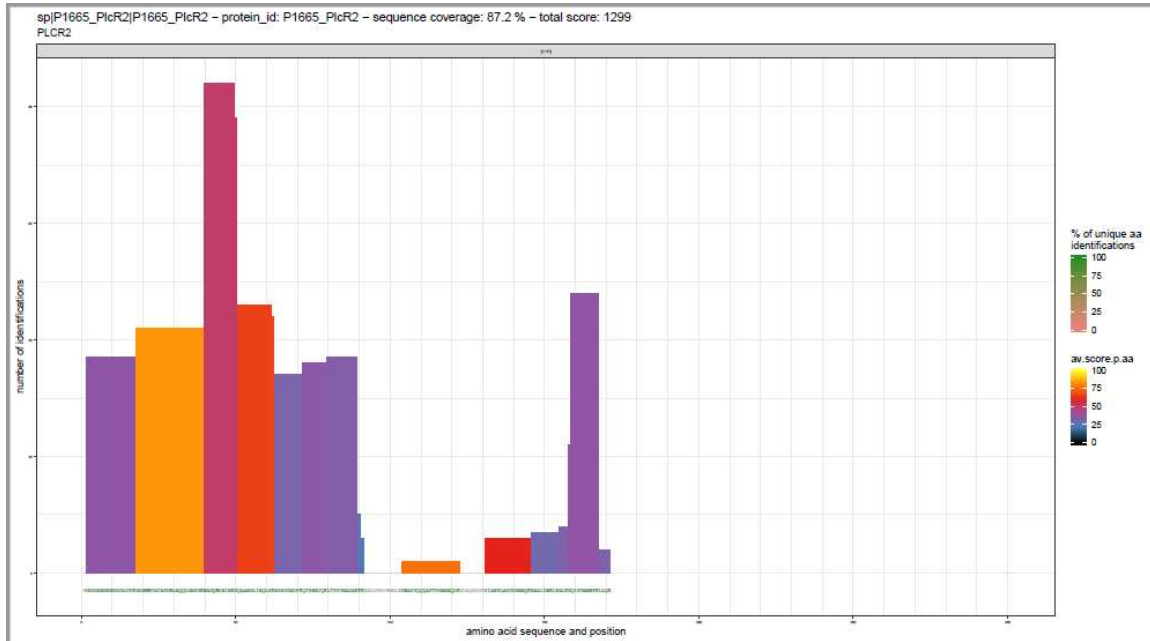
Now that the proteins' purity, completeness, and the quantity have all been evaluated, the subsequent step was to carry out characterization using biophysical and biochemical methods.

A



### 3. Results

**B**



**C**

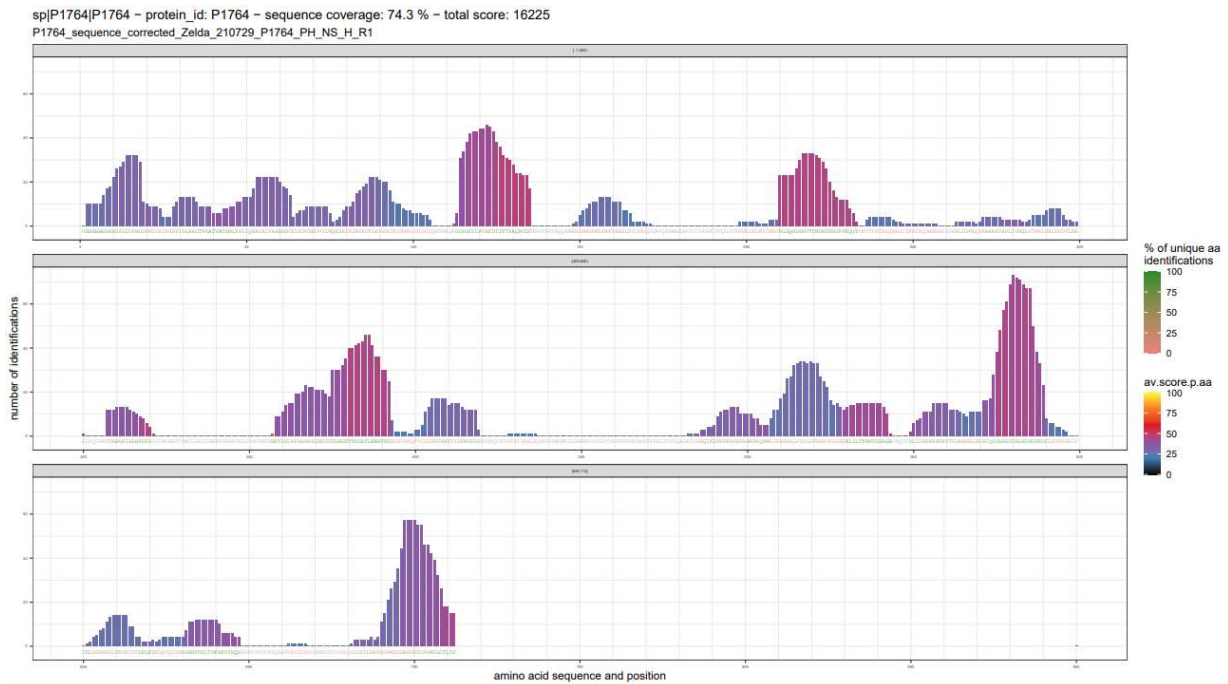


**Figure 3.10 Peptides identification by LC-MS/MS analysis**

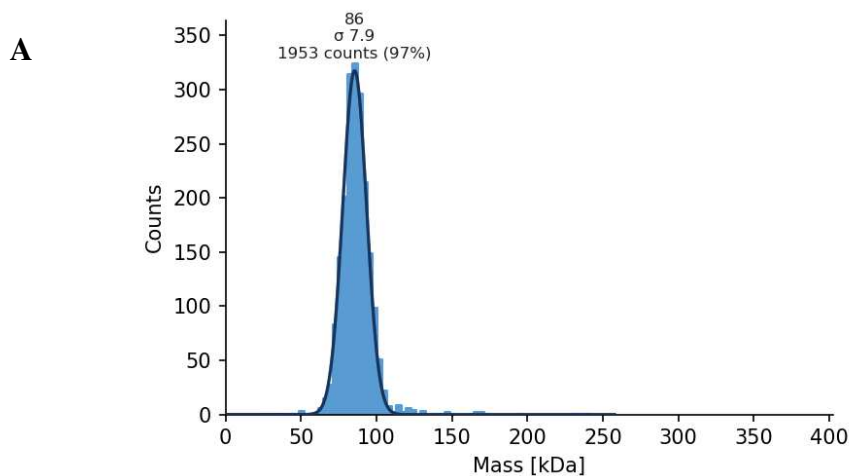
LC-MS/MS gave N terminal end to C terminal end sequence coverage **A.** PLCH, **B.** PLCR2, **C.** PLCN where, Y-axis is number of identifications and X-axis is amino acid sequence and position. All the proteins were expressed in full length.

### 3.4 Biophysical Characterization

It is essential to achieve the correct configuration of a protein's higher-order structure (HOS), which includes the secondary and tertiary structures, as well as aggregation and oligomerization, in order to ensure that the protein will function effectively and remain stable. In order to access the above, several biophysical techniques such as Circular Dichroism (CD), Fluorescence spectrometry (FL), Mass photometry, Mass Spectrometry (MS), Dynamic Light Scattering (DLS), X-Ray Crystallography, Cryo-Electron Microscopy were used to determine the secondary structure, oligomerisation or aggregation along with the tertiary or quaternary structure.

#### 3.4.1 Mass Photometry

The distribution of the measured landing events is depicted in Figure 3.11 as a function of the number of counts per molecular weight. For PLCN protein, the Gaussian function includes a range from 60 kDa to 100 kDa, encompasses 1953 counts in total, and accounts for 97% of the total counts. For PLCHR2 complex, Gaussian function includes a range from around 80 kDa to 120 kDa with a total of 1797 counts i.e. 93%. PLCN, with a predicted molecular weight of 79,3 kDa, and PLCHR2 heterodimer with a molecular weight of 103.6 kDa both falls inside this Gaussian function . The peak maxima was observed at 86 kDa, and 105 kDa with a standard deviation of 7.9 and 9.6 for PLCN and PLCHR2, respectively.<sup>167</sup>. It is evident that the sample is homogeneous because there are no additional peaks. Despite the limitations of mass photometry, I was able to get the apparent molecular weights closer to the theoretical weights while also demonstrating sample purity.



### 3. Results

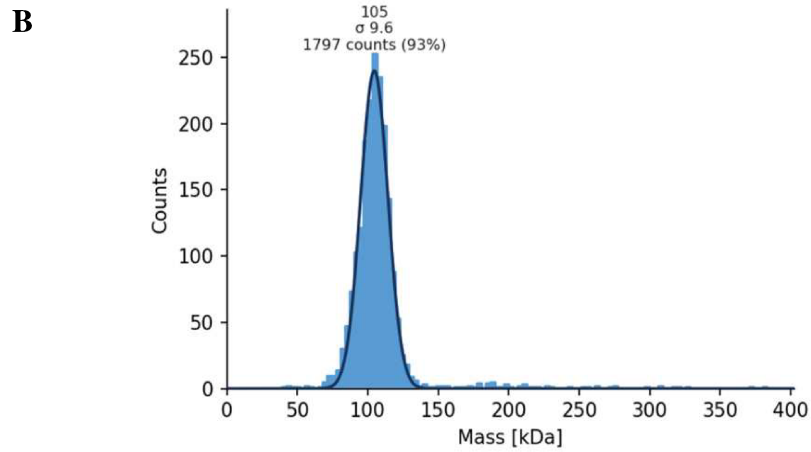


**Figure 3.11 Mass distribution histogram of A: PLCN B: PLCHR2**

Mass distribution histogram of the expressed PLCN and PLCHR2 complex from *E.coli* showed the mass distribution function as a Gaussian distribution with a peak at 86kDa for PLCN and at 105kDa for PLCHR2 complex. No additional peaks are visible indicating homogeneity.

#### 3.4.2 Dynamic Light Scattering

The purified protein sample was then subjected to DLS analysis so that the purity, homogeneity, and oligomerization behavior of the protein could be determined. The buffer exhibits a Gaussian intensity distribution on a logarithmic scale from 0.1 nm to 50.000 nm at low intensities (4%), indicating low background scattering (data not shown). The DLS data obtained from the DLS measurements for both the proteins are listed in Table 3.3 & 3.4. Both the protein samples were of high quality and contained single species (Figure 3.12 & 3.13).

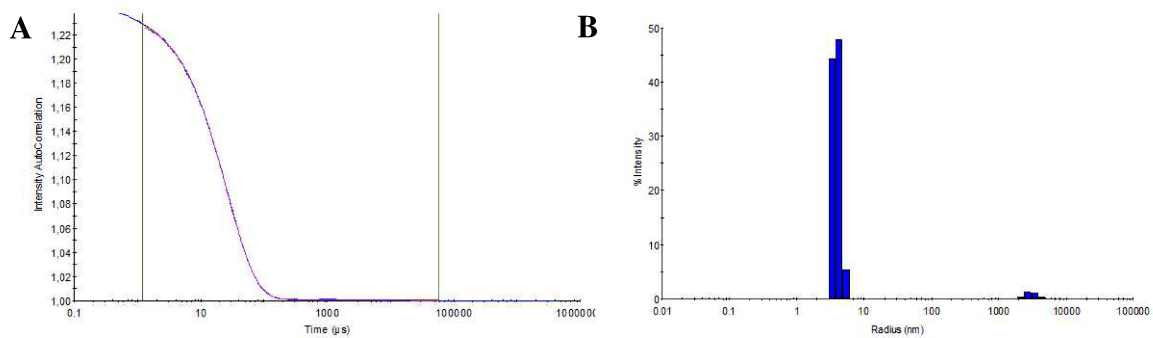


**Figure 3.12 Autocorrelation function and distribution of particle sizes using DLS of PLCN**

DLS showed the autocorrelation function with its corresponding error curve (A) and radius distribution plot (B) for 0.85mg/ml of PLCN. The autocorrelation functions show the theoretically calculated function in red and the measured curve in blue

### 3. Results

**Table 3.3 Physical Characterization of PLCN using DLS**

Peak	Radius (nm)	%Pd	Mw-R (kDa)	%Intensity	%Mass	%Number
Peak 1 (True)	4.0	14.51	84.2	97.3	99.8	100.0
Peak 2 (True)	3110.7	20.35	500925768.3	2.7	0.2	0.0

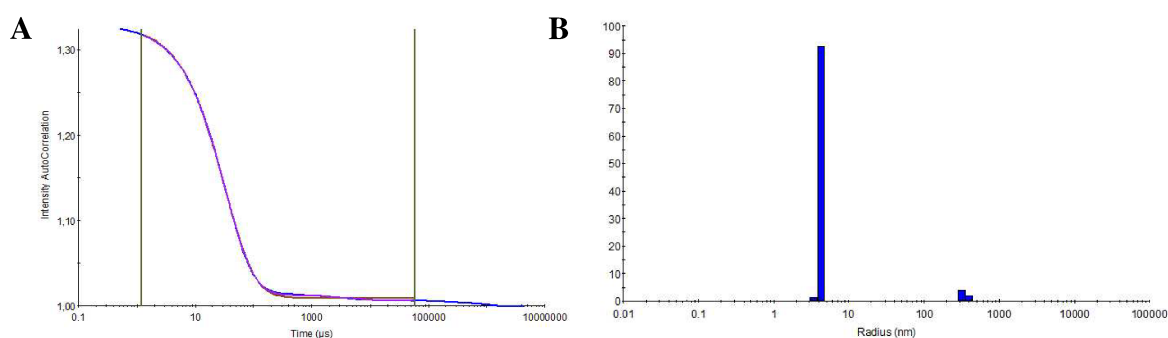


**Figure 3.13 Autocorrelation function and distribution of particle sizes using DLS of PLCHR2**

DLS showed the autocorrelation function with its corresponding error curve (A) and radius distribution plot (B) for 1mg/ml of PLCHR2. The autocorrelation functions show the theoretically calculated function in red and the measured curve in blue.

**Table 3.4 Physical Characterization of PLCHR2 using DLS**

Peak	Radius (nm)	%Pd	Mw-R (kDa)	%Intensity	%Mass	%Number
Peak 1 (True)	4.3	2.46	102.2	93.8	99.9	100.0
Peak 2 (True)	347.5	11.70	2967595.4	6.2	0.1	0.0

### 3.4.3 Circular Dichroism of PLCN and PLCHR Complex

LC-MS/MS was used to analyze the primary structure of the PLCHR2 complex and PLCN, while CD spectroscopy was used to determine the secondary structure and melting temperature i.e. stability. PLCHR2 and PLCN's CD spectra were obtained by measuring it in a buffer containing 10 mM potassium phosphate, pH 7.4.

The far-UV CD spectra of the PLCHR2 complex showed predominantly an  $\alpha$ -helical profile with double minima at 208 nm and 222 nm, However, a minima at 217 nm was also observed indicating the presence of  $\beta$  sheet structure (Figure 3.15). Far-UV CD spectra of an intact PLCN at 4°C reveals a local minimum in the range of 215 - 220 nm, indicating more  $\beta$  sheet secondary structure. This could be due to measurement errors caused by the rising inaccuracy towards shorter wavelengths. Despite the limitations in the measurements, the spectrum of the refolded denatured PLCN differs significantly from that of the intact PLCN (Figure 4.2). Local emission minima or maxima are observed in the spectrum of the native protein, which is indicative of its secondary structure, but not in the heated sample. Heat treatment likely prevented the protein from reforming into secondary or tertiary structure. The deconvolution of the CD spectra for both the proteins are shown in Table 3.5 and was calculated using BeStSel<sup>168</sup> (Beta Structure Selection) an online tool used for the determination of secondary structure and recognition of protein folds from circular dichroism spectra.

The temperature scan from 4°C to 98° C with an increment of 2°C was also done and selected data from several temperature points were plotted. The CD signal of the buffer was eliminated from all of the values of the sample spectra. After that, a plot of the adjusted intensities was produced against the wavelength (190-260nm). All intensities observed at wavelengths below 200 nm indicated a significant amount of variation for CD due to the increased absorption in 190-200nm wavelength. Therefore, values less than 200 nm were ignored for the purposes of further calculations.

Plotting the intensity at 222 nm or 217nm against temperature illustrated how the temperature gradient affects the CD intensity. The linear shifts in CD between folded and unfolded proteins was adjusted prior to plotting the data as a function of temperature. The calculations were based on the work by Santoro and Bolen (1988)<sup>169</sup>. They proposed a single expression equation that was used to nonlinearly fit CD data. Equation 1 was rewritten based on their formula as follows:

$$y = \frac{(a_N + b_N x) + (a_D + b_D x) e^{E(\frac{1}{x_0} - \frac{1}{x})}}{1 + e^{E(\frac{1}{x_0} - \frac{1}{x})}} \quad (1)$$

### 3. Results

Where, the linear function of the hypothetical native state before unfolding is referred to as  $(a_N + b_Nx)$ , and the denatured state is referred to as  $(a_D + b_Dx)$ . According to Santoro and Bolen (1998), the value of E represents the free energy of the unfolding process and is equivalent to the extrapolated intercept of the unfolding process. Equating the second deviation of the fitted graph with 0 yields the x-value where the slope of the original curve is greatest, corresponding to the melting temperature of the protein.

The negative signals seen in far-ultraviolet circular dichroism (CD) spectra steadily decrease as temperature rises. Figure 3.14A displays the CD temperature gradient scan for PLCN. It demonstrates a changing relationship between the two states: Unfolded, denatured protein has a flattened local minimum between 210 and 220 nm, in contrast to the intact protein's 200–205 nm maximum and distinct local minimum. The change takes place during a temperature increase from 40°C to 50°C. In order to calculate the melting temperature of the protein from the CD spectra, the emission intensity at 217 nm was compared to the temperature gradient (Figure 3.14B). Tm for PLCN came out to be 45°C. Figure 3.15A shows the temperature scan for PLCHR2 complex. Similarly, here also, the local minima and maxima flattened with the rise in temperature. The change between the folded and unfolded state happened between 50°C to 60°C. The melting temperature for PLCHR2 complex was calculated to be 60°C. (Figure 3.15B).

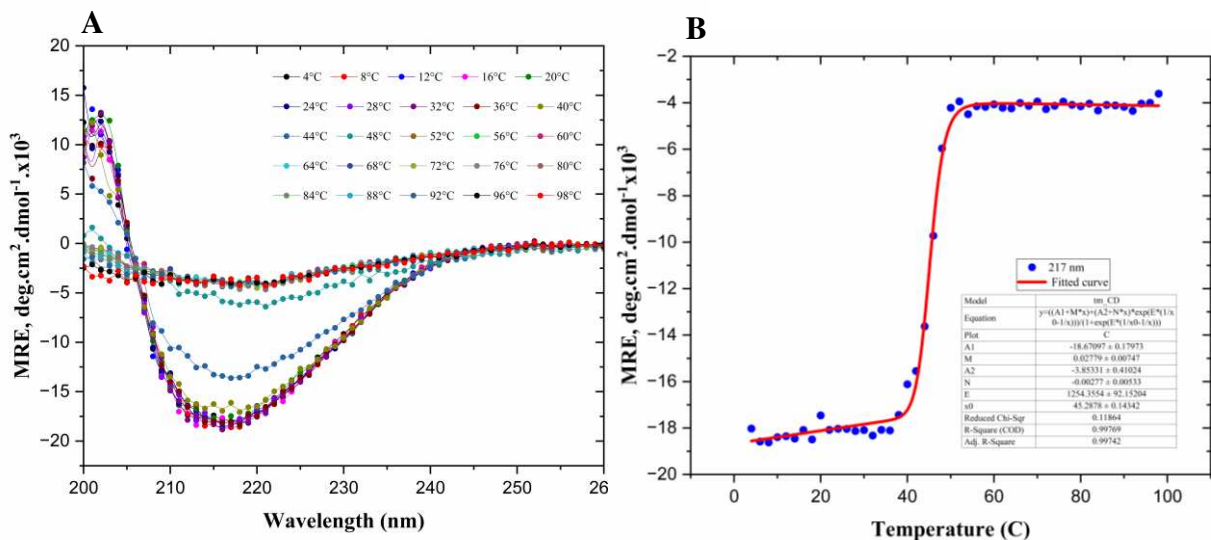


**Figure 3.14 CD Spectroscopy of PLCN**

(A) Far-UV CD spectra (260 nm to 185 nm) in 4 °C increments from 4 to 98 °C (B) and Thermal stability (Tm determination) at 217nm of PLCN

### 3. Results

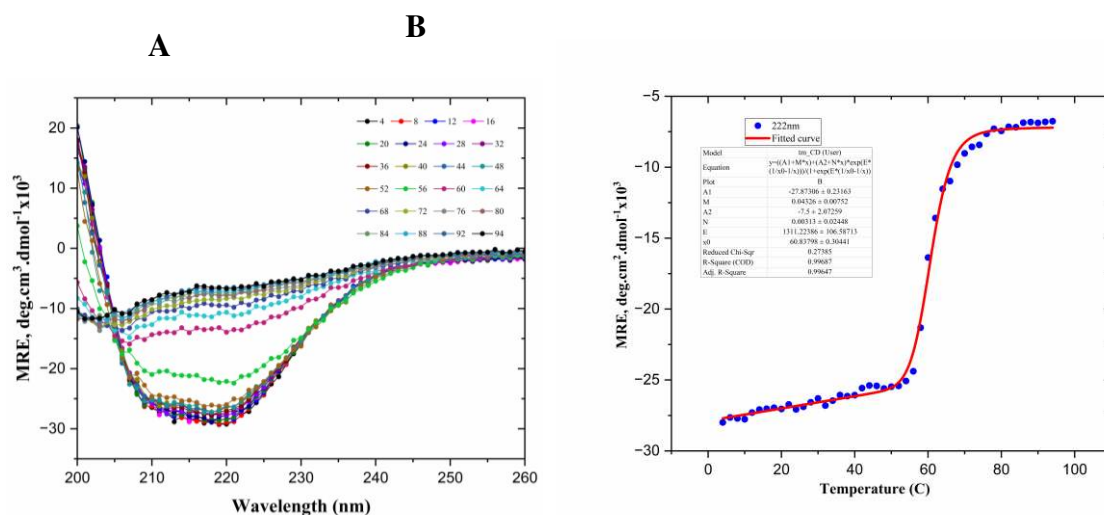


**Figure 3.15 CD Spectroscopy of PLCHR2 complex**

(A) Far-UV CD spectra (260 nm to 185 nm) in 4 °C increments from 4 to 98 °C (B) and Thermal stability (T<sub>m</sub> determination) at 222nm of PLCHR2 complex

**Table 3.5 Deconvolutions of CD signal of PLCHR2 complex and PLCN**

Protein	Wavelength	Helix %	B-sheets %	Melting temperature (T <sub>m</sub> )
PLCHR2	195-250nm	38.8	16.8	60°C
PLCN	195-250nm	31.5	55.6	45°C

#### 3.4.4 Fluorescence Spectroscopy

Figure 3.16 shows the fluorescence spectrum of PLCN and Figure 3.17 shows the fluorescence spectrum of PLCHR2 complex. The stability of the tertiary structures of both proteins was investigated using fluorescence spectroscopy. For both excitation wavelengths of 275 nm and 295 nm, the intact protein exhibited emission maxima at 330 nm. After being heated to 98 °C and then cooled to 4°C to allow for refolding, the emission peak at 330 nm decreased. The quenching happened because of tryptophan residues being exposed to the aqueous microenvironment as a result of protein denaturing. When excited at 295nm and 275 nm, a signal peak at 295nm is observed in both which is due to the scattering from the aggregated particles. In Figure 4.3 we can see a graph plotted between fluorescence and temperature and it was seen that the aggregation onsets around 40°C for both PLCN and PLCHR2. During the

### 3. Results

unfolding of the both the proteins, the emission maximum ( $\lambda_{Em, max}$ ) exhibits a redshift, moving from  $\lambda_{Em, max} = \sim 330$  nm in the native state to an average of  $\lambda_{Em, max} = \sim 340$  nm (Figure 3.16C & 3.17C). This provides additional support for the existence of structural transition.

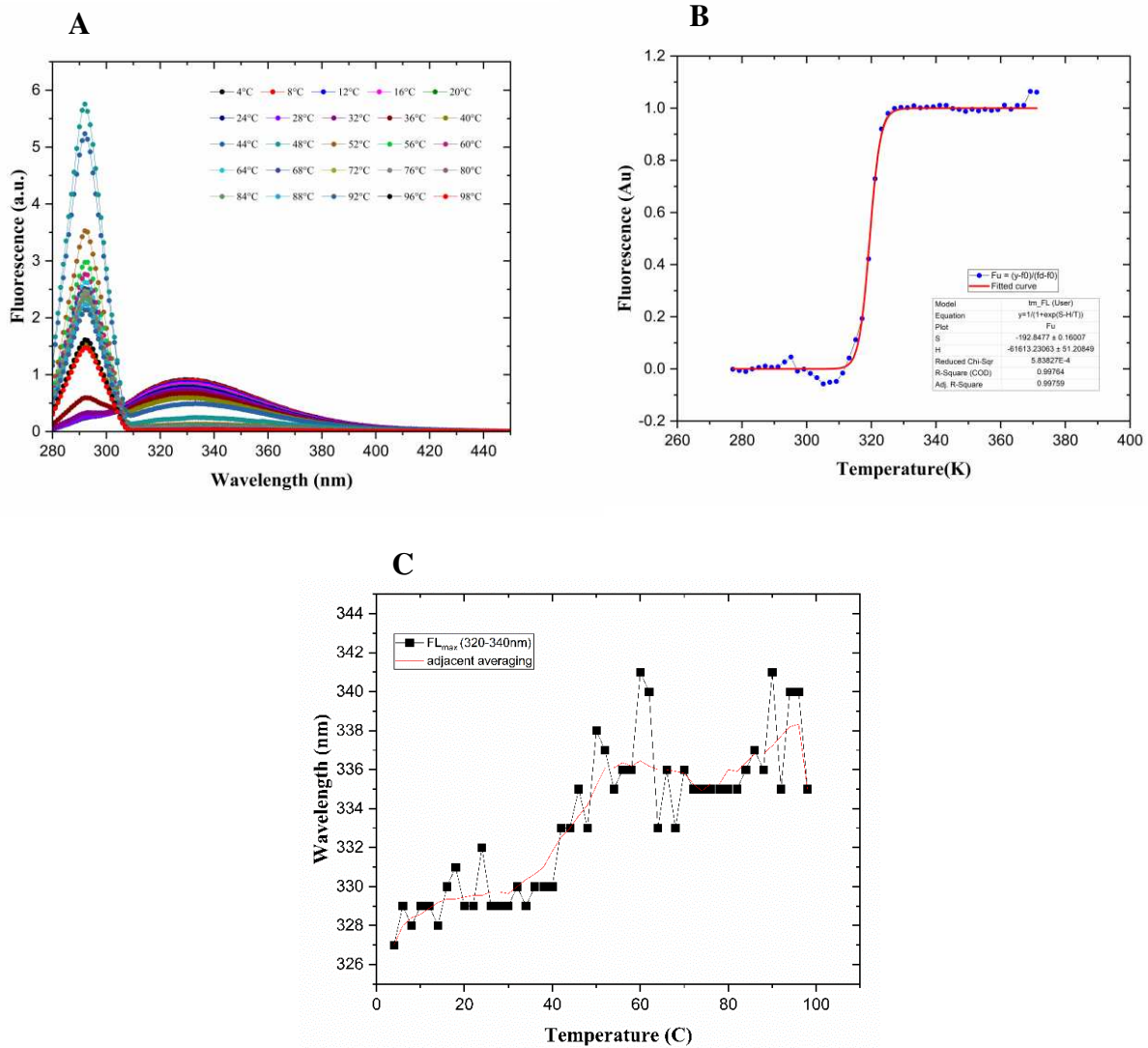


**Figure 3.16 Fluorescence spectrometry of PLCN**

A. Tryptophan fluorescence emission spectra, B. Thermal unfolding ( $T_m$  determination) and C. Emission maximum ( $\lambda_{Em, max}$ ) shows a redshift during the unfolding of PLCN

The fluorescence spectrum was obtained by measuring the fluorescence intensity vs wavelength. Plotting the 330 nm emission versus the temperature gradient provides a first order

### 3. Results

assessment of the fluorescence behavior during protein unfolding. The fluorescence of indole groups and their derivatives, such as tryptophan, is affected by temperature. Therefore, the calculations for the melting temperature ( $T_m$ ), which are based on the intrinsic tryptophan fluorescence of the protein, needed to be modified to account for the effect of temperature<sup>170</sup>. The calculations for this experiment were based on Kirby and Steiner (1970).

$$\frac{1}{Q} - 1 = \frac{f}{K_f} e^{-\frac{E}{RT}} \quad (1)$$

Here,  $Q$  represents the quantum yield, which in this context refers to the fluorescence that was measured by the instrument.  $f$  represents the frequency factor;  $k_f$  represents the first order rate constant for fluorescence emission from excited tryptophan;  $E$  indicates the activation energy of fluorescence quenching;  $R$ , the gas constant; and  $T$  symbolizes the absolute temperature in Kelvin. The natural logarithmic function is given by equation 2:

$$\ln\left(\frac{1}{Q} - 1\right) = -\frac{E}{RT} + \ln\frac{f}{K_f} \quad (2)$$

Using the emission at 330 nm as  $\ln\left(\frac{1}{Q} - 1\right)$  versus  $\frac{1}{T}$ , a curve, indicating no less than one temperature-dependent fluorescence shift and, therefore, an unfolding process was observed. It culminates in two unique states: the initial state ( $f_0$ ), which exists before the unfolding process, and the final, denatured state ( $f_d$ ), which can be seen as roughly linear, both before and after the shift. The slope, denoted by  $\left(-\frac{E}{R}\right)$ , and the intercept, denoted by  $\left(\ln\frac{f}{K_f}\right)$  were obtained using the linear regression curves from the linear states mentioned above. Therefore, equation 3

$$Q = \frac{1}{1 + \frac{f}{K_f} e^{-\frac{E}{RT}}} \quad (3)$$

To account for the effect of temperature dependence, the raw fluorescence signal was corrected for the difference between the initial state  $f_0$  and the final state  $f_d$ . This was accomplished by employing equation 6.

$$f_0 = \frac{1}{1 + e^{-\frac{E}{RT} * \text{intercept}}} \quad (4)$$

$$f_d = \frac{1}{1 + e^{-\frac{E}{RT} * \text{intercept}}} \quad (5)$$

$$f_u = \frac{y - f_0}{f_d - f_0} \quad (6)$$

### 3. Results

In equation 6,  $y$  is the raw measurement data for fluorescence. The  $f_0$  and  $f_d$  were calculated using equation 4 and 5 respectively and the raw fluorescence signal  $Q$ , as well as the slope  $(-\frac{E}{R})$ , and intercept  $(\ln \frac{f}{K_f})$  values were obtained from the linear regression of the two states.

When  $f_u$  versus temperature ( $T$ ) in Kelvin was plotted, it created a graph that was nonlinearly fitted to equation 6. The  $x$ -value where the slope of the original curve was greatest, corresponded to the melting temperature of the protein, and was obtained by equating the second deviation of the function with 0.

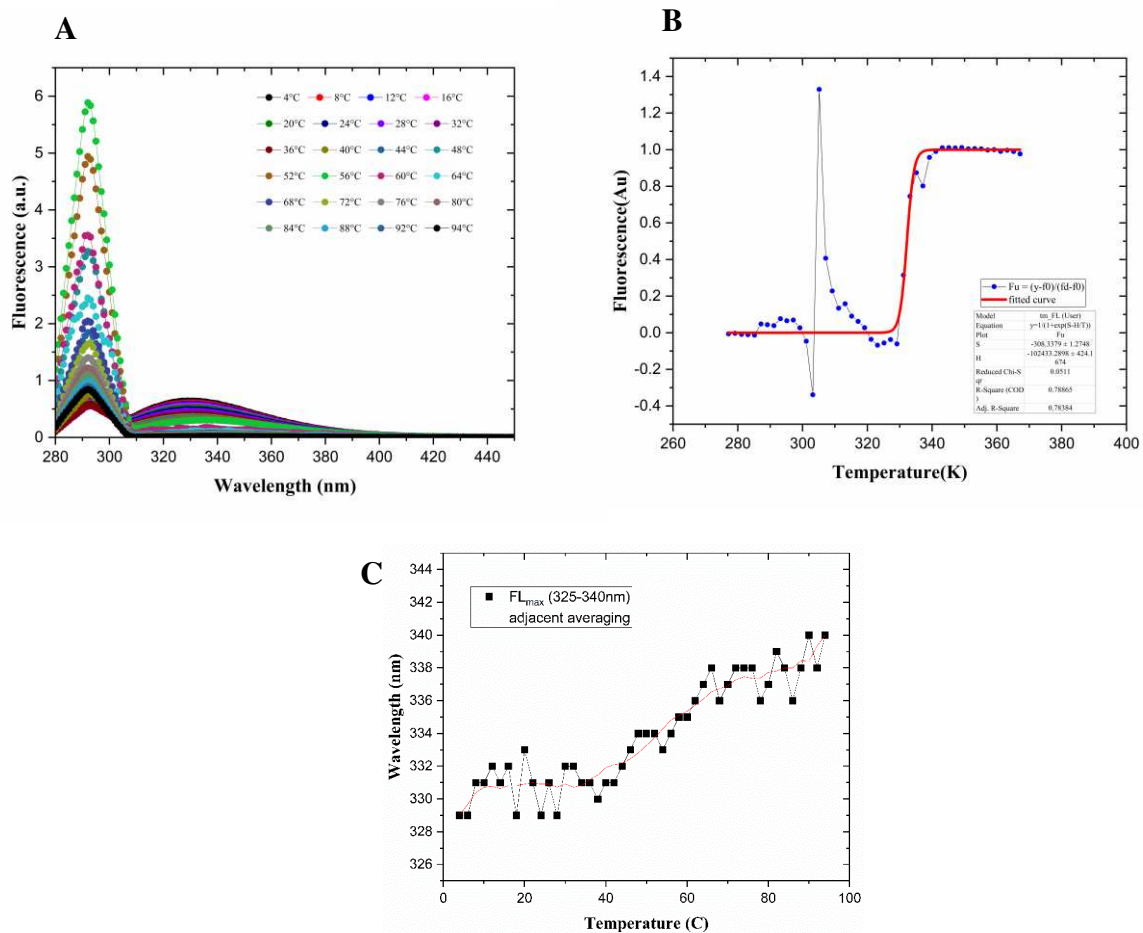


**Figure 3.17 Fluorescence spectrometry of PLCHR2 complex**

A. Tryptophan fluorescence emission spectra, B. Thermal unfolding ( $T_m$  determination) and C. Emission maximum ( $\lambda_{Em,max}$ ) shows a redshift during the unfolding of PLCHR2 complex.

### 3. Results

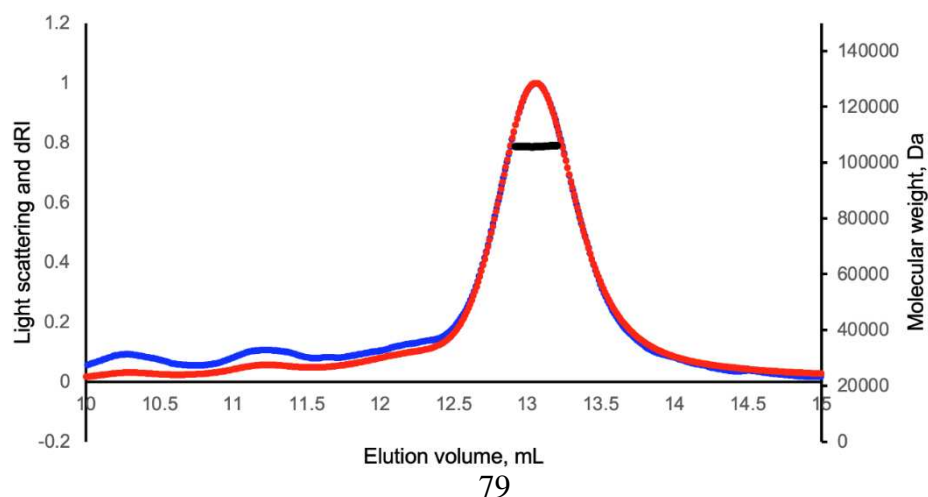
$R^2$  for PLCN curve was calculated to be 0.998 showing a good accordance with the measured data points. The point of inflection of the graph indicates the juncture at which the two states are in the middle of their transition, which is also the melting point of the protein. It was calculated by equating the second derivation of the fitted function, resulting in the melting temperature of 320.18 kelvin, which is equivalent to 47.03 °C.

However, the fact that for PLCHR2 the  $R^2$  is only 0.789 suggests that there are some values that are inconsistent with the fitted curve. This could have arisen from the local minimum, which was recorded at ~ 308 K. This may be a sign that there is a further conformational shift that takes place before the denaturing of the complete protein. The  $T_m$  was calculated for to be 335.6K or 62.45°C.

In conclusion, melting temperature ( $T_m$ ) came out to be 62.45°C and 47.03°C for the PLCHR2 complex and PLCN respectively. Thus, the PLCHR2 complex has much more stable tertiary structure than PLCN. Along with that, these are similar however, the  $T_m$  from FL are higher than the melting temperature from the CD measurements suggesting that the tertiary structures have more stability than the secondary structure.

#### 3.4.5 SEC-SAXS

In order to evaluate the stoichiometry of the PLCH and PLCR2 in solution SEC SAXS was performed. The MW correlation through the SEC elution trace of obtained from the light scattering data is shown in Figure 3.18 calculated from MALLS/RI measurements. The data collection and analysis was done by Cy Jeffries from P12 EMBL. The results demonstrate that the two proteins form a 1:1 complex in solution: MW expected = 104 kDa; MW MALLS/RI = 111 kDa (compare to the previous offline SEC-MALLS/RI MW estimate of 106 kDa). The median  $R_H$  of the PLCHR2 complex determined from the QELS measurements is around 4.3 nm.



### 3. Results

**Figure 3.18 A. MALLS,  $\text{cm}^{-1}$  (blue) and dRI,  $\text{ml}\cdot\text{g}^{-1}$  (red) data obtained for the SEC of PLCHR2.**

The MW correlation through the peak is shown as a black line with an average of around 111 kDa. Figure 3.19 displays the final merged SAXS profile measured from the three SEC-SAXS runs. The corresponding Guinier plot ( $\ln I(s)$  vs  $s^2$ ) calculated via a simple transformation of the SAXS data at the lowest of scattering angles<sup>171</sup> is displayed. The plot is linear ( $R^2 > 0.9963$ ) within the  $sR_g$  range of  $0.47 < sR_g < 1.3$  indicating that, in combination with the MW estimates, the merged data represent the scattering from a monodispersed complex. The final Guinier  $R_g$  estimate is 3.12 nm.

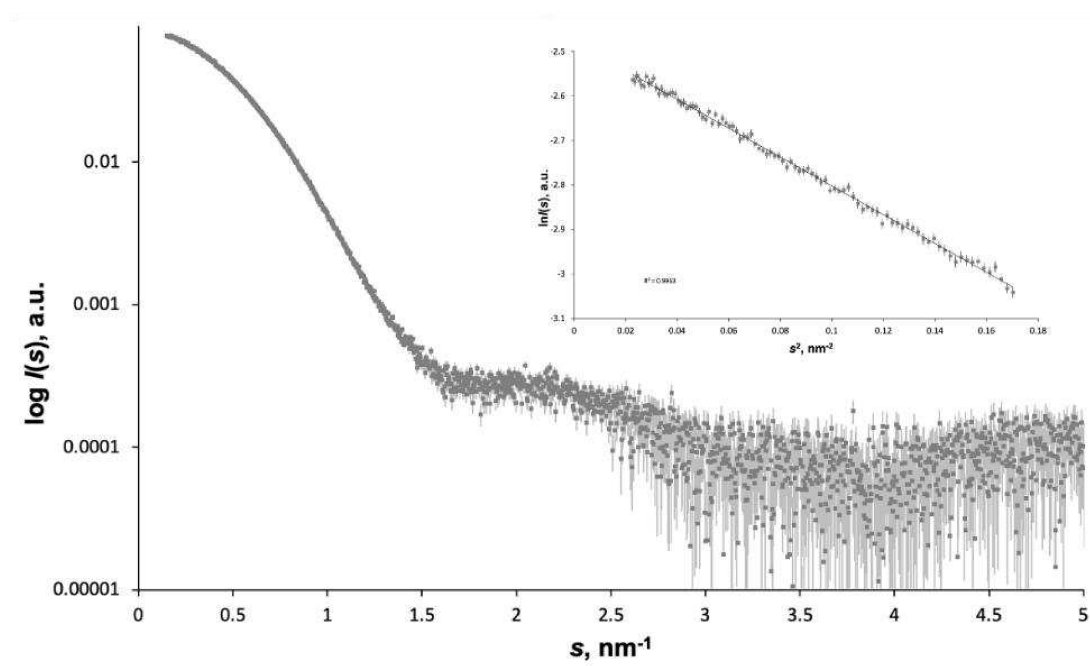


**Figure 3.19 Final merged SAXS profile of the PLCHR2 complex, and corresponding linear Guinier plot (inset).**

PLCHR2 complex at three different concentrations i.e. 3.5mg/ml, 7mg/ml and 14mg/ml in 25mM Tris, pH 7.5, 100mM NaCl, 3mM BME were subjected to SEC-SAXS

A Kratky plot representation of the SAXS data,  $I(s)s^2$  vs  $s$ , is shown in Figure 3.20A. The Kratky plot is consistent with a protein complex that is overall highly compact. Indeed the  $R_g/R_H$  ratio – or shape factor – of 0.73 speaks to the compact nature of the complex. The probable

### 3. Results

frequency,  $p$ , of real-space distances,  $r$  – or the  $p(r)$  profile<sup>172</sup> – of the PLCHR2 complex is shown in Figure 3.20B. The  $R_g$  determined from the  $p(r)$  at 3.16 nm is consistent with the Guinier  $R_g$  estimate. The maximum particle dimension,  $D_{max}$ , from the  $p(r)$  profile is approximately 12 nm. Overall, the  $p(r)$  profile also demonstrates the overall compact nature of the complex. Automated shape classification also places the complex in the compact regime.

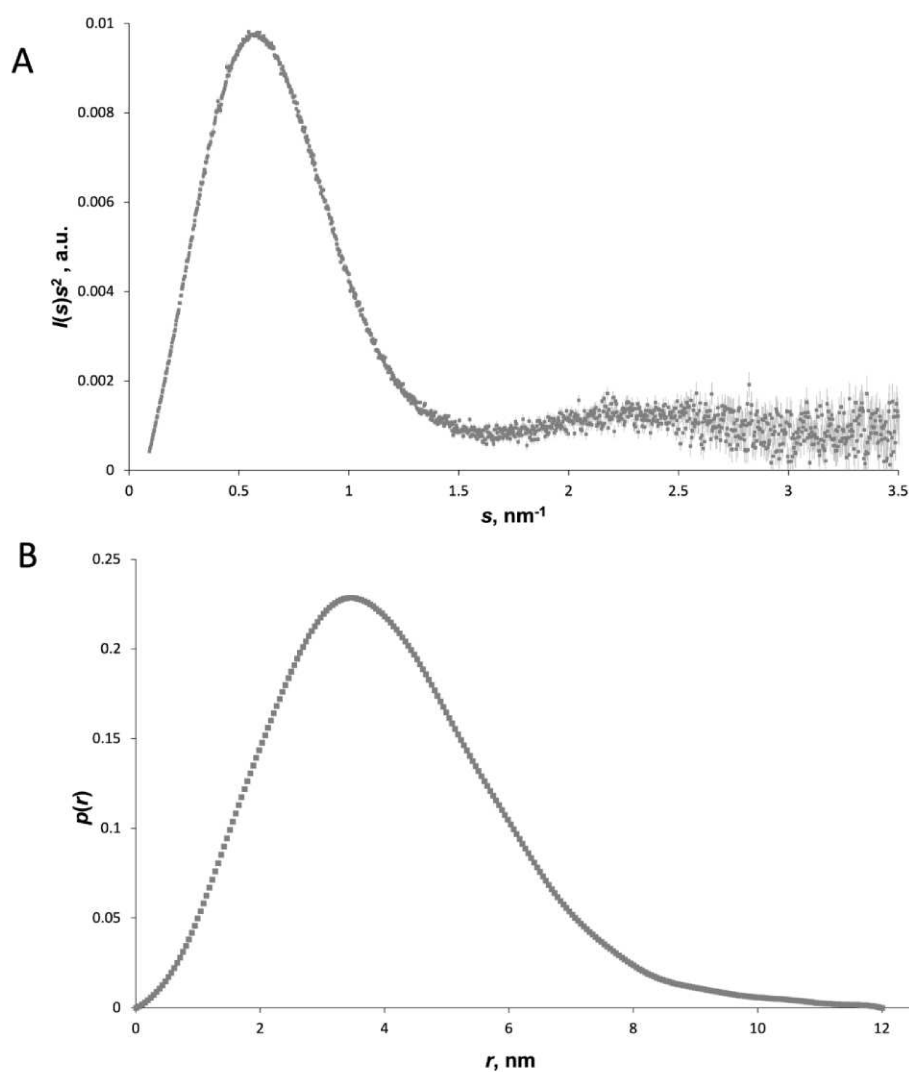


**Figure 3.20 A. A Kratky plot representation of the SAXS data. B. The calculated  $p(r)$  vs profile of the compact PLCHR2 complex.**

### 3. Results

Concentration-independent MW estimates were also evaluated directly from the final SAXS profile using DATMW (Bayesian MW estimator from scattering invariants)<sup>173</sup>. The MW from SAXS is consistent with the MW from MALLS/RI. All structural parameters and MW estimates are reported in Table 3.6, including the Porod volume (obtained from the SAXS data from area under the Kratky plot) that are all consistent with a 1:1 complex.

**Table 3.6 SEC-SAXS, MALLS and parameter summary for PLCHR2**

<b>Instrument Parameters</b>	
Column Type	S200 Increase 10/300
Flow rate (ml/min)	0.7
Injection volume ( $\mu$ l)	50-70
Load Concentration (mg/ml)	3.5-14
Temperature ( $^{\circ}$ C)	20
Buffer	25 mM TRIS, pH 7.5, 100 mM NaCl, 3 mM BME
sample to detector distance (m)	3
Exposure time/number of frames	1s/2100
X-ray wavelength (nm)	0.124

<b>Guinier analysis</b>	
Guinier I(0) ( $\sigma$ )	0.084 (0.0002)
$R_g$ (Guinier, nm) ( $\sigma$ )	3.12 (0.01)
s $R_g$ range/(points used)	0.47-1.29(1;95)

<b>pI analysis</b>	
I(0), POR ( $\sigma$ )	0.08405 (0.0001)
$R_g$ (POR, nm) ( $\sigma$ )	3.16 (0.01)
$D_{max}$ (nm)	12
Porod volume (nm <sup>3</sup> )	156

<b>MW analysis</b>	
--------------------	--

### 3. Results

Calculated MW, from amino acid sequence	104 kDa (assuming 1:1 complex)
MW from MALLS (kDa)	106-111
MW (Bayes, kDa)	93
Shape classification and hydrodynamics	
$R_h(\sigma)$ nm	4.3
$R_g/R_h$ ratio	0.73
Ambimeter score( $sR_g^{\max}$ )	0.48
#shape topologies	3
Uniqueness	Potentially unique
Shape classification	compact

#### ***Ab initio* modelling of PLCHR2**

The assessment of the non-uniqueness of the PLCHR2 scattering data was performed using AMBIMETER<sup>174</sup>, which also generated a likely model-independent shape-topology of the protein. This step was performed to evaluate the overall ambiguity of the SAXS data, as it can be the case that multiple shapes with different topologies can fit the same SAXS profile. The AMBIMETER score of 0.48 (calculated to an  $sR_g$  of 4.5) categorizes the scattering as ‘potentially unique’ which is advantageous.

The *ab initio* bead modelling of the complex was performed using the programs DAMMIN<sup>175</sup> and are summarized in Figure 3.21 along with the most likely shape topology from AMBIMETER. ( $\chi^2$  DAMMIN = 1.25; CorMap p = 0.2). Consistent with the primary structural parameter analysis and the data plots shown above, the compactness of the PLCHR2 complex is evident, forming a slightly flattened overall globular shape in solution.

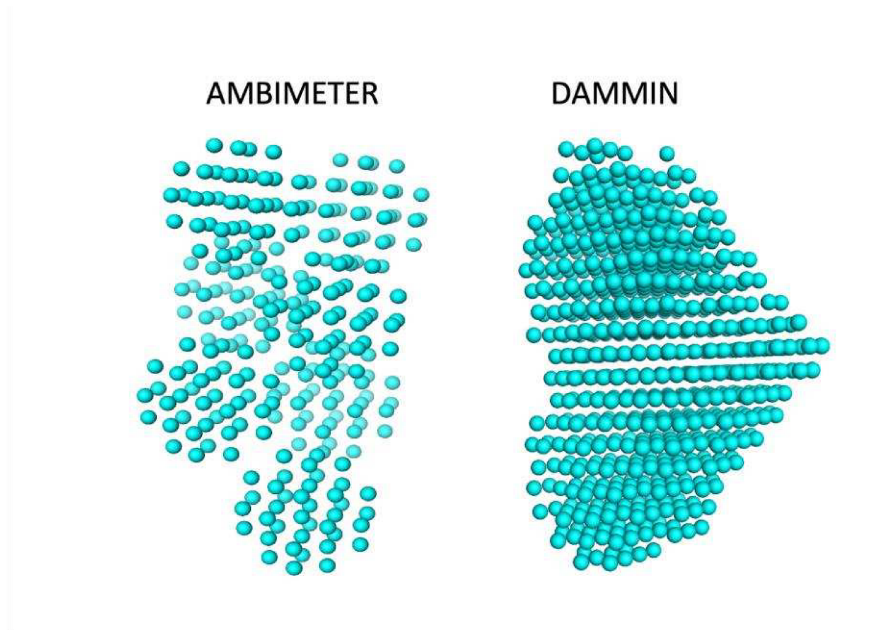


**Figure 3.21 The most likely predicted shape topology of PLCHR2**

The PLCHR2 complex topology was determined by using AMBIMETER (model-independent prediction) and a selected DAMMIN ab initio model.

### **Rigid-body modelling of PLCHR2**

Atomistic representations of PLCH and PLCHR2 were obtained from the AlphaFold Protein Structure Database (<https://alphafold.ebi.ac.uk>) using amino acid sequence alignments of both proteins extracted via the EBI Protein Similarity Search Tool (<https://www.ebi.ac.uk/Tools/sss/fasta/>). The direct links to the AlphaFold database entries are:

<https://alphafold.ebi.ac.uk/entry/A0A0H2Z768>

<https://www.uniprot.org/uniprotkb/A0A6N0KHT9/entry>

The respective predicted structures are shown in Figure 3.22.

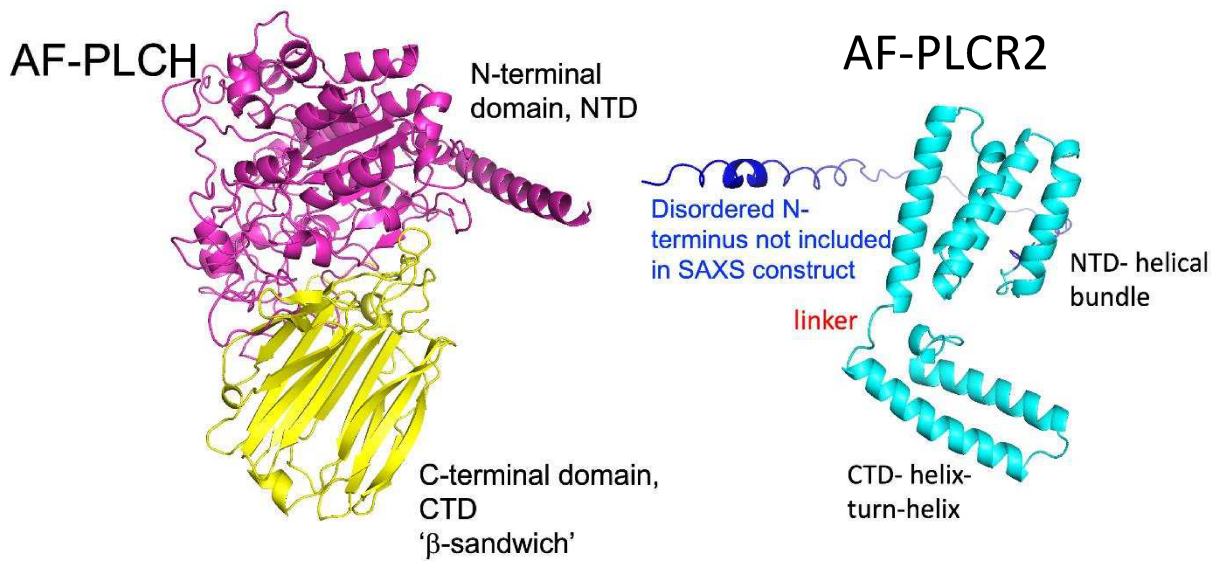


**Figure 3.22 Alphafold predicted models of PLCH and PLCR2 (yielding relatively high confidence).**

The PLCH has two distinct domains, an N-terminal domain (magenta) and a C-terminal 'b-sandwich' like domain (yellow). The Alphafold-predicted structure of PLCR2 includes a 56 amino acid, likely disordered, N-terminal extension, not included in the protein construct used for SAXS (refer to amino acid sequence alignment in the Appendix V).

These Alphafold predicted models – that score with reasonably high confidence – were used as templates for CORAL rigid body modelling, guided by the amino acid sequence alignments shown in the Appendix V to represent the exact protein constructs used for SAXS. Specifically, for the PLCH, 14 dummy amino acids were added to the N-terminus to take into account the mass of the N-terminal polyhistidine affinity tag. For the PLCR2, the somewhat long predicted disordered region at the N-terminus (encompassing the first 56 amino acids) were removed from the Alphafold template and replaced by a 24 dummy amino acid linker to represent the mass of the affinity tag in the protein used for SAXS.

CORAL modelling was performed using a zero-assumption approach, i.e., no distant constraints or other assumptions (e.g., surface electrostatic potentials) were made regarding binding interfaces between the two proteins. Briefly the complex was modelled either as two rigid-bodies (PLCH and PLCR2) that were allowed to refine their spatial positions relative to the fit to the SAXS data, or alternatively using three rigid bodies where a linker was introduced

### 3. Results

between the N-terminal helical bundle and the C-terminal helix-turn-helix of PLCR2 (i.e., PLCR2 amino acids 147–QATP–152 were replaced by a linker). The three-body CORAL modelling was employed to evaluate potential movement between the N- and C-terminal domains of PLCR2 relative to the initial AlphaFold conformation on binding to PLCH. Flexibility between the PLCH N- and C-terminal domains was not employed. CORAL modelling was performed twenty times, and those models that fit the SAXS data as assessed using CRY SOL<sup>176</sup> are presented in Figure 3.23. Each model generates excellent fits to the experimental data, in the  $\chi^2$  range of 1.20–1.3 and CorMap p = 0.04–0.16.

General features.

- A majority of the models generated for the complex orient the PLCR2 toward the top of N-terminal domain of PLCH.
- Due to the inherent low resolution of SAXS, the exact details of PLCR2 binding to the PLCH N-terminal domain cannot be determined using ‘no assumption’ rigid-body modelling. For example, the exact orientation of the PLCR2 bound to PLCH N-terminal domain cannot be determined. This would require additional contact information.
- However, and of interest, if the putative enzyme active site of the PLCH is mapped into the CORAL models, it appears that the PLCR2 acts as a steric block over the active site. **The working hypothesis obtained from SAXS is that the regulatory mechanism of PLCR2 acts, in part, by occluding the active site of the PLC enzyme.** Due to the number of modelling possibilities to satisfy the SAXS data, it is not possible to conclude whether the occlusion of the active site is mediated by the PLCR2 N-terminal domain helical bundle or – if rotating the bound PLCR2 orientation – the C-terminal helix-turn helix.
- As with all things SAXS, other possible binding orientations of PLCR2 to PLCH remain a possibility, requiring further biophysical characterization (e.g., hydrogen-deuterium exchange analysis).

### 3. Results

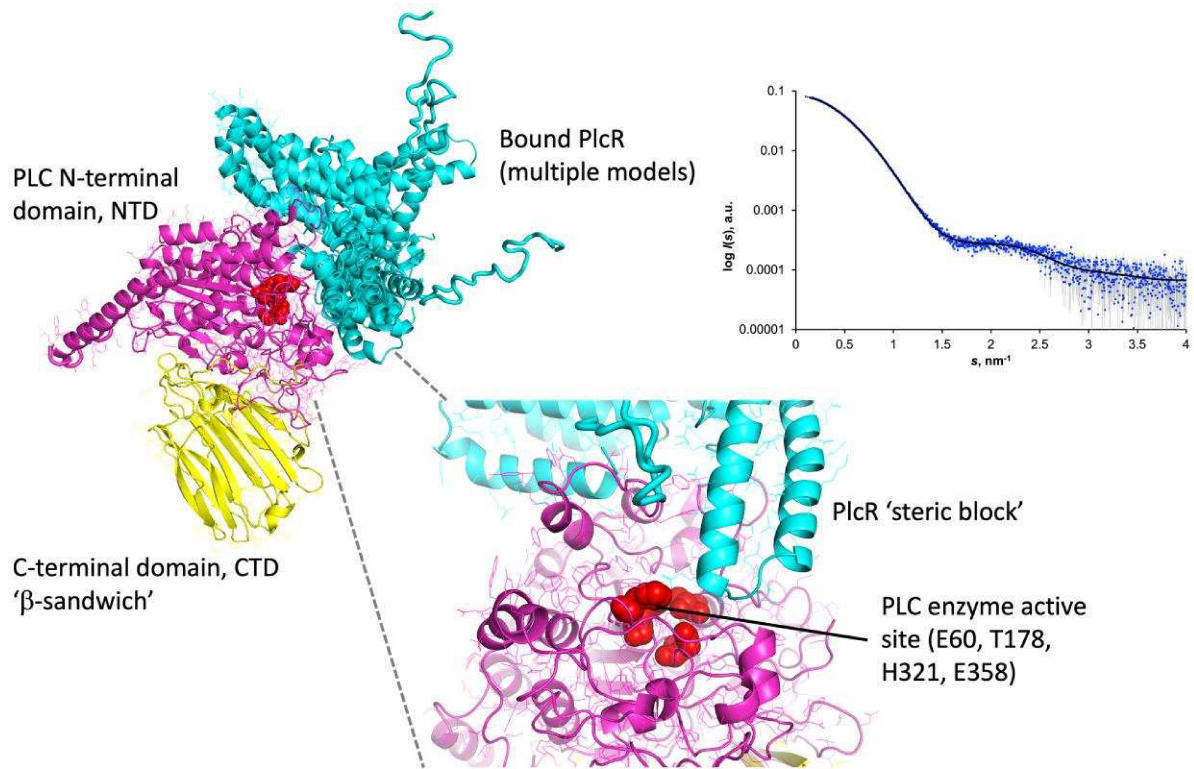


**Figure 3.23 Coral-refined rigid body models of PLCR2 bound to the N-terminal domain of PLCH**

PLCR2 possibly acting to occlude the enzyme active site as a steric block. An example model fit (black line) to the SAXS data (blue) is also shown.

## 3.5 Biochemical Characterization

The following phase, which came after the biophysical characterization of the proteins and the determination of the quality, quantity and oligomerization state, was to examine the functionality of the proteins. Methods both *in vivo* and *in vitro*, including the NPPC (p-nitrophenylphosphorylcholine) assay, the MTT (mono-tezolium) assay, and the hemolytic assay, were utilized in order to biochemically characterize the protein.

### 3.5.1 *In vitro* activity assay

The NPPC assay was used to perform the initial *in vitro* test to determine the functional state of the protein. Cleavage of the substrate p-nitrophenylphosphorylcholine (NPPC) by the proteins resulted in the production of a yellow colored substance (p-nitrophenol), and the absorbance was measured at 405nm<sup>132</sup>.

### 3. Results

In addition, the influence of EDTA and other cations on the proteins' enzyme activities was evaluated. Furthermore, mutant forms of both proteins were also tested for their respective activities.

#### 3.5.1.1 Activity assay for wild-type PLCN and PLCHR complex

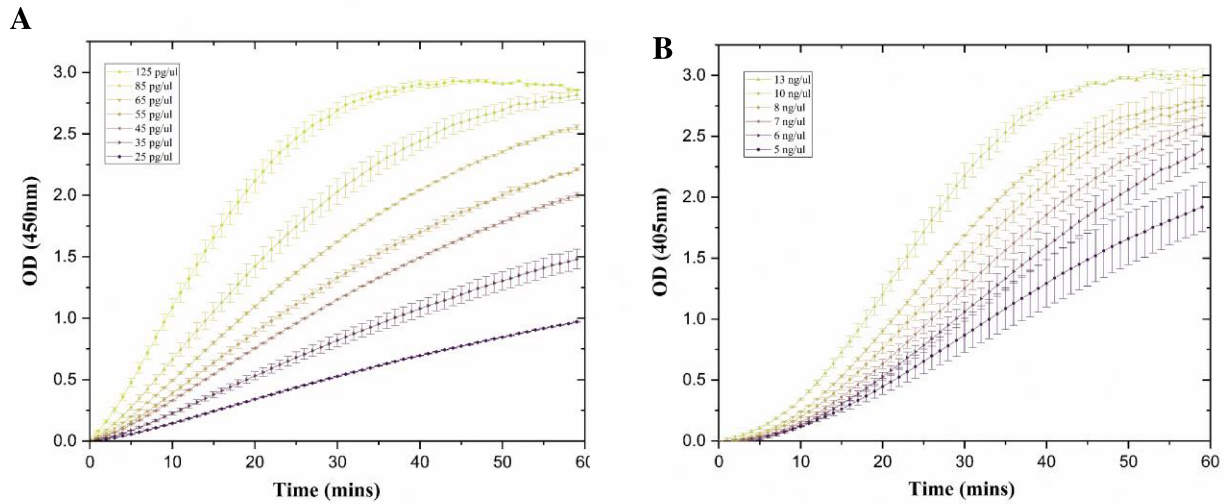


**Figure 3.24** *In vitro* enzyme activity using NPPC assay.

OD405 plotted against time for different protein concentrations showing a sigmoidal curve for each. **A:** PLCHR2 and **B:** PLCN. OD405nm was plotted against standard amount with linear fit for calculations of the enzymatic activity. Concentration for PLCN used was from 5ng/ $\mu$ l to 13ng/ $\mu$ l and for PLCHR2 complex Concentrations from 25pg/ $\mu$ l to 125pg/ $\mu$ l

Figure 3.24 depicts the absorbance at 405 nm plotted against the assay time for all screened PLCN and PLCHR2 complex concentrations. Every curve exhibited a sigmoidal progression throughout its progression. Each of the sigmoidal curve reached an OD<sub>405</sub> value that was greater than the maximum value attained by the standard i.e. OD<sub>405</sub> = 0.8 (supplementary data). For each of the protein a suitable concentration was chosen that fell within the standard and enzyme activity was calculated using the equation given below:

$$\text{Sample enzymatic activity (nmol/min)} = [\text{SlopeSample}] / [\text{SlopeStd}] \times \text{DF}$$

where, SlopeSample = The slope of the blank-subtracted sample curve (O.D. / min), SlopeStd = The slope of the blank-subtracted standard curve (O.D. / nmol) and DF = Dilution factor (if the sample is not diluted, the DF value is 1).

### 3. Results

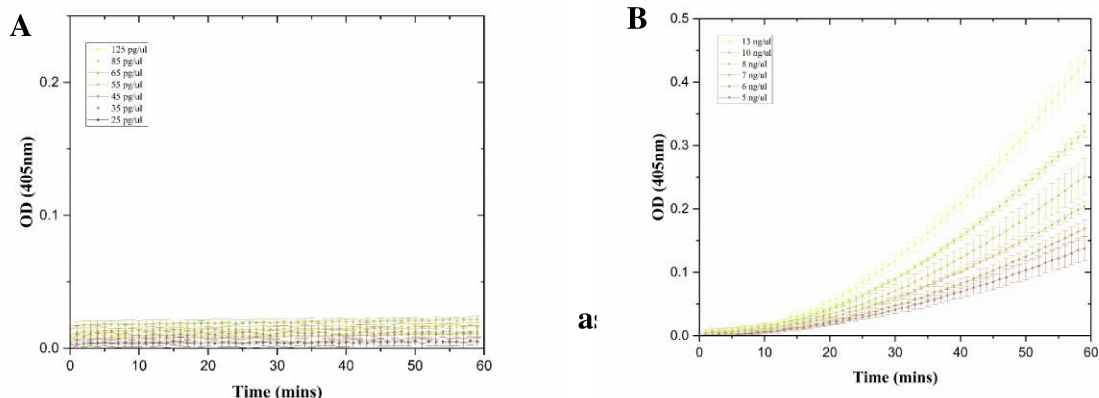
After performing a linear fit for the curve that was obtained at a concentration of 35 pg/l for the PLCHR2 complex, the specific enzyme activity was calculated to be  $3 \times 10^5$  nmol/min.mg. Furthermore, in the instance of PLCN, a linear fit was performed on the curve at 5ng/l, and the resultant value for specific enzyme activity was calculated to be  $3 \times 10^3$  nmol/min.mg.

Based on these findings, I am able to draw the conclusion that PLCHR2 possesses a two fold higher level of enzymatic activity than PLCN. Therefore, PLCHR2 perhaps has a greater effect on *P.aeruginosa's* pathogenicity.

#### 3.5.1.2 Activity assay for mutants PLCN and PLCHR complex

According to the published research, the threonine residue that is found at position 178 in PLCH and at position 176 in PLCN may be the most significant residue and plays an important role in the active site<sup>177,51,32</sup>. In order to determine whether or not threonine is essential for its activity, point mutations were introduced into the protein, and the resulting variants were put through an activity test.

Both mutants' activity levels were measured with the same activity kit. The graph in Figure 3.25 depicts the correlation between absorbance and time for various concentrations of mutant PLCN and mutant PLCHR2. The activity level has dropped dramatically, and the graph reveals that it is now nearly absent. A comparison of the wild type protein and the mutant versions is shown in the Figure3.26. The results reveal that there was essentially no activity remaining for the PLCHR2 mutant, while the activity level of the PLCN mutant decreased dramatically.



When threonine in the active site was mutated to alanine, the activity for both proteins reduced significantly. OD<sub>405nm</sub> plotted against time for different protein concentrations showing almost flat curve for each of the proteins **A** T178A PLCHR2 and **B** T 176A PLCN

### 3. Results

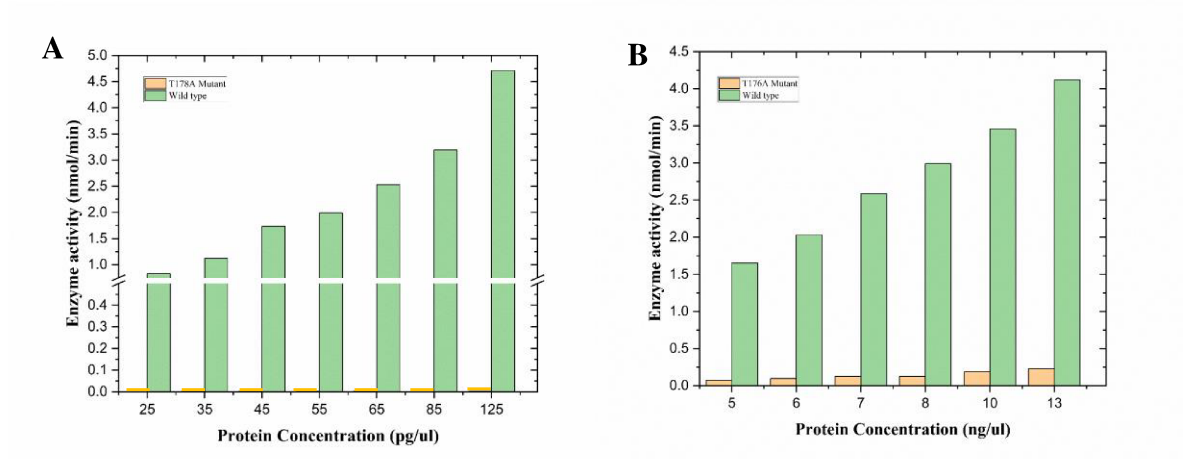


**Figure 3.26 Comparison of wild type *in vitro* enzymatic activity using NPPC assay mutants**

Wild type enzyme activity when plotted along with the threonine point mutants against different protein concentrations showed that PLCHR2 mutant activity was completely abolished whereas PLCN mutant activity was significantly reduced **A** PLCHR2 T178A, **B** PLCN T176A

#### 3.5.1.3 Activity assay with different cations and EDTA

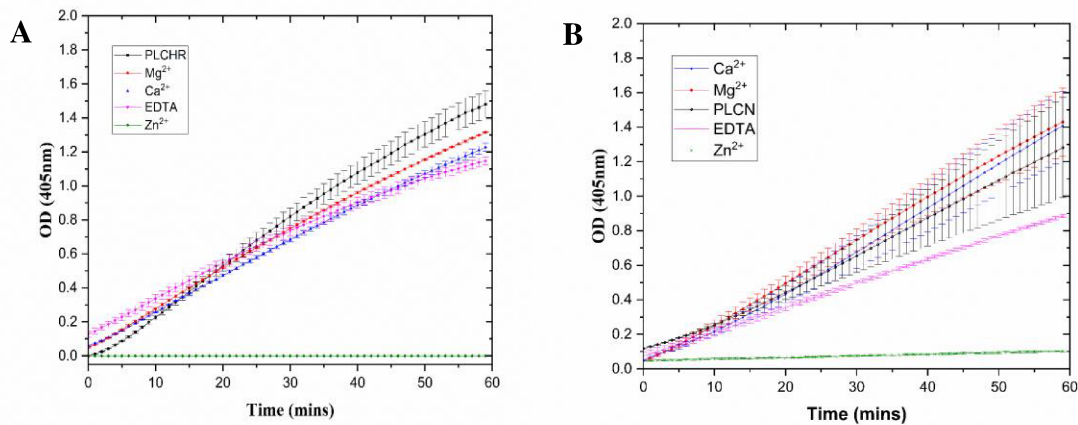


**Figure 3.27 Effect cations Ca<sup>2+</sup>, Mg<sup>2+</sup>, Zn<sup>2+</sup> and EDTA on enzymatic activity**

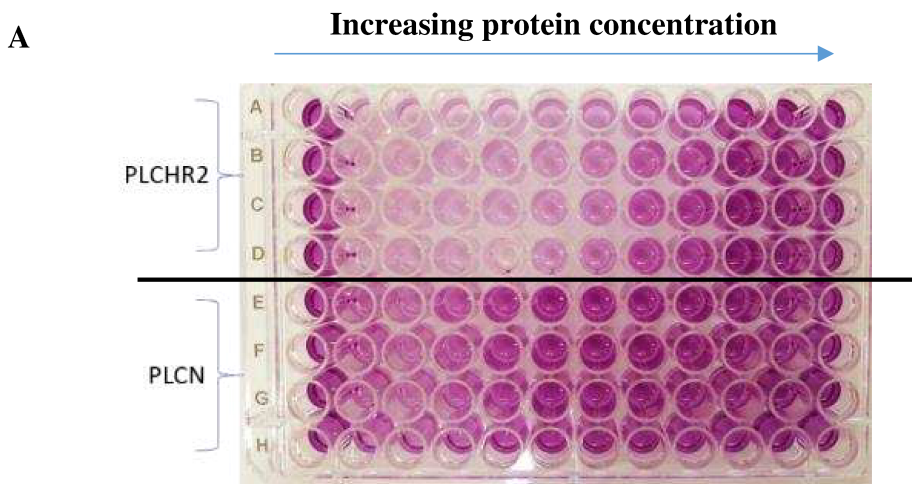
EDTA did not show any influence on the activities of both proteins. Cations such as Ca<sup>2+</sup> and Mg<sup>2+</sup> had no impact on PLCHR2, while in the case of PLCN, their activity slightly increased. However, Zn<sup>2+</sup> completely inhibited the enzymatic activity of both proteins. Optimal concentrations for activity were used, with PLCHR2 at 70 pg/μl and PLCN at 5 ng/μl. **A:** PLCHR2 and **B** PLCN

### 3. Results

Additionally, the PLCN and PLCHR2 complex was examined in the presence of a number of divalent cations, including  $\text{Ca}^{2+}$ ,  $\text{Mg}^{2+}$ , and  $\text{Zn}^{2+}$ , as well as ethylenediaminetetraacetic acid (EDTA), which is a metal chelator. This was carried out in order to determine whether or not the activity of the enzyme is dependent on the presence of any metal.

For the purpose of this experiment, the optimal concentration for the activity was chosen, which has been demonstrated to be  $35 \text{ pg}/\mu\text{l}$  for the PLCHR2 complex and  $5 \text{ ng}/\mu\text{l}$  for the PLCN. This optimal concentration falls somewhere in the range that the standard curve. The Figure 3.27 illustrates how the proteins were affected by the presence of the cations  $\text{Ca}^{2+}$ ,  $\text{Mg}^{2+}$ , and  $\text{Zn}^{2+}$  as well as EDTA having a concentration of  $1\text{mM}$ . As can be seen in the illustration, zinc completely inhibits both enzymes, whereas calcium, magnesium, and ethylenediaminetetraacetic acid have very little impact on PLCHR2. However, PLCN is somewhat influenced by  $\text{Ca}^{2+}$  and  $\text{Mg}^{2+}$ , which cause the activity increase slightly, whereas EDTA has the opposite effect and causes the activity to fall marginally. Nevertheless, the change is not substantial, so we can presume that it will not have any effect. Furthermore, I observe artifacts here because the standard deviation is also a little high for these parameters.

#### 3.5.2 In vivo cellular assay



### 3. Results

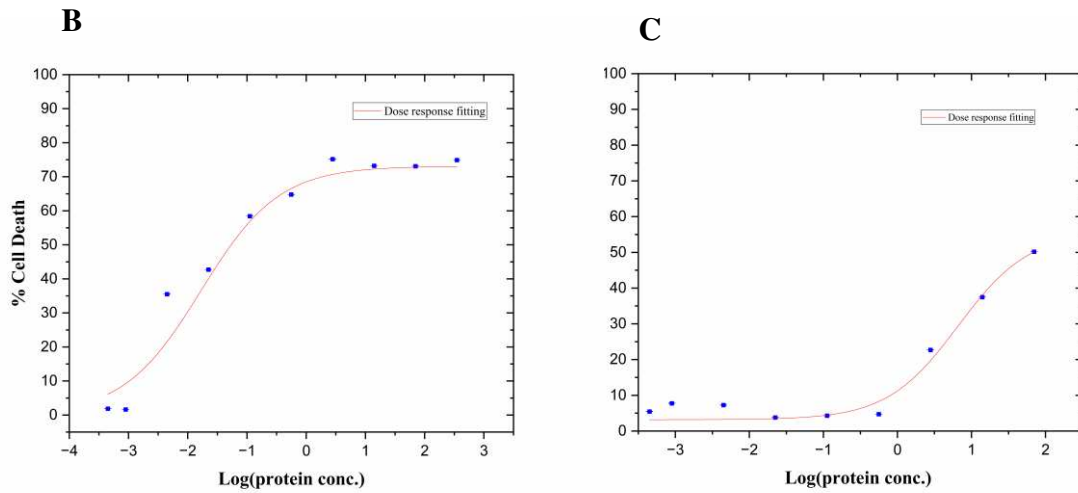


**Figure 3.28** *In vivo* enzyme activity using MTT assay

A. plate showing MTT assay with PLCHR2 and PLCN with 2-fold serial dilution starting from 350 ng/ $\mu$ l of protein concentration B. Graphs plotted percentage of dead cells vs the log of protein concentrations PLCHR2 and PLCN. The concentration at which PLCHR2 caused a lethal dose (LD50) in HeLa cells was determined to be 0.016 ng/ $\mu$ l, whereas PLCN exhibited an LD50 at a concentration of 6.6 ng/ $\mu$ l.

As was effectively demonstrated above, the enzyme is clearly active on the artificial substrate NPPC. However, the activity of the enzyme was hindered when I mutated the enzyme at the active site or when zinc was present. On the other hand, this was done with a substitute for the phospholipids. Therefore, an MTT test was carried out in order to validate the activity with the phospholipids that are present in the cellular membrane.

As was discussed in the section under "2.7.2," the HeLa cells were exposed to varying concentrations of the enzymes, and the MTT assay was used to determine how well the cells were able to survive after being treated. The absorbance at 570 nm was determined. A graph depicting the relationship between the percentage of dead cells and the log of protein concentrations is shown in Figure 3.28. OriginLab was utilized in order to arrive at the value of the Lethal Dose 50. The lethal dose (LD50) in HeLa cells for PLCHR2 was found to be at a concentration of 0.016 ng/ $\mu$ l, while the LD50 for PLCN was at 6.6 ng/ $\mu$ l. These amounts are much less than the proteins that is overexpressed in *E.coli* i.e. more than 20mg/ml from 3 grams of cells.

### 3. Results

The LD50 that was measured using HeLa cells was consistent with the activity that was determined via in vitro experiments. In accordance with the findings obtained in vitro (NPPC assay), PLCHR2 is a more virulent variant than PLCN.

#### 3.5.3 Qualitative Hemolytic Assay for PLCN and PLCHR Complex

It is established that several PLCs have hemolytic properties. PLCH has been shown to be hemolytic in *Pseudomonas aeruginosa*, whereas PLCN is unable to lyse red blood cells (RBCs). For the purpose of demonstrating this, both proteins were put through a qualitative hemolytic experiment utilizing sheep blood agar plates. The Figure 3.29 depicts the 5% sheep blood agar plates containing both proteins. It was noted that PLCN demonstrates no evidence of hemolysis, whereas PLCHR2 complex demonstrates the presence of a white halo surrounding the hole in which the protein sample was placed. Despite the fact that the halo that was observed is not particularly bright, I nevertheless was able to draw the conclusion that PLCHR does demonstrate Beta type hemolysis, whereas PLCN does not.

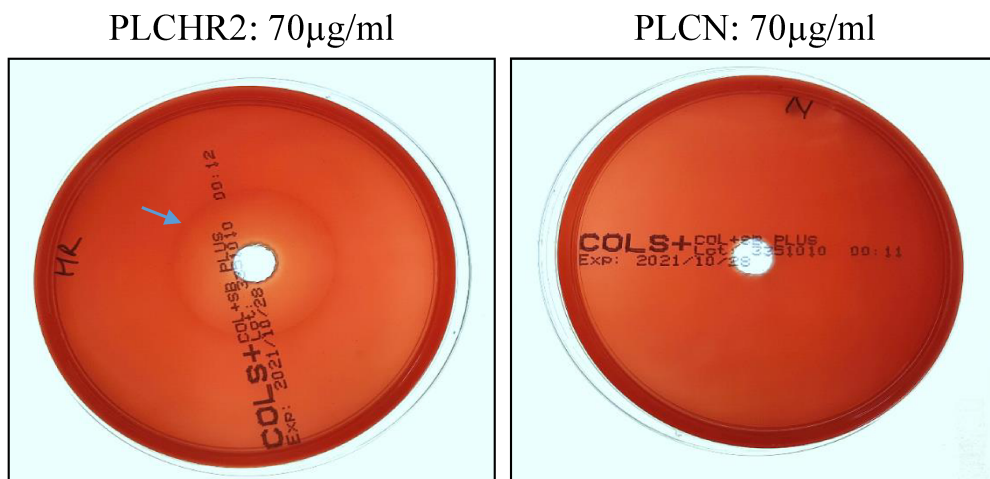


**Figure 3.29 Qualitative Hemolytic assay**

PLCHR2 and PLCN incubated with 5% sheep blood agar plate with 70µg/ml of protein concentration. PLCHR2 showed  $\beta$ -hemolysis after 16 hours of incubation at 37°C. PLCN had no effect on red blood cells

#### 3.5.4 Atomic Force Microscopy

Based on these findings, we know that PLCHR2 is more lethal than PLCN and can destroy living cells by degrading their membrane phospholipids. Since I wanted to know how it might

### 3. Results

affect the membranes, I proceeded to do an AFM experiment. Dr. Udom helped in collecting and analysis of the data.

#### 3.5.4.1 Experimental controls

An exemplary AFM image of a freshly cleaved mica (Figure 3.30) in ambient conditions showed a smooth surface with an approximated roughness of 1 nm<sup>178,179</sup>. After adding PBS, the mica substrate was imaged again (Figure 3.31). It showed a slight roughness increase to about 1.5 nm due to the increased fluctuation of the cantilever vibration in liquid. Lastly, for the control experiment, phospholipase enzyme was subsequently added. An AFM image showed the same roughness (1 to 1.5 nm). Several bright spots of about 4-nm diameter were also observed (Figure 3.32). These spots were the enzyme; however, the AFM resolution limited by the cantilever tip size was tens of nanometers<sup>180</sup>. Therefore, the exact shape or geometry of the enzyme could not be extracted from the AFM images.

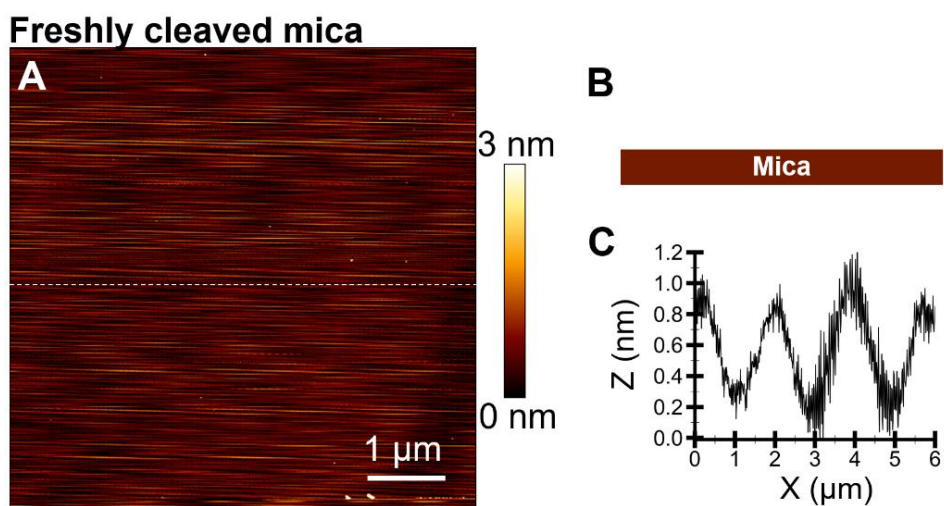


**Figure 3.30 AFM image of mica freshly cleaved mica**

**A.** Exemplary AFM image of freshly cleaved mica. The scanned area was 6 μm x 6 μm. The horizontal scale bar was 1 μm. The vertical color scale bar (0-3 nm) indicated the height profile of the surface. **B.** A diagram showed a naked mica substrate. **C.** The cross-section height profile of the white dashed line in (A) showed a roughness of about 1 nm.

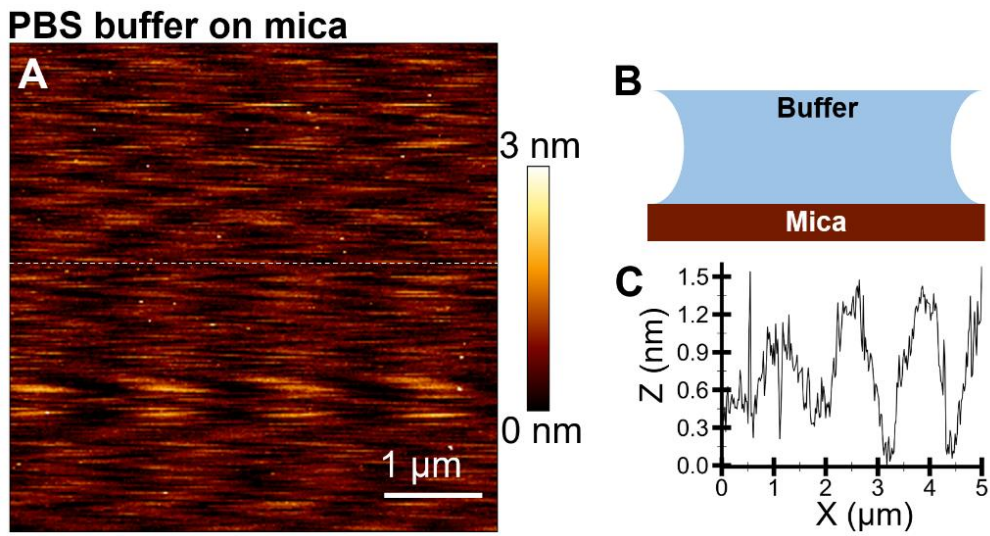


**Figure 3.31 AFM image of PBS buffer on mica**

**A.** Exemplary AFM image of PBS buffer on mica. The scanned area was  $5 \mu\text{m} \times 5 \mu\text{m}$ . The horizontal scale bar was  $1 \mu\text{m}$ . The vertical color scale bar (0-3 nm) indicated the height profile of the surface. **B.** A diagram showed PBS buffer on a naked mica substrate. **C.** The cross-section height profile of the white dashed line in (A) showed a roughness of about 1.5 nm.

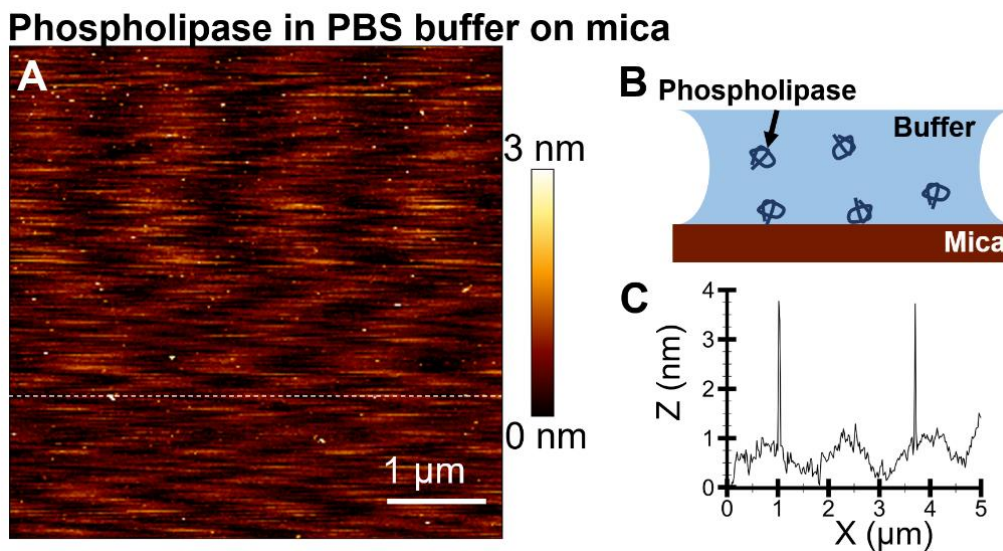


**Figure 3.32 AFM image of phospholipase C (PLCHR2) in PBS buffer on mica**

**A.** Exemplary AFM image of phospholipase enzyme in PBS buffer on mica. The scanned area was  $5 \mu\text{m} \times 5 \mu\text{m}$ . The horizontal scale bar was  $1 \mu\text{m}$ . The vertical color scale bar (0-3 nm) indicated the height profile of the surface. **B.** A diagram showed phospholipase enzyme in PBS buffer on a naked mica

### 3. Results

substrate. **C.** The cross-section height profile of the white dashed line in (A) showed a roughness of about 1 nm. The white spots on the dashed line showed a height profile of about 4 nm.

#### 3.5.4.2 Imaging of lipid membrane

DMPC liposome spread on the mica substrate and formed a lipid bilayer<sup>181</sup>. The lipid bilayer was stable for at least two hours in our imaging conditions. An AFM image showed a primarily smooth surface of the membrane (Figures 3.33 & 3.34). However, the formation of the bilayer was not perfect. A liposome that did not spread to form the bilayer, which was indicated by a vesicle with a 4-nm diameter, was found on the surface (Figure 3.33). A few holes were also found (Figure 3.34).

#### Lipid membrane on mica

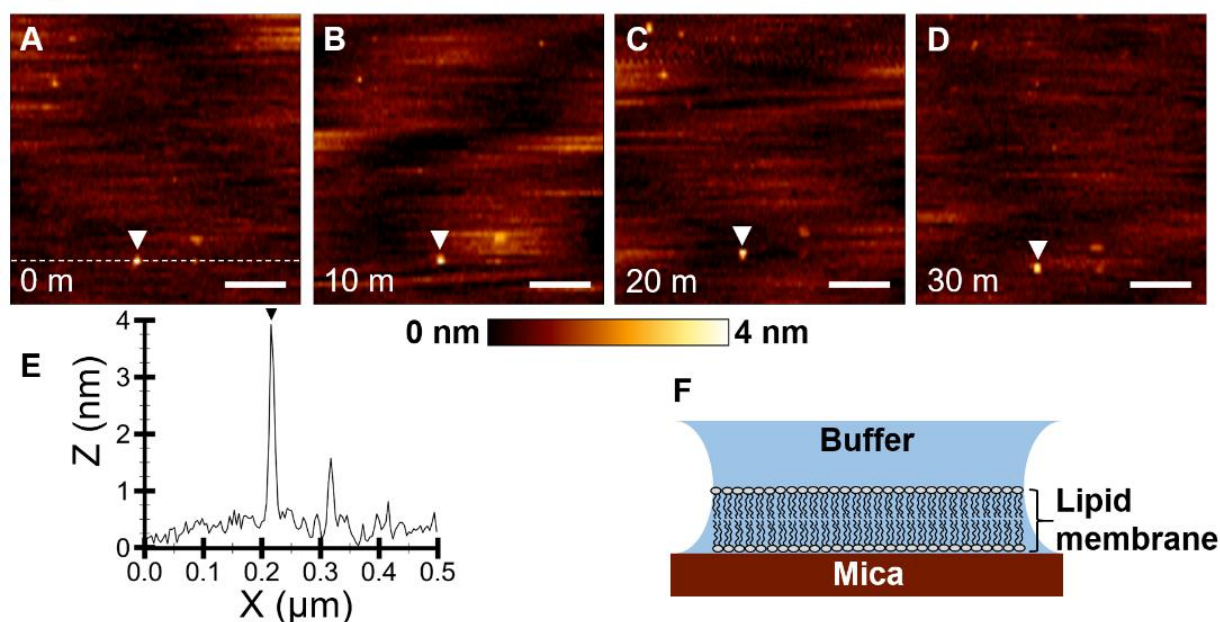


**Figure 3.33 AFM image of lipid membrane in PBS buffer on mica**

**A-D.** Exemplary AFM images of DMPC lipid bilayer in PBS buffer on mica. The number in the lower left corner indicated the time after starting to image. The scanned area was  $0.5 \mu\text{m} \times 0.5 \mu\text{m}$ . The horizontal scale bar was 100 nm. The vertical color scale bar (0-4 nm) indicated the height profile of the surface. The white arrow indicated a liposome. **E.** The cross-section height profile of the white dashed line in (A). The white spot on the dashed line showed a height profile of about 4 nm. **F.** A diagram showed a lipid bilayer in PBS buffer on a naked mica substrate

## Lipid membrane on mica

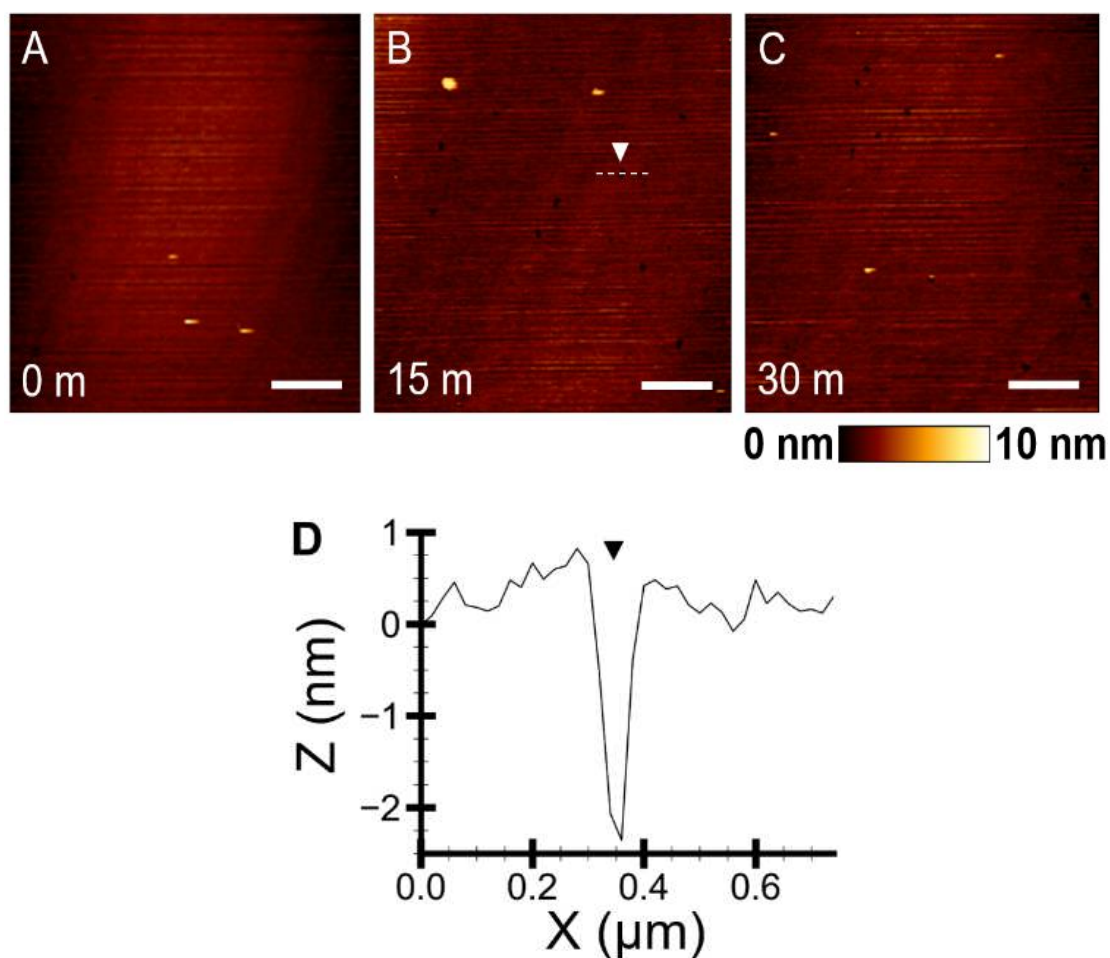


**Figure 3.34 AFM image of lipid membrane in PBS buffer on mica**

**A-C.** Exemplary AFM images of DMPC lipid bilayer in PBS buffer on mica. The number in the lower left corner indicated the time after starting to image. The scanned area was  $5\ \mu\text{m} \times 5\ \mu\text{m}$ . The horizontal scale bar was  $1\ \mu\text{m}$ . The vertical color scale bar (0-10 nm) indicated the height profile of the surface. The white arrow indicated a liposome. **D.** The cross-section height profile of the white dashed line in (B). The hole on the dashed line showed a depth profile of about 3 nm.

### 3.5.4.3 Lipid membrane lysis by phospholipase

The DMPC lipid membrane lysis by phospholipase enzyme was observed by AFM-based imaging in a liquid milieu at room temperature over time. Based on the AFM image analysis, the lysis mechanisms were divided into three intervals. During the first period (0-21

### 3. Results

minutes after the enzyme was added), the holes in the membrane were nucleated and expanded (Figure 3.35). We tracked each hole (blue, white, and yellow arrows) and found that the hole sizes became larger. The average volume of the digested membrane extracted from the analysis of the AFM images increased (Figure 3.36) from about 13000 to 71000 nm<sup>182</sup>. We also observed a formation of a lipid vesicle close to the hole (yellow arrow). We believe the vesicle was formed due to the lysed lipid bilayer detached from the supporting mica. The depth of the hole was about 3 nm (Figure 3.37), which agreed with the thickness of the lipid bilayer<sup>183,184</sup>.

## Phospholipase with lipid membrane (1)

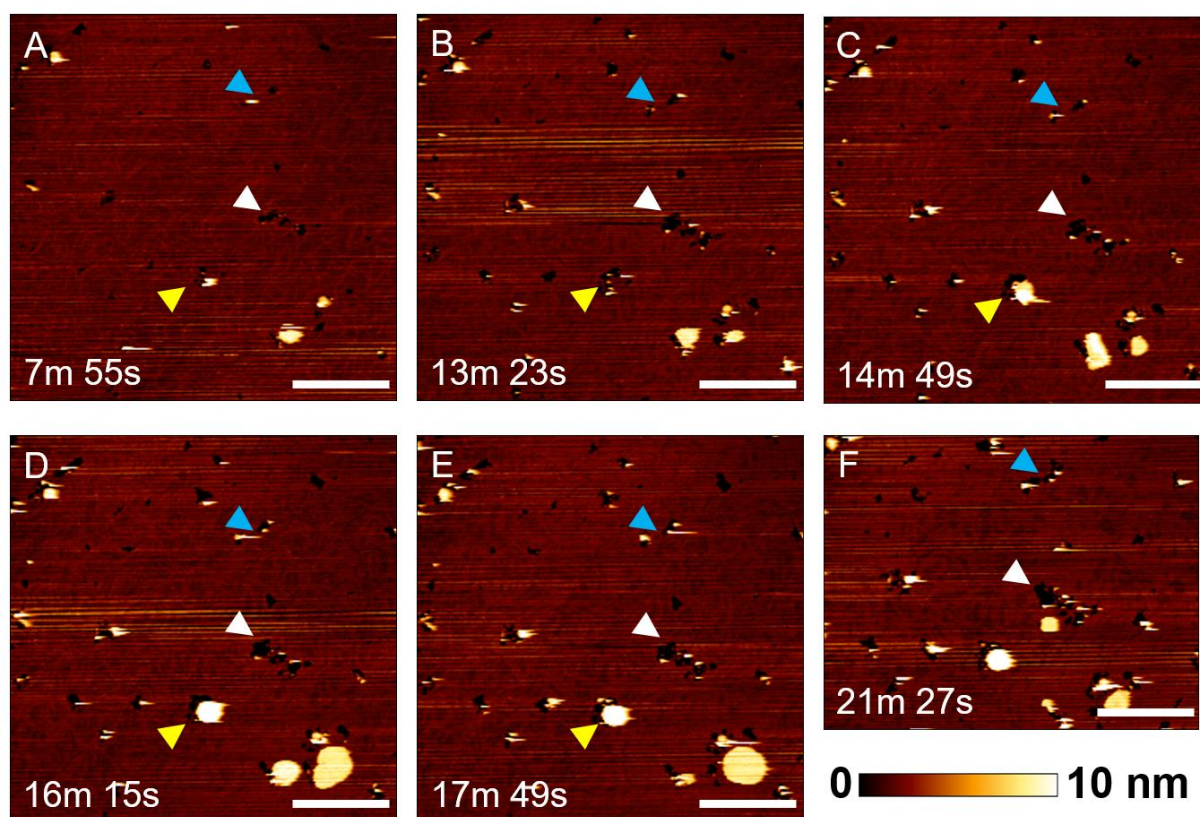


**Figure 3.35 AFM image with PLCHR2 with lipid bilayer in buffer on mica scanned for 7 to 21 minutes**

(A-F) Exemplary AFM images of DMPC lipid bilayer lysis by 10 $\mu$ g of PLCHR2 during the first time window. The number in the lower left corner indicated the time after the enzyme was added. The scanned area was 4  $\mu$ m x 4  $\mu$ m. The horizontal scale bar was 1  $\mu$ m. The vertical color scale bar (0-10 nm) indicated the height profile of the surface. The arrows (blue, white, and yellow) tracked the hole nucleation and expansion.

### 3. Results

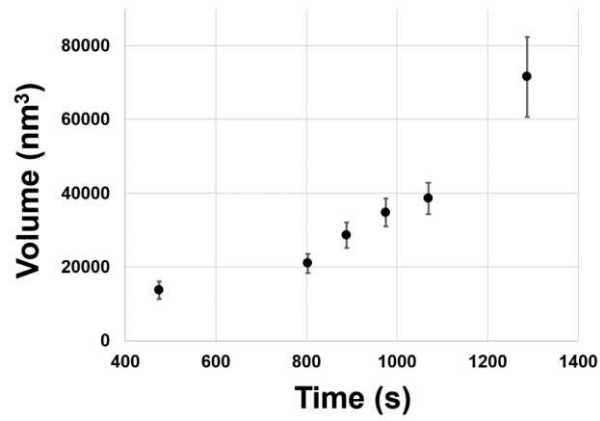
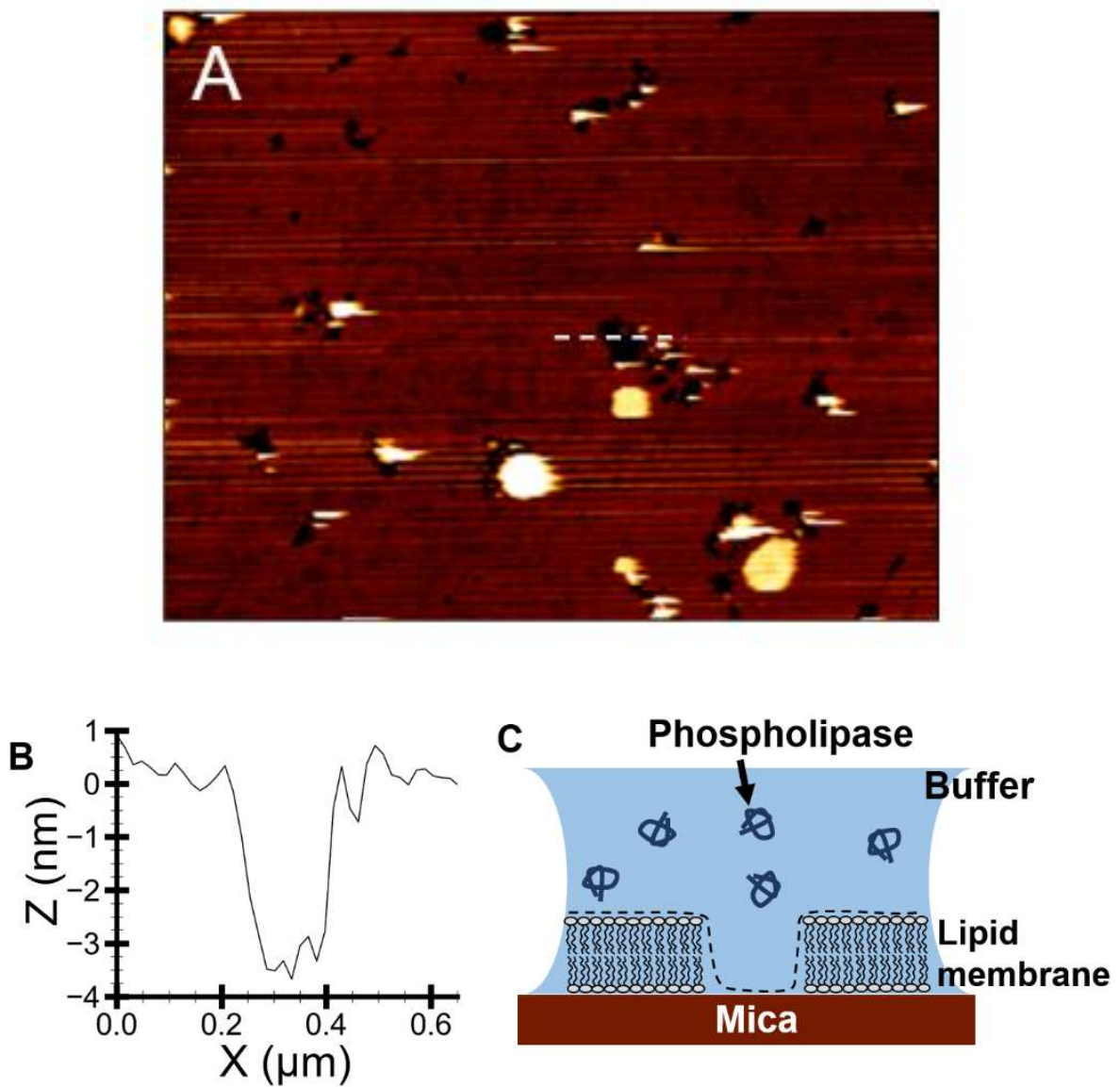


**Figure 3.36** The average volume of the digested membrane incubated with PLCHR2 from 475 s to 1287 s.



### 3. Results

#### Figure 3.37 Analysis of AFM image with PLCHR2 with lipid bilayer in buffer on mica after 20 minutes

**A.** AFM image of DMPC lipid bilayer lysis by PLCHR2 at 21 minutes 27 seconds after the enzyme was added. This image was the same as Figure 3.35(F). **B.** The cross-section height profile of the white dashed line in (A). The hole on the dashed line showed a depth profile of about 3 nm. **C.** A diagram showed experimental components in this measurement.

During the second interval (21-30 minutes after the enzyme was added), we observed that the holes began to close (Figure 3.38), which was indicated by the height profile at the bottom of the hole (Figure 3.39). We also observed some aggregate, which could be the lipid or the enzyme, at the top of the hole rim (Figure 3.40).

## Phospholipase with lipid membrane (2)

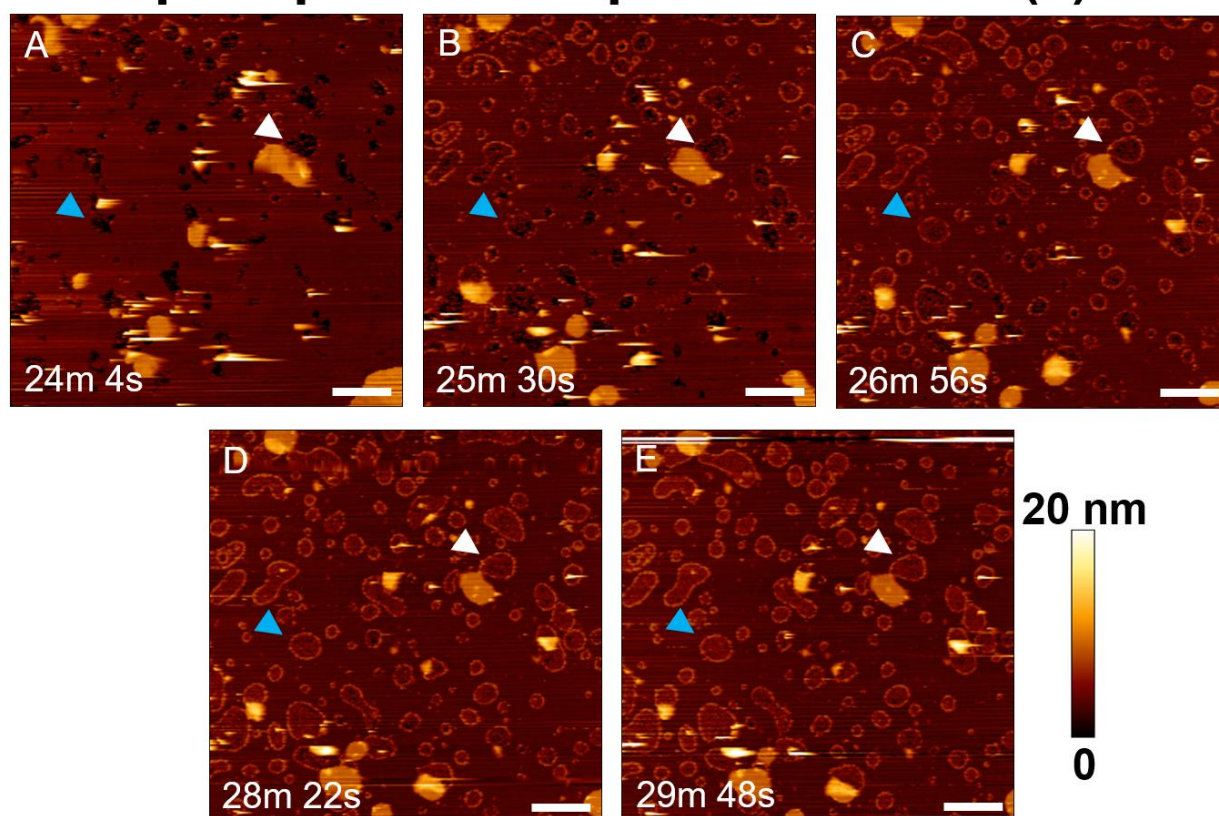


**Figure 3.38** AFM image with PLCHR2 with lipid bilayer in buffer on mica scanned for 24 to 30 minutes

**A-E.** Exemplary AFM images of DMPC lipid bilayer lysis by phospholipase enzyme during the second time window. The number in the lower left corner indicated the time after the enzyme was added. The

### 3. Results

scanned area was  $3.5\ \mu\text{m} \times 3.5\ \mu\text{m}$ . The horizontal scale bar was 500 nm. The vertical color scale bar (0-20 nm) indicated the height profile of the surface. The arrows (blue and white) tracked the hole closing.

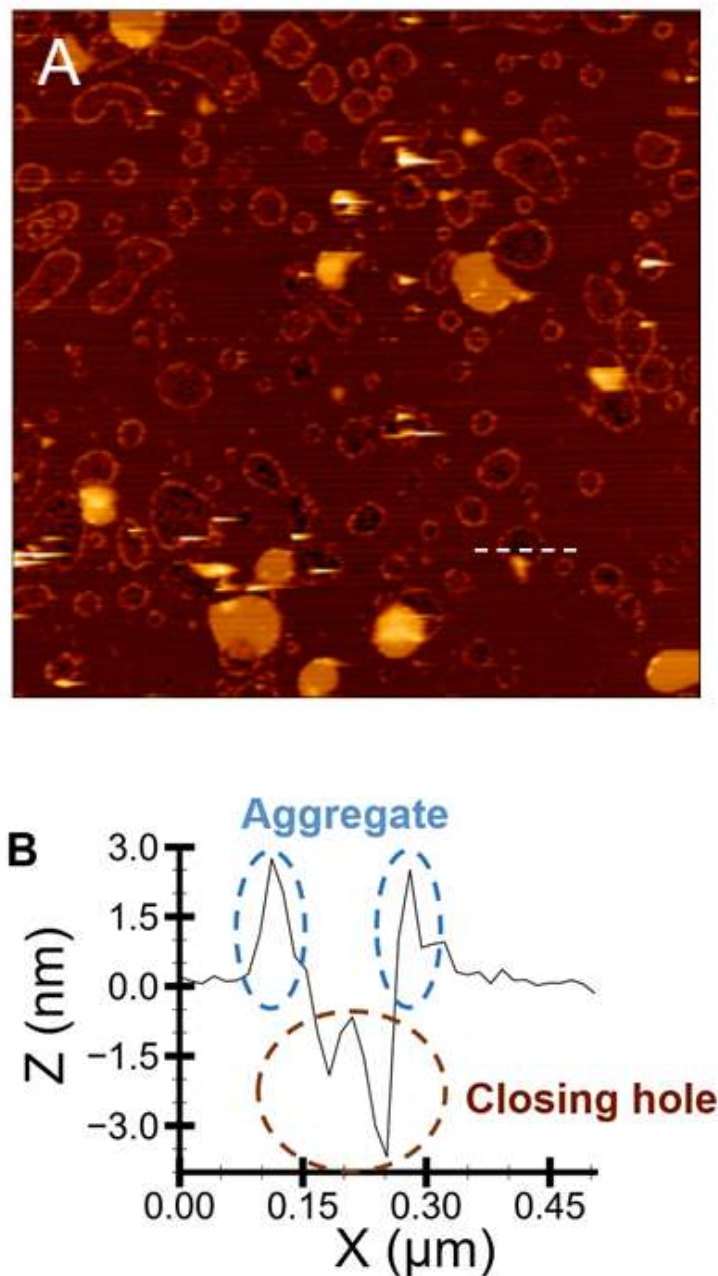


**Figure 3.39 Analysis of AFM image with PLCHR2 with lipid bilayer in buffer on mica after 30 minutes**

**A.** AFM image of DMPC lipid bilayer lysis by PLCHR2 at 26 minutes 56 seconds after the enzyme was added. This image was the same as Figure 3.37(C). **B.** The cross-section height profile of the white dashed line in (A). The brown dashed circle showed the profile of the closing hole, and the blue dashed circles showed the profile of the aggregates.

### 3. Results

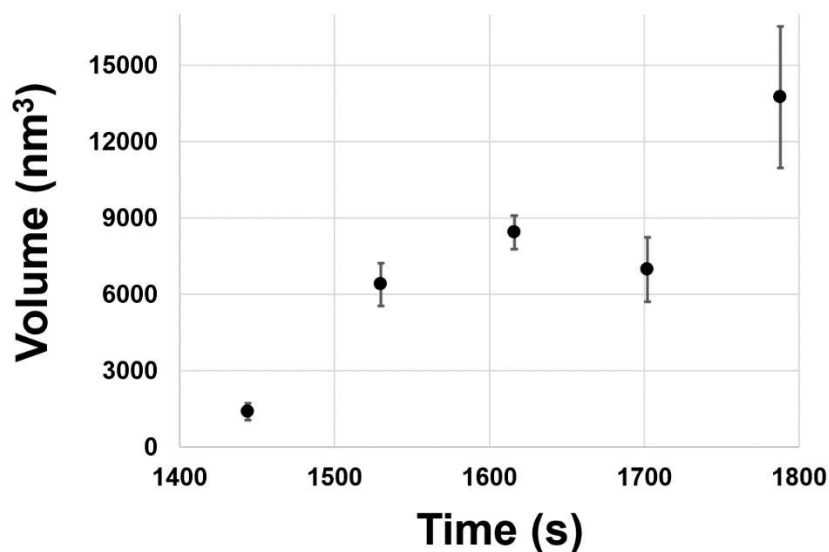
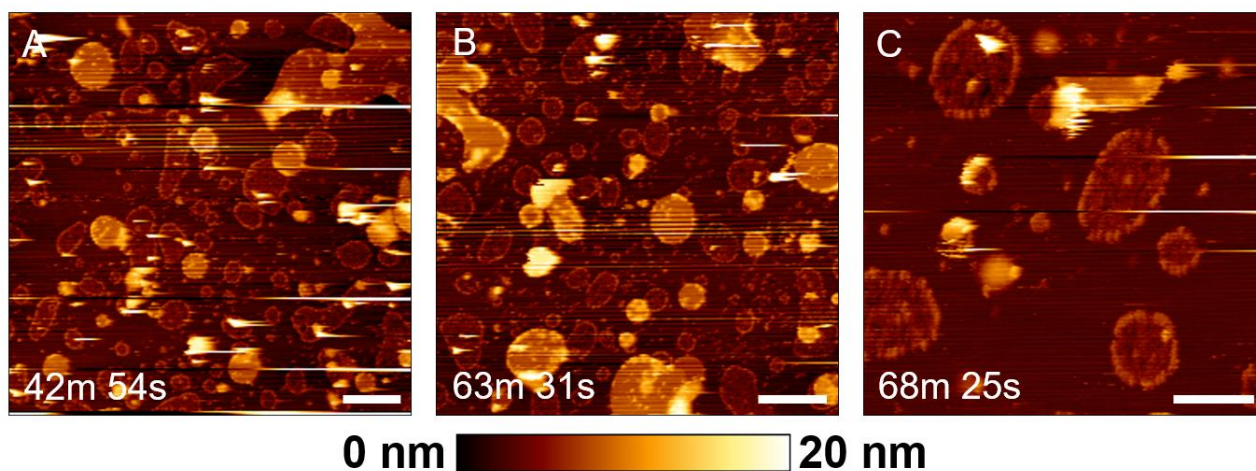


**Figure 3.40** The average volume of the ring-like structures at the top of the hole rims from 1444 s to 1788 s after the enzyme incubation.

During the final interval (30-68 minutes after the enzyme was added), we observed the completely closed holes indicated by the diminished hole depth (Figures 3.41 & 3.42). The closed holes and aggregates around the hole remained stable during the experiment period.

## Phospholipase with lipid membrane (3)



### 3. Results

**Figure 3.41. AFM image with PLCHR2 with lipid bilayer in buffer on mica scanned for 48 to 68 minutes**

**A-C.** Exemplary AFM images of DMPC lipid bilayer lysis by phospholipase enzyme during the third time window. The number in the lower left corner indicated the time after the enzyme was added. The horizontal scale bars were 500, 500, and 200 nm in A, B, and C, respectively. The vertical color scale bar (0-20 nm) indicated the height profile of the surface

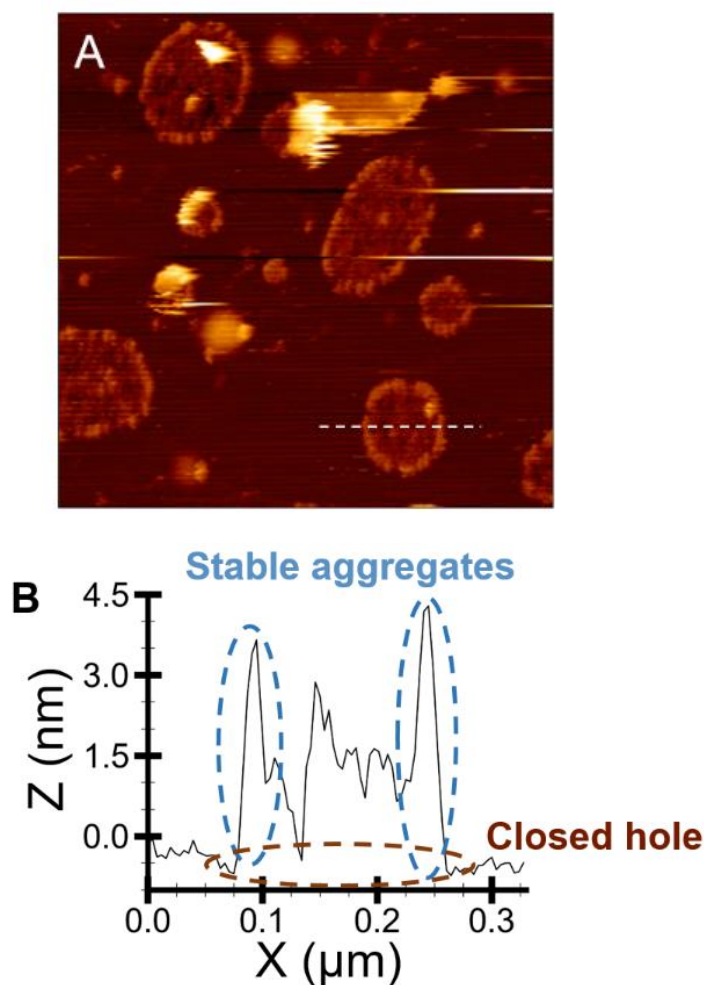


**Figure 3.42 Analysis of AFM image with PLCHR2 with lipid bilayer in buffer on mica after 1 hour**

**A.** AFM image of DMPC lipid bilayer lysis by PLCHR2 at 68 minutes 25 seconds after the enzyme was added. This image was the same as Figure 3.39(C). **B.** The cross-section height profile of the white dashed line in (A). The brown dashed circle showed the profile of the completely closed hole, and the blue dashed circles showed the profile of the stable aggregates

## 3.6 X-ray crystallography for PLCN

As explained in detail in section 2.8.1.1, both the proteins were used for setting crystallization experiments using several screening conditions.

### 3.6.1 Crystallization of PLCN

Several conditions such as I and II of the JCSG Core, Morpheus<sup>TM</sup> HT-96 and Morpheus<sup>TM</sup> II from Molecular Dimensions, screens from Qiagen, such as PEGs II suite, pH clear II, NeXtal PEG, NeXtal AmSO<sub>4</sub> suite were tested. Approximately 700 conditions were tested. After 14 days of the Morpheus<sup>TM</sup> II plate being set up, the initial needle crystals were observed. The conditions present in two wells that they appeared in were identical with regard to the composition of the buffer, the pH, and the precipitants; they differed only in the additives – trace amounts of compounds that may have a beneficial effect on crystallization by binding to the protein. (Table 3.7). The volumetric ratio of each drop that resulted in a successful hit was 2:1 (protein: precipitant). Figure 3.43 shows UV pictures collected to exclude the possibility of salt crystals. Next, the crystals were prepared for X-ray diffraction experiments. The needle shaped crystals were mounted using loops with a diameter of 0.1 to 0.2 millimeters, flash frozen in liquid nitrogen and then transferred to transport containers that were stored in liquid nitrogen. The crystals were tested for diffraction at the PETRA III P11 beamline. The maximum resolution that could be achieved with the needle crystals was 7 Å (Appendix IV). In order to achieve better resolution, crystal quality had to be increased.

More conditions with needle-like formations were seen on the Morpheus<sup>TM</sup> II plates after 10 to 14 weeks of incubation. The shape of these crystals ranged from large needles to smaller needle. Mounting these crystals was complicated this time due to a skin of denatured protein at the surface of the droplets. At the P11 beamline, only a few crystals diffracted, and the best crystal obtained diffracted at a resolution of 12 Å. For optimization, a crystallization screen (fine screen) was set up which varied the conditions under which the needles were obtained. Four plates, each with a constant pH condition and distinct conditions, were set up. The fine screen prepared with the Scorpion Screen Builder exhibited heavy precipitation immediately after plate setup. In every instance, the solubility of the protein showed to be most dependent on PEG 8000 concentration. In plates with experiments at pH 6, 6.5, and 6.8 199 of 288 drops precipitated immediately, whereas at pH 7, 216 of 288 drops precipitated immediately. In general, 10% (w/v) and 13% (w/v) PEG 8000 resulted in precipitation under all conditions, whereas 7% (w/v) PEG 8000 resulted in precipitation under 75% of conditions. At 7% (w/v) PEG 8000, only conditions containing both the additive mixtures i.e. alkaline mix and

### 3. Results

monosaccharides were exempt from precipitation. However, precipitation increased with the increase in the precipitant and 1, 5-Pentenediol concentration. At 4% (w/v) PEG 8000, conditions with both additive mixtures exhibited no immediate precipitation. Conditions with only alkali mix, monosaccharide mix, or no additives exhibited increasing precipitation with increasing drop ratio and 1, 5-Pentenediol concentration at 4% (w/v) PEG 8000. PEG screening was based on these findings. Precipitates or Spherulites were formed after 22h and developed over 13 days.

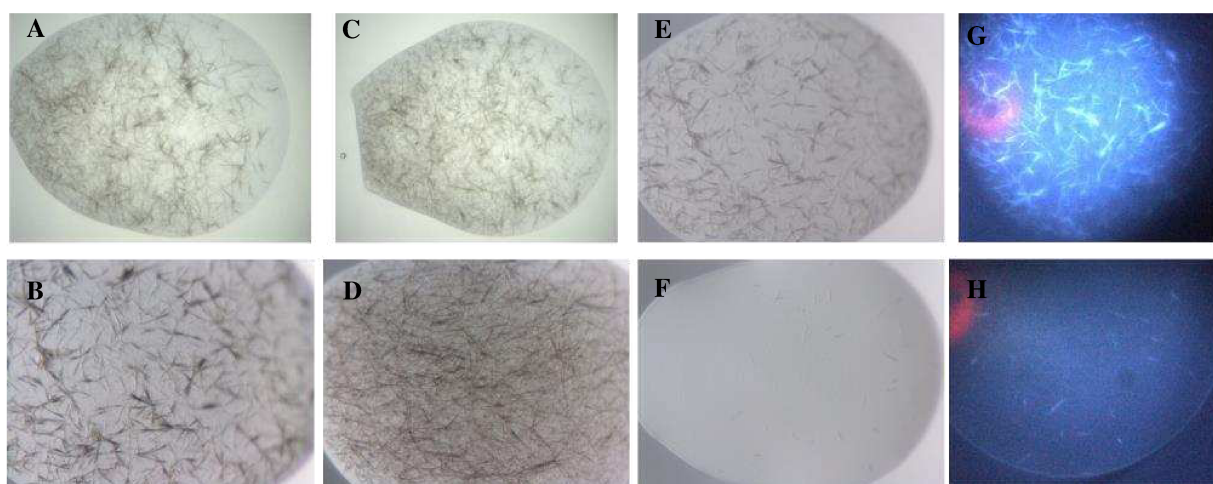


**Figure 3.43 Thin needle crystals of PLCN under visible (A-F) light and UV (G,H)**

The subsequent stage of experiments consisted of just lowering the protein concentration so that it was now 9 mg/ml rather than 12 mg/ml, and using the same fine screen in order to set up the crystallization plates. After a week, needle crystals were observed and now some of the needle crystals were a little bigger than the previous ones (Figure 3.44). However, the crystals did not diffract more than  $7\text{\AA}$ . (Appendix IV)

Following a number of iterations, the needle crystals did not show any signs of improvement; hence, an in situ proteolysis procedure was utilized. In this approach, the protease i.e. trypsin was added to remove the flexible region at the termini which might help in achieving a crystal with diffraction at better resolution (section 3.7.3).

3. Results

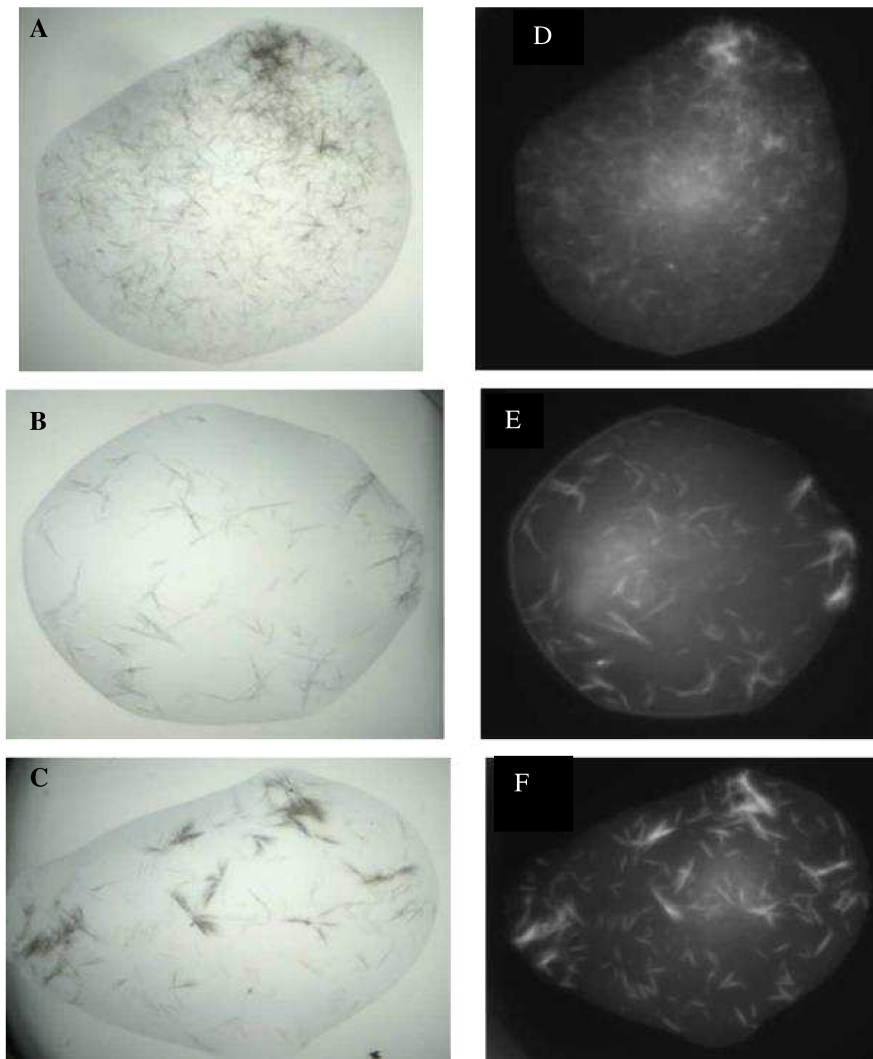


**Figure 3.44 Needle crystals of PLCN obtained after 10-14 weeks using fine screen under visible (A-F) light and UV (G,H)**

### 3. Results

**Table 3.7 Crystallization hits for initial crystallization screen and optimization steps.**

<b>Morpheus II</b>	<b>Precipitant</b>	<b>Cryoprotectant</b>	<b>Buffer system</b>	<b>Additive</b>
C3.1	10% PEG 8K	20% 1,5 Pentanediol	0,1M MOPSO/BisTris pH 6.5	1 mM Alkali mix
F3.1	10% PEG 8K	20% 1,5 Pentanediol	0,1M MOPSO/BisTris pH 6.5	20 mM Monosaccharide mix
H3.1	10% PEG 8K	20% 1,5 Pentanediol	0,1M MOPSO/BisTris pH 6.5	10 mM Polyamine
F2.1	12,5% PEG 4K	20% 1,2,6-Hexanetriol	0,1M MOPSO/BisTris pH 6.5	20 mM Monosaccharide mix
C2.1	12,5% PEG 4K	20% 1,2,6-Hexanetriol	0,1M MOPSO/BisTris pH 6.5	1 mM Alkali mix
G6.1	12.5%(w/v) PEG 4K	20% 1,2,6-hexanetriol	0,1M BES/TEA pH 7.5	20 mM AminoAcid Mix2
G7.1	10% PEG 8K	20% 1,5 Pentanediol	0,1M BES/TEA pH 7.5	20 mM AminoAcid Mix2
H7.1	10% PEG 8K	20% 1,5 Pentanediol	0,1M BES/TEA pH 7.5	10 mM Polyamine
G11.2	10% PEG 8K	20% 1,5 Pentanediol	0,1M GlyGly/AMPD pH 8.5	20 mM AminoAcid Mix2
Fine Screen I D7	13% (w/v)PEG 8K	11%1,5-Pentanediol	0,1 MMOPSO/BisTris pH 6.5	-
PEGs I	20% (w/v) PEG 3350	-	-	200 mM Calcium acetate
Fine screen pH 6.5 G2-G5	4% PEG 8K	14%,17%,23%1,5-Pentanediol	0,1 MMOPSO/BisTris pH 6.5	1 mM Alkali mix 20 mM Monosaccharide mix
Fine screen pH 6.8 G1-G6	4% PEG 8K	11%,14%,17%,20%,23%, 26% 1,5-Pentanediol	0,1 MMOPSO/BisTris pH 6.5	1 mM Alkali mix 20 mM Monosaccharide mix

### 3. Results

#### 3.6.2 Crystallization of PLCN with trypsin

The next step, in-situ proteolysis, was carried out with the goal of improving the needle crystals (section 3.7.1). Cleaving off the flexible regions of the protein was anticipated to be another way to achieve a more stable form of the protein that would crystallize faster and more effectively.

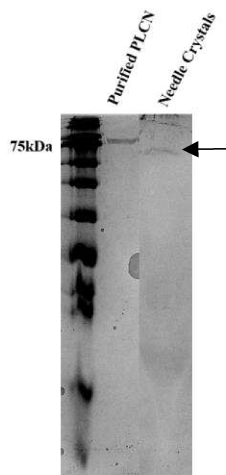


**Figure 3.45 SDS PAGE of PLCN in solution and PLCN as a crystal**

Purified PLCN runs at a molecular weight of 79kDa and the needle crystals were running at lower than 75kDa showing degradation while incubation for crystallization.

For the purpose of these tests, the same fine screen as where the initial needle crystals appear was used. The protein to trypsin ratio was varied from 1:800, and 1:1200. In these experiments as well, 9 mg/ml of protein was utilized. Both a 1:1 and a 1:2 ratio of protein to precipitant were used in the experiment, and the protein and trypsin were mixed together right before setting up the experiments. The plate were incubated at 19°C. The Figure 3.46 displays two crystals obtained through this screening at 1:1200 ratio. The following are the conditions : 11%1,5, pentadiol, 0.1M BisTris/MOPSO pH 6.5, 7%PEG 8000, 0.001M alkali mix and 11%1,5, pentadiol, 0.1M BisTris/MOPSO pH 6.5, 7%PEG 8000. Both crystals diffracted at around 1.5Å. Since the condition already contained 11% 1,5 pentadiol, therefore a similar solution with 20% 1,5, pentadiol was used as a Cryo protectant was used. The molecular structure of PLCN was finally deduced with the help of the second crystal (Figure 3.47).

### 3. Results

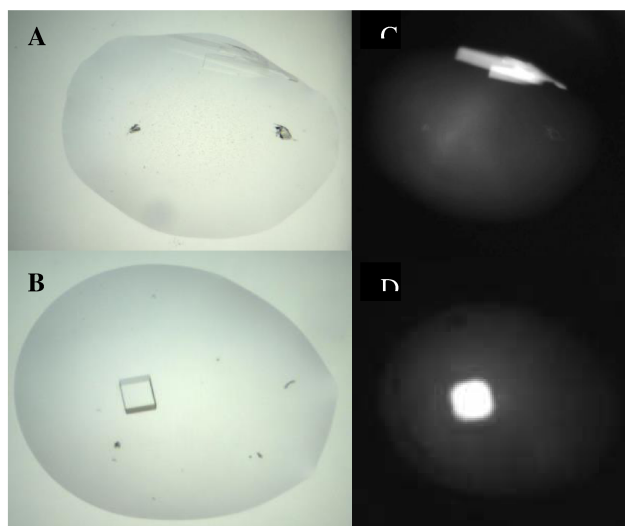


**Figure 3.46** PLCN crystals obtained after 15 days of incubation under visible (A, B) and UV light (C, D)

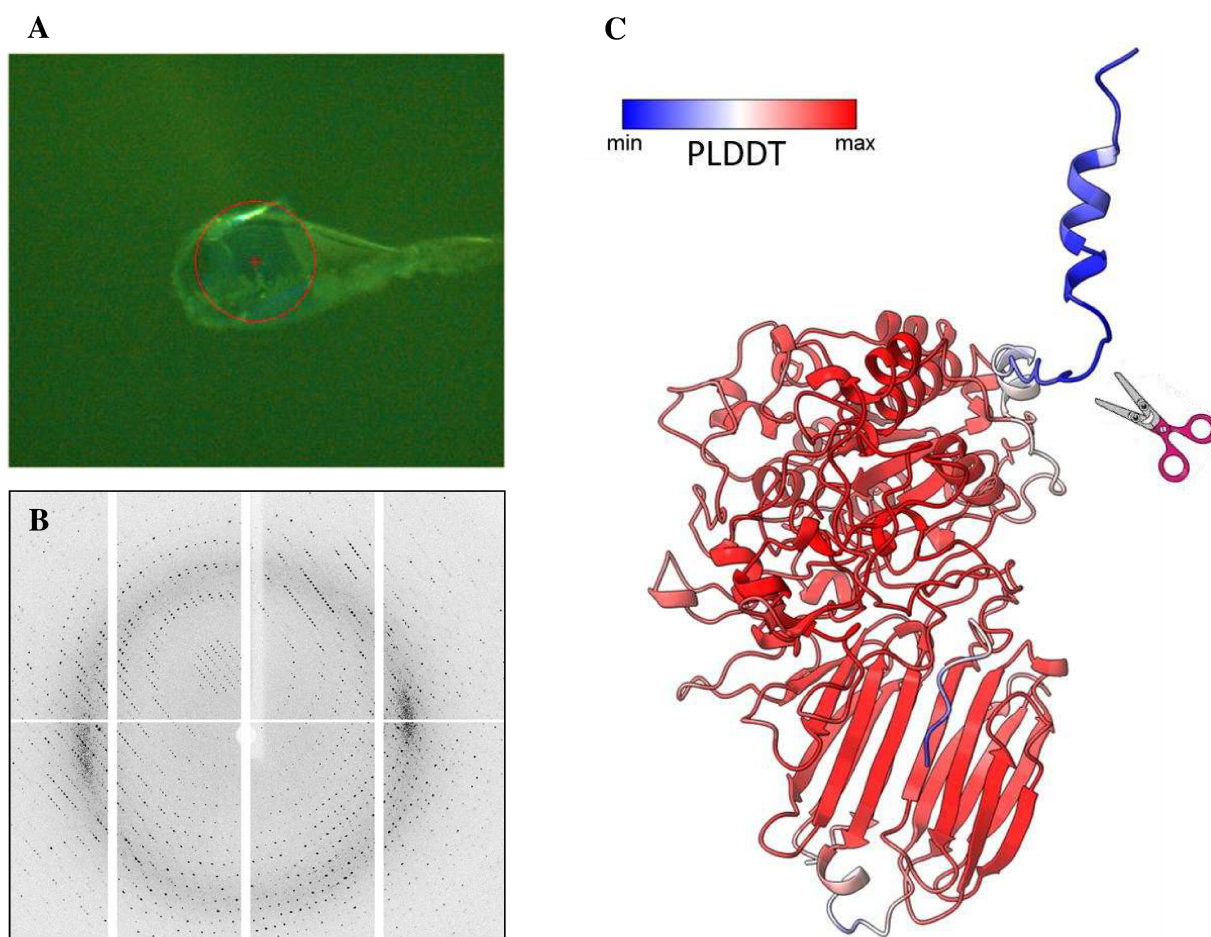


**Figure 3.47** Data processing of PLCN crystal

A. PLCN crystal in a 0.5mm loop used for diffraction, B. Diffraction pattern obtained at 1.5Å resolution, C. Alpha fold model used as a search model for Molecular replacement

#### 3.6.3 Data Processing and model building

The crystals were diffracted at the Petra P11 beamline at DESY, Hamburg. The crystal belonged to the monoclinic space group P1 21 1 with unit cell dimensions of  $a = 61.27\text{\AA}$ ,  $b = 110.43$ ,  $c = 98.610$  (appendix IV). The solvent content was calculated to be 31.74%. The data was merged and scaled using XDS.

The novel phospholipases from *Pseudomonas aeruginosa* are distinct from existing phospholipases, a 3-D structural homology search using the program DALI160 showed that PLCs have significant sequence similarity with any other phospholipases. The acid phosphatase A (AcpA), an enzyme from *Francisella tularensis*<sup>25</sup>, which hydrolyzes phosphate monoester, showed the closest sequence similarity (Fig. 2). The molecular replacement was carried using an alpha fold model in MOLREP129. For the search model, a truncated version of the alpha fold model, without all the N-terminal part (start of the model sequence: NLKDVEHV). Furthermore, some parts of the model with low expected accuracy were removed. The used search model contained 644 of the 712 amino acids of the target molecule. Apart from this, some parts with low accuracy, were flexible, or that resulted in clashes during the 1st run of molecular replacement were also cleaved off. After a model oriented and paced by Molecular replacement, the refinement was performed using a phenix.refine. The refinement statistics can be found in Table 3.8.

The asymmetric unit contains two molecules of PLCN, in other words a crystallographic dimer. The PLCN protein consists of two domains: - the N-terminal domain and the C terminal domain. The N-terminal domain is primarily composed of alpha-helical structure, while the other domain is dominated by beta sheets. The approximate measurements of one molecule are  $60\text{\AA} \times 48\text{\AA} \times 66\text{\AA}$ . the structure is comprised of the following elements: 7 sheets, 2 beta alpha beta units, 8 beta hairpins, 1 psi loop, 3 beta bulges, 29 strands, 26 helices, 21 helix-helix interactions, 53 beta turn, and 4 gamma turn (see pic). Only 643 of the 712 residues that make up the PLCN could be modeled since trypsin digestion removed some of the residues. The first 63 residues from the N- terminal were probably cleaved off by trypsin. A 7 residue loop (643-649 residues) in the C terminal domain could also not be modeled because of poor or missing density. There are a total of three cysteine residues, but no disulfide linkages. Proper 2-fold symmetry can be seen in the two molecules of the asymmetric unit, hydrogen bonds as well as in some of the noncontact bonds.

Both molecules in the asymmetric unit were found to have a phosphorylated Threonine 176, which is acknowledged as part of the active site. In close proximity to the phosphorylated

### 3. Results

threonine was a cation, which according to the electron density was modeled as a calcium. Calcium was selected after testing several cations that could fit in the electron density. Temperature and occupancy refinements were also performed to confirm the calcium ion at the active site. In the vicinity of the active site, there was also a density of an unknown type. This was modeled as either calcium ion or  $\beta$ -mercaptoethanol (BME) - since it was present in the purification buffers. The  $R_{work}$  and  $R_{free}$  values were same in both models, regardless of whether calcium or BME was modeled.

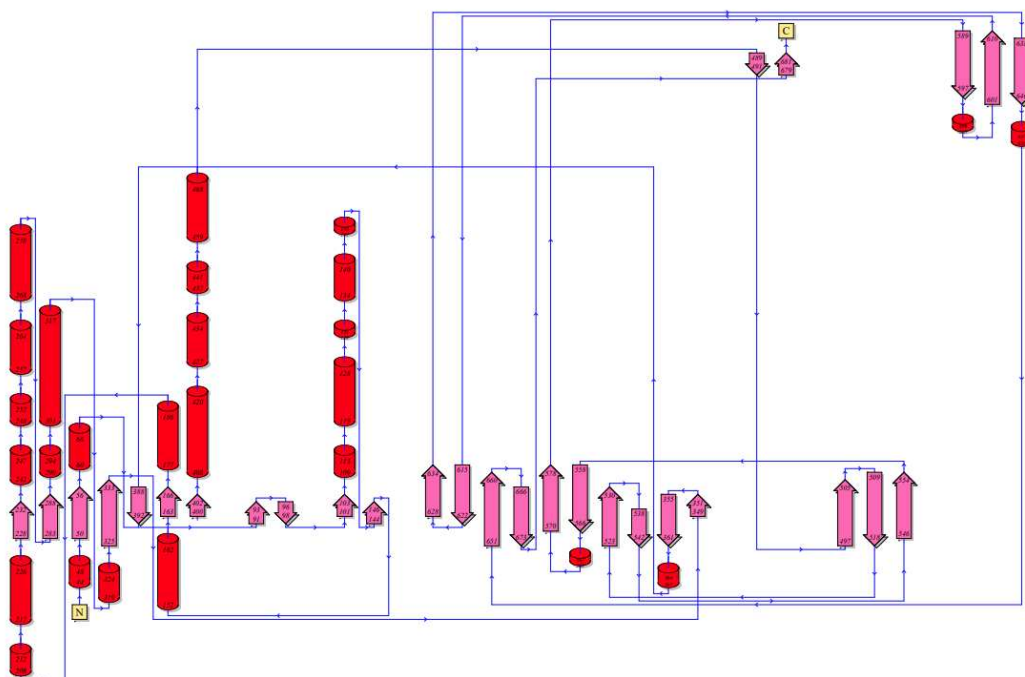


**Figure 3.48** Topology and secondary structure content of PLCN

### 3. Results

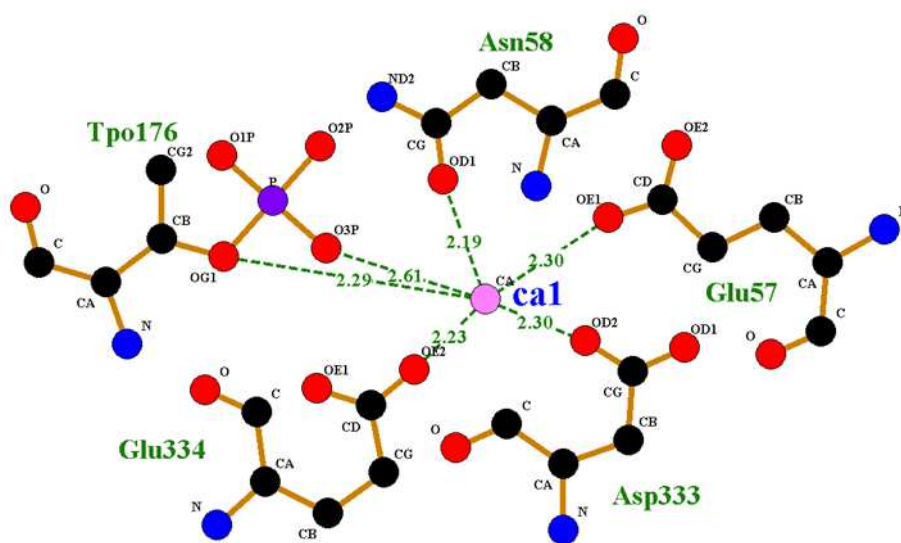


**Figure 3.49** Coordination of calcium ion present in the active site of PLCN

**Table 3.8** Data collection and refinement statistics for a PLCN crystal

(Values for the outer resolution shell of data are given in parentheses)

	PLCN_BME	PLCN_Ca
Wavelength	1.033	1.033
Resolution range	44.33 - 1.57 (1.626 - 1.57)	44.33 - 1.57 (1.626 - 1.57)
Space group	P 1 21 1	P 1 21 1
Unit cell a, b, c $\alpha, \beta, \gamma$	61.27 110.432 98.619 90 101.028 90	61.27 110.432 98.619 90 101.028 90
Total reflections	1175850 (117710)	1175850 (117710)
Unique reflections	170201 (16915)	170201 (16915)
Multiplicity	6.9 (7.0)	6.9 (7.0)
Completeness (%)	95.03 (94.87)	95.03 (94.87)
Mean I/sigma(I)	20.20 (2.08)	20.20 (2.08)
Wilson B-factor	20.13	20.13
R-merge	0.0524 (0.8219)	0.05241 (0.8219)
R-meas	0.0567 (0.8879)	0.05669 (0.8879)
R-pim	0.0214 (0.3332)	0.02143 (0.3332)
CC1/2	1 (0.847)	1 (0.847)
CC*	1 (0.958)	1 (0.958)
Reflections used in refinement	170197 (16915)	170197 (16915)
Reflections used for R-free	8509 (844)	8509 (844)
R-work	0.1434 (0.2355)	0.1435 (0.2355)
R-free	0.1686 (0.2529)	0.1684 (0.2522)
CC(work)	0.961 (0.687)	0.961 (0.688)

### 3. Results

CC(free)	0.947 (0.665)	0.947 (0.667)
Number of non-hydrogen atoms	11408	11405
macromolecules	10223	10223
ligands	22	4
solvent	1175	1178
Protein residues	1291	1291
RMS(bonds)	0.008	0.008
RMS(angles)	1.00	0.99
Ramachandran favored (%)	97.18	97.18
Ramachandran allowed (%)	2.66	2.66
Ramachandran outliers (%)	0.16	0.16
Rotamer outliers (%)	0.47	0.47
Clashscore	1.84	1.55
Average B-factor	24.87	24.89
macromolecules	24.07	24.11
ligands	26.26	22.20
solvent	31.80	31.74
Number of TLS groups	1	1

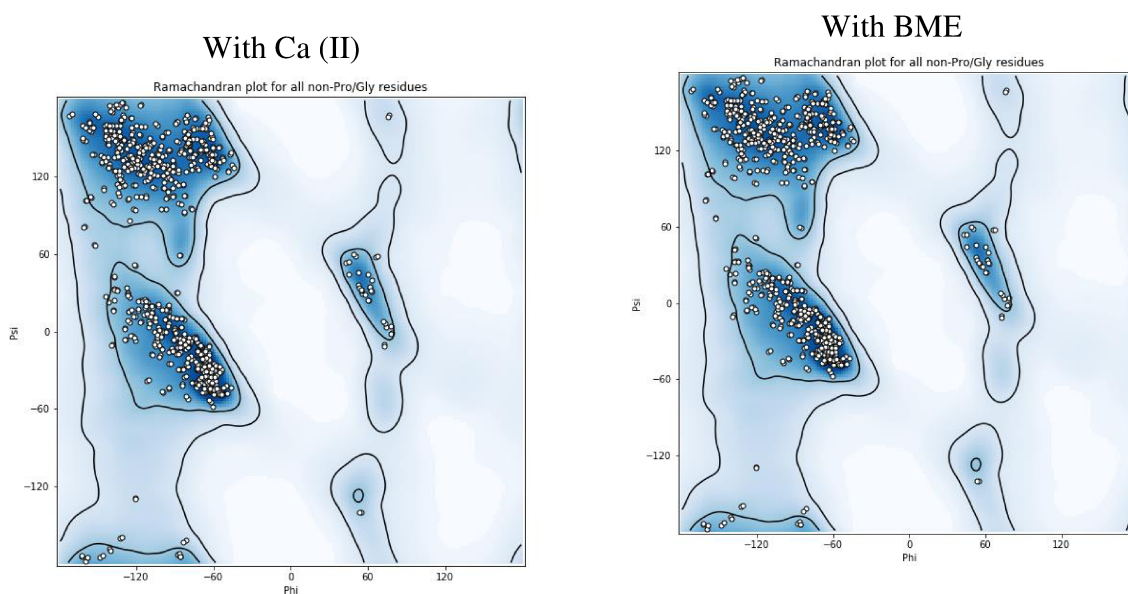


**Figure 3.50** Ramachandran plot obtained after phenix refine with calcium and  $\beta$ -mercaptoethanol.

### 3. Results

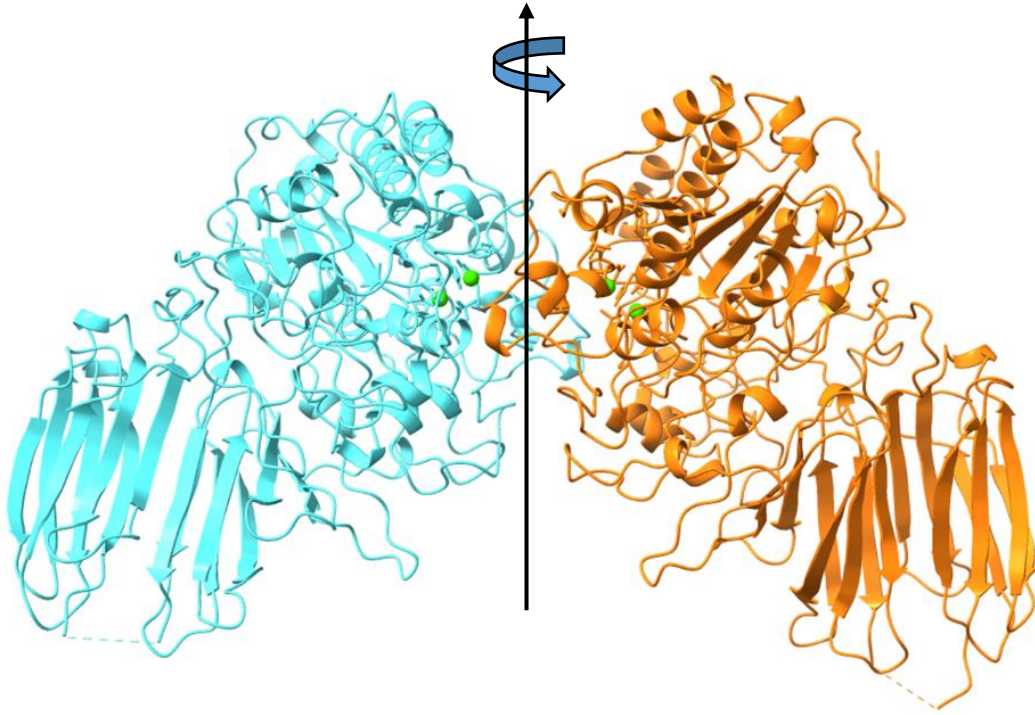
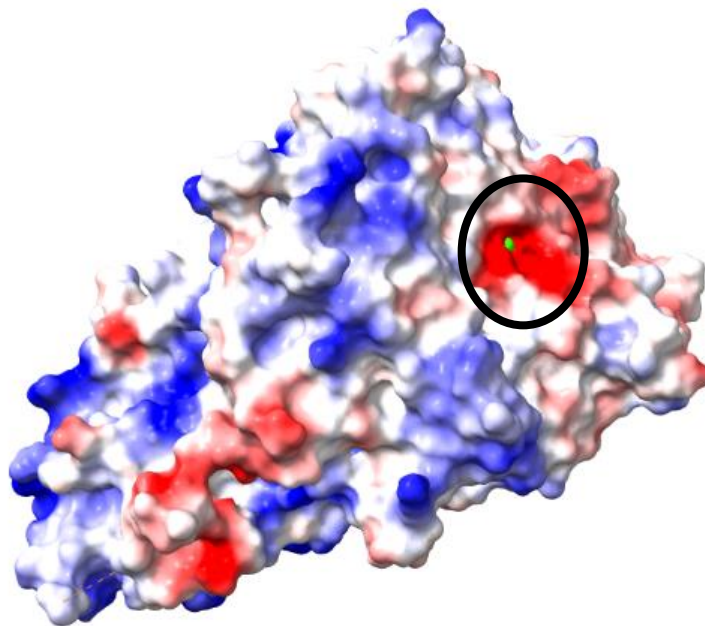


**Figure 3.51** Dimeric structure of PLCN, the arrow denotes the non-crystallographic molecular 2-fold symmetry axis

**A**



### 3. Results

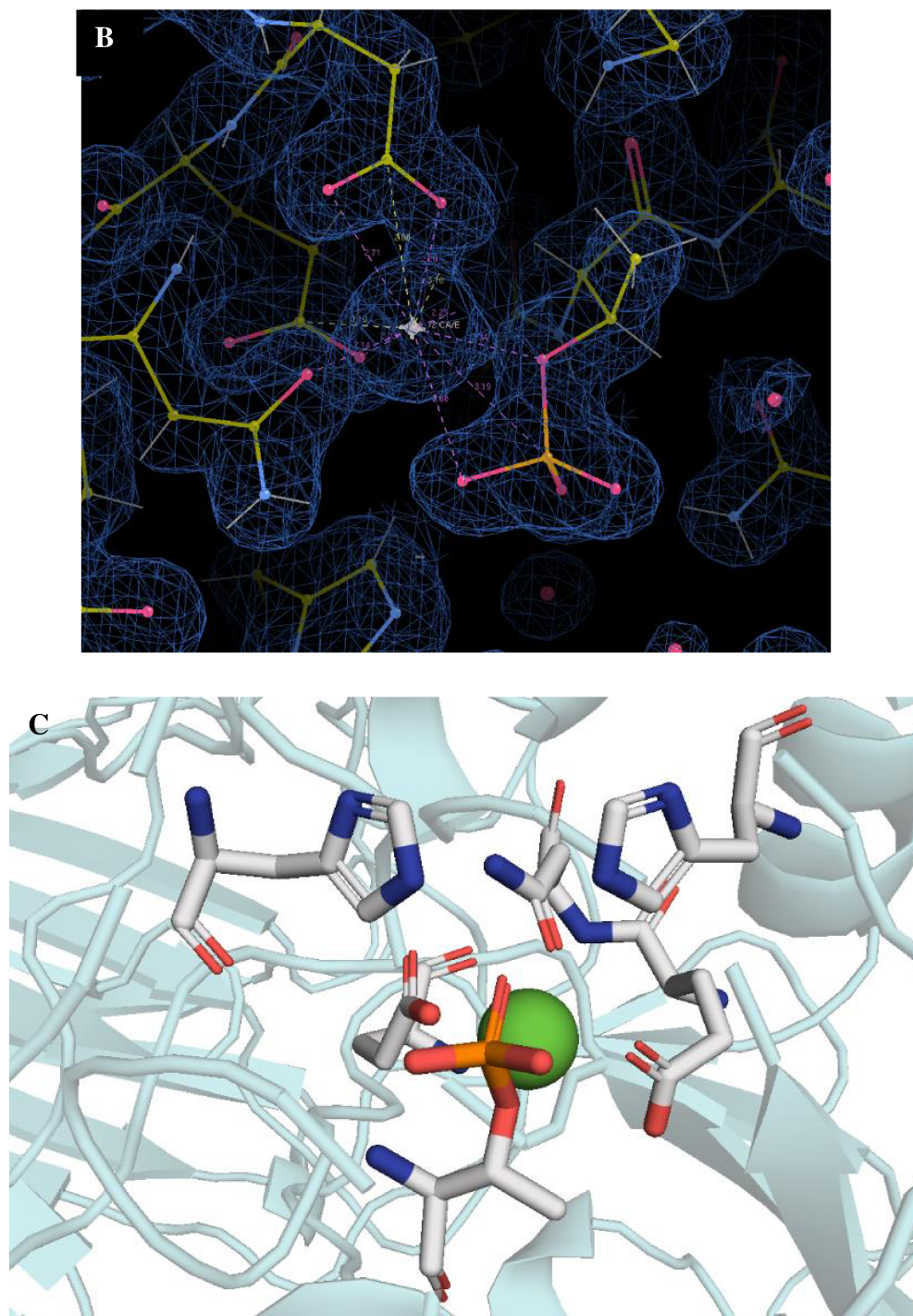


**Figure 3.52 Active site of PLCN**

A. Electrostatic surface of PLCN colored in terms of electrostatic potential, displayed in a scale from red (-) to blue (+), **B.** stereographic drawing of the PLCN metal center covered by electron density map. **C.** Key residues (T176 -linked phosphate and Ca<sup>2+</sup>) involved in substrate hydrolysis



### 3.7 Electron Microscopy for PLCHR

#### 3.7.1 Mono-dispersed particles in Negative staining

Many attempts were made to crystallize the PLCHR2 complex, but it could not be crystallized. Due to the PLCHR2 complex's size, which was just above the Cryo-EM threshold at 103kDa, Cryo electron microscopy was chosen to solve the 3-D structure. For a first step, the suitability of the sample was analyzed by negative staining. It helped in determining the appropriate protein concentration for the Cryo electron microscopy and to monitor the homogeneity of the particles. The TEM micrographs shown in the Figure 3.54A consists of monodispersed particles that have been negatively stained with 1% uranyl acetate, Figure 3.54B is the negative stain of the buffer as a control.

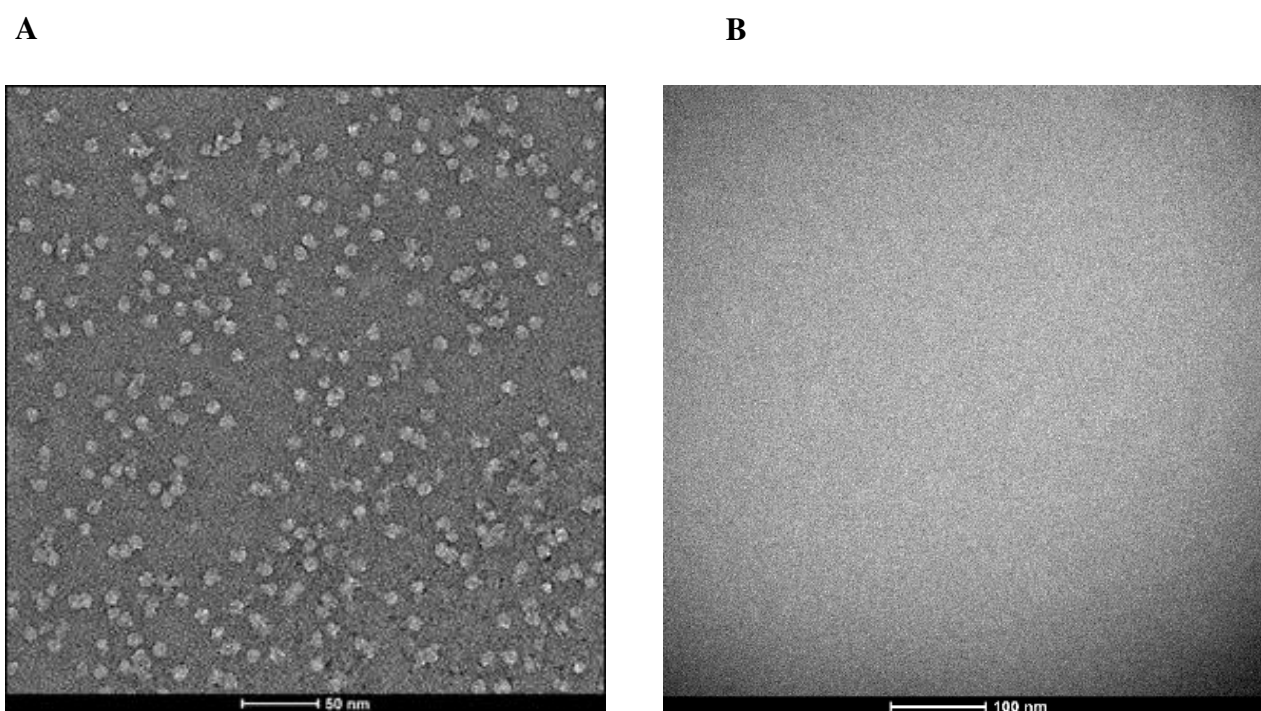


**Figure 3.54 Micrographs negatively stained with 1% uranyl acetate showing monodispersed particles (A) using buffer (B) as a control**

#### 3.7.2 Cryo-EM data processing at 0°, 30°, 45°

PLCHR2 complex was used for the Cryo EM approach. Predominant percentage of the particles had the shape of a horseshoe. Following the processing of the data, it was discovered that the micrograph had three distinct forms of oligomeric species: a trimer, a dimer, and a monomer. The most abundant form was a trimer, followed by monomers and then dimers. Data were

### 3. Results

processed differently depending on whether it was going to be used for the reconstruction of a monomer map or a trimer map.

#### **Cryo-EM data processing – Trimer**

Frames were aligned using the Relion 4.01<sup>162,185</sup> implementation of Motioncor2<sup>186</sup> with the dose-weighting procedure and a b-factor value of 150. Particles were picked using Cryolo 1.8.4<sup>187</sup> with the general Phosaurus model trained for low-pass filtered images (cutoff 0.1, confidence threshold 0.1, minimal particle distance 90 pixels). Defocus values were estimated with Gctf 1.06<sup>188</sup> using the per-particle local refinement. For each dataset two or three rounds of 2D-classification were performed with Relion. After each round, the particles belonging to noisy classes were removed. Particles belonging to trimeric classes were then merged to obtain a set of 2,824,689 particles. These particles were then subjected to 3D-classification with Relion, resulting in three classes: one class showing a more open horseshoe conformation (1,030,594 particles), one class with a more closed conformation (723,933 particles), and the third class generating a noisy reconstruction. We then imported the particles belonging to the first two classes into CryoSPARC 4.2.1<sup>189,190</sup> and used the ab-initio reconstruction task to obtain two maps that we used as reference for non-uniform refinement (non-default parameters: Optimize per-particle defocus, Optimize per-group CTF params, Initial lowpass resolution 15 Å), which produced two reconstructions at 3.08 Å and 3.07 Å resolution, respectively, as determined by the gold-standard procedure with FSC threshold 0.143. The two maps were finally post-processed with DeepEMhancer version 0.15.0<sup>191</sup> using the tight target model. No symmetry constraints were imposed during the processing

#### **Cryo-EM data processing – Monomer**

Cryo-EM data were processed using cryoSPARC v3, and the procedure is outlined in Figure 3.55. In brief, dose-fractionated movies were subjected to Patch motion correction and Patch CTF estimation. Particles from one micrograph were then manually picked using Blob picker followed by blob tuner. Picked particles were then cured and extracted with 256 pix with a binning factor of 2. Junk particles were removed through iterative 2D classifications. The particles from classes with clear secondary structure features were selected and served as a template picker for the whole dataset. Movies collected from 0, 30 and 45 degree were processed separately before pooling all the selected particles from 2D classification together for Ab-initio reconstruction. Ab-initio reconstruction was performed with 3 classes, a maximum resolution of 5 angstroms, an initial resolution of 7 angstroms, initial minibatch size of 300 and

### 3. Results

final minibatch size of 1000 while keeping Correct for per-micrograph optimal scales and compute per-image optimal scales functions switching on. The best class was directly subjected to non uniform refinement<sup>190</sup> with an initial low pass resolution of 15 Å by employing the functions such as the Minimize over per-particle scale, Optimize per-particle defocus and Optimize per-group CTF functions. The overall resolution was estimated in CryoSPARCv3 using the FSC = 0.143 cutoff. Local resolution estimations were also calculated using the 0.5 FSC cutoff. The two half maps were used as inputs to assess various post-processing strategies such as the CryoSPARC's sharpening tool, DeepEMhancer<sup>191</sup>, and Resolve\_cryo-em<sup>192</sup>, LocScale<sup>193</sup>. The map with best interpretability was chosen for atomic-model refinement.

The initial models were generated using AlphaFold2, and refined against the experimental maps iteratively with Coot<sup>158</sup> and Phenix<sup>194</sup>. The monomer map had a resolution of around 3.5Å at FSC = 0.143 cutoff and 3.8Å at 0.5FSC cutoff. The resolution obtained using CryoEM for PLCH was much lesser than the crystal structure of PLCN (1.5 Å). Hence, some of the regions, which were at the surface of the protein, were built with the help of the trimer map. Table 3.9 shows the structure statistics obtained by refining the monomer using real space refine in Phenix.

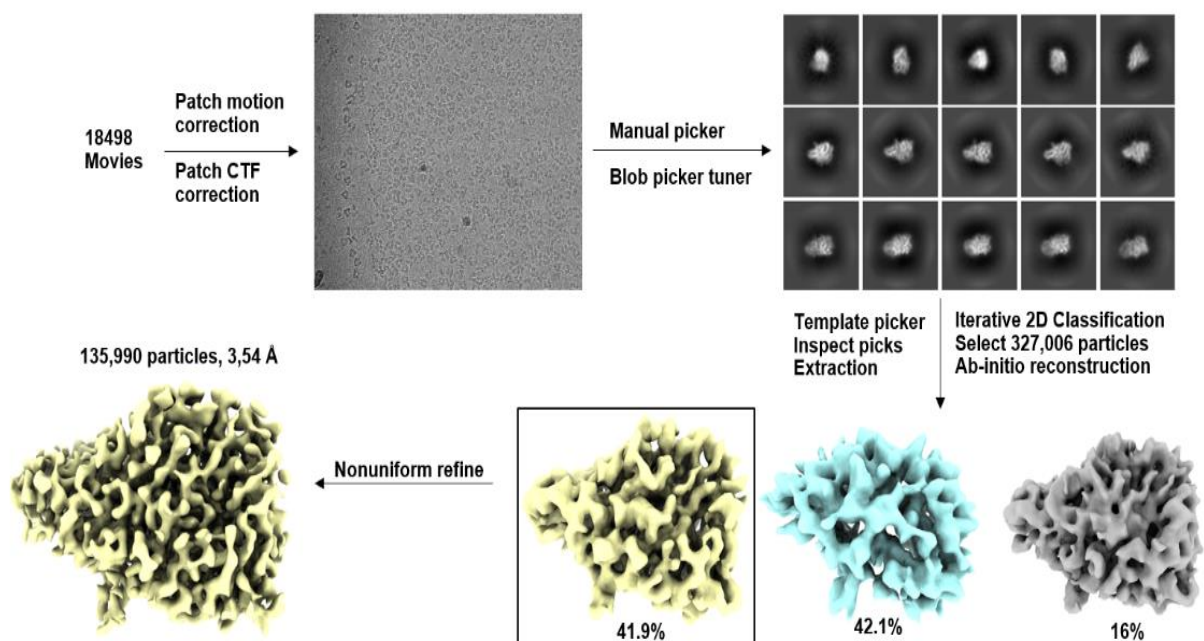


**Figure 3.55 Cryo-EM processing of monomeric PLCH A. Workflow of single-particle cryo-EM analysis;**

### 3. Results

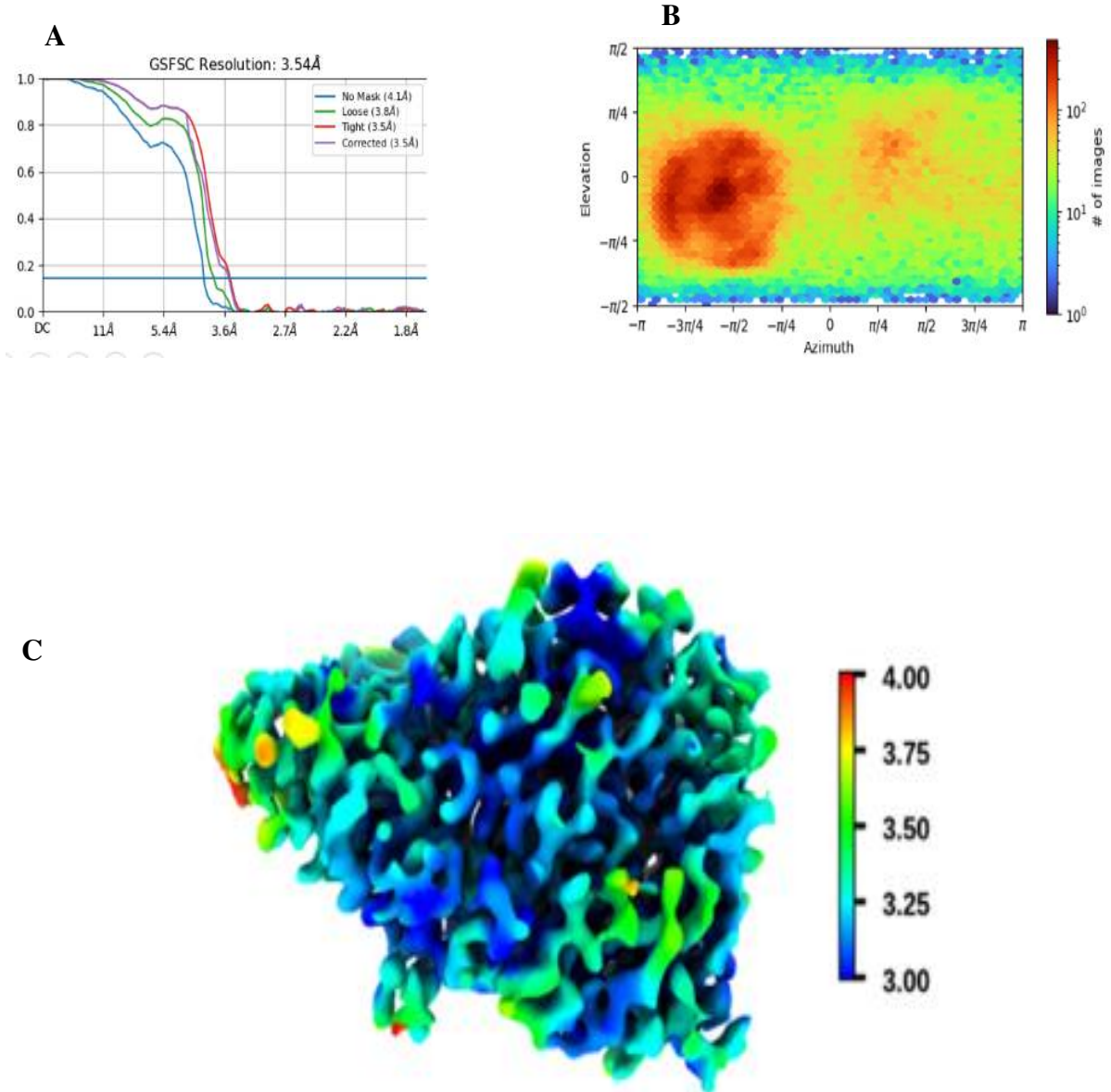


**Figure 3.56 CryoEM data processing of monomeric PLCH**

**A.** FSC curves indicating a resolution of 3.54 Å (FSC 0.143). **B.** Angular distribution heat map of particle projections for monomeric Pseudomonas Phospholipase reconstruction; **C.** Final globally refined maps colored by local resolution (FSC 0.5).

### 3. Results

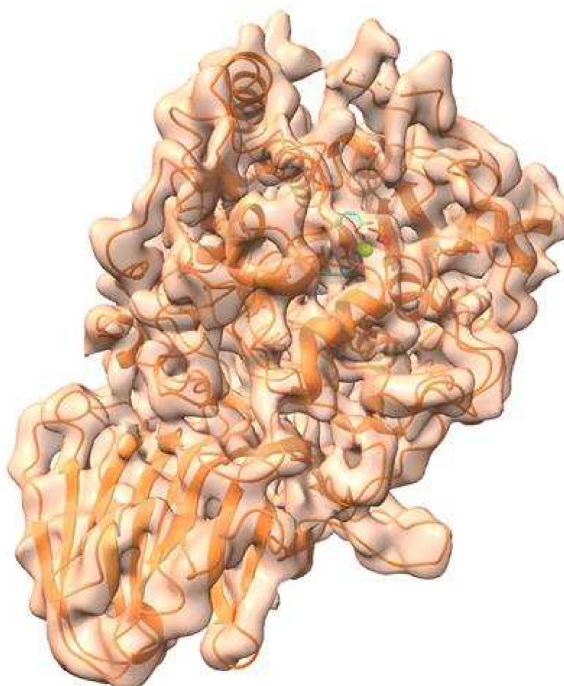


**Figure 3.57 PLCH alpha fold model fitted into the map structure by CryoEM**

The resolution obtained from the CryoEM structure for monomeric PLCH is 3.54 Å (FSC 0.143)

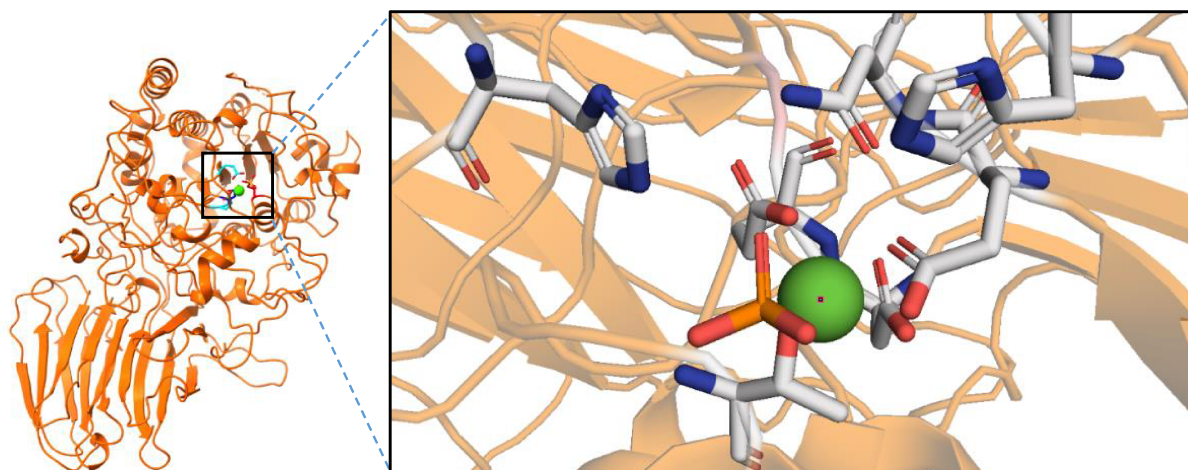


**Figure 3.58 Active center of PLCH**

A. 3D structure of PLCH Monomer, B. Key residues (T176 -linked phosphate and Ca<sup>2+</sup>) involved in substrate hydrolysis

### 3. Results

In the case of the trimer model, the 2D class averaging generated two distinct classes (Figure 3. 60). Class 1 appears to be more open, whereas class 2 seems to be more closed. Both classes were used for separate ab-initio reconstruction. Both of these classes have their subunits organized in a head-to-tail manner, which means that the N terminal interacts with the C terminal of the other subunit. Despite the fact that the PLCHR2 complex was used to prepare the samples for Cryo EM, all that we observe in the micrographs generated by microscope was PLCH, which seems to lack any density of PLCHR2 coupled to it. CryoEM reconstruction shows that the PLCH exists in all three forms (trimer, dimer, and monomer) without its chaperon. However, SAXS and other experimental data show that the PLCHR2 binds to the PLCH to form a complex. This could be because of several reasons. It could be possible that since we see also higher oligomers in the EM micrographs so the formation of these oligomers lead to the falling off the chaperon. Additionally, the PLCHR2 chaperon might be too flexible hence; we did not observe any density for it.

The structure that was obtained for PLCN is quite similar to the structure that was obtained for PLCH. Both include two domains, with one being an N terminal domain and the other being a C terminal domain. 6 sheets, 2 beta alpha beta units, 8 beta hairpins, 1 psi loop, 3 beta bulges, 25 strands, 21 helices, 23 helix-helix interactions, 61 beta turns, and 8 gamma turns are all components of the secondary structure that is present in PLCH monomer. Only 685 of the protein's 644 residues were modeled since the first 58 residues of the N-terminal domain did not have any electron density, probably because of the flexibility of this region.

**Table 3.9 Cryo-EM structure refinement statistics for PLCH monomer.**

<b>Model</b>	
=====	
<b>Composition (#)</b>	
Chains	2
Atoms	5393 (Hydrogens: 0)
Residues	Protein: 674 Nucleotide: 0
Water	0
Ligands	CA: 1
<b>Bonds (RMSD)</b>	
Length (Å) (# > 4)	0.003 (0)
Angles (°) (# > 4)	0.580 (0)
MolProbity score	1.95
Clash score	13.85
<b>Ramachandran plot (%)</b>	
Outliers	0.15

### 3. Results

Allowed	4.20
Favored	95.65
<b>Rama-Z (Ramachandran plot Z-score, RMSD)</b>	
whole (N = 667)	-0.25 (0.33)
helix (N = 129)	1.33 (0.49)
sheet (N = 155)	-0.25 (0.42)
loop (NE = 383)	-0.62 (0.32)
Rotamer outliers (%)	0.18
C $\beta$ outliers (%)	0.00
Peptide plane (%)	
Cis proline/general	0.0/0.2
Twisted proline/general	0.0/0.0
CaBLAM outliers (%)	2.85
ADP (B-factors)	
Iso/Aniso (#)	5393/0
min/max/mean	
Protein	153.99/260.22/183.30
Nucleotide	---
Ligand	209.00/209.00/209.00
Water	---
Occupancy	
Mean	1.00
occ = 1 (%)	100.00
0 < occ < 1 (%)	0.00
occ > 1 (%)	0.00

<b>Data</b>		
<b>Box</b>		
Lengths (A)	68.00, 72.25, 98.60	
Angles (")	90.00, 90.00, 90.00	
Supplied Resolution (A)	3.5	
Resolution Estimates (A) Unmasked	Masked	Unmasked
d FSC (half maps: 0.143)	---	'---
d 99 (full/half1/half2)	4.5/---/---	4.5/---/---
d model	4.1	4.1
d FSC model (0/0.143/0.5)	3.2/3.5/4.0	3.4/3.6/4.1
Map min/max/mean	-0.12/0.36/0.01	
<b>Model vs. Data</b>		
=====		
CC (mask)	0.82	

### 3. Results

CC (box)	0.9
CC (peaks)	0.76
CC (volume)	0.82
Mean CC for ligands	0.87

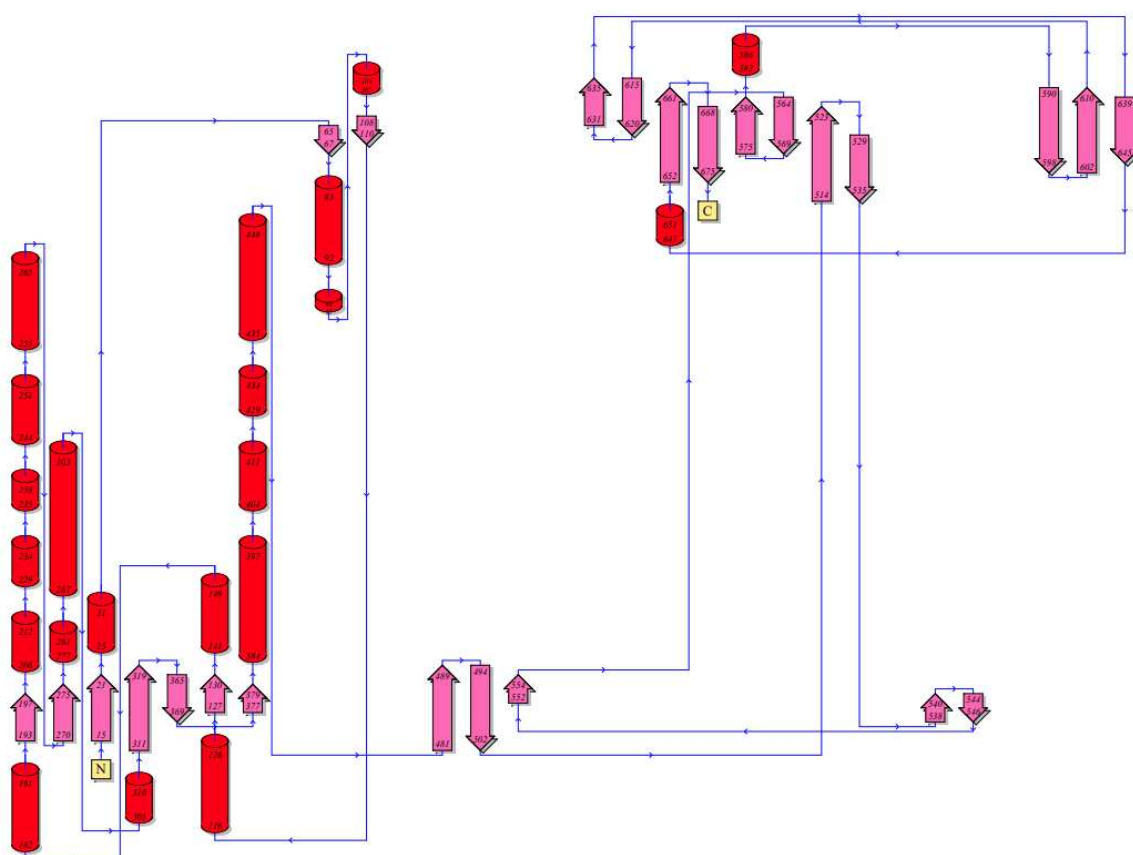


**Figure 3.59** Topology and secondary structure content of PLCH monomer

### 3. Results

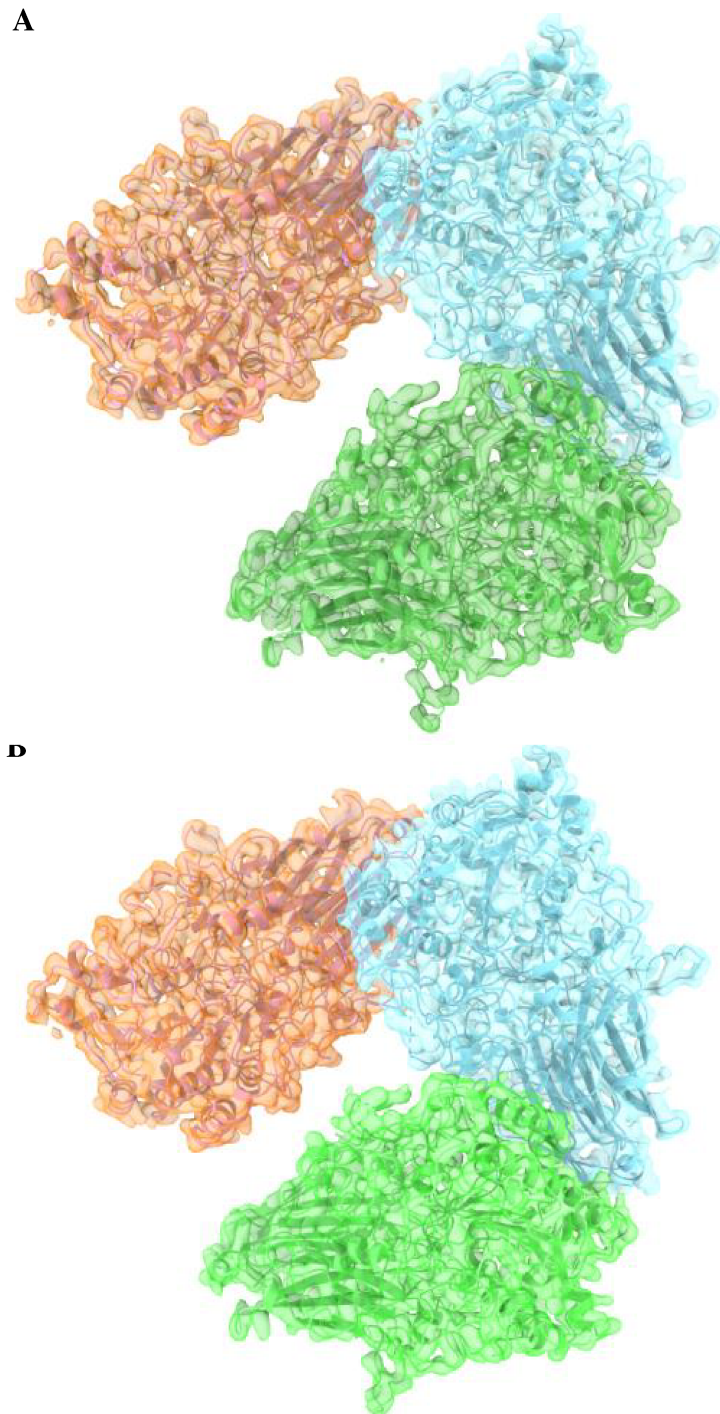


**Figure 3.60 Two classes of PLCH Trimer obtained from CryoEM data processing,**

Two classes drawn in ribbon representation and covered with a semi-transparent molecular surface. A. Class 1 (wide space), B. Class 2 (narrow space)

### 3. Results

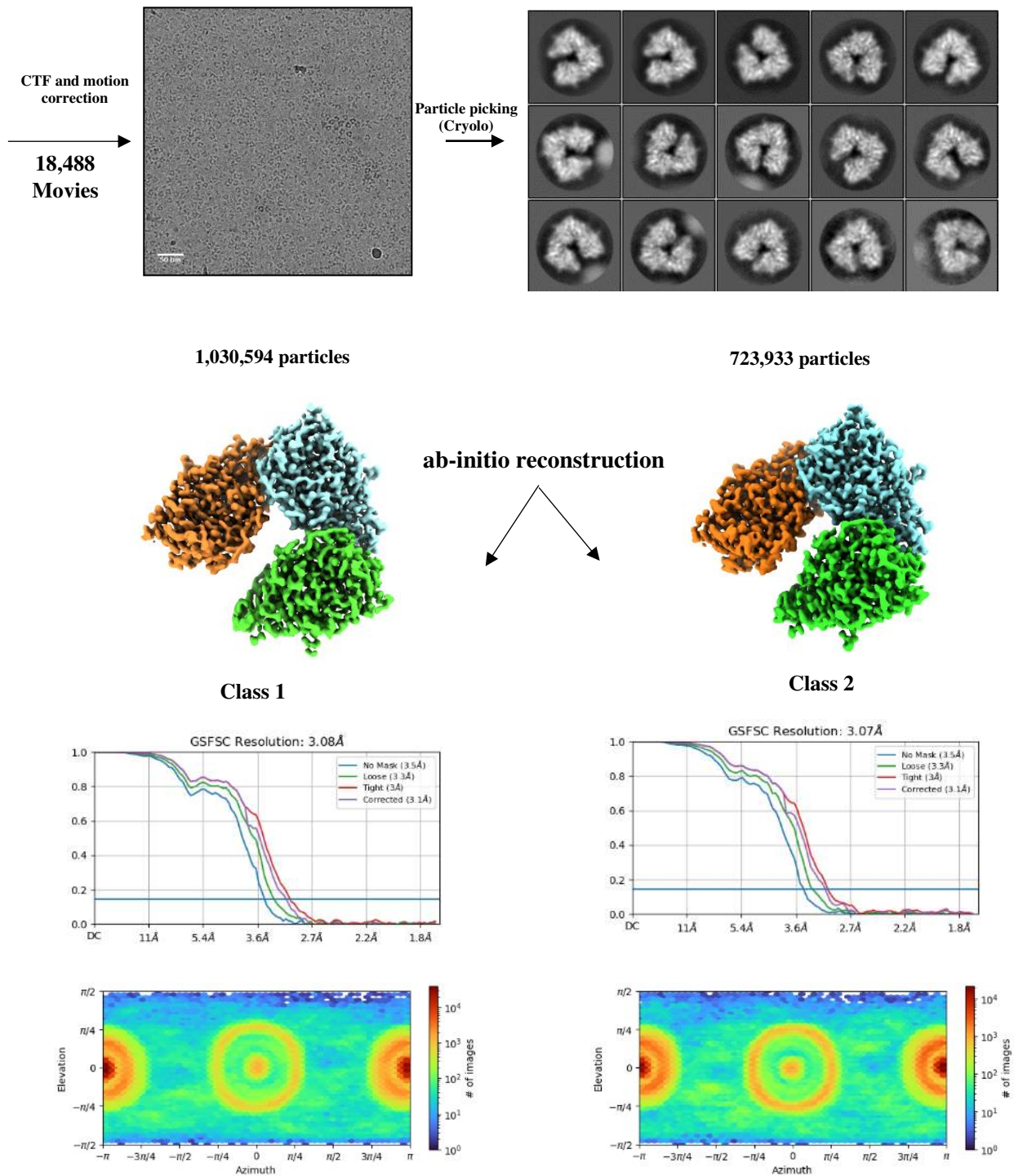


**Figure 3.61 Two classes of trimer obtained after data processing**

Two classes of trimer: Class 1 (wide space), B. Class 2 (narrow space) with FSC curves indicating a resolution of 3.08 Å and 3.07 Å (FSC 0.143) respectively, and Angular distribution heat map of particle projections for trimeric PLCH reconstruction

## 4 Discussion

### 4.1 Overexpression and Functionality of PLCs of *P. aeruginosa* PA14

In this study, Phospholipases C (PLCs) of *Pseudomonas aeruginosa* were cloned and expressed in the *E.coli* model system. *E.coli* is commonly used in molecular biology and biotechnology due to its well-characterized genetics and rapid growth<sup>195</sup>. However, challenges arise when expressing foreign genes with different codon usage and regulatory elements. Usually, gene optimization is necessary for *E.coli* systems when working with foreign genes or genes from other organisms. Gene optimization involves modifying the gene sequence to match *E.coli*'s codon preferences, ensuring efficient translation<sup>196,197</sup>. It also replaces regulatory elements to align with *E.coli*'s expression machinery. mRNA stability is improved by optimizing sequences, preventing degradation. Gene optimization avoids toxic elements and addresses post-translational modifications that *E.coli* may lack<sup>196</sup>. By optimizing the gene, adaptational stress on the host is reduced, promoting better compatibility<sup>196</sup>. However, for this study, no gene optimization was done, the PLC genes were taken directly from the PA14 genomic DNA. One modification was used in the cloning step i.e. DMSO was used for PCR amplification of the genes due to the presence of high GC content in *Pseudomonas* genomic DNA. DMSO (dimethyl sulfoxide) helps in cloning high GC-content DNA by disrupting stable secondary structures, reducing melting temperature, and enhancing PCR and ligation efficiency, allowing for successful manipulation and amplification<sup>198</sup>. Despite of no optimization PLCs were shown to be highly expressed, stable, and had no toxic effect on the *E.coli* cells.

In *Pseudomonas aeruginosa*, both PLCH and PLCN migrate from the cytoplasm to the periplasm via the TAT pathway, and subsequently from the periplasm to the extracellular medium via the T2SS pathway<sup>71</sup>. However, the PLCs expressed in *E.coli* did not transport to the periplasm, as the signal peptidase of *E.coli* that cleaves the TAT signal peptide of the protein is not compatible with *Pseudomonas*' TAT signal peptide. Therefore, the proteins expressed were present in the cytoplasm of *E.coli*<sup>63</sup>. The PLCN was present as inclusion bodies in the cytoplasm at 37°C but at 20°C, it exists as a soluble protein in the cytosol (Figure 3.3). This was because, at lower temperatures, the metabolic processes of *E.coli* become slow, and protein expression decreases, making the protein folding process more efficient and hence the proteins become soluble. Furthermore, PLCH was also present in the inclusion bodies at all the tested temperatures, even at lower temperatures. This could be because of over expression even at lower temperatures, resulting in the formation of improperly folded proteins. According to published reports, PLCR is required for the secretion and solubility of PLCH protein.

#### 4. Discussion

Interestingly, the PLCH chaperone exists as an overlapping gene and translates into PLCR1 and PLCR2 (explained in detail in Section 1.5). PLCR2 aids in the secretion and solubility of PLCH. Thereby, when chaperone, PLCR2 was co-expressed with PLCH it expressed as a soluble complex PLCHR2 in the cytoplasm as shown in section 3.2 (Figure 3.4).

Both the proteins PLCHR2 and PLCN were soluble and purified with the help of N-terminal 6X His using affinity chromatography. In the next step, gel filtration was done which showed a single peak for PLCN implying that it exists as a monomer in solution. The apparent molecular weight given by SEC was 76kDa. The molecular weights provided by SEC were imprecise, as they also depend on the protein's shape. Consequently, the theoretical mass of PLCN is 79.3 kDa, which lies closer to the apparent molecular weight from SEC i.e. 76 kDa (Figure 3.5). For that reason, the elution fraction obtained from this peak represented the purified PLCN. Furthermore, the PLCHR2, the complex eluted at 15.31ml, with an apparent molecular weight of 106kDa, which is also closer to the theoretical mass of the complex, i.e. 103.3kDa. This indicated the presence of PLCHR2 complex (Figure 3.7).

After obtaining both the purified proteins in good quantity, the identity and integrity of the proteins were checked. PLCN and PLCHR2 complex both had a N terminal 6X His tag and therefore western blot was used to confirm the identity of the proteins anti-His antibodies. PLCN gave a strong western blot signal, whereas for the PLCHR2 complex the PLCR2 signal was not as strong as the PLCH. This could be because of the different rates of transfer for PLCH and PLCR2 as PLCR2 has almost 3 times less mass than PLCH. Nevertheless, the PLCHR2 complex identity was also confirmed. Western blot confirmed the intactness of the N-terminal end, where the His tag was located. However, the N to C terminal completeness was still unknown. The completeness of the PLCN and PLCHR2 before proceeding to the characterization of these proteins was investigated using Mass spectrometry and LC-Mass/mass. Mass spectrometry of PLCN gave a molecular mass of 78.91kDa, which was 390 Da less than the theoretically calculated mass. This could mean that ionization of the PLCN might have caused the degradation of a few terminal amino acids. Moreover, when calculated, the measured molecular weight corresponded to a protein with five fewer amino acids (MGSSH) at the N-terminal end. In addition to that, the weight that was measured also incorporated a  $PO^3$  (78.97g/mol). For the PLCHR2 complex, the mass spectrometry provided an exact molecular weight for PLCR2, which was 19.27 kDa. On the other hand, the single charged species of PLCH was not observed at all; nevertheless, the double charged species observed in the measurement had a molecular weight of 40.28 kDa. Similarly, when calculated,

#### 4. Discussion

the measured molecular weight corresponded to a protein with 16 fewer amino acids plus a phosphate. Since the protein standard used for calibrating mass spectrometry lay between 10kDa - 66kDa, the measurements were not very precise (see section 3.4). To overcome these limitations, lastly LC-mass/mass was used to confirm the presence of full-length PLCH, PLCHR2, and PLCN (see section 3.4). LC-mass/mass then finally confirmed the N to C terminal sequence coverage, concluding that the full length PLCN, PLCH and PLCHR2 were expressed and purified using *E.coli* model system.

Oligomerization state of the proteins in the solution was also investigated to understand the quality of the protein. Mass photometry showed that PLCN and PLCHR2 complex both are present in their monomeric state in solution. DLS also confirmed this by measuring the molecular weight, and radius (nm) of the proteins. DLS also showed low polydispersity for both of the protein suggesting high purity and homogeneity (Table 3.3).

PLCN in both mass photometry and DLS showed that it was present as a monomer in solution whereas, PLCHR2 was present as a heterodimer of PLCH and PLCHR2. Because of the limitations of the previous methods, stoichiometry of the heterodimer was investigated using SEC-SAXS (see section 3.5.5). The measured parameters are as follows: MW expected = 104 kDa; MW MALLS/RI = 111 kDa (compared to the previously estimated offline SEC-MALLS/RI MW of 106 kDa). According to the results of the QELS experiments, the RH of the PLCHR2 complex was approximately 4.3 nm on average. The molecular weight (MW) from SAXS was in accordance with the MW from MALLS/RI. SEC-SAXS measurements allowed the conclusion that the PLCHR2 heterodimer was present in a 1:1 ratio. The measured radius corresponded to the theoretical size of the PLCHR2 complex.

In order to investigate PLCN and PLCHR2 for the presence of secondary structure, the far-UV-CD spectrometry was employed. The secondary structure's stability was accessed through to the melting temperature computed from the CD-signals at different temperatures i.e. from 4°C to 98°C with a rate of change of 2° (See 3.5.3 below). The melting temperature measured for both PLCN and PLCHR2 using the CD spectra were substantially different, with 45°C and 60°C respectively, despite their high sequence similarity. This could be explained by the presence of the chaperon PLCHR2 in the PLCHR2 complex. According to literature, PLCHR2 is required for PLCH to be secreted into the extracellular medium<sup>65</sup>. This chaperone makes the protein more stable and, as also was observed, is required for both the protein's stability and solubility.

#### 4. Discussion

Besides the differences in  $T_m$  determined as the inflection point, the slopes at  $T_{onset}$  were also different for PLCN and the PLCHR2 complex (Figure 4.1). The sensitivity of PLCN to secondary structural changes due to temperature was dramatically greater than that of the PLCHR2 complex. This might indicate that the PLCHR2 complex has to be functional longer to fulfill its biological role.

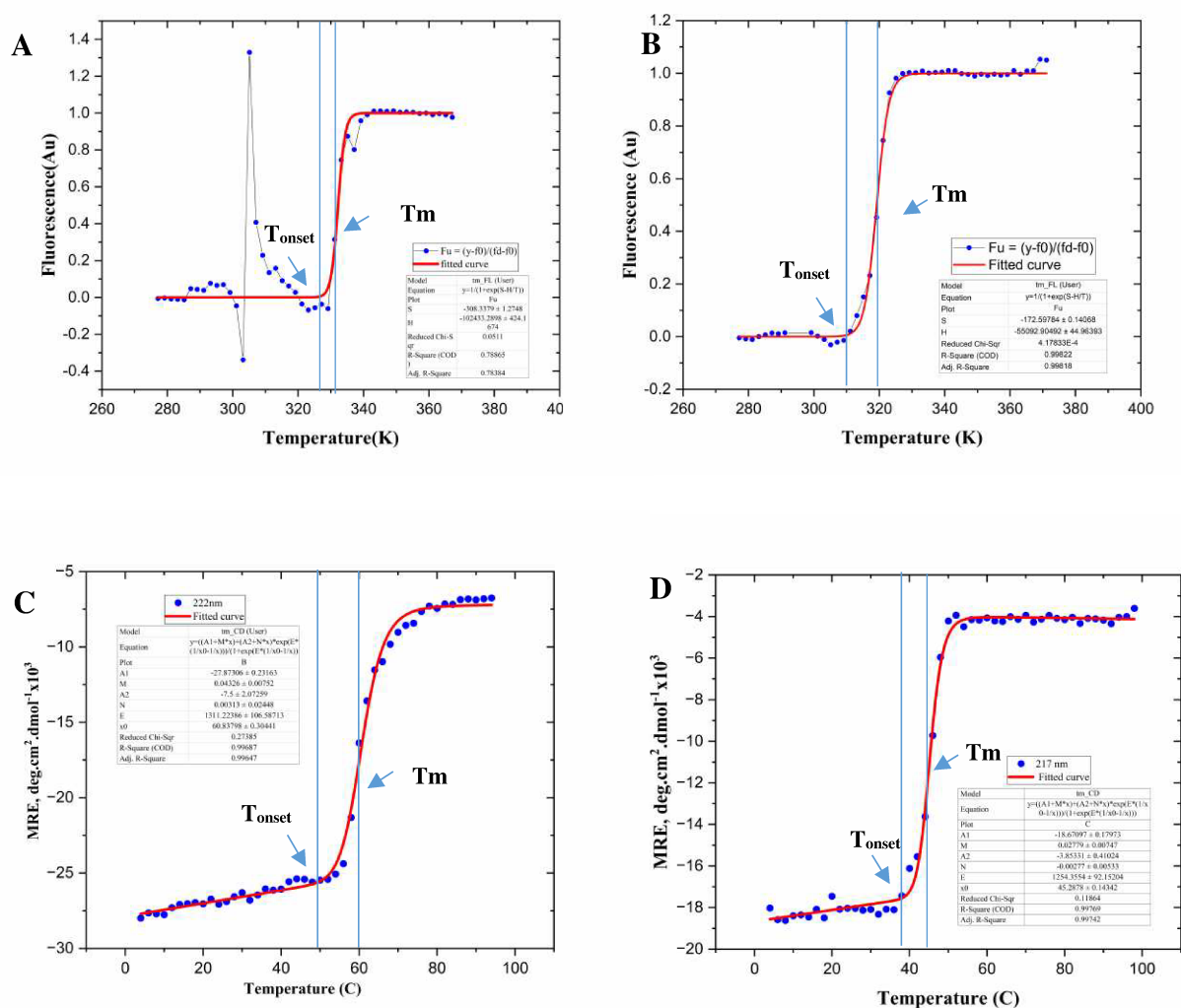


**Figure 4.1 Visualization of  $T_m$  at the inflection point and the change in the slope ( $T_{onset}$ )**

PLCN and PLCHR2 showed substantially different melting temperatures, with 45°C and 60°C, respectively, despite their high sequence similarity. This difference may be explained by the presence of the chaperone PLCHR2 in the PLCHR2 complex. PLCHR2 is known to be essential for PLCH secretion into the extracellular medium and enhances protein stability and solubility. Additionally, the slopes at  $T_{onset}$  for PLCN and the PLCHR2 complex were different. PLCN exhibited higher sensitivity to temperature-induced secondary structural changes compared to the PLCHR2 complex. This suggests that the PLCHR2 complex might need to remain functional for a longer duration to fulfill its biological role.

#### 4. Discussion

Furthermore, the protein recovery rate was low. PLCN was unfolded entirely when heated to 98°C and did not recover when the temperature was gradually decreased to 4°C. Similar behavior was seen in PLCHR2 complex (Figure 4.2).

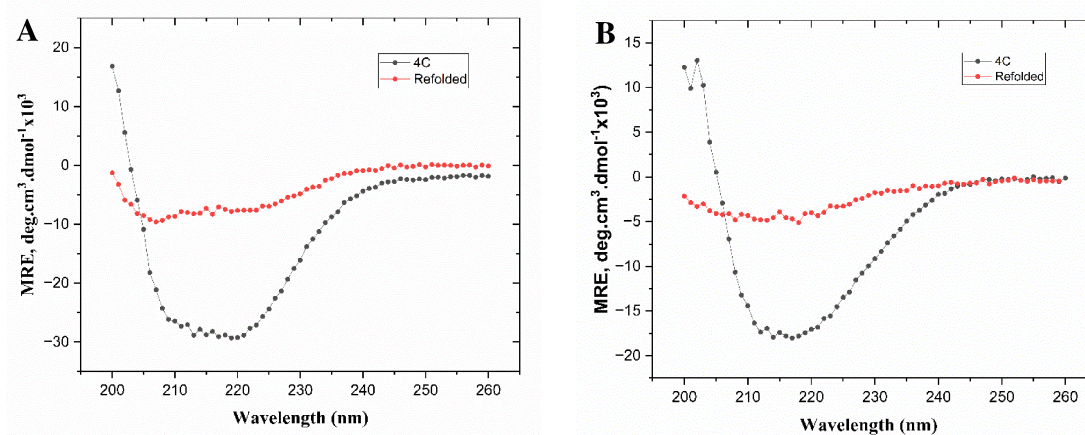


**Figure 4.2 Far UV CD spectrum of native sample sand denatured samples.**

The graphs showing local minima characteristics for secondary structure and the denatured sample showing a flat curve for **A. PLCHR2 B.PLCN**

After analyzing the secondary structure, the tertiary structure stability was also analyzed. Figure 3.16 shows that the weakening of the emission peak in the fluorescence spectra. The signal showed the quenching of fluorescence, which could come by changes in the mobility, solvent quenching indicating changes in the environment of the tryptophan residues, or could also be due to interaction upon aggregation. As the temperature increased from 4°C to 98°C, the fluorescence signal at the excitation wavelength of 295 nm increased, accompanied by a decrease in emission peaks. These observations imply that the rise in temperature led to protein aggregation, which in turn resulted in protein denaturation.

Both of the proteins had a maximum emission wavelength of around 330 nm, which indicated that some of the tryptophan side chains might be buried in a hydrophobic microenvironment. The emission maxima shift occurred from roughly 330 to 340 nm during the temperature scan. As a result, a red shift was observed in both PLCN and PLCHR2 while the unfolding process was taking place. This indicates the existence of a structural change. The T<sub>m</sub> obtained from the FL was 47°C, which was 2°C more than the T<sub>m</sub> acquired by CD spectroscopy, which is unusual as loss of tertiary structure typically precedes loss of secondary structure. This most likely could

#### 4. Discussion

be because of the early onset of protein aggregation that hide the tryptophan from being exposed to the solvent. In a comparable manner, As was previously mentioned, the  $T_m$  that was derived from analyzing FL data was 62.5°C, which is also 2°C higher than the  $T_m$  that was acquired from CD. Similarly, here also an early protein aggregation could be initiated, resulting in the concealment of tryptophan residues from solvent exposure. The onset of aggregation at around 40°C was observed when the FL signal at excitation wavelength (295nm) was plotted against the temperature for both the proteins (Figure 4.3).

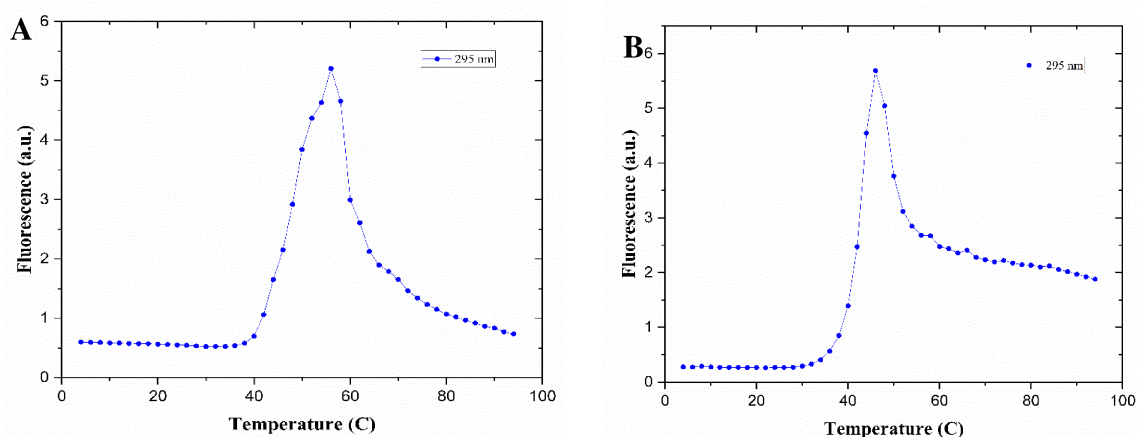


**Figure 4.3 Graph between FL signals at excitation temperature vs wavelength (295nm)**

Both the graph shows the onset of aggregation at around 40°C **A. PLCHR2 B. PLCN**

Additionally, a spike in the FL signal was observed at around 308K (34°C) (Figure 4.1 A&B). This could happen when the plot of that yields the slope and intercept of the initial and the denatured state (explained in section 3.5.4) was plotted, because of the low FL measured and its division led to these artifacts. However, it could also be that some low temperature structural changes are happening at 34°C or aggregation (Figure 4.1 A & B). To understand these changes this further investigations are required.

I nevertheless was able to reach the conclusion that the tertiary structure of the PLCHR2 complex is significantly more stable than that of the PLCN. In addition,  $T_m$  at the point of infection and slope shift at  $T_{onset}$  were different between PLCN and PLCHR2 complex (Figure 4.1). In contrast to the secondary structure, the sensitivity of the PLCHR2 complex to changes in the tertiary structure because of temperature was greater than that of the PLCN.

#### 4. Discussion

Furthermore, It was also demonstrated that recombinant PLCN and PLCHR2, when produced in *E.coli*, had the ability to cleave phospholipids in vitro when using an artificial substrate (NPPC), In vitro both the PLCN and PLCHR2 complexes demonstrated activities comparable to that reported in the literature. (See section 3.6.1 and 3.6.2).

Overall, the results demonstrated that the expression of PLCs (Phospholipase C) in the *E.coli* model yielded remarkably high quantities of these enzymes. The expression levels in *E.coli* were significantly higher than those observed in their original host, *Pseudomonas aeruginosa*. The stability of the expressed PLCN and PLCHR2 complex proteins is particularly encouraging, as it means that, they can be handled and stored without concerns about significant denaturation or degradation. This finding indicates that the *E.coli* expression system can be considered a highly effective and advantageous platform for producing these enzymes at a large scale for further studies.

#### 4.2 PLCs in Microbial Infections

Due to rising antibiotic resistance, treating Gram-negative bacterial infections is one of the biggest concerns. *Pseudomonas aeruginosa* is the most common opportunistic organism responsible for infections in hospitalized and immunocompromised individuals<sup>75</sup>. In recent years, there has been a discernible rise in the prevalence of multi-drug resistance (MDR), which is now acknowledged as a major problem on a global scale<sup>199,4</sup>. *P. aeruginosa*, is capable of secreting a variety of extracellular virulence factors such as exotoxins, proteases, hemolysins, and phospholipases. *P. aeruginosa* produces two homologous extracellular PLCs, PLCH and PLCN. PLCH is a hemolytic PLC, while PLCN is a non-hemolytic PLC. PLCH and PLCN share 40% of their amino acid sequence, but their substrate specificities are very distinct from one another. These have different substrate affinities (Table1.2). These phospholipases cleave the phospholipids present in the cell membrane and ultimately causes cell lysis. PLCH is also know Several reports have drawn attention to the role of *P. aeruginosa* PLCs in the pathogenicity of the bacteria. According to prior investigations, LepA and PLCH's partnership may let *P. aeruginosa* employ erythrocytes as its sole source of nutrients<sup>70</sup>. Yukata et.al. suggested that LepA and PLCH may contribute to *P. aeruginosa*'s in vivo pathogenicity and expansion<sup>70</sup>. Furthermore, the PLCH and PLCN are present in more than 90% of the MDR isolates of *P.aeruginosa*. PA14, one of the most virulent strains, possesses three different types of phospholipases: PLCH, PLCN, and PLCB. PLCB is the phospholipase discovered most recently, and it has not been demonstrated to directly serve as a virulence factor<sup>53,50</sup>. On the other hand, PLCH and PLCN play an essential part in the acute pathogenicity of *Pseudomonas*.

#### 4. Discussion

Phosphatidylinositol (PI) specific phospholipases C, Zn<sup>2+</sup> metallophospholipases C, Phospholipases C from the acid phosphatase superfamily, and other phospholipases C are the broad structurally different categories that are used to categorize bacterial PLCs (Table 1.1)<sup>51</sup>. PLCH and PLCN are members of a novel class of phospholipases C found in Gram-negative bacteria. These enzymes belong to the superfamily of acid phosphatases. PLCH is the most characterized phospholipase of this novel group. There have been studies that show that in this acid phosphatase can also act as a PLC and digest lipids. Perhaps similarly, the PLCs might also can act as a phosphatase (Discussed below with mechanism).

The PLCs of *P.aeruginosa* are involved in direct lysis/death of the cells by making pores in the cell membrane as we also observed in this study (discussed below) or also by starting some signal cascade that can either induce apoptosis or cell proliferation (cancer). The PLC of *Pseudomonas aeruginosa* has been shown to induce platelet aggregation in platelet-rich human plasma in a concentration-dependent manner. The enzymatic activity of PLC is essential for this platelet aggregation<sup>200</sup>. PLC exhibits heat-labile properties<sup>201</sup>. *P. aeruginosa* may possess two hemolytic virulence factors that can lead to paralysis, dermonecrosis, footpad swelling, increased vascular permeability, and even death in mice<sup>202</sup>.

In pulmonary infections caused by *P. aeruginosa*, inflammation is a hallmark feature (Titball, 1998). PLCH has been demonstrated to elicit an inflammatory response in human neutrophils and polymorphonuclear cells in vitro. Neutrophils treated with PLCH but not PLCN, showed increased production of inflammation markers such as oxygen metabolites, leukotriene-B4 (LTB4), and histamine<sup>203</sup>. Moreover, PLCs from *P. aeruginosa* triggers an enzyme activity-dependent inflammatory response in mice. Intraperitoneal injection of PLC resulted in the accumulation of plasma proteins, inflammatory cells, and arachidonic acid metabolites such as LTB4, LTC4, LTD4, prostaglandin E2 (PGE2), PGF2-alpha, and thromboxane B2 in mice<sup>204</sup>. These molecules have specific roles in inflammation, such as stimulating chemotactic aggregation of granulocytes, causing the wheal and flare response, and promoting vasodilation, edema, erythema, and pain.

Elevated levels of PLC antibodies have been observed in cystic fibrosis (CF) patients chronically infected with *P. aeruginosa*, suggesting its involvement in chronic infection<sup>205</sup>. In vitro studies with human bronchial cells indicate that *P. aeruginosa* PLC contributes to exacerbated inflammation in CF lungs, leading to poor prognosis<sup>206,207</sup>. Neutrophils and pulmonary macrophages play a pivotal role in clearing pathogenic bacterial infections from the human host<sup>206</sup>. Despite the abundance of neutrophils in the lung tissues, PLCHR aids *P.*

#### 4. Discussion

*aeruginosa* in surviving adverse conditions by suppressing the respiratory neutrophil burst response<sup>68</sup>.

PLC also appears to play a role in lung function by destroying lung surfactants. PLCH of *P. aeruginosa* is reported to be a destructive determinant for lung surfactant. The wild-type strain of *P. aeruginosa* significantly impairs lung surfactant function, while the PLCHR mutant strain is less potent in causing infection<sup>208</sup>. PLC helps hydrolyze a phospholipid called PC, which is abundant in lung surfactants, converting it into glycine betaine. The accumulation of glycine betaine within the bacterial cell protects against the high osmolarity conditions in the lung tissue, facilitating bacterial colonization<sup>39,209</sup>. Moreover, PLC plays a role in biofilm formation in vitro and in animal models, further emphasizing its central role in *P. aeruginosa*-associated morbidity and mortality in CF patients<sup>207,210</sup>. Therefore, understanding these mechanisms is essential to combat infections and mitigate their impact on human health.

As discussed above, the recombinant PLCs in this study were biochemically active. Therefore, in order to demonstrate that highly purified PLCN and PLCHR2 are also digesting the original phospholipids present in the mammalian cell membranes, the MTT assay was used. The PLCHR2 and PLCN was found to be both cytotoxic to the mammalian cells (HeLa cells). However, only HeLa cells were tested in this study. As described by Michael L. Vasil, PLCHR exhibits selective cytotoxicity, it does not show cytotoxicity to mammalian cells lines such as HeLa (epithelial); L929 mouse fibroblasts; J774 macrophage, A549 lung cells and is cytotoxic to Chinese hamster ovary cells (CHO); and Human Umbilical Vascular Endothelial Cells (HUVEC). However, in this study, it was observed that both PLCHR2 complex and PLCN were cytotoxic to the HeLa cells and at even much lower concentrations (as LD<sub>50</sub> was calculated to be 0.016ng/μl for PLCHR2 and 6.6ng/μl for PLCN. This could be due to the different composition of the phospholipids in the HeLa cell membrane. The variation in phospholipid composition within HeLa cells may arise due to their different growth conditions. Since Vasil et.al did not specify the media used in their study, it is plausible that the distinct phospholipid content in the cell membranes caused the difference in the cytotoxicity<sup>67</sup>. Additionally, the recombinant PLCs were also active on the original phospholipids and PLCHR2 is more cytotoxic than PLCN. This could be because of the different phospholipid affinity (Table 1.2)

In some Gram-positive bacteria, phospholipases C are responsible for lysing red blood cells. *Pseudomonas aeruginosa*'s PLCH also has been shown to be hemolytic which cleaves the phospholipids (PLs) present in the red blood cells; nevertheless, it does not lyse all types of red blood cells (RBCs) for example, Horse red blood cells. RBCs have generally a high content of

#### 4. Discussion

PC and SM in their cell membrane, which are the substrates for PLCH. PLCN has greater affinity towards phosphatidylserine, which is present on the inner leaflet of RBCs. The reason for this specificity is unknown. In this study, the hemolytic capabilities of the PLCHR2 and PLCN were examined by subjecting them to sheep red blood cells. PLCHR2 easily lysed the RBCs, while PLCN had no effect on the hemolysis of the cells (See section 3.6.3). This could also be because of their affinities for different phospholipids. Since, PC is generally present on the outer leaflet of the bilayer and PS on the inner leaflet, it could be postulated that the coexistence of PLCN and PLCHR2 might lead to increased virulence compared to their individual presence. As a consequence of this research, we know that the PLCHR2 complex is far more virulent than the PLCN. Both of the proteins i.e. PLCN and PLCHR2 degrade the lipids in both natural and artificial membranes.

The next step was to examine the lysing process of the PLCHR2 complex. Using atomic force microscopy, I was able to monitor the creation of holes in the bilayer and learn more about this phenomenon. The experiment spanned 68 minutes in total, with three 20-minute intervals investigated. Between 0 and 21 minutes, the PLCHR2 heterodimer began to puncture holes into the bilayer, and throughout the course of that time, the holes gradually grew larger and more volumetric. The observed depth on the mica support was around 3 nm, which is consistent with the dimension of lipid bilayers. In addition to this, I observed an increase of the height in AFM images near the holes. This could be a consequence of PLCHR2's degrading lipids, which leads to phase separation of the free fatty acids or an accumulation of the protein. The puncturing of holes in the lipid bilayer elucidates the role of PLCHR2 in virulence by making pores in the cell membranes, lysing the cells and ultimately causing cell death and subsequently allows tissue invasion. (ADD citation for the cell death by pores)

The following time interval, which lasted from 21 to 30 minutes, was when the holes began to close up. Additionally, throughout that period, I noticed a rim developing around each of the holes. These rings might be the enzyme PLCHR2 or the aggregates resulting from the breakdown of lipids. Because of the AFM's low resolution, I was unable to differentiate between the two. Nonetheless, protein surrounding the periphery of the holes would be more biologically significant in order to stabilize the holes. As it would happen in a living cell, the cellular phospholipids would attempt to seal the cell membrane and prevent pore formation. The micrographs obtained from the EM (discussed in section 3.8.2) revealed oligomerisation, suggesting the enzymes might assemble and potentially play a role in maintaining the punctured holes. All of the holes completely closed or filled up during the last 30–68 minutes of the

#### 4. Discussion

experiment. This might not happen in an infected cell as in the case of a *Pseudomonas* infection, the bacteria would sense (2 component system) the gradients of reaction products and utilize them (Figure 1.9). Therefore, hole filling might not be happening in a real infection. In addition, the observed aggregates have not changed throughout the course of the previous two intervals. A number of different reasons could have caused these holes to start closing; for example, the aggregated fatty acids resulting from the cleavage of the phospholipid (DMPC) could have simply filled them in. The enzyme's ability to perform its function could have been compromised by suboptimal micro environmental conditions that developed after the cleavage of the lipids. It could also be possible that the cleavage of the lipid DMPC resulted in an abundance of products, halting the catalysis due to a phenomenon of product inhibition. Nevertheless, based on all of these observations, we can draw the conclusion that the proteins cause a hole to form, and then they begin to degrade the lipid from the inside out, all while expanding it. They also could form and stabilize the holes by forming the wall like structure as observed by just binding to the lipids and preventing the closure of the holes.

In conclusion, the findings from this study provide compelling evidence that the highly purified PLCHR2 and PLCN from *Pseudomonas aeruginosa* are potent cytotoxic agents against mammalian cells. Notably, PLCHR2 was also found to possess hemolytic properties, indicating its ability to disrupt red blood cells. These virulent PLCs exhibit a remarkable ability to invade tissues by creating puncturing holes in cells, leading to their lysis and eventual cell death. The significance of these findings cannot be underestimated, as they highlight the extreme toxicity of these PLCs, even at picomolar (pM) concentrations. Such potent cytotoxicity suggests that these toxins are highly effective at inducing cell damage and contribute significantly to the pathogenicity of *Pseudomonas aeruginosa* infections by promoting tissue invasion. The fact that they can exert their harmful effects at such low concentrations underscores their virulence and potential threat to host organisms. Given the detrimental impact of these virulent PLCs on mammalian cells, targeting and inhibiting their activity could be a promising approach to reduce the pathogenicity of *Pseudomonas aeruginosa* infections. By developing interventions that specifically target and neutralize these proteins, it may be possible to limit the damage they cause and improve outcomes for those affected by such infections.

#### 4.3 Structures of the Gram-negative PLCs (Novel class of PLCs)

Since the 1980s, we have had knowledge of the PLCs of *P. aeruginosa*, which are PLCH and PLCN. More work went into characterizing PLCH as compared to PLCN. In spite of an extensive research, there is no experimental information on the 3D structure of both the

#### 4. Discussion

proteins. This project reveals the very first structures for a class of Gram-negative phospholipases that belong to acid phosphatase family (Table 1.1). PLCN and PLCHR2 were purified in high quality and quantity in order to set up initial crystallization screening. Before proceeding with the structure solution using either X-ray crystallography or Cryo-EM, Circular Dichroism and Fluorescence spectroscopy to investigate the secondary and the tertiary structure stability (discussed above). In short, LC-MS/MS technique to investigate the primary structure, CD spectroscopy to establish the secondary structure. Furthermore, I examined the tertiary conformation of the complex using fluorescence spectroscopy, and monitored the quaternary structure of the complex using SEC and EM.

Both the proteins were subjected to crystallization. Both PLCN and PLCHR2 were initially subjected to the crystallization process using commercial screens that were available. Screens such as I and II of the JCSG Core, Morpheus<sup>TM</sup> HT-96 and Morpheus<sup>TM</sup> II from Molecular Dimensions, and screens from Qiagen such as PEGs II suite, pH clear II, NeXtal PEG, and NeXtal AmSO<sub>4</sub> were among the many that were used to put initial screening tests. Varying protein concentrations, ranging from 8 mg/ml to 12 mg/ml was used. The conditions used for PLCHR2 yielded no positive results under these conditions. On the other hand, with PLCN, needle crystals appeared under certain conditions of the Morpheus<sup>TM</sup> II (see Table 3.7). The P11 Petra beamline at DESY in Hamburg was used to test these needle crystals for diffraction; diffraction spots were only found up to 7Å resolution. Neither by reproduction or slight variation of the conditions, including PEG filters and fine screening, an improvement of the crystal size or quality could be achieved. In spite of all of these tests, the needle crystals began to form after approximately three months, and their size did not improve. These needle crystals were analyzed on SDS-PAGE, and it was discovered that the protein that was forming crystals was running 5 kDa lower (75kDa) than the original size (79kDa) (Figure 3.45). This result suggests that the flexible part of the protein was degraded because the plates were maintained for a lengthy period. Therefore, in order to cut the flexible sections, in situ proteolysis using trypsin was performed. After only 15 days, at a 1:1200 protein ratio, two crystals had formed and they were used to perform a diffraction experiment. The conditions in which the crystals appeared were 11% 1,5, pentadiol, 0.1M BisTris/MOPSO pH 6.5, 7% PEG 8000, 0.001M alkali mix and 11% 1,5, pentadiol, 0.1M BisTris/MOPSO pH 6.5, 7% PEG 8000 (see section 3.7.2). Because the condition contained 11% 1,5 pentadiol, an identical solution that had 20% 1,5 pentadiol was utilized as a cryoprotectant instead to avoid the formation of ice crystals. These protein crystals diffracted to 1.5Å.

#### 4. Discussion

The data obtained from the beamline was indexed, scaled and merged with the help of XDS. The alpha fold model obtained from AlphaFold2 was used for molecular replacement, as it does not share sequence or structural homology. For molecular replacement the alpha fold model was truncated before using, the first 63 residues from N terminal were cleaved off which contained the His tag sequence before the start of the PLCN protein i.e. MGSSHHHHHSSGLVPRGSH and rest was the TAT signal peptide i.e. MISKSRRSFIRLAAGTVGATVATSMLPSSIQAALAIPAHRRHG. After obtaining a final model from Molrep<sup>154</sup> (CCP4), it was subjected to several rounds of model building using coot and refining the respective model in Phenix using phenix.refine<sup>155</sup>.

Using PISA<sup>211</sup>, it was observed that there were three most favorable intermolecular surface interaction, generated by the two protein molecules that build the asymmetric unit (Figure 4.4). The largest interface buries 766.7 Å<sup>2</sup> of surface area, while the next largest contact buries just 490.0 Å<sup>2</sup> of surface area. Both of them point toward the asymmetric unit from A to B, that is the C-terminal domain of one molecule interacts with the N-terminal domain of the other one. However, the third one had a 425.0 Å<sup>2</sup> buried interface, which suggests that B and A are interacting with one another, that is the N terminal domain interacts with the N-terminal domain of the other molecule. In addition, each of these interfaces had the lowest possible PISA Complex Formation Significance Score (CSS), with 1 being the best possible score and 0 being the lowest possible score for the formation of a complex by the interacting molecules. Therefore it is unlikely that the molecular packing indicates a biological dimer which is in agreement with the results from mass photometry and SEC. Both the molecules in the asymmetric unit exhibit a proper two-fold symmetry. Also, the number of cysteine residues in PLCN is three and no disulfide bonds were present.

#### 4. Discussion

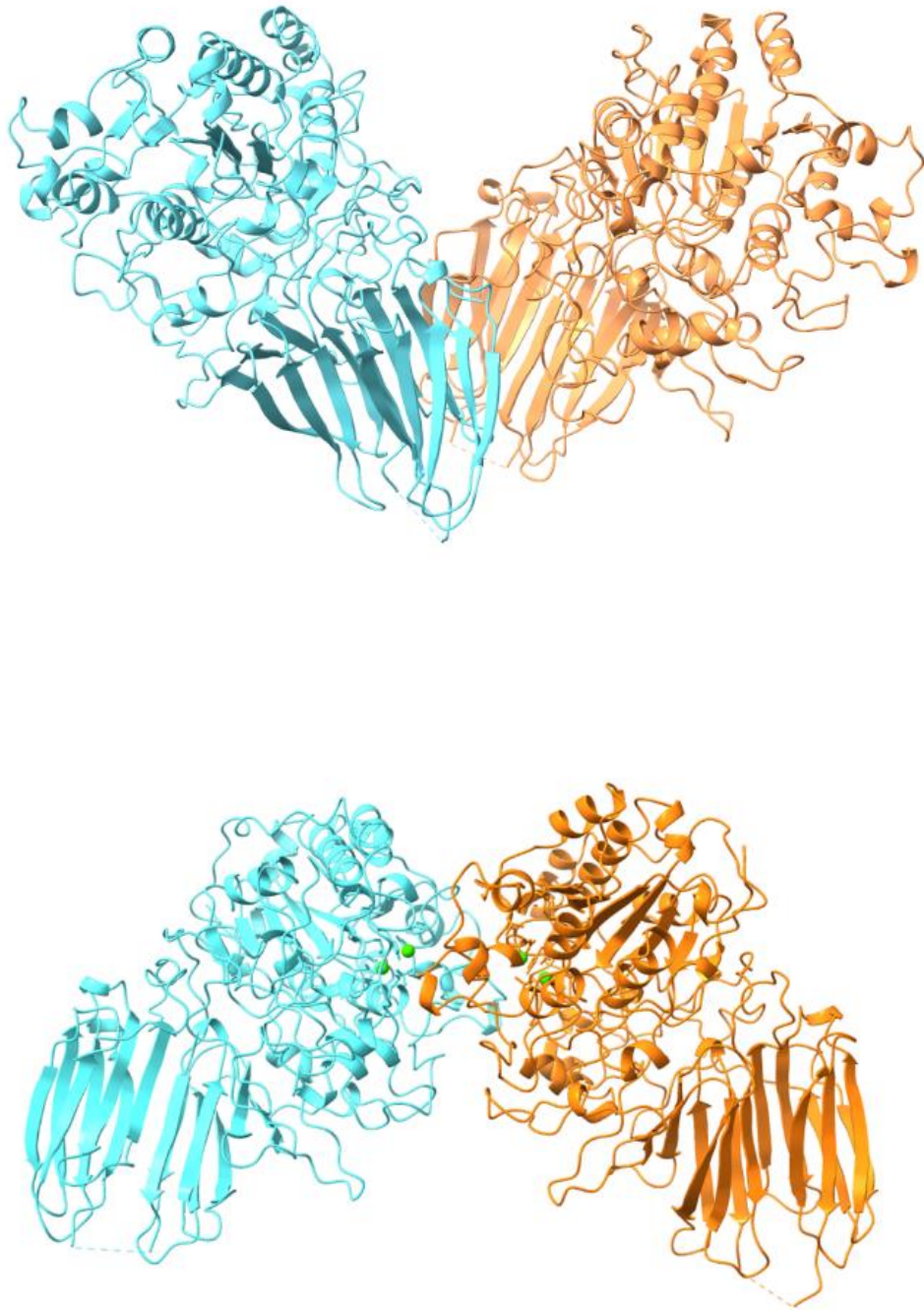


**Figure 4.4 Two possible asymmetric units in crystal structure of PLCN**

Two major kinds of interaction between the two molecules in the asymmetric unit of the crystal structure of PLCN, calculated using PISA

#### 4. Discussion

Trypsin cleaved off the first 61 residues from the N-terminal end. Additionally, 7 residues (located between 643-649 residues) in the C terminal domain were not modeled due to insufficient or absent density. In summary the residues 62 to 712 could be modelled, apart from a loop region of 7 amino acids which showed lacking density, probably due to high mobility.

This novel class of PLCs belong to the acid phosphatase superfamily. The N-terminal domain of PLCH and PLCN shares a ~22% sequence identity with the AcpA, acid phosphatase of *Francisella*. In spite of the fact that it shares such a low sequence similarity with the AcpA, one is still able to deduce a few key pieces of information from the structure of the *Francisella* phosphatase. The alignment of AcpA and PLCH superfamily members' amino acid sequences demonstrated that the conserved residues are located in the active region. This domain is the catalytic domain and contains the active site with 8 conserved active site residues i.e. Active site residues: Glu 57, Asn 58, His 118, Asn 201, His296, GLU 334, Thr-PO3 176. As for the C-terminal domain of both the Phospholipases C i.e. PLCN and PLCH, belong to the novel group of gram negative PLCs and have no function. It is known also known as Domain of unknown function (DUF).

Based on the literature regarding this class of protein, the active site residues could be identified as conserved residues across the class. Aside from that, a very strong density feature of the phosphate in association with the threonine validated the location of the active site. The active site of the PLCN protein forms a negatively charged cleft with the main residues that are responsible for the catalysis of the phospholipids. The validity of the assignment of the active site was experimentally confirmed by mutating the Threonine at 176 position to alanine and it was observed that the enzymatic activity reduced dramatically. Other members of the eukaryotic phospholipase family, such as phospholipase D, PI-PLC, and phospholipase A2, likewise possessed a funneled-negative charged cleft heading to the catalytic pocket. Further evidence for the role of Thr was provided by the covalent binding of orthovanadate in the case of AcpA. The use of orthovanadate as an inhibitory transition state analogue is a well established approach in crystallography allowing to identify the nucleophile and possibly the stabilization of the transition state by other residues in the active site. Phosphorylation of active site residues are not uncommon for phospholipases as the catalytic pocket of PLD showed comparable site-specific phosphorylation of a histidine as an alternative nucleophile (mechanism is discussed in detail in section 4.4).

#### 4. Discussion

The a posteriori analysis of the suitability of the alphafold model for MR was examined by the superposition of the experimental and the alpha fold model. Chimera was used to align the two protein structures. It gave the sequence alignment score of 3252, the alignment score using BLOSUM62 and the Needleman-Wunsch method depends on the specific sequences being aligned. It is calculated based on the substitution scores given in the BLOSUM62 matrix during the global alignment process. RMSD between 618 pruned atom pairs was 0.647 angstroms; (across all 643 pairs: 1.207). This shows that the model predicted by Alphafold2 for PLCN was significantly similar to the structure obtained experimentally.

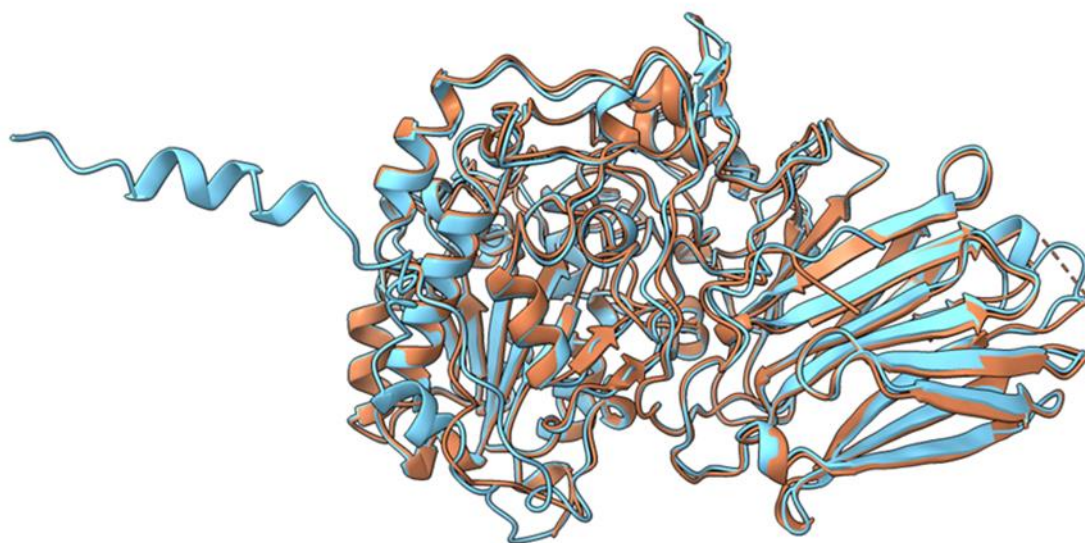


**Figure 4.5 X-ray crystallography structure of PLCN (brown) superposed on Alphafold model of PLCN (Blue)**

As discussed above the PLCN only shares 22.62% sequence identity with the AcpA acid phosphatase of *Francisella tularensis*. When the PLCN structure solved using Xray crystallography was aligned with the acid phosphatase it gave sequence alignment score of 581 and RMSD between 223 pruned atom pairs was 0.946 angstroms; (across all 386 pairs: 8.424). The alignment X-ray crystallography PLCN aligned with the AcpA acid phosphatase of *Francisella tularensis* shows that the N terminal domain of PLCN is conserved, (along with the active site). However, the C terminal domain of PLCN, which is the domain of unknown function, is whole together missing in the AcpA.

#### 4. Discussion

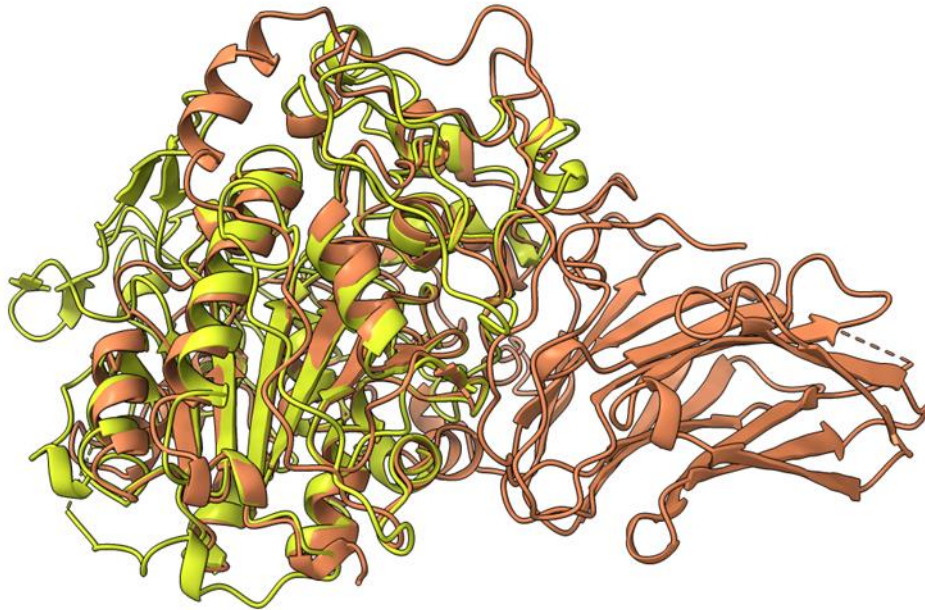


**Figure 4.6 X-ray crystallography structure of PLCN (brown) aligned with the AcpA acid phosphatase of *Francisella tularensis* (yellow)**

The PLCN protein crystals were acquired through the utilization of trypsin protease. To assess the activity of the trypsin cleavage product, a modified protein construct with the first 63 amino acids removed was created. This truncation included the TAT signal peptide. However, upon removing these initial 60 amino acids, the protein's solubility decreased. The solubility decreased roughly from milligrams to micrograms. Because of the low solubility and poor purification, the exact amounts were not measured. The insolubility could be because of improper folding during the expression. Unfortunately, the protein's activity could not be quantified accurately. As a result, the activity of the cleaved enzyme was not compared with that of the intact protein.

None of the attempts to grow PLCHR2 crystals were successful. Because the PLCHR2 complex is around 103 kDa in size, which is within the range of the cryo electron microscopy method, the structure was ultimately determined by employing this method. Before proceeding directly to the cryo EM, negative staining was performed, to determine whether or not the particles are monodispersed on the grid and whether or not they remain on the grid, as some hydrophobic proteins do not stay on the glow discharged grids. The micrographs that were acquired revealed (Figure 3.54) the presence of monodispersed particles of PLCH. Because of the low resolution

#### 4. Discussion

we could not conclude if the PLCR2 was also present with PLCH as a heterodimer. Negative staining was helpful in addressing the particle stability on the grids, general shape, and having some understanding about the concentrations to employ for CryoEM.

After that, grids were plunge-frozen with the PLCHR2 complex, and then viewed under an Cryo electron microscope (See section 2.8.2). The micrographs acquired from the CryoEM indicated multimeric particles, such as trimer, dimer, and monomer (see picture). The data were gathered and then processed (see to section 3.8.2 for further information). It was discovered that the particles showed a very strong preferred orientation, and that all of the particles generally displayed a favored interaction surface with the grid, which did not met the required random views for three-dimensional reconstruction. Several approaches were taken to address this issue, including the use of detergents, TMV, and changing the freezing conditions. None of these modifications were helpful. In the end, it was required to collect the datasets at titled angles in order to get images from a range of angles. Therefore, datasets were collected at tilt angles of 0°, 30° and 45°

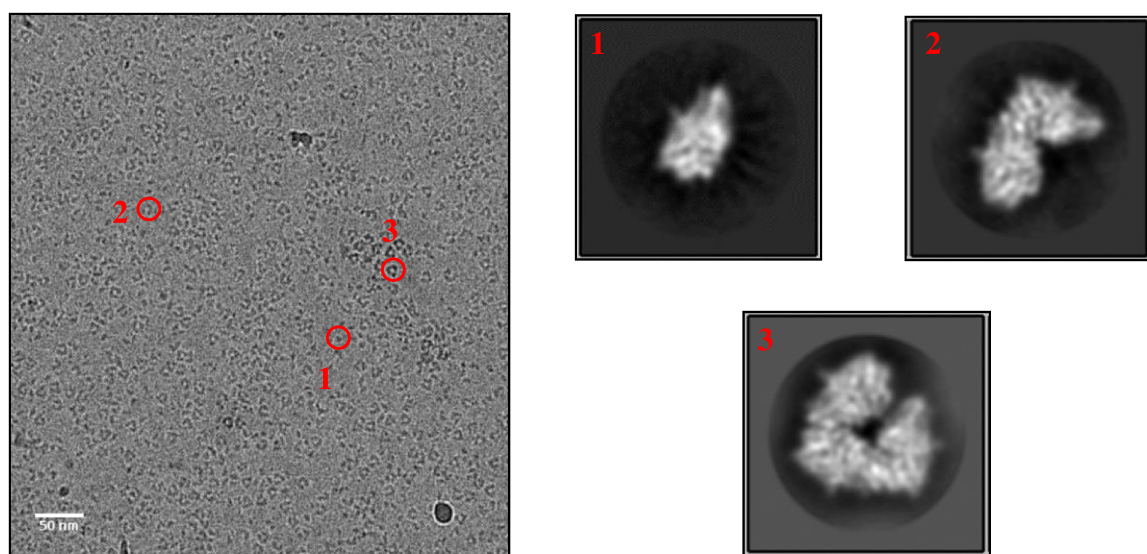


**Figure 4.7 Micrograph obtained from CryoEM showing different oligomers 1. Monomer, 2, Dimer 3. Trimer.**

Following the collection of data sets at three different angles, around 18000 movies were collected, and particles that belonged to trimeric classes were subsequently merged in order to generate a set of 2,824,689 particles. Thereafter, 2D class averaging and 3D class averaging was done (see section 3.8.2), where two distinct classes of trimers were found. The ab initio reconstruction was carried out in order to obtain a map of these two classes at 3.08 Å and 3.07

#### 4. Discussion

Å resolution respectively, which were designated as class 1 (the open class) and class 2 (the closed class) (Figure 3.60). The non-bonded contacts with different subunits were seen in both classes. The subunits were orientated in a head-to-tail fashion, which means that the N-terminus of one subunit contacts the C-terminus of the other subunit. In a similar manner, 327006 monomer particles were selected and utilized for the construction of the final map, which had a resolution of 3.58 at 0.143 FSC cutoff.

AlphaFold2 was used to create the initial monomer models, and Coot and Phenix were used in a series of iterations to refine the models against the experimental maps (see section 3.8.2).

The suitability of the alpha-fold model was evaluated using the secondary structure deconvolution of the far-UV CD spectra that revealed that beta sheets, in addition to the alpha-helical structures, prevail in the PLCN. On the other hand, the PLCHR2 complex predominantly contains alpha-helical structures. It demonstrates that the secondary structures derived from the CD spectra are not particularly comparable to the secondary structures composition that was derived from the experimental structures of PLCN (x-ray crystallography) and PLCHR2 (Cryo-electron microscopy). The observed discrepancies in secondary structure are affected by the noise, but most likely, a good deconvolution requires a proper reference data set, which was not available for PLCH. The deconvolution by Bestsel uses an ab initio approach, which turned out to be quite inaccurate.

The secondary and tertiary structures of the PLCN and PLCH were significantly similar. The Table 4.1 & 4.2 below shows the comparison of the secondary structure obtained from the CD spectrometry and the experimental data.

**Table 4.1 Comparison of secondary structures of PLCN measured from X-ray crystallography and CD spectrometry (190-250nm)**

	<b>Strand</b>	<b>Alpha helix</b>	<b>3-10 helix</b>	<b>Other</b>	<b>Total residues</b>
PLCN (X-ray crystallography)	152 (23.7%)	106 (16.5%)	36 (5.6%)	348 (54.2%)	642
190-250nm (CD spectrometry)	55.6%		31.5%	-	712

#### 4. Discussion

**Table 4.2 Comparison of secondary structures of PLCHR2 measured from X-ray crystallography and CD spectrometry (190-250nm)**

	Strand	Alpha helix	3-10 helix	Other	Total residues
PLCH(Cryo-EM)	126 (18.4%)	115 (16.8%)	18 (2.6%)	426 (62.2%)	685
190-250nm (CD spectrometry)	23.4%		33.7%	42.8%	915(PLCHR2)

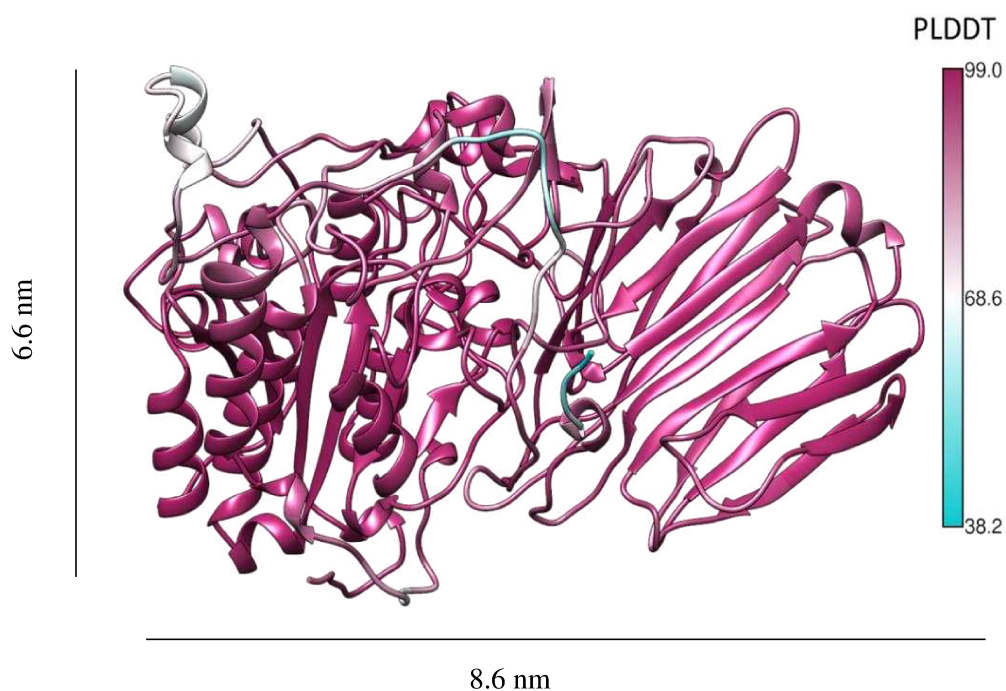


**Figure 4.8 Alpha fold model of PLCH used to fit the maps obtained from CryoEM data processing.**

This Figure 3.58 illustrates the active site of the PLCH molecule. Phosphorylation of threonine at the active site and a metal ion, here modeled as calcium, are shared features between PLCN and PLCH. In addition, the PLCH active site comprised 8 conserved active site residues. These amino acids are as follows: 60Glu, 61Asn, 120His, 203Asn, 321His, 357Asp, 358Glu, and Thr-

#### 4. Discussion

PO3 178. The first domain is composed of a core  $\beta$  sheet that has seven strands, and it is surrounded by  $\alpha$ -helices. The second domain is composed of a 14-stranded  $\beta$  sandwich. The PLCR2 chaperon was not at all visible in any of the oligomeric states, which were observed in the micrographs. The PLCR2 chaperon may be too flexible, as was also observed no density for it. This could be due to a variety of factors. It is likely that because we find trimer and dimer formation in the EM micrographs, the formation of these oligomers caused the chaperon to come off.

As suggested by the SAXS data (discussed above), PLCR2 might occlude activity of PLCH. However, the PLCHR2 was demonstrated to be biochemically functional, and it displayed higher specific activity than PLCN. This indicates that there may be some conformational changes occurring in PLCR2 or that PLCR2 may dissociate from the complex in order to catalyze the substrate. Additionally, SAXS data analysis also showed some other general features: The models with high confidence score for the complex depict PLCR2 in a configuration facing toward the top of the N-terminal domain of PLCH. The intrinsic low resolution of SAXS made it impossible to determine, by the use of 'no assumption' rigid-body modeling, the precise properties of PLCR2 binding to the PLCH N-terminal domain. For instance, it was not possible to detect the precise orientation of the PLCR2 molecule attached to the PLCH N-terminal domain. On the other hand, when the PLCH active site mapped into the CORAL models, it appeared that the PLCR2 presented itself as a steric barrier over the active site of the PLCH. If this is the case, PLCR2 prevents the PLCH from functioning properly. The preliminary findings from SAXS led to the formation of the working hypothesis that the regulatory mechanism of PLCR2 is partially responsible for blocking the active site of the PLC enzyme. However, this was in contrast with the results from the activity assays unless the observed activity would be due to the small equilibrium fraction of enzyme that could escape the binding by the chaperone. In this case, the activity of free PLCH should be even higher. Due to the various modelling possibilities to satisfy the SAXS data, it is impossible to establish with absolute certainty whether the helical bundle present at the N-terminal domain of PLCR2 causes the blockage of the active site or, if rotating the bound PLCR2 orientation, the C-terminal helix-turn-helix. In order to investigate this possibility, additional biophysical characterization, such studies on the exchange of hydrogen and deuterium, are required.

PLCs derived from Gram-positive bacteria, such as *Bacillus* or *Clostridium*, need cations in order to perform their functions effectively; on the other hand, this novel class of phospholipases derived from Gram-negative bacteria does not need any cations for their

#### 4. Discussion

activity<sup>174,175,176</sup>. In this investigation, EDTA did not influence the enzymatic activity, which confirms that cations do not affect the phospholipase activity of either PLCHR2 or PLCN. In addition, Ca(II) and Mg(II) increased the activity slightly. This could be because the positive charges may e.g. help in substrate polarization and enhance its reactivity. In EDTA treated protein H<sub>3</sub>O<sup>+</sup> could replace these cations and demonstrate similar activity to that in the presence of the cations. In this case the observed preference for metal ion binding would be simply a consequence of the high negative charge density in the active site.

PLCH and PLCN share 42.4% sequence identity and gave upon sequence alignment of the structures in ChimeraX a score of 1579.2 with a RMSD of 1.054 angstroms between 492 pruned atom pairs; (across all 625 pairs: 3.276). The PLCH structure obtained from CryoEM and the alpha fold model were also superposed. Their sequence alignment score of 3411 and RMSD between 635 pruned atom pairs was 0.879 angstroms; (across all 686 pairs: 2.001). Despite having highly similar secondary and tertiary structures, PLCN and PLCH exhibit contrasting functions. Their roles diverge significantly: PLCH has been experimentally proven to act as a SM synthase, and it also possesses phospholipase and hemolytic activities, whereas PLCN is limited to functioning solely as a phospholipase. Moreover, their lipase activities differ substantially as they display varying affinities for distinct substrates. Curiously, despite the structural similarities, the underlying reasons for these functional discrepancies remain elusive. It is puzzling that the seemingly minor differences in their structures such as the disordered structures (loops) do not provide enough insight into why their functions diverge to such a degree. Hence, it is plausible that the variation in their functions might be associated with the dynamic behaviors of these proteins. To fully comprehend the intricacies of these proteins and unveil the mechanisms driving their functional divergence, further research and in-depth studies on their dynamic properties and interactions are imperative. By exploring the dynamic aspects, one may gain deeper insights into how subtle structural variances can lead to vastly different functional outcomes in PLCN and PLCH.

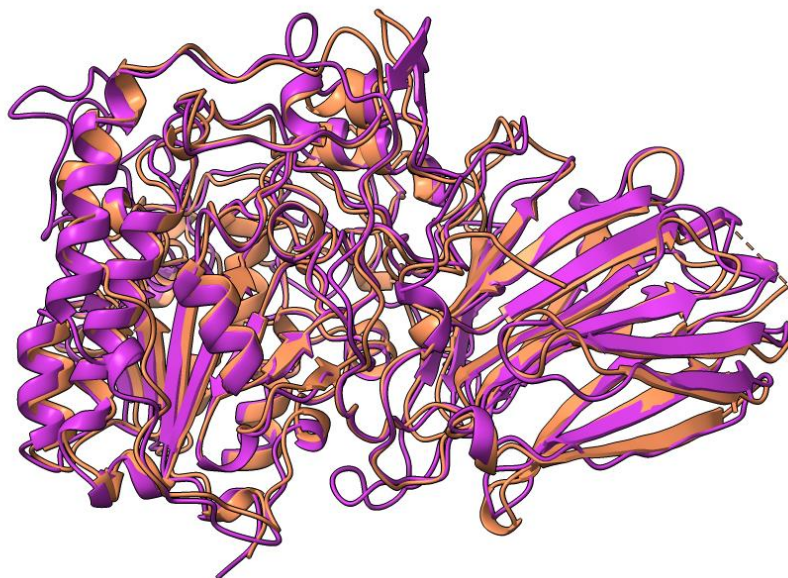


**Figure 4.9 X-ray crystallography structure of PLCN (brown) aligned with Cryo EM structure of PLCH (magenta)**

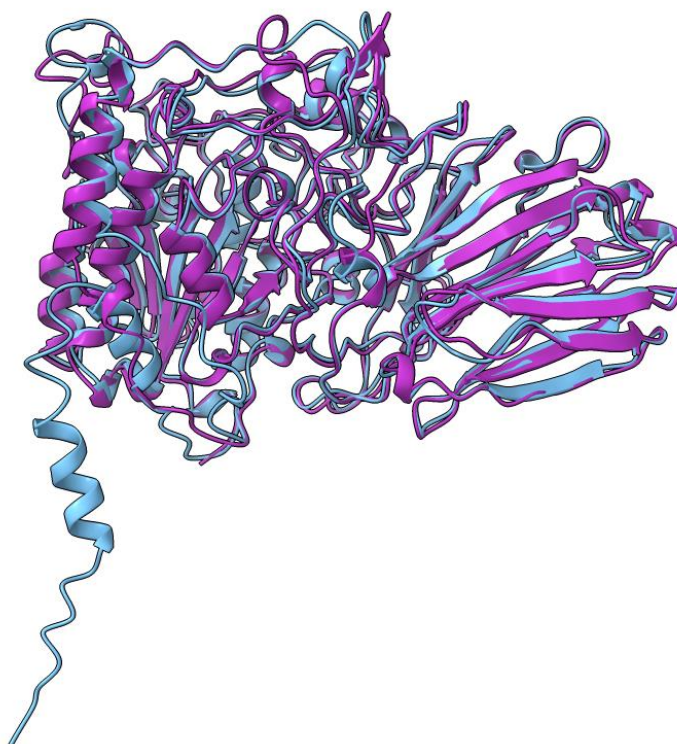


**Figure 4.10 Cryo EM structure of PLCH (magenta) superposed on Alphafold model of PLCH (Blue)**

#### 4. Discussion

Lastly, as was mentioned previously, the sequence similarity between the PLCH and the AcpA acid phosphatase from *Francisella tularensis* is only 22.13%. In a sequence alignment with acid phosphatase, the CryoEM solved structure of PLCH yielded a sequence alignment score = 585.3 and RMSD between 214 pruned atom pairs was 1.104 angstroms; (across all 395 pairs: 8.596)



**Figure 4.11 CryoEM structure of PLCH (magenta) aligned with the AcpA acid phosphatase from *Francisella tularensis* (yellow)**

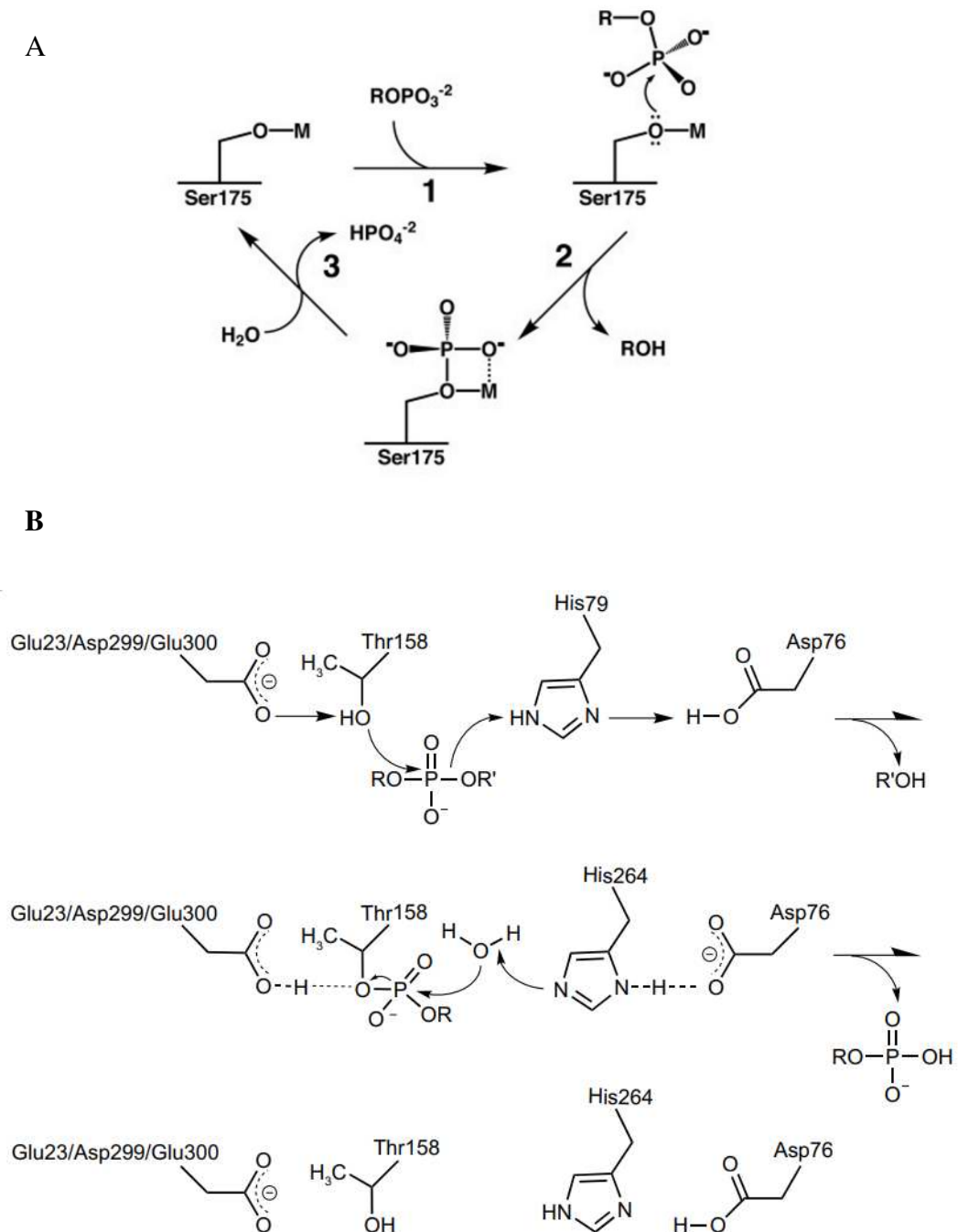
Last but not the least, the PLCHR2 complex was observed as a heterodimer (1:1) of PLCHR2 in SEC, mass photometry and SEC-SAXS. However, I still observed the higher oligomers of PLCH on the Cryo EM grids. It was not investigated in this study if these higher species have some physiological relevance. In addition to other experiments, we used the “in plate” and “on grid” DLS experiments to study the role of EM grids in the oligomerization of the PLCHR2 complex. These experiments were performed with Dr. Arne from Xtal concepts and the results are not shown here. It was observed that aggregation in the protein was noticeably increased when copper grids were utilized, and gold grids prevented the formation of any higher mass species. It was found that this was due to the gradual release of Cu (II) ions from the copper grids and the aggregation started in about 1000 seconds.

#### 4. Discussion

In addition, there is no evidence to support the claim that for the catalytic activity of PLCs in *P. aeruginosa* requires the presence of a metal ion. On the other hand, the electron density indicates the presence of a divalent ion. After numerous trials of fitting different cations into the density, calcium was the one that was in accordance with the strong density and coordination. The presence of these ions was not a buffer artefact and furthermore in accordance with the data published by Martin Stonehouse, where they found that calcium binds to both PLCH and PLCR2. The calcium ion was bound via 7 coordinating Oxygen atoms. Since there was no cation present, the fulfillment of the two positive charges could have been accomplished with the assistance of H<sub>3</sub>O<sup>+</sup>. Conversely, the introduction of Zn (II) resulted in the cessation of enzyme activity. The exact cause behind this remains uncertain. One potential explanation is that Zinc may destabilize the protein changing the charge density and coordination.

The bacterial Phospholipases C exhibit clear distinctions from their mammalian counterparts (Mammalian PLCs, explained in introduction). Bacterial PLCs are primarily involved in breaking down lipids, while the mammalian PLCs mainly function as regulators. Regarding their structure, bacterial PLCs typically share conservation only in the catalytic domain. For example, *Pseudomonas* PLCs have only two conserved histidines in common. Moreover, while mammalian PLCs are commonly referred to as PI-PLCs, *Pseudomonas* PLCs are known as PC-PLCs. The differentiation between PLCs can also be based on the biochemical environment, such as the presence of metal cofactors like Zinc or Calcium. Consequently, the structural and functional dissimilarities between bacterial and mammalian PLCs make them distinct from each other.

Additionally, there is currently no available data concerning the C-terminal domain of these PLCs. The PLC *Clostridium perfringens* (alpha toxin) contains a beta sandwich domain. It has been shown that this domain has a function of binding to the cell membrane and aiding the catalytic site to reach the lipids of the bilayer membrane. However, PLCN and PLCH doesn't have any sequence or structure similarity, apart from the fact that C terminal domain of *P.aeruginosa*'s PLCs are also rich in beta sandwich. It is plausible that this domain could play a role in membrane binding. In order to understand the role of the other domain of unknown function, further experiments are required.

4.4 Insights into the proposed branched mechanism of *Pseudomonas* PLCs

**Figure 4.12** The Proposed mechanisms of action of Phospholipase C (PLCs)

A: Proposed mechanism for AcpA, acid phosphatase. B: Proposed mechanism for Nonspecific PLCs of Arabidopsis.

#### 4. Discussion

In general, phospholipases have been the subject of research for quite some time. Human phospholipases are very well studied and are different from the bacterial phospholipases (discussed above). Bacterial Phospholipases of various types such as PLA, PLB, PLC and PLD have also been investigated in detail, along with their mechanisms of action. For the class of phospholipases C, the Gram-positive phospholipases C have been well characterized and the mechanism of phospholipid cleavage is well understood. Phospholipases C, which belong to novel type of Gram-negative bacteria or a member of the Acid phosphatase superfamily, have a mechanism that has yet to be fully elucidated.

*Pseudomonas aeruginosa's* two phospholipases C, PLCN and PLCH, are completely distinct from any other phospholipases C. They share neither their structure nor their sequence with any other phospholipases C. *Francisella tularensis* acid phosphatase AcpA is the only protein with which it shares very low sequence homology (22%)<sup>212</sup>. Felts et al. have solved the structure of AcpA with and without orthovanadate<sup>212</sup>. They had proposed a mechanism for the AcpA using their structures. They hypothesized that PLCs from Gram-negative bacteria might follow the same mechanism for the breakdown of phospholipids as the PLCH type of phospholipases since they share the same conserved amino acids in the active site. The Figure 4.12 A provides a summary of the suggested mechanism of AcpA. Within the active site of AcpA, the serine residue (S175) serves as the first nucleophile that attacks the substrate<sup>212</sup>. This nucleophile requires a metal ion in order to become active. It causes the release of an alcohol group and the production of an intermediate, phosphorylated enzyme. The phosphorylated product is released with the assistance of activated water, and the active site, which consists of the enzyme and the metal, is regenerated<sup>212</sup>.

Up until January of 2023, there was no alternative proposed mechanism. Fan et al. proposed a mechanism of action by using the structure of the plant enzyme known as Non specific Phospholipase C (NPC)<sup>213</sup>. The NPC that they had characterized was found in Arabidopsis, and with the help of the structure that they had obtained, they were able to suggest a modification of the mechanism tailored to their results. The Figure 4.12B shows another possible chemical mechanism for NPC. They discovered a phosphothreonine in their structure, and they discovered that it overlaps with the transition state of AcpA that contains orthovanadate. Thereby, T158 of NPC was therefore assumed to be the first nucleophile and belongs to the active site. They suggested that the oxygen side-chain atom of T158 is activated by E23, D299, and E300 (which serve as general bases), and it works as the initial nucleophile that attacks the phosphorus atom of the substrate<sup>213</sup>. Meanwhile, the H79 acts as the acid protonating the

#### 4. Discussion

oxygen atom of the departing diacylglycerol moiety. The resulting phosphoenzyme intermediate has a covalent P-O bond at position T158<sup>213</sup>. The H264 deprotonates water, turning it into an activated form that can act as a nucleophile to attack the phosphoenzyme intermediate and liberate the product. Structure shows that D76 is hydrogen-bound to two histidines, H79 and H264, serving to stabilize them in distinct ionic states necessary for catalysis<sup>213</sup>. By establishing a network of hydrogen bonds, N24 probably stabilizes the catalytic pocket and the intermediate<sup>213</sup>. The residues above are highly conserved in plant NPCs, and even a single point mutation affects NPC4 activity, demonstrating their importance for function<sup>213</sup>.

The catalytic pocket of PLD showed similar site-specific phosphorylation of a histidine as an alternative nucleophile<sup>213,214</sup>. Hydrolysis of phospholipid substrates by PLD involves the formation of a transition state involving phosphohistidine after the first nucleophilic attack of a substrate by the catalytic histidine<sup>215,216,217,218</sup>. Further attack by activated water on the phosphoenzyme intermediate forms the final product. In the absence of a substrate, the phosphohistidine may indicate that PLD is autoinhibited since its phosphorylation prevents the nucleophilic atom from launching the initial attack. Their structural analysis suggests that the oxygen side-chain atom of T176 initiates the initial nucleophilic attack in NPC4, and that phosphorylation of this atom inhibits the enzyme's substrate-hydrolysis activity<sup>213</sup>. The active site of PLCs consists of a hydroxyl nucleophile (like Thr-178 in PLCH) with a metal ion. The use of a threonine nucleophile in PLC and related PLCs is consistent with a double-displacement catalytic mechanism, in which a covalent intermediate is produced between the nucleophilic threonine and the phosphoryl head group of the substrate. Zinc metallophospholipases, such as *C. perfringens* -toxin and *B. cereus* phosphatidylcholine-preferring PLC, use a mechanism in which an activated water molecule makes a single nucleophilic attack on the phosphodiester substrate, by passing the need for a covalent intermediate<sup>219</sup>.

In the light of both the proposed mechanism and our findings from the structures, I can propose that the PLCs of *P.aeruginosa* might also be acting as a phosphatase. The common feature in both the above-mentioned mechanisms is that the oxygen atom of the threonine side chain acts as first nucleophile and attacks the phosphate of the phospholipid. As suggested by Fen et al. the adjacent conserved residues of the PLC active site such as E57, D334, and E333 in PLCN or E57, D334, and E333 in PLCH may serve as a general bases to activate the side chain oxygen atom of the threonine. At the same time, H118 acts as the acid that protonates the oxygen atom of the leaving diacylglycerol molecule resulting in the formation of a phosphoenzyme

#### 4. Discussion

intermediate where T178 forms a covalent P-O bond with the head group. As previously discussed, in our structures, as a transition state of the enzyme i.e. phosphate without the head group covalently bound to the threonine was found. This could be caused by the cleavage of the monoester bond between the phosphate and the head group with the help of an activated water, hence acting as a phosphatase within a phospholipase. After this step, phosphoenzyme intermediate will be formed however, now only with the phosphate. This phosphate can be removed again with an activated water or on the arrival of another molecule of phospholipid. The rest of the mechanism perhaps would be the same including the residues that are needed for activation of the waters or for the stability of the overall active site. However, it is conceivable that there exists a branching of mechanisms within Phospholipase C (PLC) (Figure 4.13). Fan et al. put forth a two-step mechanism hypothesis, suggesting that the phospholipid undergoes initial cleavage to form a phosphoenzyme, retaining the head group, which is subsequently hydrolyzed by water to yield free threonine<sup>213</sup>. Importantly, this process could take place under conditions where synthase activity is absent. Despite this proposal, the structural data I have acquired in structural investigation does not align with this particular branch of the mechanism, as I have observed the presence of the phosphorylated enzyme without the associated head group. Instead, the findings indicate an alternative scenario where the enzyme might exhibit phosphatase-like behavior, causing the breakdown of the phospholipid into its constituent components: fatty acids, head group (e.g. choline, serine etc.), and phosphate. This intriguing mechanism suggests potential implications in the direction of sphingomyelin synthesis, where the enzyme necessitates the presence of head groups for the synthesis process. Furthermore, it would allow *Pseudomonas* to fulfill its phosphate requirements. Apart from this there also have been studies showing that these AcpA can also cleave the synthetic substrate (NPPC) suggesting PLC activity<sup>220</sup>. Hence, this AcpA acid phosphatase behave as phospholipase. Similarly, perhaps these class of phospholipases could also behave as phosphatases. The inbuilt phosphatase within a phospholipase can also be supported by some other studies as it was recommended by Prakash et.al that by comparing the degree of hydrolysis towards p-NPPC artificial substrate for phospholipases, and phosphatases, and p-NPP, which is an artificial substrate for phosphatases, one could differentiate between PLC- and phosphatase activity<sup>221</sup>. Flieger et. al. analyzed the various enzyme preparations to determine their levels of phosphatase activity by measuring the amount of inorganic phosphate that was liberated from phosphomonoesters<sup>132</sup>. They were able to show that the breakdown of p-NPP by phosphatases was a substantially higher than that of the other enzymes. On the other hand, they were able to demonstrate that other enzymes, such as PC-PLC and PLD, were also

#### 4. Discussion

capable of hydrolyzing p-NPP<sup>132</sup>. Therefore, it may be challenging to correctly differentiate PLC and phosphatase by comparing p-NPPC and p-NPP hydrolysis in circumstances where enzyme quantities are unknown<sup>132</sup>. Therefore, PLCs in this context could also potentially function as a PLD, responsible for cleaving free head groups.

Nonetheless, the importance of the calcium ion in the synthetase activity has been proven limited. Although the presence of calcium does lead to a slight increase in SM synthetase activity, the introduction of EDTA or EGTA did influence the SM synthesis<sup>222</sup>. In the PLCN and PLCH structures, both were discovered to have undergone phosphorylation at the threonine active site. While PLCH is recognized as a well-known SM synthase, the phosphorylation of PLCN suggests that it might also operate through a similar 3-step mechanism and might act as a synthetase. PLCN has been subject to investigation, and its ability to produce SM has been ruled out. However, the synthesis of other phospholipids using PLCN has yet to be thoroughly explored.

In conclusion, the divergent mechanisms proposed for PLC warrant further exploration and scrutiny to elucidate the precise processes at play and the specific conditions that influence the enzyme's behavior. By understanding these mechanisms better, we can gain valuable insights into various cellular processes where PLC and sphingomyelin synthesis are involved, potentially opening up new avenues for therapeutic interventions by selective inhibition and advancing our understanding of cellular signaling pathways.

Fen et. al. also reported the presence of phosphorylated threonine in their crystal structure but they explained with the presence of phosphate buffer in their crystallization condition<sup>213</sup>. For the PLCs investigated in this work this explanation can be excluded because, there was no phosphate present in the buffers used for purification or crystallization. Moreover, they suggest that the activity is inhibited by the presence of phosphate at the active site, which is contrary to my results as the phosphorylated enzyme was active (phosphorylation was confirmed by LC/mass-mass, showing that phosphorylation occurred inside the *E.coli* cells). However, whether all the threonine residues are phosphorylated, is still needed to be further validated with more experimental data.

#### 4. Discussion

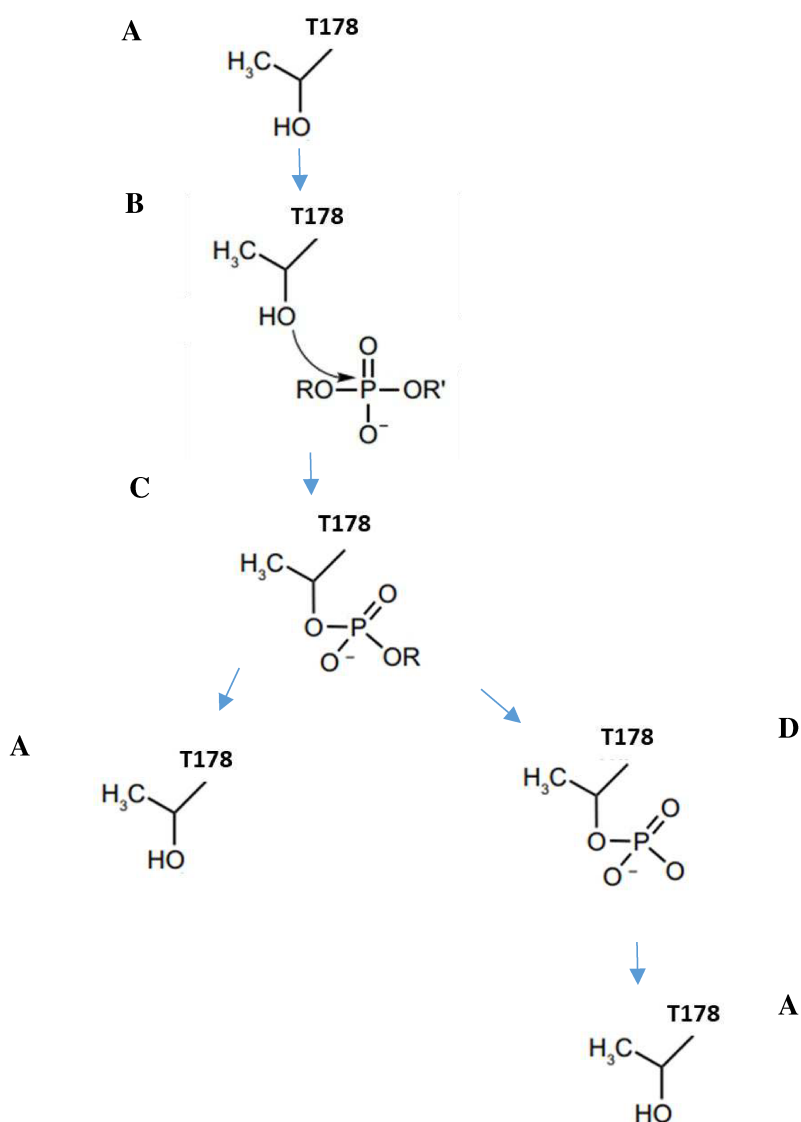


**Figure 4.13 Proposed branched pathway for PLCs of *Pseudomonas aeruginosa*.**

This proposed branched pathway explains the phosphatase or PLD activity of *Pseudomonas aeruginosa*'s PLCs. Previously known mechanism suggests a two-step hydrolysis (A- B-C A) with first nucleophilic attack by threonine side chain oxygen atom and the second by an activated water. Here, in this study, three-step mechanism (A-B-C-D-A) has been proposed with an intermediate step of phosphorylated enzyme with the head group. **A** free threonine, **B** nucleophilic attack by threonine side chain oxygen atom, **C** phosphorylated enzyme with the head group, **D** phosphorylated enzyme without the head group. (Metal ion here calcium might also play in stabilizing the D stage of the enzyme. Three-step mechanism perhaps is necessary for the synthetase activity of the PLCs. Since the PLCs cannot store the head groups to wait and synthesize another phospholipid because of small active site cleft. The phosphatase/PLD activity helps the enzyme to simultaneously cleave the head group, making it

## 4. Discussion

available for the phospholipid synthetic reaction. However, metal ion is not necessary for the PLC activity but it could be playing a role in synthetase activity of PLCs by stabilizing the cleaved protein for the incoming synthetase activity.

### 4.5 Outlook

The phospholipases C of *Pseudomonas aeruginosa* are members of the acid phosphatase superfamily and belong to a novel class of Gram-negative PLCs. There is sufficient data showing that PLCH and PLCN play a role in the enhanced increased pathogenicity of *P. aeruginosa*. During the acute phase of the infection, they play a crucial role as virulence factors. Clinical isolates obtained from patients with burns or cystic fibrosis indicated that PLCH and PLCN are present in more than 90% of the strains, and in high titration values<sup>223</sup>. It has also been explored that PLCH knockout reduce *P.aeruginosa* pathogenicity by about 50%<sup>69</sup>.

In this study, both the PLCH and PLCN have been successfully characterized biochemically, biophysically and structurally. The next steps for taking this project forward would be the screening the inhibitors for both of the PLCs with the help of the activity assays. However, before screening the Gram-negative PLCs inhibitors a careful comparison with human phosphatases and phospholipases is required in order to narrow the spectrum of potential inhibitors to substances that do not affect these human proteins by modeling the compounds or using Bioinformatics' tools. Secondly, co-crystallization of the inhibitors or ligands like artificial substrate or product should be done to perhaps prove the proposed mechanism experimentally. Additionally, cellular assays can also be done to see which cell lines are resistant to these PLCs and which ones are susceptible. Cellular assays can also perhaps help in understanding the synthetase activity of the PLCs. Apart from that, the role of the chaperon PLCR1 and PLCR2 in PLCH activity or perhaps inhibition of PLCH merits further investigation. In this research, AFM experiments provided an initial insight into pore formation. Furthermore, cellular assays can aid in comprehending the localization of the PLCs, as well as the mechanism behind pore formation and the lysis of infected cells. Lastly, one can also try to understand the physiological relevance, if any, of the higher oligomers observed in this study.

## Summary

Antibiotic resistance has become a major concern in treating bacterial infections, particularly Gram-negative bacterial infections. Among these, *Pseudomonas aeruginosa* is an opportunistic pathogen causing infections in hospitalized and immunocompromised individuals. Multi-drug resistance (MDR) has become increasingly prevalent, making treatment challenging. *P. aeruginosa* is capable of secreting various extracellular virulence factors, including phospholipases, which play a crucial role in its pathogenicity. In this study, I focused on characterizing two types of phospholipases C present in *Pseudomonas aeruginosa*: PLCH, and PLCN. I conducted various experiments to understand the functionality and structures of these phospholipases. I expressed both PLCH with its chaperon PLCHR2 and PLCN in *E.coli*. Affinity chromatography and size exclusion chromatography was used to purify the proteins having 6 N terminal His tag. To ensure the integrity and identity of the proteins, I conducted Western blot analyses using anti-His antibodies, confirming the intactness of the N-terminal. Additionally, Mass spectrometry and LC-Mass/mass helped confirm the presence of full-length PLCH, PLCHR2, and PLCN. Moreover, I found that PLCH exhibited a posttranslational modification in the form of phosphorylation. Biophysical and biochemical characterizations followed. I determined the oligomerization state of the proteins in solution using Mass photometry and Dynamic Light Scattering (DLS). Both PLCHR2 and PLCN were present as monomers in solution. PLCHR2 was a heterodimer of PLCH and PLCHR2. Further investigations were necessary to understand the stoichiometry of the heterodimer. I employed SEC-SAXS measurements, which revealed that the PLCHR2 heterodimer was present in a 1:1 ratio. Next, I explored the enzymatic activity of the phospholipases. Recombinant PLCN and PLCHR2 demonstrated the ability to cleave phospholipids both in vitro and in vivo, using an artificial substrate (NPPC) and the original substrate found in cell membranes (HeLa cells), respectively. Moreover, I discovered that threonine phosphorylation occurred in the active site of PLCN and PLCHR2, with mutants T176A and T178A showing significantly lower activity, highlighting the residue's importance in catalysis. Interestingly, unlike phospholipases derived from Gram-positive bacteria, PLCH and PLCN did not require cations for their activity. EDTA did not influence their enzymatic activity, indicating that cations did not affect their functionality. However, Ca (II) and Mg(II) slightly increased the activity, possibly due to the need for positive charges to stabilize the active site's negatively charged cleft. I also investigated the hemolytic capability of PLCHR2 and PLCN on sheep red blood cells. PLCHR2 effectively lysed the cells, while PLCN had no effect on hemolysis. Additionally, atomic force microscopy allowed me to observe the formation of holes in lipid bilayers caused by the PLCHR2 complex.

These holes gradually grew larger and eventually closed or filled up. In this project, I aimed to elucidate the first structures of a novel class of Gram-negative phospholipases, specifically the PLCs of *P. aeruginosa*. Two types of PLCs, PLCH and PLCN, have been known since the 1980s, but their 3D structures were still unknown. Before proceeding with X-ray crystallography or Cryo-EM for structure determination, I first investigated the stability of their secondary and tertiary structures. I employed Circular Dichroism (CD) and Fluorescence spectroscopy to study secondary and tertiary structure stability, respectively. CD spectra indicated that beta sheets and alpha-helical structures prevail in PLCN, while PLCHR2 predominantly contains alpha-helical structures. For insight into the secondary structure's stability, I computed the melting temperature ( $T_m$ ) by observing changes in CD spectra at different temperatures. PLCN and PLCHR2 showed  $T_m$  values of 45°C and 60°C, respectively, with PLCHR2 being more stable. The  $T_m$  difference could be attributed to the presence of chaperon PLCR2 in the PLCHR2 complex, providing enhanced stability and secretion abilities. Moving on to tertiary structure stability, I used fluorescence spectroscopy and observed a red shift during thermal denaturation, indicating the exposure of tryptophan residues. These residues were predominantly present on the outer surface of the protein, contributing to its disordered structure. With a deeper understanding of secondary and tertiary structures, I attempted crystallization. With the help of in situ proteolysis using trypsin, crystals improved, and diffraction data was collected at 1.5 Å resolution. For PLCHR2, I used CryoEM for solving its structure. Overall, this project successfully revealed the first structures of a novel class of Gram-negative phospholipases, providing crucial insights into their secondary and tertiary structures, as well as their catalytic mechanisms. These findings open new avenues for understanding the functional significance of PLCs in *P. aeruginosa* and their potential roles as therapeutic targets. Based on the proposed mechanisms in literature and my own structural findings, I also propose that PLCs of *P. aeruginosa* may act as phosphatases within a phospholipase. Looking forward, the PLCs of *P. aeruginosa*, are promising targets for understanding their role in enhancing pathogenicity. To experimentally validate the proposed mechanism, co-crystallization of inhibitors or ligands, such as artificial substrates or products, can be conducted. Cellular assays could reveal information about the enzymes' impact on different cell lines, their localization, and how they may disrupt infected cells. In conclusion, this research provides valuable insights into the unique mechanisms of PLCs in *P. aeruginosa* and paves the way for future explorations to understand their pathogenic role and potential therapeutic implications.

## Zusammenfassung

Die Antibiotikaresistenz ist ein zunehmendes Problem bei der Behandlung von bakteriellen Infektionen, insbesondere bei Gram-negativen Bakterien. *Pseudomonas aeruginosa* ist ein opportunistischer Krankheitserreger, der bei hospitalisierten und immungeschwächten Personen Infektionen verursacht. Die hohe Multiresistenz (MDR) erschwert die Behandlung zunehmend. *P. aeruginosa* ist in der Lage, verschiedene extrazelluläre Virulenzfaktoren, einschließlich Phospholipasen, auszuschleiden, die eine entscheidende Rolle bei ihrer Pathogenität spielen. In dieser Studie konzentrierte ich mich auf die Charakterisierung von zwei Typen von Phospholipasen C in *Pseudomonas aeruginosa*: PLCH und PLCN. Verschiedene Experimente wurden durchgeführt, um die Funktionalität und Struktur dieser Phospholipasen zu verstehen. Beide Proteine wurden in *E.coli* exprimiert und durch Affinitätschromatographie und Größenausschlusschromatographie gereinigt. Western-Blot-Analysen bestätigten die Integrität der N-terminalen His-Tag. Massenspektrometrie und LC-Mass/mass bestätigten die Anwesenheit von vollständigem PLCH, PLCHR2 und PLCN. Ich entdeckte, dass PLCH eine posttranslationale Modifikation in Form von Phosphorylierung aufwies. Biophysikalische und biochemische Charakterisierungen folgten. Die Oligomerisierungszustände der Proteine wurden durch Massenphotometrie und Dynamic Light Scattering (DLS) bestimmt. Beide Proteine lagen als Monomere vor. PLCHR2 war ein Heterodimer aus PLCH und PLCHR2. Die enzymatische Aktivität der Phospholipasen wurde untersucht. Rekombinantes PLCN und PLCHR2 zeigten die Fähigkeit, Phospholipide sowohl in vitro als auch in vivo zu spalten, wobei ein künstliches Substrat (NPPC) und das ursprüngliche Substrat in Zellmembranen (HeLa-Zellen) verwendet wurden. Ich entdeckte auch, dass die Phosphorylierung von Threonin in der aktiven Stelle von PLCN und PLCHR2 stattfand und Mutanten T176A und T178A eine signifikant geringere Aktivität zeigten. Interessanterweise benötigten PLCH und PLCN im Gegensatz zu Phospholipasen aus Gram-positiven Bakterien keine Kationen für ihre Aktivität. EDTA beeinflusste ihre enzymatische Aktivität nicht. Die Untersuchung der hämolytischen Fähigkeit von PLCHR2 und PLCN an Schafsroten Blutkörperchen ergab, dass PLCHR2 die Zellen effektiv lysierte, während PLCN keine Wirkung auf die Hämolyse hatte. Atomic Force Microscopy ermöglichte es, die Bildung von Löchern in Lipiddoppelschichten durch das PLCHR2-Komplex zu beobachten. Ich habe versucht, die erste Struktur einer neuen Klasse von Gram-negativen Phospholipasen zu entschlüsseln, insbesondere die PLCs von *P. aeruginosa*. Bevor ich mit der Röntgenkristallographie oder der Kryo-Elektronenmikroskopie zur Strukturbestimmung fortfahre, habe ich die Stabilität ihrer sekundären und tertiären Strukturen untersucht. Mit Hilfe von Zirkulardichroismus (CD) und Fluoreszenzspektroskopie konnte ich

die Sekundär- und Tertiärstrukturstabilität bestimmen. Mit einem besseren Verständnis der Struktur versuchte ich die Kristallisation. Insgesamt hat dieses Projekt erfolgreich die erste Struktur einer neuen Klasse von Gram-negativen Phospholipasen aufgedeckt, was entscheidende Einblicke in ihre sekundären und tertiären Strukturen sowie ihre katalytischen Mechanismen liefert. Diese Erkenntnisse eröffnen neue Möglichkeiten, die funktionelle Bedeutung von PLCs in *P. aeruginosa* und ihre potenzielle Rolle als therapeutische Zielstrukturen zu verstehen. Um den vorgeschlagenen Mechanismus experimentell zu bestätigen, könnte die Co-Kristallisation von Inhibitoren oder Liganden wie künstlichen Substraten oder Produkten durchgeführt werden. Zelluläre Assays könnten Informationen über den Einfluss der Enzyme auf verschiedene Zelllinien, ihre Lokalisation und ihre Fähigkeit, infizierte Zellen zu stören, liefern. Zusammenfassend liefert diese Forschung wertvolle Einblicke in die einzigartigen Mechanismen von PLCs in *P. aeruginosa* und ebnet den Weg für zukünftige Erkundungen, um ihre pathogene Rolle und potenzielle therapeutische Anwendungen zu verstehen.

## Bibliography

1. Smith, A. & Hussey, M. American Society for Microbiology: Gram Stain Protocols. *Am. Soc. Microbiol.* 1–9 (2020).
2. Oliveira, J. & Reygaert, W. C. *Gram Negative Bacteria*. (StatPearls Publishing, Treasure Island (FL), 2022).
3. Silhavy, T. J., Kahne, D. & Walker, S. The Bacterial Cell Envelope1 T. J. Silhavy, D. Kahne and S. Walker, . *Cold Spring Harb Perspect Biol* **2**, 1–16 (2010).
4. Moore, N. M. & Flaws, M. L. Introduction: Pseudomonas aeruginosa. *Clin. Lab. Sci.* **24**, 41–42 (2011).
5. Tsang, K. W. *et al.* Pseudomonas aeruginosa adherence to human basement membrane collagen in vitro. *Eur. Respir. J.* **21**, 932–938 (2003).
6. Grace, A., Sahu, R., Owen, D. R. & Dennis, V. A. Pseudomonas aeruginosa reference strains PAO1 and PA14: A genomic, phenotypic, and therapeutic review. *Front. Microbiol.* **13**, 1–15 (2022).
7. Abdulhaq, N., Nawaz, Z., Zahoor, M. A. & Siddique, A. B. Association of biofilm formation with multi drug resistance in clinical isolates of pseudomonas aeruginosa. *EXCLI J.* **19**, 201–208 (2020).
8. Ladner, C. L., Yang, J., Turner, R. J. & Edwards, R. A. Visible fluorescent detection of proteins in polyacrylamide gels without staining. *Anal. Biochem.* **326**, 13–20 (2004).
9. Vasil, M. L. Pseudomonas aeruginosa: Biology, mechanisms of virulence, epidemiology. *J. Pediatr.* **108**, 800–805 (1986).
10. Qin, S. *et al.* Pseudomonas aeruginosa: pathogenesis, virulence factors, antibiotic resistance, interaction with host, technology advances and emerging therapeutics. *Signal Transduct. Target. Ther.* **7**, 1–27 (2022).
11. Pollack, M. The virulence of Pseudomonas aeruginosa. *Rev. Infect. Dis.* **6 Suppl 3**, (1984).
12. Jurado-Martín, I., Sainz-Mejías, M. & McClean, S. Pseudomonas aeruginosa: An audacious pathogen with an adaptable arsenal of virulence factors. *Int. J. Mol. Sci.* **22**, 1–37 (2021).
13. Kipnis, E., Sawa, T. & Wiener-Kronish, J. Targeting mechanisms of Pseudomonas aeruginosa pathogenesis. *Med. Mal. Infect.* **36**, 78–91 (2006).
14. Ma, Q., Zhai, Y., Schneider, J. C., Ramseier, T. M. & Saier, M. H. Protein secretion systems of Pseudomonas aeruginosa and P. fluorescens. *Biochim. Biophys. Acta - Biomembr.* **1611**, 223–233 (2003).
15. Filloux, A. Protein secretion systems in Pseudomonas aeruginosa: An essay on diversity, evolution, and function. *Front. Microbiol.* **2**, 1–21 (2011).
16. Green, E. R. & Mecsas, J. Bacterial Secretion Systems: An Overview. *Microbiol. Spectr.* **4**, (2016).
17. Bleves, S. *et al.* Protein secretion systems in Pseudomonas aeruginosa: A wealth of

- pathogenic weapons. *Int. J. Med. Microbiol.* **300**, 534–543 (2010).
18. Wu, W., Jin, Y., Bai, F. & Jin, S. *Pseudomonas aeruginosa*. *Molecular Medical Microbiology* (Elsevier Ltd, 2014). doi:10.1016/B978-0-12-397169-2.00041-X.
  19. Sheremet, A. B., Nesterenko, L. N. & Zigangirova, N. A. The Type Three Secretion System of *Pseudomonas aeruginosa* as a Target for Development of Antivirulence Drugs. *Mol. Genet. Microbiol. Virol.* **35**, 1–13 (2020).
  20. Engel, J. & Balachandran, P. Role of *Pseudomonas aeruginosa* type III effectors in disease. *Curr. Opin. Microbiol.* **12**, 61–66 (2009).
  21. Hauser, A. R. The type III secretion system of *Pseudomonas aeruginosa*: Infection by injection. *Nat. Rev. Microbiol.* **7**, 654–665 (2009).
  22. Juhas, M., Crook, D. W. & Hood, D. W. Type IV secretion systems: Tools of bacterial horizontal gene transfer and virulence. *Cell. Microbiol.* **10**, 2377–2386 (2008).
  23. Leighton, T. L., Buensuceso, R. N. C., Howell, P. L. & Burrows, L. L. Biogenesis of *Pseudomonas aeruginosa* type IV pili and regulation of their function. *Environ. Microbiol.* **17**, 4148–4163 (2015).
  24. Da Mata Madeira, P. V. *et al.* Structural Basis of Lipid Targeting and Destruction by the Type v Secretion System of *Pseudomonas aeruginosa*. *J. Mol. Biol.* **428**, 1790–1803 (2016).
  25. Li, Y., Chen, L., Zhang, P., Bhagirath, A. Y. & Duan, K. ClpV3 of the H3-Type VI Secretion System (H3-T6SS) Affects Multiple Virulence Factors in *Pseudomonas aeruginosa*. *Front. Microbiol.* **11**, 1–14 (2020).
  26. Freudl, R. Signal peptides for recombinant protein secretion in bacterial expression systems. *Microb. Cell Fact.* 1–10 (2018) doi:10.1186/s12934-018-0901-3.
  27. Sandkvist, M. Type II secretion and pathogenesis. *Infect. Immun.* **69**, 3523–3535 (2001).
  28. Sauvage, S. & Hardouin, J. Exoproteomics for better understanding *Pseudomonas aeruginosa* virulence. *Toxins (Basel)*. **12**, (2020).
  29. Ball, G., Durand, É., Lazdunski, A. & Filloux, A. A novel type II secretion system in *Pseudomonas aeruginosa*. *Mol. Microbiol.* **43**, 475–485 (2002).
  30. Ramrakhiani, L. & Chand, S. Recent Progress on Phospholipases : Different Sources , Assay Methods , Industrial Potential and Pathogenicity. 991–1022 (2011) doi:10.1007/s12010-011-9190-6.
  31. Vasil, M. L. *Pseudomonas aeruginosa* phospholipases and phospholipids. in *Pseudomonas* vol. 4 69–97 (2006).
  32. Flores-díaz, M., Monturiol-gross, L., Naylor, C. & Alape-girón, A. Bacterial Sphingomyelinases and Phospholipases as Virulence Factors. **80**, 597–628 (2016).
  33. Lee, V. T. *et al.* Pseudolipasin A is a specific inhibitor for phospholipase A2 activity of *Pseudomonas aeruginosa* cytotoxin ExoU. *Infect. Immun.* **75**, 1089–1098 (2007).
  34. Phillips, R. M., Six, D. A., Dennis, E. A. & Ghosh, P. In Vivo Phospholipase Activity of the *Pseudomonas aeruginosa* Cytotoxin ExoU and Protection of Mammalian Cells with Phospholipase A2 Inhibitors. *J. Biol. Chem.* **278**, 41326–41332 (2003).

35. Jiang, F., Huang, S., Imadad, K. & Li, C. Cloning and expression of a gene with phospholipase B activity from *Pseudomonas fluorescens* in *Escherichia coli*. *Bioresour. Technol.* **104**, 518–522 (2012).
36. Macfarlane, M. G. & Knight, B. C. The biochemistry of bacterial toxins: The lecithinase activity of *Cl. welchii* toxins. *Biochem. J.* **35**, 884–902 (1941).
37. McDermott, M. I., Wang, Y., Wakelam, M. J. O. & Bankaitis, V. A. Mammalian phospholipase D: Function, and therapeutics. *Prog. Lipid Res.* **78**, 101018 (2020).
38. Yao, Y. *et al.* Phospholipase D as a key modulator of cancer progression. *Biol. Rev.* **95**, 911–935 (2020).
39. Shoriridge, V. D., Lazdunski, A. & Vasil, M. L. Osmoprotectants and phosphate regulate expression of phospholipase C in *Pseudomonas aeruginosa*. *Mol. Microbiol.* **6**, 863–871 (1992).
40. Marquis, H., Goldfine, H. & Portnoy, D. A. Proteolytic pathways of activation and degradation of a bacterial phospholipase C during intracellular infection by *Listeria monocytogenes*. *J. Cell Biol.* **137**, 1381–1392 (1997).
41. Chadha, J., Harjai, K. & Chhibber, S. Revisiting the virulence hallmarks of *Pseudomonas aeruginosa*: a chronicle through the perspective of quorum sensing. *Environ. Microbiol.* **24**, 2630–2656 (2022).
42. Hélène Marquis\* and Elizabeth J. Hager. pH-regulated activation and release of a bacteria-associated phospholipase C during intracellular infection by *Listeria monocytogenes*. *Bone* **23**, 1–7 (2008).
43. Schmiel, D. H. & Miller, V. L. Bacterial phospholipases and pathogenesis. *Microbes Infect.* **1**, 1103–1112 (1999).
44. de Sousa, T. *et al.* Study of Antimicrobial Resistance, Biofilm Formation, and Motility of *Pseudomonas aeruginosa* Derived from Urine Samples. *Microorganisms* **11**, (2023).
45. McDaniel, C. T., Panmanee, W. & Hassett, D. J. An Overview of Infections in Cystic Fibrosis Airways and the Role of Environmental Conditions on *Pseudomonas aeruginosa* Biofilm Formation and Viability. *Cyst. Fibros. Light New Res.* (2015) doi:10.5772/60897.
46. Kadamur, G. & Ross, E. M. Mammalian phospholipase C. *Annu. Rev. Physiol.* **75**, 127–154 (2013).
47. Singh, V. *et al.* Phospholipase C: underrated players in microbial infections. *Front. Cell. Infect. Microbiol.* **13**, 1–17 (2023).
48. Fukami, K., Inanobe, S., Kanemaru, K. & Nakamura, Y. Phospholipase C is a key enzyme regulating intracellular calcium and modulating the phosphoinositide balance. *Prog. Lipid Res.* **49**, 429–437 (2010).
49. Bunney, T. D. & Katan, M. PLC regulation: Emerging pictures for molecular mechanisms. *Trends Biochem. Sci.* **36**, 88–96 (2011).
50. Bogiel, T., Prażyńska, M., Kwiecińska-Piróg, J., Gospodarek-Komkowska, E. & Mikucka, A. Carbapenem-resistant *pseudomonas aeruginosa* strains-distribution of the essential enzymatic virulence factors genes. *Antibiotics* **10**, 1–10 (2021).
51. Monturiol-Gross, L., Villalta-Romero, F., Flores-Díaz, M. & Alape-Girón, A. Bacterial

- phospholipases C with dual activity: phosphatidylcholinesterase and sphingomyelinase. *FEBS Open Bio* **11**, 3262–3275 (2021).
52. Gray, G. L. & Vasil, M. L. Mapping of a gene controlling the production of phospholipase C and alkaline phosphatase in *Pseudomonas aeruginosa*. *MGG Mol. Gen. Genet.* **183**, 403–405 (1981).
  53. Stonehouse, M. J. *et al.* A novel class of microbial phosphocholine-specific phospholipases C. *Mol. Microbiol.* **46**, 661–676 (2002).
  54. Barker, A. P. *et al.* A novel extracellular phospholipase C of *Pseudomonas aeruginosa* is required for phospholipid chemotaxis. *Mol. Microbiol.* **53**, 1089–1098 (2004).
  55. Gray, G. L., Berka, R. M. & Vasil, M. L. Phospholipase C Regulatory Mutation of *Pseudomonas aeruginosa* That Results in Constitutive Synthesis of Several Phosphate-Repressible Proteins. **150**, 1221–1226 (1982).
  56. López, D. J. *et al.* Multiple phospholipid substrates of phospholipase C/sphingomyelinase HR2 from *Pseudomonas aeruginosa*. *Chem. Phys. Lipids* **164**, 78–82 (2011).
  57. Liu, P. V. The roles of various fractions of *pseudomonas aeruginosa* in its pathogenesis. *J. Infect. Dis.* **116**, 481–489 (1966).
  58. Kurioka, S. & Liu, P. V. Effect of the hemolysin of *Pseudomonas aeruginosa* on phosphatides and on phospholipase c activity. *J. Bacteriol.* **93**, 670–674 (1967).
  59. Berka, R. M. & Vasil, M. L. Phospholipase C ( Heat-Labile Hemolysin ) of *Pseudomonas aeruginosa* : Purification and Preliminary Characterization. **152**, 239–245 (1982).
  60. Vasil, M. L., Berka, R. M., Gray, G. L. & Nakai, H. Cloning of a phosphate-regulated hemolysin gene (phospholipase C) from *Pseudomonas aeruginosa*. *J. Bacteriol.* **152**, 431–440 (1982).
  61. Sage, A. E. & Vasil, M. L. Osmoprotectant-dependent expression of *plcH*, encoding the hemolytic phospholipase C, is subject to novel catabolite repression control in *Pseudomonas aeruginosa* PAO1. *J. Bacteriol.* **179**, 4874–4881 (1997).
  62. Wargo, M. J. Choline Catabolism to Glycine Betaine Contributes to *Pseudomonas aeruginosa* Survival during Murine Lung Infection. *PLoS One* **8**, 1–7 (2013).
  63. Snyder, A., Vasil, A. I., Zajdowicz, S. L., Wilson, Z. R. & Vasil, M. L. Role of the *Pseudomonas aeruginosa* *PlcH* Tat Signal Peptide in Protein Secretion , Transcription , and Cross-Species Tat Secretion System Compatibility. **188**, 1762–1774 (2006).
  64. Shen, B., Tai, P. C., Pritchard, A. E. & Vasil, M. L. Nucleotide Sequences and Expression in *Escherichia coli* of the In-Phase Overlapping *Pseudomonas aeruginosa* *plcR* Genes. 4602–4607 (1987).
  65. Cota-Gomez, A. *et al.* *plcR1* and *plcR2* are putative calcium-binding proteins required for secretion of the hemolytic phospholipase C of *Pseudomonas aeruginosa*. *Infect. Immun.* **65**, 2904–2913 (1997).
  66. Luberto, C. *et al.* Purification, characterization, and identification of a sphingomyelin synthase from *Pseudomonas aeruginosa*: *PlcH* is a multifunctional enzyme. *J. Biol. Chem.* **278**, 32733–32743 (2003).

67. Vasil, M. L. *et al.* A Complex Extracellular Sphingomyelinase of *Pseudomonas aeruginosa* Inhibits Angiogenesis by Selective Cytotoxicity to Endothelial Cells. **5**, (2009).
68. Terada, L. S., Johansen, K. A., Nowbar, S., Vasil, A. I. & Vasil, M. L. *Pseudomonas aeruginosa* hemolytic phospholipase C suppresses neutrophil respiratory burst activity. *Infect. Immun.* **67**, 2371–2376 (1999).
69. Ostroff, R. M., Wretling, B. & Vasil, M. L. Mutations in the hemolytic-phospholipase C operon result in decreased virulence of *Pseudomonas aeruginosa* PAO1 grown under phosphate-limiting conditions. *Infect. Immun.* **57**, 1369–1373 (1989).
70. Kida, Y., Shimizu, T. & Kuwano, K. Cooperation between LepA and PlcH contributes to the in vivo virulence and growth of *Pseudomonas aeruginosa* in mice. *Infect. Immun.* **79**, 211–219 (2011).
71. Romé Voulhoux, Geneviève Ball, Bérengère Ize, Michael L. Vasil, Andrée Lazdunski, Long-Fei Wu, 1 and Alain Filloux. Involvement of the twin-arginine translocation system in protein secretion via the type II pathway. **20**, 6735–6741 (2001).
72. Davies, C. *et al.* Hyperbiofilm phenotype of *Pseudomonas aeruginosa* defective for the PlcB and PlcN secreted phospholipases. *Lewenza*. 1–26 (2020).
73. Ostroff, R. M., Vasil, A. I. & Vasil, M. L. Molecular comparison of a nonhemolytic and a hemolytic phospholipase C from *Pseudomonas aeruginosa*. *J. Bacteriol.* **172**, 5915–5923 (1990).
74. Elleboudy, N. S., Aboulwafa, M. M. & Hassouna, N. A. H. Phospholipase C from *Pseudomonas aeruginosa* and *Bacillus cereus*; characterization of catalytic activity. *Asian Pac. J. Trop. Med.* **7**, 860–866 (2014).
75. Bassetti, M., Vena, A., Croxatto, A., Righi, E. & Guery, B. How to manage *Pseudomonas aeruginosa* infections. *Drugs Context* **7**, 1–18 (2018).
76. Kordes, A. *et al.* Establishment of an induced memory response in *Pseudomonas aeruginosa* during infection of a eukaryotic host. *ISME J.* **13**, 2018–2030 (2019).
77. Miles, J. S. & Wolf, C. R. Principles of DNA cloning. *Br. Med. J.* **299**, 1019–1022 (1989).
78. Vosberg, H. P. The polymerase chain reaction: an improved method for the analysis of nucleic acids. *Hum. Genet.* **83**, 1–15 (1989).
79. Saiki, R. K. *et al.* Primer-directed enzymatic amplification of DNA with a thermostable DNA polymerase. *Science (80-. )*. **239**, 487–491 (1988).
80. Di Felice, F., Micheli, G. & Camilloni, G. Restriction enzymes and their use in molecular biology: An overview. *J. Biosci.* **44**, (2019).
81. Carroll, D. Recombinant DNA. *Brenner's Encycl. Genet. Second Ed.* **68**, 79–80 (2013).
82. Voytas Daniel. Resolution and Recovery of DNA Fragments. *Curr. Protoc. Immunol.* 1–8 (2001) doi:10.1002/0471142735.im1004s02.
83. Deng, W. P. & Nickoloff, J. A. Site-directed mutagenesis of virtually any plasmid by eliminating a unique site. *Anal. Biochem.* **200**, 81–88 (1992).
84. Fisher, C. L. & Pei, G. K. Modification of a PCR-based site-directed mutagenesis

- method. *Biotechniques* **23**, 570–574 (1997).
85. Ho, S. N., Hunt, H. D., Horton, R. M., Pullen, J. K. & Pease, L. R. Site-directed mutagenesis by overlap extension using the polymerase chain reaction. *Gene* **77**, 51–59 (1989).
  86. Berkner, K. L. & Folk, W. R. Polynucleotide kinase exchange reaction. Quantitative assay for restriction endonuclease generated 5' phosphoryl termini in DNAs. *J. Biol. Chem.* **252**, 3176–3184 (1977).
  87. Murphy, C. I. *et al.* Expression and Purification of Recombinant Proteins Using the Baculovirus System. *Curr. Protoc. Mol. Biol.* **123**, (2018).
  88. Pots, J. Alfresco Developers Guide. *Am. J. Epidemiol.* **172**, NP (2010).
  89. Schmitt, J., Hess, H. & Stunnenberg, H. G. Affinity purification of histidine-tagged proteins. *Mol. Biol. Rep.* **18**, 223–230 (1993).
  90. Priestersbach, A., Kubicek, J., Schäfer, F., Block, H. & Maertens, B. Purification of His-Tagged Proteins. *Methods Enzymol.* **559**, 1–15 (2015).
  91. Crowe, J., Masone, B. S. & Ribbe, J. One-step purification of recombinant proteins with the 6xHis tag and Ni-NTA resin. *Methods Mol. Biol.* **58**, 491–510 (1996).
  92. Hartley, J. L., Temple, G. F. & Brasch, M. A. DNA cloning using in vitro site-specific recombination. *Genome Res.* **10**, 1788–1795 (2000).
  93. Hong, P., Koza, S. & Bouvier, E. S. P. A review size-exclusion chromatography for the analysis of protein biotherapeutics and their aggregates. *J. Liq. Chromatogr. Relat. Technol.* **35**, 2923–2950 (2012).
  94. Chromatography, G., Fágáin, C. Ó., Cummins, P. M. & Connor, B. F. O. Chapter 2. **681**, 25–33.
  95. Fekete, S., Beck, A., Veuthey, J. L. & Guillaume, D. Theory and practice of size exclusion chromatography for the analysis of protein aggregates. *J. Pharm. Biomed. Anal.* **101**, 161–173 (2014).
  96. Barth, H. G. & Boyes, B. E. Size Exclusion Chromatography. *Anal. Chem.* **62**, 268–303 (1990).
  97. Laemmli, U. K. 227680a0. *Nature* **227**, 680–685 (1970).
  98. Studier, F. W. Slab-gel electrophoresis. *Trends Biochem. Sci.* **25**, 588–590 (2000).
  99. Kielkopf, C. L., Bauer, W. & Urbatsch, I. L. Sodium dodecyl sulfate-polyacrylamide gel electrophoresis of proteins. *Cold Spring Harb. Protoc.* **2021**, 494–504 (2021).
  100. Al-Tubuly, A. A. SDS-PAGE and Western Blotting. **40**, 391–405 (2000).
  101. Kim, J., Otto, N., Conti, C. J., Gimenez-Conti, I. B. & Walker, C. L. *Immunohistochemical analysis of mTOR activity in tissues. Methods in Molecular Biology* vol. 821 (2012).
  102. Mahmood, T. & Yang, P. C. Western blot: Technique, theory, and trouble shooting. *N. Am. J. Med. Sci.* **4**, 429–434 (2012).
  103. Alegria-Schaffer, A. *Western blotting using chemiluminescent substrates. Methods in Enzymology* vol. 541 (Elsevier Inc., 2014).

104. Fenn, J. B. Electrospray wings for molecular elephants (Nobel lecture). *Angew. Chemie - Int. Ed.* **42**, 3871–3894 (2003).
105. Tanaka, K. The origin of macromolecule ionization by laser irradiation (Nobel lecture). *Angew. Chemie - Int. Ed.* **42**, 3860–3870 (2003).
106. Hou, T. Y., Chiang-Ni, C. & Teng, S. H. Current status of MALDI-TOF mass spectrometry in clinical microbiology. *J. Food Drug Anal.* **27**, 404–414 (2019).
107. Singhal, N., Kumar, M., Kanaujia, P. K. & Viridi, J. S. MALDI-TOF mass spectrometry: An emerging technology for microbial identification and diagnosis. *Front. Microbiol.* **6**, 1–16 (2015).
108. Thomas, S. N., French, D., Jannetto, P. J., Rappold, B. A. & Clarke, W. A. Liquid chromatography–tandem mass spectrometry for clinical diagnostics. *Nat. Rev. Methods Prim.* **2**, 1–14 (2022).
109. Wu, D. & Piszczek, G. Standard protocol for mass photometry experiments. *Eur. Biophys. J.* **50**, 403–409 (2021).
110. Stetefeld, J., McKenna, S. A. & Patel, T. R. Dynamic light scattering: a practical guide and applications in biomedical sciences. *Biophys. Rev.* **8**, 409–427 (2016).
111. Ve´ronique Receveur-Bre´chot, 1 Jean-Marie Bourhis, 1 Vladimir N. Uversky, 2, 3 Bruno Canard, 1 and Sonia Longhi1\*. Proteins - 2005 - Receveur-Br chot - Assessing protein disorder and induced folding.pdf.
112. Kelly, S. & Price, N. The Use of Circular Dichroism in the Investigation of Protein Structure and Function. *Curr. Protein Pept. Sci.* **1**, 349–384 (2005).
113. Abdul-Gader, A., Miles, A. J. & Wallace, B. A. A reference dataset for the analyses of membrane protein secondary structures and transmembrane residues using circular dichroism spectroscopy. *Bioinformatics* **27**, 1630–1636 (2011).
114. Rogers, D. M. *et al.* Electronic Circular Dichroism Spectroscopy of Proteins. *Chem* **5**, 2751–2774 (2019).
115. Whitmore, L. & Wallace, B. A. Protein secondary structure analyses from circular dichroism spectroscopy: Methods and reference databases. *Biopolymers* **89**, 392–400 (2008).
116. Greenfield, N. J. Using circular dichroism spectra to estimate protein secondary structure. *Nat. Protoc.* **1**, 2876–2890 (2007).
117. Lakowicz, J. R. *Principles of fluorescence spectroscopy, 3rd Principles of fluorescence spectroscopy, Springer, New York, USA, 3rd edn, 2006. Principles of fluorescence spectroscopy, Springer, New York, USA, 3rd edn, 2006.* (2006). doi:10.1007/978-0-387-46312-4.
118. Ghisaidoobe, A. B. T. & Chung, S. J. Intrinsic tryptophan fluorescence in the detection and analysis of proteins: A focus on Förster resonance energy transfer techniques. *Int. J. Mol. Sci.* **15**, 22518–22538 (2014).
119. Blanchet, C. E. *et al.* Versatile sample environments and automation for biological solution X-ray scattering experiments at the P12 beamline (PETRA III, DESY). *J. Appl. Crystallogr.* **48**, 431–443 (2015).
120. Graewert, M. A. *et al.* Automated pipeline for purification, biophysical and X-ray

- analysis of biomacromolecular solutions. *Sci. Rep.* **5**, 1–8 (2015).
121. Hajizadeh, N. R., Franke, D. & Svergun, D. I. Integrated beamline control and data acquisition for small-angle X-ray scattering at the P12 BioSAXS beamline at PETRAIII storage ring DESY. *J. Synchrotron Radiat.* **25**, 906–914 (2018).
  122. Franke, D. *et al.* ATSAS 2.8: A comprehensive data analysis suite for small-angle scattering from macromolecular solutions. *J. Appl. Crystallogr.* **50**, 1212–1225 (2017).
  123. Franke, D., Kikhney, A. G. & Svergun, D. I. Automated acquisition and analysis of small angle X-ray scattering data. *Nucl. Instruments Methods Phys. Res. Sect. A Accel. Spectrometers, Detect. Assoc. Equip.* **689**, 52–59 (2012).
  124. Panjkovich, A. & Svergun, D. I. CHROMIXS: Automatic and interactive analysis of chromatography-coupled small-angle X-ray scattering data. *Bioinformatics* **34**, 1944–1946 (2018).
  125. Franke, D., Jeffries, C. M. & Svergun, D. I. Correlation Map, a goodness-of-fit test for one-dimensional X-ray scattering spectra. *Nat. Methods* **12**, 419–422 (2015).
  126. Ruffino, F., Catania, U. & Sofia, S. Atomic Force Microscopy : Principles , Instrumentation , and Applications Part 1 : AFM , instrumentations , principles and.
  127. Johnson, D., Hilal, N. & Bowen, W. R. *Basic Principles of Atomic Force Microscopy. Atomic Force Microscopy in Process Engineering: An Introduction to AFM for Improved Processes and Products* (Elsevier Ltd, 2009). doi:10.1016/B978-1-85617-517-3.00001-8.
  128. Khurshudov, A. & Kato, K. Volume increase phenomena in reciprocal scratching of polycarbonate studied by atomic force microscopy. *J. Vac. Sci. Technol. B Microelectron. Nanom. Struct.* **13**, 1938–1944 (1995).
  129. NagDas S. K. & Bhattacharyya A. K. The kinetics of inhibition of human seminal plasma acid phosphatase by sodium fluoride. *Biochem. Int.* **9**, 659–668 (1984).
  130. Johan van Meerloo, Gertjan J.L. Kaspers, and J. C. & Abstract. Cell Sensitivity Assays: The MTT Assay. *Cancer Cell Cult.* **731**, 237–245 (2003).
  131. Losada-Garcia, N., Jimenez-Alesanco, A., Velazquez-Campoy, A., Abian, O. & Palomo, J. M. Enzyme/Nanocopper Hybrid Nanozymes: Modulating Enzyme-like Activity by the Protein Structure for Biosensing and Tumor Catalytic Therapy. *ACS Appl. Mater. Interfaces* **13**, 5111–5124 (2021).
  132. Flieger, A., Gong, S., Faigle, M. & Neumeister, B. Critical evaluation of p-nitrophenylphosphorylcholine (p-NPPC) as artificial substrate for the detection of phospholipase C. *Enzyme Microb. Technol.* **26**, 451–458 (2000).
  133. Moroz, O. V, Blagova, E., Lebedev, A. A., Nørgaard, A. & Segura, D. R. The structure of a calcium-dependent phosphoinositide- specific phospholipase C from *Pseudomonas* sp-62186 , the first from a Gram-negative bacterium. **73**, (2017).
  134. Lyu, Y. *et al.* Recent research progress with phospholipase C from *Bacillus cereus*. *Biotechnol. Lett.* **38**, 23–31 (2016).
  135. Buxton, R. Blood Agar Plates and Hemolysis Protocols. *Am. Soc. Microbiol.* 1–9 (2016).
  136. Savardi, M., Ferrari, A. & Signoroni, A. Automatic hemolysis identification on aligned

- dual-lighting images of cultured blood agar plates. *Comput. Methods Programs Biomed.* **156**, 13–24 (2018).
137. Huxford, T. X-Ray Crystallography. *Brenner's Encycl. Genet. Second Ed.* 366–368 (2013) doi:10.1016/B978-0-12-374984-0.01657-0.
  138. McPherson, A. & Gavira, J. A. Introduction to protein crystallization. *Acta Crystallogr. Sect. F Structural Biol. Commun.* **70**, 2–20 (2014).
  139. Pederson, T. Present at the Flood: How Structural Molecular Biology Came About. *FASEB J.* **20**, 809–810 (2006).
  140. Schenker, B., Jenkins, J. & Smith, D. Fast, reliable automation of protein crystallisation drop set-up. *Acta Crystallogr. Sect. A Found. Adv.* **70**, C1755–C1755 (2014).
  141. Gaisford, W., Schertler, G. & Edwards, P. mosquito® LCP: Making membrane protein crystallization accessible to the research scientist. *Nat. Methods* **8**, i–ii (2011).
  142. Gorrec, F. The MORPHEUS II protein crystallization screen. *Acta Crystallogr. Sect. Struct. Biol. Commun.* **71**, 831–837 (2015).
  143. CP Protein Science - 1997 - Hickman - Principles of Macromolecular X-Ray Crystallography.pdf.
  144. Burkhardt, A. *et al.* Status of the crystallography beamlines at PETRA III. *Eur. Phys. J. Plus* **131**, 0–8 (2016).
  145. Meents, A. *et al.* Development of an in-vacuum x-ray microscope with cryogenic sample cooling for beamline P11 at PETRA III. *X-Ray Nanoimaging: Instruments and Methods* **8851**, 88510K (2013).
  146. Taylor, G. L. Introduction to phasing. *Acta Crystallogr. Sect. D Biol. Crystallogr.* **66**, 325–338 (2010).
  147. Ke, H. Overview of isomorphous replacement phasing. *Methods Enzymol.* **276**, 448–461 (1997).
  148. Hendrickson, W. A., Smith, J. L. & Sheriff, S. Direct phase determination based on anomalous scattering. *Methods Enzymol.* **115**, 41–55 (1985).
  149. Cianci, M. *et al.* Anomalous scattering in structural chemistry and biology. *Crystallogr. Rev.* **11**, 245–335 (2005).
  150. Evans, P. & McCoy, A. An introduction to molecular replacement. *Acta Crystallogr. Sect. D Biol. Crystallogr.* **64**, 1–10 (2007).
  151. McCoy, A. J. Solving structures of protein complexes by molecular replacement with Phaser. *Acta Crystallogr. Sect. D Biol. Crystallogr.* **63**, 32–41 (2006).
  152. Krug, M., Weiss, M. S., Heinemann, U. & Mueller, U. XDSAPP: A graphical user interface for the convenient processing of diffraction data using XDS. *J. Appl. Crystallogr.* **45**, 568–572 (2012).
  153. van de Heetkamp, A. & Tusveld, R. Data processing with XDS and associated programs. *Orig. Manag.* 139–146 (2011) doi:10.1007/978-3-642-19808-3\_9.
  154. Vagin, A. & Teplyakov, A. MOLREP: An Automated Program for Molecular Replacement. *J. Appl. Crystallogr.* **30**, 1022–1025 (1997).

155. Afonine, P. V. *et al.* Towards automated crystallographic structure refinement with phenix.refine. *Acta Crystallogr. Sect. D Biol. Crystallogr.* **68**, 352–367 (2012).
156. Coot / Chimera CryoEM tutorial ( March. (2020).
157. Emsley, P. & Cowtan, K. Coot: Model-building tools for molecular graphics. *Acta Crystallogr. Sect. D Biol. Crystallogr.* **60**, 2126–2132 (2004).
158. Emsley, P., Lohkamp, B., Scott, W. G. & Cowtan, K. Features and development of Coot. *Acta Crystallogr. Sect. D Biol. Crystallogr.* **66**, 486–501 (2010).
159. Frank, J. Single-particle imaging of macromolecules by cryo-electron microscopy. *Annu. Rev. Biophys. Biomol. Struct.* **31**, 303–319 (2002).
160. Schultz, P. Cryo-electron microscopy of vitrified specimens. *Q. Rev. Biophys.* **21**, 129–228 (1988).
161. Henderson, R. *et al.* Model for the structure of bacteriorhodopsin based on high-resolution electron cryo-microscopy. *J. Mol. Biol.* **213**, 899–929 (1990).
162. Scheres, S. H. W. RELION: Implementation of a Bayesian approach to cryo-EM structure determination. *J. Struct. Biol.* **180**, 519–530 (2012).
163. Cheng, Y. *et al.* A Primer to Single-Particle Cryo-Electron Microscopy. *Physiol. Behav.* **176**, 139–148 (2016).
164. Bai, X. C., Rajendra, E., Yang, G., Shi, Y. & Scheres, S. H. W. Sampling the conformational space of the catalytic subunit of human g-secretase. *Elife* **4**, 1–19 (2015).
165. Doerr, A. Single-particle cryo-electron microscopy. *Nat. Methods* **13**, 23 (2016).
166. Raimondi, V. & Grinzato, A. A basic introduction to single particles cryo-electron microscopy. *AIMS Biophys.* **9**, 5–20 (2021).
167. Gasteiger, E. *et al.* Protein Identification and Analysis Tools on the ExPASy Server; The Proteomics Protocols Handbook. *Humana Press* **112**, 531–52 (2005).
168. Micsonai, A. *et al.* BeStSel: A web server for accurate protein secondary structure prediction and fold recognition from the circular dichroism spectra. *Nucleic Acids Res.* **46**, W315–W322 (2018).
169. Santoro M Marcelo, B. D. W. Unfolding free energy changes determined by the linear extrapolation method. Unfolding of phenylmethanesulfonyl alpha\_chymotrypsin using different denaturant. **87**, 186–187 (2012).
170. Kirby, E. P. & Steiner, R. F. The influence of solvent and temperature upon the fluorescence of indole derivatives. *J. Phys. Chem.* **74**, 4480–4490 (1970).
171. Guinier, A. La diffraction des rayons X aux très petits angles : application à l'étude de phénomènes ultramicroscopiques. *Ann. Phys. (Paris)*. **11**, 161–237 (1939).
172. Svergun, D. I. Determination of the regularization parameter in indirect-transform methods using perceptual criteria. *J. Appl. Crystallogr.* **25**, 495–503 (1992).
173. Hajizadeh, N. R., Franke, D., Jeffries, C. M. & Svergun, D. I. Consensus Bayesian assessment of protein molecular mass from solution X-ray scattering data. *Sci. Rep.* **8**, 1–13 (2018).

174. Petoukhov, M. V. & Svergun, D. I. Ambiguity assessment of small-angle scattering curves from monodisperse systems. *Acta Crystallogr. Sect. D Biol. Crystallogr.* **71**, 1051–1058 (2015).
175. Svergun, D. Restoring low resolution structure of biological macromolecules from solution. *Biophys. J.* **76**, 2879–2886 (1999).
176. Svergun, D., Barberato, C. & Koch, M. H. CRY SOL - A program to evaluate X-ray solution scattering of biological macromolecules from atomic coordinates. *J. Appl. Crystallogr.* **28**, 768–773 (1995).
177. Felts, R. L., Reilly, T. J. & Tanner, J. J. Structure of Francisella tularensis AcpA: Prototype of a unique superfamily of acid phosphatases and phospholipases C. *J. Biol. Chem.* **281**, 30289–30298 (2006).
178. Seiedi, O. *et al.* Atomic force microscopy (AFM) investigation on the surfactant wettability alteration mechanism of aged mica mineral surfaces. *Energy and Fuels* **25**, 183–188 (2011).
179. Lord, D. L. & Buckley, J. S. An AFM study of the morphological features that affect wetting at crude oil–water–mica interfaces. *Colloids Surfaces A Physicochem. Eng. Asp.* **206**, 531–546 (2002).
180. Liu, P. S. & Chen, G. F. Characterization Methods. *Porous Mater.* 411–492 (2014) doi:10.1016/B978-0-12-407788-1.00009-5.
181. Poturnayova, A. *et al.* Molecular Addressability of Lipid Membrane Embedded Calixarenes towards Cytochrome C. *J. Nanomed. Nanotechnol.* **5**, (2014).
182. Benaglia, S., Gisbert, V. G., Perrino, A. P., Amo, C. A. & Garcia, R. Fast and high-resolution mapping of elastic properties of biomolecules and polymers with bimodal AFM. *Nat. Protoc.* **13**, 2890–2907 (2018).
183. Hammond, K., Ryadnov, M. G. & Hoogenboom, B. W. Atomic force microscopy to elucidate how peptides disrupt membranes. *Biochim. Biophys. Acta - Biomembr.* **1863**, 183447 (2021).
184. Swana, K. W., Nagarajan, R. & Camesano, T. A. Atomic Force Microscopy to Characterize Antimicrobial Peptide-Induced Defects in Model Supported Lipid Bilayers. *Microorg. 2021, Vol. 9, Page 1975* **9**, 1975 (2021).
185. Kimanius, D., Dong, L., Sharov, G., Nakane, T. & Scheres, S. H. W. New tools for automated cryo-EM single-particle analysis in RELION-4.0. *Biochem. J.* **478**, 4169–4185 (2021).
186. Shawn Q. Zheng, Eugene Palovcak, Jean-Paul Armache, Kliment A. Verba, Yifan Cheng, and D. A. A. MotionCor2 - anisotropic correction of beam-induced motion for improved cryo-electron microscopy. *Physiol. Behav.* **176**, 139–148 (2018).
187. Wagner, T. *et al.* SPHIRE-crYOLO is a fast and accurate fully automated particle picker for cryo-EM. *Commun. Biol.* **2**, 1–13 (2019).
188. Zhang, K. Gctf: Real-time CTF determination and correction. *J. Struct. Biol.* **193**, 1–12 (2016).
189. Punjani, A., Rubinstein, J. L., Fleet, D. J. & Brubaker, M. A. CryoSPARC: Algorithms for rapid unsupervised cryo-EM structure determination. *Nat. Methods* **14**, 290–296

- (2017).
190. Punjani, A., Zhang, H. & Fleet, D. J. Non-uniform refinement: adaptive regularization improves single-particle cryo-EM reconstruction. *Nat. Methods* **17**, 1214–1221 (2020).
  191. Sanchez-Garcia, R. *et al.* DeepEMhancer: a deep learning solution for cryo-EM volume post-processing. *Commun. Biol.* **4**, 1–8 (2021).
  192. Terwilliger, T. C., Ludtke, S. J., Read, R. J., Adams, P. D. & Afonine, P. V. Improvement of cryo-EM maps by density modification. *Nat. Methods* **17**, 923–927 (2020).
  193. Jakobi, A. J., Wilmanns, M. & Sachse, C. Model-based local density sharpening of cryo-EM maps. *Elife* **6**, 1–26 (2017).
  194. Afonine, P. V. *et al.* Real-space refinement in PHENIX for cryo-EM and crystallography. *Acta Crystallogr. Sect. D Struct. Biol.* **74**, 531–544 (2018).
  195. Lee, P. S. & Lee, K. H. Escherichia coli - A Model System That Benefits from and Contributes to the Evolution of Proteomics. *Biotechnol. Bioeng.* **84**, 801–814 (2003).
  196. Elena, C., Ravasi, P., Castelli, M. E., Peirú, S. & Menzella, H. G. Expression of codon optimized genes in microbial systems: Current industrial applications and perspectives. *Front. Microbiol.* **5**, 1–8 (2014).
  197. Lipinski, Z. *et al.* Enhancing the Translational Capacity of E. coli by Resolving the Codon Bias. *ACS Synth. Biol.* **7**, 2656–2664 (2018).
  198. Jensen, M. A., Fukushima, M. & Davis, R. W. DMSO and betaine greatly improve amplification of GC-rich constructs in de novo synthesis. *PLoS One* **5**, 1–5 (2010).
  199. Asano, K. Attention-getting cross infections: Multidrug resistant Pseudomonas aeruginosa infections. *Nihon Naika Gakkai Zasshi.* **96**, 2465–2469 (2007).
  200. Coutinho, I. R., Berk, R. S. & Mammen, E. Platelet aggregation by a phospholipase C from Pseudomonas aeruginosa. *Thromb. Res.* **51**, 495–505 (1988).
  201. Berka, R. M., Gray, G. L. & Vasil, M. L. Studies of phospholipase C (heat-labile hemolysin) in Pseudomonas aeruginosa. *Infect. Immun.* **34**, 1071–1074 (1981).
  202. Berk, R. S., Brown, D., Coutinho, I. & Meyers, D. In vivo studies with two phospholipase C fractions from Pseudomonas aeruginosa. *Infect. Immun.* **55**, 1728–1730 (1987).
  203. König, B. & Vasil, M. L. Role of hemolytic and nonhemolytic phospholipase c from pseudomonas aeruginosa for inflammatory mediator release from human granulocytes. *Int. Arch. Allergy Immunol.* **112**, 115–124 (1997).
  204. Meyers, D. J. & Berk, R. S. Characterization of phospholipase C from Pseudomonas aeruginosa as a potent inflammatory agent. *Infect. Immun.* **58**, 659–666 (1990).
  205. GRANSTRÖM, M. *et al.* Relation between Antibody Response to Pseudomonas aeruginosa Exoproteins and Colonization/Infection in Patients with Cystic Fibrosis. *Acta Paediatrica* **73**, 772–777 (1984).
  206. Şener, B., Hasçelik, G., Özçelik, U., Günalp, A. & Göçmen, A. Neutrophil chemotaxis in acutely infected and clinically stable cystic fibrosis patients. *Pediatr. Int.* **41**, 514–518 (1999).

207. Wargo, M. J. *et al.* Hemolytic phospholipase C inhibition protects lung function during *Pseudomonas aeruginosa* infection. *Am. J. Respir. Crit. Care Med.* **184**, 345–354 (2011).
208. Montes, L. R. *et al.* Leakage-free membrane fusion induced by the hydrolytic activity of PlcHR2, a novel phospholipase C/sphingomyelinase from *Pseudomonas aeruginosa*. *Biochim. Biophys. Acta - Biomembr.* **1768**, 2365–2372 (2007).
209. Fitzsimmons, L. F., Hampel, K. J. & Wargo, M. J. Cellular choline and glycine betaine pools impact osmoprotection and phospholipase C production in *Pseudomonas aeruginosa*. *J. Bacteriol.* **194**, 4718–4726 (2012).
210. Jackson, A. A. *et al.* Anr and Its Activation by PlcH Activity in *Pseudomonas aeruginosa* Host Colonization and Virulence. **195**, 3093–3104 (2013).
211. Krissinel, E. & Henrick, K. Inference of Macromolecular Assemblies from Crystalline State. *J. Mol. Biol.* **372**, 774–797 (2007).
212. Felts, R. L., Reilly, T. J. & Tanner, J. J. Structure of *Francisella tularensis* AcpA: Prototype of a unique superfamily of acid phosphatases and phospholipases C. *J. Biol. Chem.* **281**, 30289–30298 (2006).
213. Fan, R. *et al.* Insights into the mechanism of phospholipid hydrolysis by plant non-specific phospholipase C. *Nat. Commun.* **14**, 1–11 (2023).
214. Johansen, K. A., Gill, R. E. & Vasil, M. L. Biochemical and molecular analysis of phospholipase C and phospholipase D activity in mycobacteria. *Infect. Immun.* **64**, 3259–3266 (1996).
215. Forrest Z. Bowling, Christian M. Salazar, Justin A. Bell, Tahrima S. Huq, Michael A. Frohman, M. V. A. Crystal structure of human PLD1 provides insight into activation by PI(4,5)P2 and RhoA. *Physiol. Behav.* **176**, 139–148 (2019).
216. Leiros, I., McSweeney, S. & Hough, E. The reaction mechanism of phospholipase D from *Streptomyces* sp. strain PMF. Snapshots along the reaction pathway reveal a pentacoordinate reaction intermediate and an unexpected final product. *J. Mol. Biol.* **339**, 805–820 (2004).
217. Leiros, I., Secundo, F., Zambonelli, C., Servi, S. & Hough, E. The first crystal structure of a phospholipase D. *Structure* **8**, 655–667 (2000).
218. Gottlin, E. B., Rudolph, A. E., Zhao, Y., Matthews, H. R. & Dixon, J. E. Catalytic mechanism of the phospholipase D superfamily proceeds via a covalent phosphohistidine intermediate. *Proc. Natl. Acad. Sci. U. S. A.* **95**, 9202–9207 (1998).
219. Martin, S. F. & Hergenrother, P. J. Catalytic cycle of the phosphatidylcholine-preferring phospholipase C from *Bacillus cereus*. Solvent viscosity, deuterium isotope effects, and proton inventory studies. *Biochemistry* **38**, 4403–4408 (1999).
220. Reilly, T. J., Baron, G. S., Nano, F. E. & Kuhlenschmidt, M. S. Characterization and sequencing of a respiratory burst-inhibiting acid phosphatase from *Francisella tularensis*. *J. Biol. Chem.* **271**, 10973–10983 (1996).
221. Srivastava, P. N., Brewer, J. M. & and Robert A. White, J. Hydrolysis of p-nitrophenylphosphorylcholine by alkaline phosphatase and phospholipase c from rabbit sperm-acrosome. **108**, 9–25 (2019).

222. Luberto, C. *et al.* Purification , Characterization , and Identification of a Sphingomyelin Synthase from *Pseudomonas aeruginosa*. **278**, 32733–32743 (2003).
223. Edward, E. A., El Shehawy, M. R., Abouelfetouh, A. & Aboulmagd, E. Prevalence of different virulence factors and their association with antimicrobial resistance among *Pseudomonas aeruginosa* clinical isolates from Egypt. *BMC Microbiol.* **23**, 1–13 (2023).

## Appendices

### Appendix I: DNA and protein sequences

>PLCH\_nucleotide\_sequence

ATGACCGAAAACCTGGAAATTCGCGCGTCGAACCTTTCTCAAGCACGGCGCCCAGG  
CCGCTACCCTGGCCGGCCTTTCCGGGCTGTTCCCGGAGACGCTCCGGCGCGCCCT  
GGCCATCGAGCCGGACATCCGCACCGGAACCATCCAGGACGTCCAGCACGTGGT  
CATCCTGATGCAGGAGAACCGCAGCTTCGATCACTACTTCGGCCACCTCAACGGC  
GTCCGCGGCTTCAACGATCCTCGCGCGCTCAAGCGCCAGGACGGCAAGCCGGTCT  
GGTACCAGAACTACAAGTACGAGTTCTCCCCCTATCACTGGGATACCAAAGTCAC  
CAGCGCCCAGTGGGTGAGTTCGCAGAACCATGAATGGTTCGGCCTTCCACGCGATC  
TGGAACCAGGGCCGCAACGACAAGTGGATGGCGGTGCAGTACCCCGAAGCCATG  
GGCTACTTCAAGCGCGGCGACATTCCCTACTACTACGCCCTGGCCGACGCCTTCA  
CCCTGTGCGAGGCCTACCACCAGTCGATGATGGGCCCCGACCAATCCGAACCGCCT  
CTACCACATGAGCGGACGCGCCGCCCCAGCGGGCGACGGCAAGGACGTACACAT  
CGGCAACGACATGGGCGACGGCACCATCGGCGCCAGCGGCACGGTGGACTGGAC  
CACCTATCCCGAGCGGCTAAGCGCCGCTGGCGTGGACTGGCGGGTCTACCAGGA  
AGGCGGCTACCGCTCCTCGTCACTCTGGTACCTGTACGTGACGCCTACTGGAAA  
TACCGGCTCCAGGAGCAGAACAACACTACGACTGCAACGCCCTCGCCTGGTTCAGGA  
ACTTCAAGAACGCTCCGCGCGATTTCGGACCTCTGGCAGCGCGCCATGCTCGCCCG  
CGGCGTCGACCAGTTGCGCAAGGATGTGCAAGAAAACACGCTGCCCGCAGGTGTC  
CTGGATCGTCGCGCCCTACTGCTACTGCGAGCATCCCTGGTGGGGCCCCCTCGTTC  
GGCGAGTACTACGTGACCCGGGTGCTCGACGCGCTGACCAGCAACCCCGAGGTCT  
GGGCCAGGACCGTGTTTCATCCTCAACTACGACGAGGGCGACGGCTTCTATGACCA  
CGCCAGCGCCCCGGTGCCGCCGTGGAAGGATGGCGTCGGCCTTTCACGGTCAGC  
ACCGCCGGCGAGATCGAGGCATCCAGCGGGCTGCCCATCGGGCTCGGCCACCGC  
GTCCCGCTGATCGCCATCTCGCCCTGGTTCGAAGGGCGGCAAGGTCAGCGCCGAAG  
TGTTTCGACCATACTCGGTGCTGCGCTTCTCGAACGCCGCTTCGGCGTCGTCGAG  
GAAAACATCTCGCCCTGGCGGCGTGCCGTCTGCGGGCGACCTGACTTCGCTGTTTCG  
ACTTCCAGGACGCAGGCGATAACCCAGGTGCGCCCCGACCTGACCAACGTCCCGCA  
GAGCGACGCGCGCAAGGAGGACGCCTACTGGCAGCAGTTCTACCGGCCAGCCC  
CAAGTACTGGTCTACGAGCCCAAGAGCCTGCCCCGGCCAGGAAAAGGGCCAGCG  
CCCTACCCTCGCGGTGCCCTACCAGTTGCACGCCACGCTGGCCCTCGACATCGCC  
GCCGGCAAGCTGCGCCTGACCCTGGGCAACGACGGCATGAGCCTGCCGGGCAAT  
CCGCAGGGACACTCCGCTGCGGTATTCCAGGTGCAGCCGCGGGAAGTCGGCAAT  
CCGCGTTTCTATACCGTGACCAGCTATCCGGTGGTCCAGGAAAGCGGAGAGGAAC  
TGGGCCGGACCCTCAACGACGAACTCGACGACCTGCTCGACGCCAACGGCCGCT  
ACGCCTTCGAGGTGCACGGCCCCAACGGCTTCTTCCGCGAGTTCCACGGCAACCT  
GCATCTCGCCGCGCAGATGGCGCGGCCCGAGGTATCGGTACCTATCAACGCAAC  
GGCAACCTGCAGTTGAACATCCGCAATCTCGGCCGCTGCCGTGCAGCGTGACGG  
TGACGCCGAACCCGGCCTATACCCAGGAGGGCAGCCGTCGCTATGAACTCGAAC  
CGAACCAGGCGATCAGTGAAGTGTGGCTGTTACGCAGCAGCCAGGGCTGGTACG  
ACCTCAGCGTGACCGCCAGCAATACGGAAGCCAACTATCTCCGCCGCTGGCCGG  
ACACGTCGAGACCGGCAAGCCGAGCAGGAGCGATCCATTGCTCGACATCGCAGC  
GACCTGA

>PLCH\_protein\_sequence\_histag Theoretical pI/Mw: 6.12 / 84281.89

MGSSHHHHHSQDPMTENWKFRRRTFLKHGAQAATLAGLSGLFPETLRRALAIEPDI  
RTGTIQDVQHVILMQENRSFDHYFGHLNGVRGFNDPRALKRQDGKPVWYQNYKY  
EFSPYHWDTKVTSAQWVSSQNHEWSAFHAIWNQGRNDKWMAVQYPEAMGYFKRG  
DIPYYYALADAFTLCEAYHQSMMGPTNPRLYHMSGRAAPSGDGKDVHIGNMDGD  
GTIGASGTVDWTTYPERLSAAGVDWRVYQEGGYRSSSLWYLYVDAYWKYRLQEQN  
NYDCNALAWFRNFKNAPRDSDLWQRAMLARGVDQLRKDVQENTLPQVSWIVAPY  
CYCEHPWWGSPFGEYYVTRVLDALTSNPEVWARTVFILNYDEGDGFYDHASAPVP  
WKDGVGLSTVSTAGEIEASSGLPIGLGHRVPLIAISPWSKGGKVS AEVFDHTSVLRFLE  
RRFGVVEENISPWRAVCGDLTSLDFDQDAGDTQVAPDLTNVPQSDARKEDAYWQQ  
FYRPSPKYWSYEPKSLPGQEKQRPTLAVPYQLHATLALDIAAGKLRLTLGNDGMSL  
PGNPQGHSAAVFQVQPREVGNPRFYTVTSYPVVQESGEELGRTLNDELDDLLDANG  
RYAFEVHGPNNGFFREFHGNLHLAAQMARPEVSVTYQRNGNLQLNIRNLGRLPCSVT  
VTPNPAYTQEGSRRYELEPNQAISEVWLLRSSQGWYDLSVTASNTEANYLRLLAGHV  
ETGKPSRSDPLLDIAAT

>PLCR2\_nucleotide\_sequence

ATGAATACAGCCACCGCTCCCGACAACCTGGAACAGCAACTCGGCGAGTTCGGC  
CGCAACGCCGGGCAGATGTCCGAGATCGAACGCAAGCAGGCCGCCGAAGGCCTG  
ATCGAACAGCTCAAGCGCGAGGTGGCGGTCGGCGCCGATCCGCGCCAGACCTTC  
GAGGAGATCCAGCGTCTGACGCCCTATGTGGAGGCCGATGCCAGGCGCCGCGAG  
GCGCTCGACTTCGAGATCTGGATGGCGCTCAAGGACAACGCCTCCGTCCAGCAGC  
AAGCGCCGACGCCTGGCGAGGAAGAGCAACTGCGCGAATACGCGCAAGAGTCGG  
ACAAGGTGATCGCCGAGGTGCTCGCCAGCGTCGACGGCGAGGAGCAGCGTCACG  
CCGCCATCGACGAACGCCTCAAGGCCCTGCGCAAGCAGATCTTCGGCGAGGAGA  
ACCCACGCCTGCTGCAACGCTGA

>PLCR2\_protein\_sequence\_histag Theoretical pI/Mw: 5.29 / 19352.41

MGSSHHHHHSSGLVPRGSHMNTATAPDNLEQQLGEFGRNAGQMSEIERKQAAEGL  
IEQLKREVAVGADPRQTFEEIQRLTPYVEADARRREALDFEIWMALKDNASVQQQAP  
TPGEEELREYAQESDKVIAEVLASVDGEEQRHAAIDERLKLALRKQIFGEENPRLLQR

>PLCN\_nucleotide\_sequence

ATGATTTGAAAAGCAGAAGAAGCTTCATCCGCCTGGCCGCCGGTACGGTTCGGCG  
CCACCGTCGCCACCAGCATGCTGCCGTCGAGCATCCAGGCGGCCCTGGCGATTCC  
CGCGCACCGCCGGCATGGCAACCTCAAGGACGTCGAGCACGTGGTGATCCTGAT  
GCAGGAGAACCGCTCCTTCGACCACTATTTCCGCACCCTCAAGGGCGTCCGCGGC  
TTCGGCGACCGCATGGCGATCCCGCTGCCCGACGGCCAGCGGGTCTGGCACCAGA  
AGGGCAGCAAGGGCGAGATCCTGCCCTACCACTTCGACACCAGCACCACCAGCG  
CCCAGCGCGTCGACGGTACCCCGCACACCTGGCCGGACGCCAGCAGGCCTGGA  
ACGAAGGGCGCATGGACAAGTGGTTGCCGGCCAAGACCGAGCGTTCCTGGGCT  
ACTACAAGGAGCAGGACATCGCCTTCCAGTTCGCGATGGCCAACGCCTTACCAT  
CTGCGACGCCTATCACTGCTCGTTCCAGGGCGGCACCAACCCCAACCGGCTGTTC  
CTCTGGACCGGCACCAACGACCCGCTCGGCCAGCATGGCGGCCCGGTAACCACC  
AACGACCACGACAGCAACGGCCCGGTGGAGCAGGGCTACACCTGGACCACCTAT  
CCCGAGCGCCTGCAGGCCCGCCGGCATCACCTGGCGGGTCTACCAGGACATGGCC

GACAACTTCTCCGACAACCCGCTGATCGGCTTCCGCCAGTACCGCGCCGCGGGCGC  
CTGACTCGCCGCTGATCGTCAACGGCCTGAGCACCTGGAAGCTCGATGCGCTGAA  
GCGCGACGTGCTGGCCAACAGCCTGCCGCAGGTGTCCTGGATCGTCGCCCCGGCC  
AAGTACTCCGAACACCCCGGCCCGTCCAGCCCGATCTGGGGGGCCGAGTACACTT  
CCTGGGTACTCGACGCGCTGACCGCCAACCCGGAGGTCTGGAGCAAGACCGCGC  
TGCTGGTGATGTTTCGACGAGAACGACGGCTTCTTCGACCACATCGCCCCGCCGGC  
CGCGCCGAGCCTGAACAAGGACGGCACGCTGCGCGGCAAGACCACCGCCGACGC  
CACCTCGAATGGCACACCAAGGGCGATATCCGTTATCGCAACCAGCCCTACGGC  
CTCGGCCCGCGGGTGCCGATGTACGTGATCTCGCCGTGGAGCAAGGGCGGCTGG  
GTCAACTCCCAGGTGTTTCGACCACACCTCGGTGATCCGCTTCTGGAGCAGCGCT  
TCGGGGTCATGGAGCCGAATATCAGTCCCTGGCGTCGTGCGGTCTGCGGCGACCT  
GACCTCGGCGTTCAACTTCGCCAACCCGAACAACGAGCCGTTCCCCGAACTGCCC  
GACACCAGCCAGGCCGACGCCATCGTCGCCAGCCAGATCAAGCTGCCGAAGCCG  
AAGCCGCCGGCGGTGGCCGCCATGCCCAAGCAGGAAATGGGCATCCGTCCGGCC  
CGCGCCTTGCCCTACGAGTTGGGCGTGCATGCGCGCTACCGCAGCGGCGGAGACG  
CGCTGAGCCTGACCTTCGCCAACACCGGCAAGGCCGGCGCGGTGTTCCAGGTGTT  
CGACCTGCTCGACAGCGAGAACCCGCCGAAACGCTACACCGTTGGCGCGCGCAA  
GCGCCTGCACGACAGCTTCCAGGGCGACGCCAGCGGCGACTACCACCTGGAAGT  
GCACGGTCCGAACGGTTTCTCCGGGTCTTCCGCGGCAACCTGCGGCGCGACCTG  
GCGGAGCGCAAGGCGCCGCTGCCGGAAGTGCGGATCGACTACGAGCCGCTGTT  
GGCAACCTGCGCGTGCAACTGATCAACCGTGGCCGCCATCCGGTCAAGCTGACGG  
TCAAGGACAACGTCTATCGCCAGGGCGAGCGGCGTACCGTCAACGTGCCGCCGG  
GACAGCGTCGGGAAGTCCGCTATTGCTGCGCAGCAGCGGCAACTGGTACGACTT  
CAGCGTCAGCGCGCAGGGGTCGGACAGCTTCTGCGGCGTTTCAGCGGTTCGCATG  
GAAGATGGTTCGCTCCGGCTTCAGCGACCCGGGCATGGGCCTGGGCACGCTGACCT  
TCTGA

>PLCN\_Protein\_sequence Molecular weight: 79338.20 Theoretical pI: 9.23

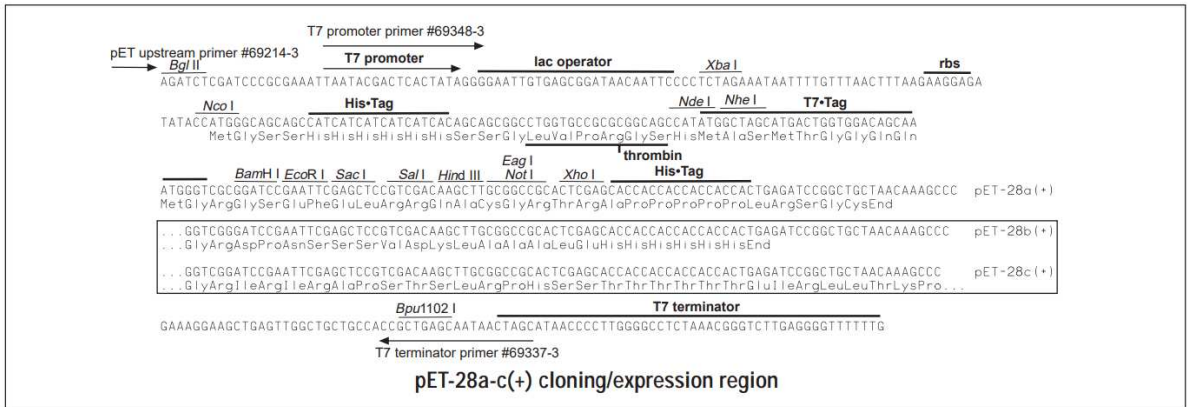
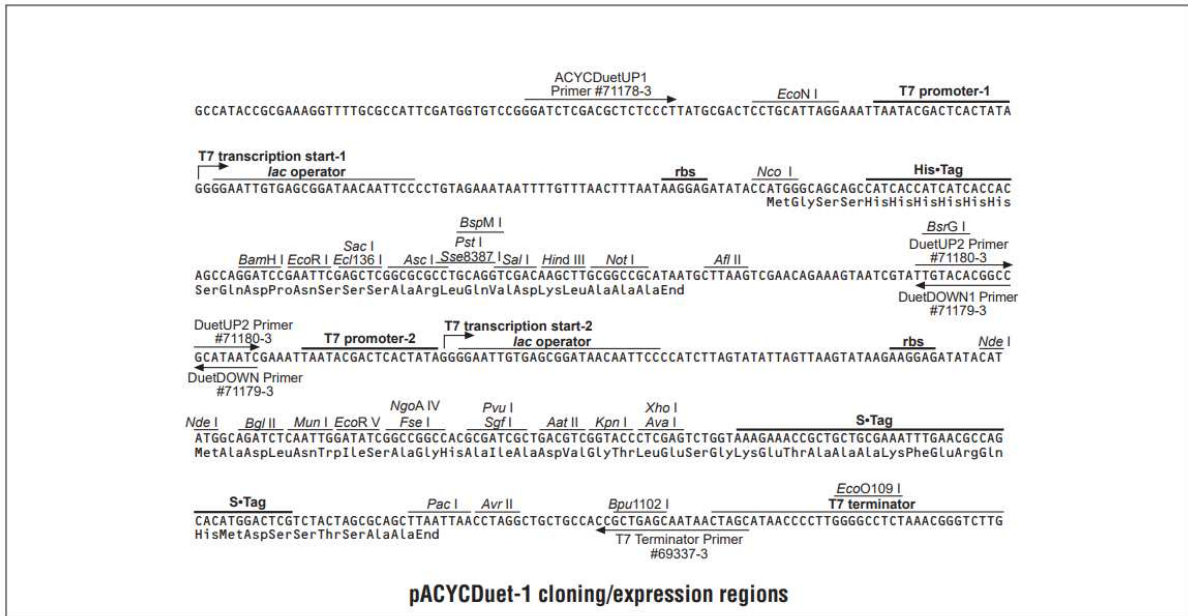
MGSSHHHHHSSGLVPRGSHMISKSRRSFIRLAAGTVGATVATSMPLSSIQAALAIIPA  
HRRHGNLKDVEHVVILMQENRSFDHYFGTLKGVRFGRMAIPLPDGQRVWHQKG  
SKGEILPYHFDTSTTSAQRVDGTPHTWPDAQQAWNEGRMDKWLPKTERSLGYYKE  
QDIAFQFAMANAFTICDAYHCSFQGGTNPRLFLWTGTNDPLGQHGGPVTTNDHDS  
NGPVEQGYTWTTPYPERLQAAGITWRVYQDMADNFSDNPLIGFRQYRAAAPDSPLIV  
NGLSTWKLDAKRDVLANSLPQVSWIVAPAKYSEHPGPSSPIWGAEYTSWVLDALT  
ANPEVWSKTALLVMFDENDGFFDHIAPPAAPSLNKDGTLRGKTTADATLEWHTKGD  
IRYRNQPYGLGPRVPMYVISPWSKGGWVNSQVFDHTSVIRFLEQRFGVMEPNISPWR  
RAVCGDLTSAFNFANPNNEPFPELPDTSQADAIVASQIKLPKPKPPAVAAMPKQEMGI  
RPARALPYELGVHARYRSGGDALSLTFANTGKAGAVFQVFDLLDSENPPKRYTVGA  
RKRLHDSFQGDASGDYHLEVHGPNGFLRVFRGNLRRDLAERKAPLPEVRIDYEPLFG  
NLRVQLINRGRHPVKLTVKDNVYRQGERRTVNVPPGQRREVRYSLRSSGNWYDFSV  
SAQGSDFSFLRRFSGRMEDGRSFGSDPGMGLGTLTF

## Appendix II: Primers

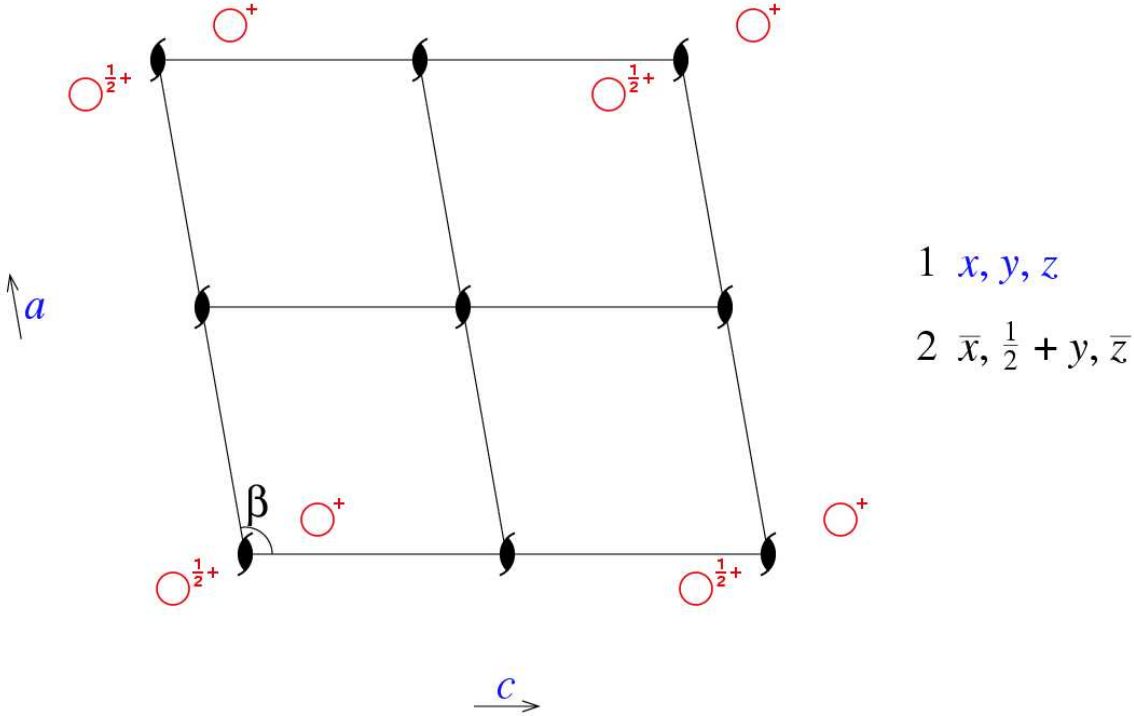
**Table II.1 Primers used for cloning**

Primers	Sequence	Base pairs (bp)	GC %	Tm (°C)
pACYCDUET-1_PLCH- _BamHI_F	AAAGGATCCGATGACCGAAA ACTGGAAATTC	31		
pACYCDUET-1_PLCH- HindIII-R	AAAAAGCTTTCAGGTCGCTG CGATG	25		
pET28a_PLCR2-NdeI-F	AAACATATGAATACAGCCAC CGCTC	25		
pET28a_PLCR2-XhoI-R	AAACTCGAGTCAGCGTTGCA GCAGG	25		
pET28a_PLCN_TAT_N deI_F	AAACATATGATTTTCGAAAAG CAGAAGAAG	29		62,8
pET28a_PLCN_TAT_X hoI_R	AAACTCGAGTCAGAAGGTCA GCGTGC	26		62
pACYCDUET- 1_PLCH_mut_T178A_F	GATGGGCCCGGCCAATCCGA ACC	23		
pACYCDUET- 1_PLCH_mut_T178A_R	ATCGACTGGTGGTAGGCCTC G	21		
pET28a_PLCN_mut_T1 76A_F	CCAGGGCGGCGCCAACCCCA ACC	23		
pET28a_ >PLCN_mut_T176A_R	AACGAGCAGTGATAGGCGTC GCAGATG	27		

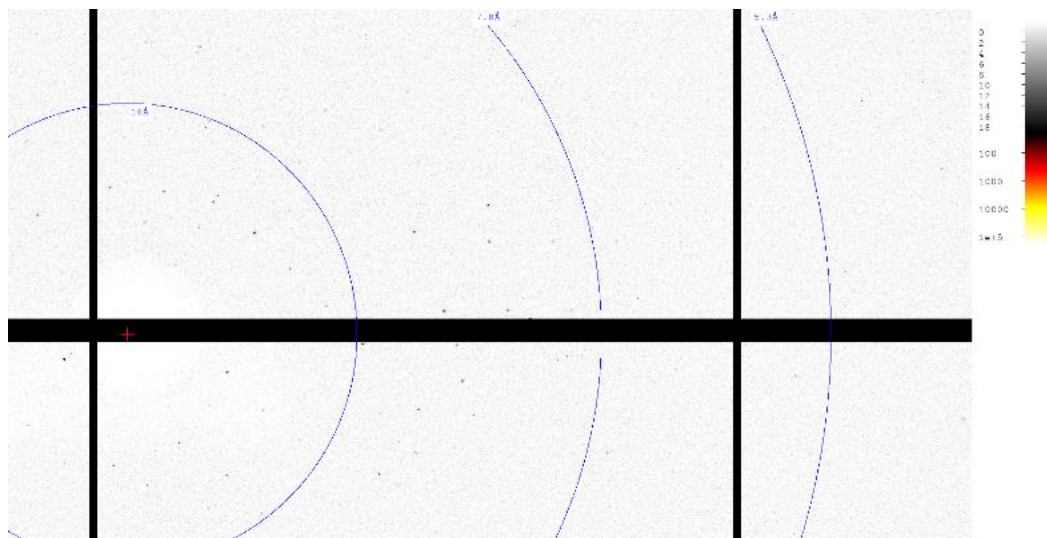
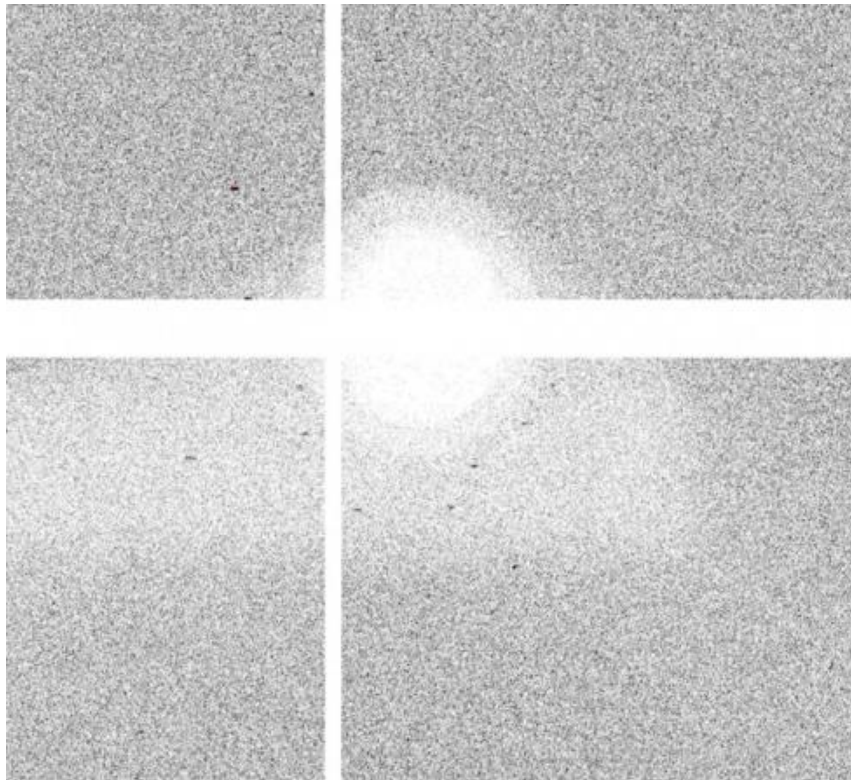
## Appendix III Vectors



**Appendix IV Space group and diffraction image**



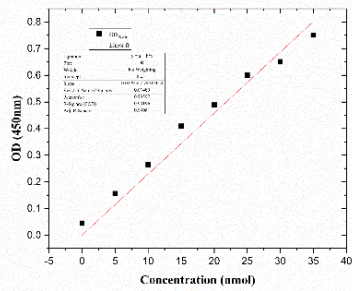
# PLCN needle crystals diffracted till 7Å resolution



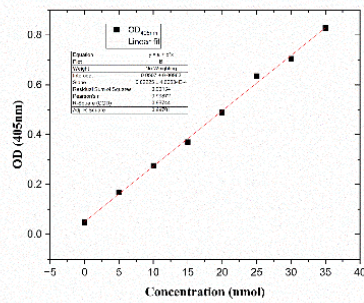
## Appendix V Activity standards and sequence alignment

NPPC Activity standards for PLCHR2 and PLCN (A and B), PLCHR2 and PLCN mutants (C and D), PLCHR2 and PLCN with different cations (E)

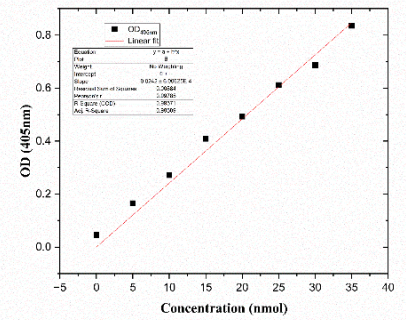
**A**



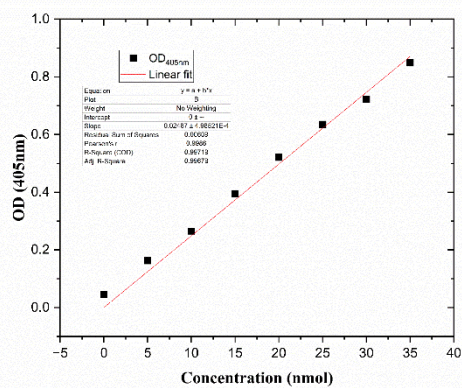
**B**



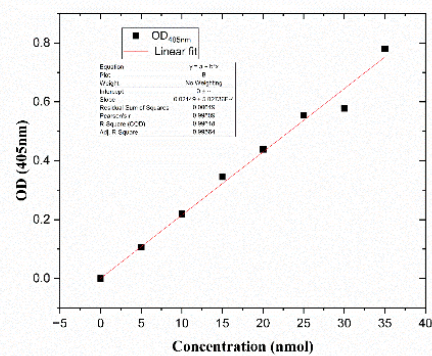
**C**



**D**



**E**



## Amino acid sequence alignments with UniProt (for SAXS)

[A0A0H2Z768: PLC](#)

```
      10   20   30   40   50   60
SAXS. MGSSHHHHHSQDPMTENWKFRRRTFLKHGAQAATLAGLSGLFPETLRRALAIEPDIRTG
      .....
UNIPRT      MTENWKFRRRTFLKHGAQAATLAGLSGLFPETLRRALAIEPDIRTG
      10   20   30   40

      70   80   90  100  110  120
SAXS. TIQDVQHVILMQENRSFDHYFGHLNGVRFNDPRALKRQDGKPVWYQNYKYEFSPYHWD
      .....
UNIPRT TIQDVQHVILMQENRSFDHYFGHLNGVRFNDPRALKRQDGKPVWYQNYKYEFSPYHWD
      50   60   70   80   90  100

      130  140  150  160  170  180
SAXS. TKV TSAQWVSSQNHEWSAFHAIWNQGRNDKWMVAVQYPEAMGYFKRGDIPYYALADAFTL
      .....
UNIPRT TKV TSAQWVSSQNHEWSAFHAIWNQGRNDKWMVAVQYPEAMGYFKRGDIPYYALADAFTL
      110  120  130  140  150  160

      190  200  210  220  230  240
SAXS. CEAYHQSMMPGPTNPRLYHMSGRAAPSGDGKDVHIGNMDMGDTIGASGTVDWTTYPERS
      .....
UNIPRT CEAYHQSMMPGPTNPRLYHMSGRAAPSGDGKDVHIGNMDMGDTIGASGTVDWTTYPERS
      170  180  190  200  210  220

      250  260  270  280  290  300
SAXS. AAGVDWRVYQEGGYRSSLWYLYVDAYWKYRLQEQNNYDCNALAWFRNFKNAPRDSLWQ
      .....
UNIPRT AAGVDWRVYQEGGYRSSLWYLYVDAYWKYRLQEQNNYDCNALAWFRNFKNAPRDSLWQ
      230  240  250  260  270  280

      310  320  330  340  350  360
SAXS. RAMLARGVDQLRKDVQENTLPQVSWIVAPYCYCEHPWWGSPFGEYVTRVLDALTSNPEV
      .....
UNIPRT RAMLARGVDQLRKDVQENTLPQVSWIVAPYCYCEHPWWGSPFGEYVTRVLDALTSNPEV
      290  300  310  320  330  340

      370  380  390  400  410  420
SAXS. WARTVFILNYDEGDGFYDHASAPVPPWKDGVGLSTVSTAGEIEASSGLPIGLGHRVPLIA
      .....
UNIPRT WARTVFILNYDEGDGFYDHASAPVPPWKDGVGLSTVSTAGEIEASSGLPIGLGHRVPLIA
      350  360  370  380  390  400

      430  440  450  460  470  480
SAXS. ISPWSKGGKVS AEVFDHTSVLRFLERRFGVVEENISPWRRVAVCGDLTSLFDFQDAGDTQV
      .....
UNIPRT ISPWSKGGKVS AEVFDHTSVLRFLERRFGVVEENISPWRRVAVCGDLTSLFDFQDAGDTQV
      410  420  430  440  450  460

      490  500  510  520  530  540
SAXS. APDLTNVPQSDARKEDAYWQQFYRPSPKYWSYEPKSLPGQEKQQRPTLAVPYQLHATLAL
      .....
UNIPRT APDLTNVPQSDARKEDAYWQQFYRPSPKYWSYEPKSLPGQEKQQRPTLAVPYQLHATLAL
      470  480  490  500  510  520

      550  560  570  580  590  600
SAXS. DIAAGKLRLTLGNDGMSLPGNPQGHSAAVFVQVQPREVGNPRFYTVTSYPVQESGEELGR
      .....
UNIPRT DIAAGKLRLTLGNDGMSLPGNPQGHSAAVFVQVQPREVGNPRFYTVTSYPVQESGEELGR
      530  540  550  560  570  580

      610  620  630  640  650  660
SAXS. TLNDELDDLLDANGRYAFEVHGPNGFFREFHGNLHAAQMARPEVSVTYQRNGNLQLNIR
      .....
UNIPRT TLNDELDDLLDANGRYAFEVHGPNGFFREFHGNLHAAQMARPEVSVTYQRNGNLQLNIR
      590  600  610  620  630  640

      670  680  690  700  710  720
SAXS. NLGRLPCSVTVTPNPAYTQEGSRRYEELEPNQAISEVWLLRSSQGWYDLSVTASNTEANYL
      .....
UNIPRT NLGRLPCSVTVTPNPAYTQEGSRRYEELEPNQAISEVWLLRSSQGWYDLSVTASNTEANYL
      650  660  670  680  690  700

      730  740
```

SAXS. RRLAGHVETGKPSRSDPLLDIAAT  
.....  
UNIPRT RRLAGHVETGKPSRSDPLLDIAAT  
710 720 730

A0A6N0KHT9: PlcR

10 20 30 40  
SAXS MGSSHHHHHSSGLVP-RGSHMNTATAPDNLEQQLGEFGRNAGQ  
.....  
UniPrt GAVLLLYPSEPAPVAPFASPPQATPAAKPSIPSRAPEMNTATAPDNLEQQLGEFGRNAGQ  
20 30 40 50 60 70

50 60 70 80 90 100  
SAXS MSEIERKQAAEGLIEQLKREVAVGADPRQTFEEIQR LTPYVEADARRREALDFEWMALK  
.....  
UniPrt MSEIERKQAAEGLIEQLKREVAVGADPRQTFEEIQR LTPYVEADARRREALDFEWMALK  
80 90 100 110 120 130

110 120 130 140 150 160  
SAXS. DNASVQQQAPTPGEEELREY AQESDKVIAEVLASVDGEEQRHAAIDERL KALRKQIFGE  
.....  
UniPrt DNASVQQQAPTPGEEELREY AQESDKVIAEVLASVDGEEQRHAAIDERL KALRKQIFGE  
140 150 160 170 180 190

170  
SAXS. ENPRL LQR  
.....  
UniPrt ENPRL LQR  
200

## **Acknowledgments**

I am deeply grateful to my supervisor, Prof. Dr. Jörg Labahn, for providing me with the opportunity to carry out my doctoral study at CSSB. His unwavering support, guidance, and mentorship have been instrumental in helping me grow and develop as a researcher. I cannot express enough how much I appreciate his patience with my project and his willingness to teach me everything I needed to know about scientific life and daily life. His support during the times of doctoral studies was particularly meaningful to me when I was not at my best. I owe him a debt of gratitude for intensive discussions on the pertinent topics and helping me become a better researcher.

I would also like to express my sincere thanks to Prof. Dr. Michael Kolbe and his group for providing me with support to complete my PhD project. When my experiment encountered difficulties, the people from Prof. Dr. Kolbe's group were always there to help me. I am especially grateful to the postdocs, Dr. Ge Yang and Dr. Michele Lunelli, for being a part of my PhD project and managing all the data processing from the Cryo-EM side. Their guidance in my experiments and various suggestions when I faced difficulties in my research have been invaluable to me. I would like to thank Andre Geisler for being part of this project. I would also like to thank Dr. Udom Sae-Ueng for helping me with the AFM experiments. I would like to thank Andre Geisler for being a part of this project and doing his Bachelors' thesis with me. (PLCN characterization)

I also want to thank Dr. Udaya Kumar Tiruttani Subhramanyam for his assistance with my professional and personal life here in Germany. His support has been instrumental in helping me navigate the challenges of living and working in a foreign country.

I am also grateful to my colleagues, Aziz Tumeh, Yajing Xiao Abhilasha Kerkmann, Dr. Chengcheng Tao and Dr. Weihou Guo, for their kindness, support, and every help. Working with them was a lot of fun, and I could not have accomplished as much without their assistance.

Furthermore, I want to acknowledge the technical support provided by the PPCF, especially Philipp Lewe at CSSB, and thank Dr. Stephan Niebling, Angelica Struve Garcia and David from EMBL for their patient instructions and guidance. I would also like to thank Dr. Cy Jeffery for helping me with the SEC-SAXS experiment. I would also like to acknowledge all the facilities at CSSB. Lastly, I would like to thank Sanchit Jain, for his immense support throughout my PhD thesis and for motivating and understanding me professionally and personally.

## **Erklärung**

Ich erkläre, dass ich die vorliegende Arbeit selbständig und ohne unerlaubte Hilfe verfasst habe. Die vorliegende Arbeit wurde weder in der jetzigen oder in ähnlicher Form bei einer anderen Institution eingereicht. Es wurden zuvor keine Promotionsversuche unternommen

Hamburg

-----

Nishika Sabharwal